
Charge collection of irradiated silicon pad
diodes and characterization of pixel sensor for
the CMS experiment

Dissertation
zur Erlangung des Doktorgrades
an der Fakultät für Mathematik, Informatik und Naturwissenschaften
Fachbereich Physik
der Universität Hamburg

vorgelegt von
Mohammadtaghi Hajheidari

Hamburg
2022

Gutachter/innen der Dissertation:

Prof. Dr. Erika Garutti

Prof. Dr. Peter Schleper

Zusammensetzung der Prüfungskommission:

Prof. Dr. Erika Garutti

Prof. Dr. Heinz Graafsmai

Prof. Dr. Nils Huse

Prof. Dr. Robin Santra

Prof. Dr. Peter Schleper

Vorsitzende/r der Prüfungskommission:

Prof. Dr. Robin Santra

Datum der Disputation:

19.09.2022

Vorsitzender Fach-Promotionsausschusses PHYSIK:

Prof. Dr. Wolfgang J. Parak

Leiter des Fachbereichs PHYSIK:

Prof. Dr. Günter H. W. Sigl

Dekan der Fakultät MIN:

Prof. Dr. Heinrich Graener

Abstract

Silicon sensors are considered for the Phase-2 upgrade of the Inner Tracker of the Compact Muon Solenoid (CMS) detector. The high radiation environment changes the properties of the sensors and degrades their performance. In this regard, two types of sensors are studied: pad diodes and hybrid pixel sensors. Both types of sensors are p -type with a thickness of $150\ \mu\text{m}$ produced by Hamamatsu Photonics K.K on the same wafer. Sensors are irradiated with $23\ \text{MeV}$ protons at the same irradiation facility.

Using Transient Current Technique with α -particles and red-light laser, Charge Collection Efficiency (CCE) of two irradiated pad diodes are measured close to their n^+ and p^+ implants. Irradiation is done at $1\ \text{MeV}$ neutron-equivalent fluences of 2 and $8 \times 10^{15}\ \text{cm}^{-2}$. For the n^+ implant, CCE measured by α -particles shows a higher value than measurements with a red-light laser for all bias voltage. By reducing the energy of α -particles, CCE results became similar to the CCE measured by a red-light laser. The results can be understood by assuming a "non-active region" with a reduced CCE. A model is developed to extract the width and CCE of this region. Next, charge collection profiles of non-irradiated and irradiated pad diodes are measured using a $5.2\ \text{GeV}$ electron beam traversing the diode parallel to the readout electrode. The CCE profiles as a function of depth are extracted by unfolding the measured charge collection profiles. The results of the measurements are compared to the simulation using three radiation damage models from the literature.

The second half of the work is related to the characterisation of hybrid pixel modules in the test-beam and lab. Planar sensors with various designs and pixel sizes of $25 \times 100\ \mu\text{m}^2$ and $50 \times 50\ \mu\text{m}^2$ are bump bonded to the RD53A readout chip. To extract parameters such as hit efficiency, spatial resolution, and cluster size, the irradiated and non-irradiated modules are tested at Deutsches Elektronen-Synchrotron (DESY) with $5.2\ \text{GeV}$ electron beam. Irradiation is done up to the $1\ \text{MeV}$ neutron-equivalent fluence of $2.0 \times 10^{16}\ \text{cm}^{-2}$. All irradiated modules, except one with a bias-dot, reach hit efficiency of 0.98 at a bias voltage below $800\ \text{V}$. The estimated spatial resolution degrades after irradiation due to the reduction of cluster size. The RD53A readout chip has a non-staggered bump-bond pattern. Therefore, the opening for passivation of the sensor pixel is not directly above its implant and routing is needed. This routing increases the cross-talk effect between neighbouring pixels in adjacent rows. Cross-talk biases the hit reconstruction by the sensor and deteriorates spatial resolution. In this work, cross-talk of three non-irradiated sensors with different designs is characterised using the charge injection method.

Kurzfassung

Für das Phase-2 Upgrade des inneren Spurdetektors des Compact Muon Solenoid (CMS) Detektors werden Siliziumsensoren in Betracht gezogen. Die hohe Strahlenbelastung im Detektor verändert die Sensoren und verschlechtert ihre Betriebseigenschaften. In diesem Zusammenhang werden zwei Arten von Sensoren untersucht: Planare Dioden und hybride Pixelsensoren. Beide Sensortypen wurden von Hamamatsu Photonics K.K auf demselben Wafer produziert und haben eine Dicke von $150\ \mu\text{m}$. Die Sensoren wurden in derselben Bestrahlungseinrichtung mit $23\ \text{MeV}$ Protonen bestrahlt.

Die Transient Current Technique mit α -Teilchen wurde genutzt, um die Ladungssammlungseffizienz (CCE) zweier bestrahlter Dioden nahe an den n^+ und p^+ Implantierungen zu messen. Die Dioden wurden zu $1\ \text{MeV}$ Neutronen äquivalenten Fluenzen von 2 und $8 \times 10^{15}\ \text{cm}^{-2}$ bestrahlt. An der n^+ Implantierungen ist, unabhängig von der angelegten Spannung, die mit α -Teilchen gemessene CCE höher als die mit rotem Laserlicht gemessene. Indem die Energie der α -Teilchen reduziert wird, gleichen sich die gemessenen CCEs an. Das Ergebnis lässt sich mit einer „inaktiven Region“, in der die CCE reduziert ist, erklären. Es wird ein Model entwickelt, mit dem sich die Breite und die CCE in dieser Region bestimmen lassen.

Als nächstes werden Ladungssammlungsprofile unbestrahlter und bestrahlter Dioden mit einem $5.2\ \text{GeV}$ Elektronenstrahl gemessen, wobei der Strahl parallel zur Ausleseelektrode der Diode ausgerichtet ist. Das Profil der CCE als Funktion der Tiefe wird durch Entfaltung aus den gemessenen Ladungssammlungsprofilen extrahiert. Die Ergebnisse werden mit Simulationen verglichen, denen drei unterschiedliche Modelle für Strahlenschäden aus der Literatur zugrunde liegen.

Die zweite Hälfte dieser Arbeit befasst sich mit der Charakterisierung hybrider Pixelmodule im Teststrahl und im Labor. Planare Sensoren mit verschiedenen Designs und Pixelgrößen von $25 \times 100\ \mu\text{m}^2$ und $50 \times 50\ \mu\text{m}^2$ werden per “bump bonding” mit dem RD53A Auslesechip verbunden. Um Größen wie die Nachweiseffizienz, das räumliche Auflösungsvermögen und die Clustergröße zu extrahieren, werden die bestrahlten und unbestrahlten Module am Deutschen Elektronen Synchrotron (DESY) mit einem $5.2\ \text{GeV}$ Elektronenstrahl getestet. Die Sensoren sind bis zu $1\ \text{MeV}$ Neutronen äquivalente Fluenzen von $2 \times 10^{16}\ \text{cm}^{-2}$ bestrahlt. Alle bestrahlten Module, bis auf jene mit einem “bias-dot”, erreichen Nachweiseffizienzen von 0.98 bei Spannungen unter $800\ \text{V}$. Das ermittelte räumliche Auflösungsvermögen reduziert sich nach der Bestrahlung wegen einer Reduktion der Clustergröße.

Aufgrund des Versatzes zwischen der Segmentierung des Sensors ($25 \times 100 \mu\text{m}^2$) und des Auslesechips ($50 \times 50 \mu\text{m}^2$) kommt es zu einem Übersprechen benachbarter Pixel. Dies beeinflusst die Trefferrekonstruktion in dem Sensor, sodass sich das räumliche Auflösungsvermögen verschlechtert. In dieser Arbeit wird das Übersprechen verschiedener Sensortypen mithilfe von Ladungsinjektion charakterisiert.

Contents

1	Introduction	1
2	Silicon Sensors	4
2.1	p-n Junction	4
2.2	Energy Loss in Silicon	7
2.3	Signal Formation in Silicon Sensors	9
2.4	Hybrid Pixel Sensor	12
2.5	Radiation Damage in Silicon	13
2.6	CMS Detector	15
2.7	Inner Tracker of the CMS Detector	17
3	Experimental setup for Test-Beam Measurements	20
3.1	An Overview of Test-Beam Infrastructures	20
3.1.1	DESY II Beam Line	20
3.1.2	Telescope	21
3.1.3	Trigger Unit	23
3.1.4	Timing Reference Module	25
3.1.5	Other Components of the Experimental Setup	25
3.2	Measurement Setup for Pixel Sensors	26
3.2.1	RD53A Readout Chip	26
3.2.2	Setup for Pixel Sensor Measurements	28
3.3	Measurement Setup for Pad Diodes	29
3.4	Specifications of Sensors	32
3.4.1	Planar Pixel Sensors	32
3.4.2	Pad Diodes	35
4	TCT measurements with pad diodes	38
4.1	Literature Review	38
4.2	Experimental Setup	40
4.3	Results for Non-Irradiated Diode	42
4.3.1	Geometrical Measurements	42
4.3.2	Energy Calibration	43
4.3.3	Results Taken at Cold Temperature	45

4.4	Results for Irradiated Diodes	47
4.4.1	Voltage-Dependent Charge Collection Efficiency	47
4.4.2	A Model for Characterisation of the Inactive Layer	49
4.5	Summary and Conclusion	51
5	Edge-on Measurements with Pad Diodes	54
5.1	Motivation	54
5.2	Definitions	57
5.3	In-situ Alignment	58
5.4	Charge Collection Profiles	62
5.4.1	Non-Irradiated Diodes	62
5.4.2	Irradiated Diodes	67
5.5	Comparison of the Data with TCAD Simulation	69
5.5.1	Hamburg Pent Trap Model	69
5.5.2	Perugia Models	71
5.5.3	Simulation of Charge Collection Profile	71
5.5.4	Comparison Between Data and HPTM	72
5.5.5	Comparison Between Data and Perugia Models	74
5.6	Extracting CCE Profile from Data	75
5.7	Summary and Conclusion	77
6	Characterisation of Planar Pixel Modules in Test-Beam	81
6.1	Tuning and Trimming of Readout Chip	81
6.1.1	Trimming of Readout Chip	82
6.1.2	Tuning of Threshold	82
6.1.3	Readout Chip Parameters	87
6.2	Installation and Online Monitoring in Test-beam	88
6.2.1	Configuring the Readout Chip	89
6.2.2	Online Monitoring	89
6.3	Analysis of Test-Beam Data for Pixel Sensors	90
6.3.1	Data Storage	91
6.3.2	Clustering Algorithm and Hit Reconstruction	92
6.3.3	Track Reconstruction	93
6.3.4	Telescope Alignment	94
6.3.5	Alignment of DUT	95
6.4	Definition of Observables	97
6.4.1	Hit Efficiency	97
6.4.2	Spatial Resolution	98
6.4.3	Cluster Size	102
6.4.4	Noisy Pixels	103

6.5	Selection Cuts	104
6.5.1	Cut 1: Link to Reference Module	104
6.5.2	Cut 2: Fiducial Region	104
6.5.3	Cut 3: Track Isolation in Reference Module	105
6.5.4	Cut 4: Track Isolation in DUT	105
6.5.5	Cut 5: Bunch Crossing ID of the DUT	105
6.5.6	Cut 6: Residual Cut	106
6.5.7	Cut 7: Charge Cut	106
6.5.8	Cut 8: Residual Pairing	107
6.6	Results and Discussion	107
6.6.1	Results of Non-Irradiated Modules	108
6.6.2	Results of Irradiated Modules	114
6.7	Summary and Conclusion	118
7	Study of Cross-Talk with Charge Injection	122
7.1	Introduction	122
7.2	Sensor Designs	122
7.3	Definition of Cross-Talk	123
7.4	Tuning of ROC	124
7.5	Cross-talk Measurement Results	125
7.6	Analysis of Data	126
7.7	Summary	127
8	Summary and Conclusion	131
	List of Figures	136
	List of Tables	136
	Bibliography	147
	Appendix A	149
	Appendix B	149
	Acknowledgments	150
	Eidesstattliche Versicherung /Declaration on oath	152

1 Introduction

The Standard Model of particle physics (SM) is our best understanding of the elementary particles and their interactions [1]. The theory has been validated by experimental observations in lepton and hadron colliders. The last missing particle was the Higgs Boson which was discovered in the Large Hadron Collider (LHC) [2, 3]. However, there are still some open questions that the SM can not resolve. The Hierarchy problem or the significant difference between the weak and gravity interactions is one of these issues [4]. The theory fails to accommodate the gravity force. Moreover, none of the SM particles fit the candidate for dark matter.

To answer these questions, new models such as Super-Symmetry [5], and Grand Unified Theory [6] have been proposed. These theories predict new particles with masses in the TeV scale. A discovery machine such as LHC is looking to find these particles [7]. Several upgrades are planned for the High-Luminosity LHC (HL-LHC) phase to extend the discovery potential of LHC and improve the statistical uncertainty of analysis efforts. It is foreseen that the integrated luminosity and the number of interactions per bunch crossing or pileup will increase by a factor of 10 in HL-LHC [8].

Compact Muon Solenoid (CMS) is one of the running experiments at LHC [9] and will undergo a significant upgrade for the next phase of data taking at HL-LHC [10]. The Inner Tracker (IT) of the detector is the closest part to the collision point and consists of the hybrid pixel sensors. These are segmented silicon sensors that are bump bonded to readout chips with equal segmentation.

For the HL-LHC phase, the IT system will be replaced entirely. The upgrade is planned to cope with the increase in instantaneous and integrated luminosity. At higher instantaneous luminosity, a higher track density is expected. Therefore, the pixel size of sensors will be reduced to keep the occupancy of the detector at an acceptable level. Moreover, the radiation fluence will increase at higher integrated luminosity, which leads to increased radiation damage in the silicon sensors. The thickness of the sensors will be reduced to minimise the damage effects.

This work aims to understand the behaviour of silicon sensors after irradiation at high fluences and their performance as a tracking detector. Hybrid pixel modules are an excellent choice as a tracking detector. However, they are not an ideal choice if one is interested in studying the physics of radiation damage. Pad diodes are a better option for that study due to their simpler structure. In this regard, the work is divided into two parts: in the first part, the results of the characterisation of pad diodes before and after

irradiation are given; in the second part, hybrid pixels sensors designed for the IT of the CMS detector for the HL-LHC phase are characterised, and their critical parameters as a tracking detector are extracted. Both types of sensors were produced on the same wafer and therefore have the same thickness and doping profiles.

This work starts with an overview of the basic principles of silicon sensors and their operation inside the CMS detector in Chapter 2. In Chapter 3, a summary of the test-beam infrastructures used for the sensor characterisations is given. The specifications of sensors studied in this work are described in the last part of the chapter.

Reduction of the measured charge by the sensor after irradiation is a known effect. This is due to the radiation-induced defects in the silicon band gap, which can act as trapping centres for free charge carriers. Several groups have used the results of the measurements with the Transient Current Technique (TCT) to extract trapping rates of electrons and holes in irradiated silicon sensors. In this method, a certain amount of charge is injected into the non-irradiated and irradiated sensors. One can estimate the trapping rate of charge carriers, electrons and holes, by comparing the charge collected in irradiated sensors to that in non-irradiated ones. The method requires stable illumination sources for charge injection. Often, alpha particles and red-light laser have been used for this purpose. A discrepancy between the published results is observed: some suggested higher trapping rates for electrons while the others found the opposite, depending on the illumination source. In Chapter 4, the results of measurements of pad diodes using TCT with both alpha particle and red-light laser are presented in terms of Charge Collection Efficiency (CCE). An empirical model which assumes a non-active region close to the implant is proposed and fitted to the data. A decrease in the active thickness of the pad diodes after irradiation is concluded. It is found that not taking into account this effect leads to underestimation of CCE in the active region.

Another important change in silicon after irradiation is the change of the doping profile. This can change the electric field and charge collection profiles as a function of depth. To investigate this effect, edge-TCT has been used in the literature. In this method, the sensor is illuminated from the side with focused Infra-Red (IR) laser light and scanned across the sensor's depth. In this work, an edge-on method using an electron beam has been developed. This type of measurement results in the charge collection profile as a function of depth for pad diodes. The method is introduced in Chapter 5, and the measured results for the non-irradiated and irradiated diodes are presented. The procedure to compare the experimental data with existing radiation damage models is then described and done for three models. At the end of the chapter, the procedure to correct the data for experimental effects, such as the limited beam resolution, is described, and CCE profiles are extracted.

The second half of this thesis is related to the characterisation of planar pixel sensors in the test-beam and lab. Chapter 6 begins with a summary of the preparation of the sensor-readout modules for the test-beam measurements. Then, the analysis flow for the data

taken in the test-beam is described, and observables are introduced. The performance parameters of the pixel modules include hit efficiency, spatial resolution, and cluster sizes. These parameters are extracted as a function of the sensor bias voltage and incident angle of tracks with respect to the sensor surface and presented in the last part of the chapter. It is concluded that the planar pixels sensors meet the hit efficiency requirements for the Phase-2 upgrade of CMS IT.

An important effect in pixel modules is the cross-talk between adjacent pixels. Due to this effect, the charge induced by a real hit in one pixel is coupled to its neighbouring pixel. The cross-talk can be either due to the design of the readout chip or capacitive coupling between two adjacent pixels. For this work, the readout chip has non-staggered bump-bond pattern. Therefore, the opening for passivation of the sensor pixel is not directly above its implant and routing is needed which increases the effect of the cross-talk. In Chapter 7, a methodology to quantify the cross-talk is introduced, and the characterisation results are shown for different sensor designs. It is shown that chipping away a part of implant close to the bump-bond connection reduces the cross-talk.

In Chapter 8, a summary of the obtained results is given. Conclusions are drawn on the impact of the radiation damage on silicon pad diodes and pixel sensors designed for the Phase-2 upgrade of the CMS detector.

2 Silicon Sensors

Silicon is a semiconductor in the IV group of the periodic table. The band gap energy of silicon is 1.12 eV at room temperature. The mean ionisation energy to produce one electron-hole pair is 3.6 eV. Silicon radiation detectors are commonly made of mono-crystals with miller indices of $\langle 100 \rangle$.

One example of using silicon as a radiation detector in high-energy physics experiments is the IT of the CMS experiment, where silicon pixel sensors are used to reconstruct the trajectory of the charged particles from the collision point. The momentum of particles is derived by measuring the curvature of their trajectories in the magnetic field. The reconstructed trajectories can also be used to link measurements in other parts of the CMS detector, such as calorimeters and muon chambers, in the context of the particle flow reconstruction [11].

In this thesis, two types of silicon sensors were studied: pad diodes and pixel sensors. In this chapter, an overview of the basic principles of silicon sensors is given. The properties of a p-n junction are introduced in Section 2.1. The energy loss mechanisms of charged particles in silicon are explained in Section 2.2. The signal formation in a silicon sensor is described in Section 2.3. The concept of the hybrid pixel sensor is introduced in Section 2.4. An overview of the radiation damages in silicon is given in Section 2.5. The CMS detector is introduced in Section 2.6. The IT of the CMS detector and its upgrade for the Phase-2 is introduced in Section 2.7.

2.1 p-n Junction

Due to their periodic structures, crystals have discrete energy bands for electrons: the lowest band, which is full at $T = 0$ K is called the valence band, and the higher band is called the conduction band. The occupancy probability of an energy state E is given by the Fermi-Dirac distribution [12]:

$$f(E) = \frac{1}{1 + e^{(E-E_F)/k_B T}} \quad (2.1)$$

Where, T is the temperature, k_B is the Boltzmann constant and E_F is the Fermi energy. At higher temperatures, electrons gain energy to excite from the valence to the conduction band. Electrons in the conduction band are free to migrate in the crystal and contribute to the electric current. The excitation of an electron leaves a hole in the valence band with

a positive electric charge. Electrons and holes are the two fundamental charge carriers in silicon.

For almost all applications in radiation detection, pure silicon is doped with impurities. As a result, new energy bands are added to silicon's band gap, and silicon's conductivity is changed. There are two types of doped materials: *n*-type, where the impurity atom is a donor, which means it adds one electron to the crystal, and *p*-type, where the impurity atom is an acceptor which means it accepts an electron from the crystal and thus adds a hole to the crystal. In terms of the energy band diagram, donors and acceptors introduce energy bands close to the conduction and valence bands, respectively. This change can be seen in Fig. 2.1 which shows the band diagrams of intrinsic, *n*-type, and *p*-type semiconductors. From the concentration of charge carriers shown in Fig. 2.1, i.e. *n* and *p*, one sees that the electrons in the conduction band and holes in the valence band are the majority of free charge carriers in *n*-type and *p*-type materials, respectively.

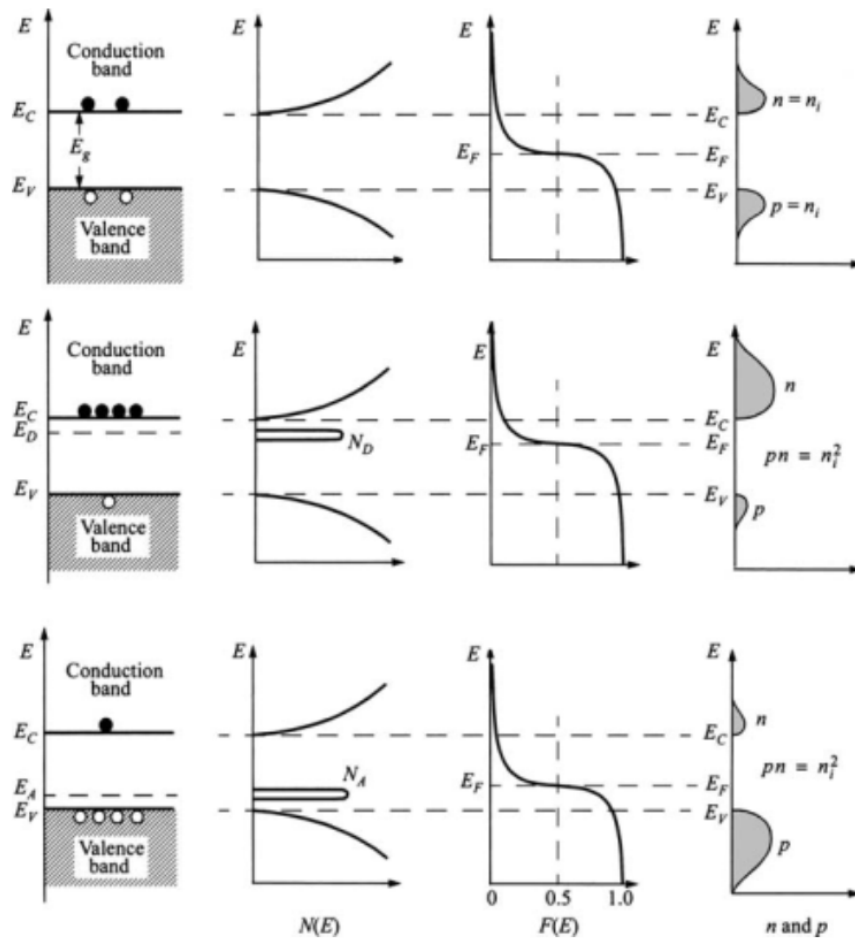


Figure 2.1: Schematic of band diagram for different types of materials. The material types from top to bottom: intrinsic, *n*-type, *p*-type. The quantities from left to right: band diagram, density of states $N(E)$, Fermi-Dirac distribution $f(E)$ and charge carrier concentration (n and p). The sketch is taken from [13].

The usual doping materials as a donor for *n*-type material are Phosphorus or Arsenic from the V group. Elements from group III, such as Boron, are an acceptor for *p*-type

material.

The basic building block of silicon sensors is a p-n junction which is the interface between a p - and a n -type material. Due to the difference in the concentration of charge carriers in the two regions, electrons diffuse from the n -type region to the p -type region and recombine with free holes. The same happens to holes in the opposite direction. As a result, a space charge region is built up, which is positive in the n -type region and negative in the p -type region. The space charge region, also called the depletion zone, has no free charge carriers and only includes the fixed ionised atoms. An electric field is built up due to the space charge region. The built-in electric field direction is opposite to the direction of the diffusion current until an equilibrium is reached.

If the doping concentrations of donors (N_D) and acceptors (N_A) in n - and p -sides are equal, the depletion zone extends equally on both sides. For a p^+n junction where $N_A \gg N_D$, the depletion zone extends mostly in the n -side region. The studied sensors for this work have a n^+p junction where the concentration of electrons in n^+ -region is ≈ 5 orders of magnitude higher than the concentration of holes in p -region. In Fig. 2.2, a sketch of a p^+n junction is shown.

To extend the depletion zone to the whole n-p junction, an external electric field is needed. By applying a bias voltage to the junction where n^+ -side is connected to the positive polarity and p -side is connected to the negative polarity, the depletion zone width, W , is increased. This configuration is called reverse bias, and the width of the depletion zone is given by:

$$W = \sqrt{\frac{2\epsilon_s\epsilon}{eN_A}(\Psi_{bi} + V_{bias})} \quad (2.2)$$

In this relation, e is the elementary charge, ϵ_0 is the vacuum permittivity ($8.85 \times 10^{-12} \text{ F} \cdot \text{m}^{-1}$), ϵ_s is the relative permittivity of silicon (11.7), N_A is the doping concentration of acceptors in p -region, Ψ_{bi} is the build-in potential, and V_{bias} is the external applied bias voltage.

Full depletion voltage, V_{FD} is the bias voltage needed to fully depleted the junction can be calculated by:

$$V_{FD} = \frac{e|N_A|d^2}{2\epsilon_s\epsilon} \quad (2.3)$$

Where d is the physical thickness of the junction. In this relation, the effect of the built-in potential (Ψ_{bi}) is neglected. At bias voltages higher than V_{FD} , the electric field strength inside the junction is increased. The depleted p-n junction can be used as a radiation sensor, as discussed in Section 2.3.

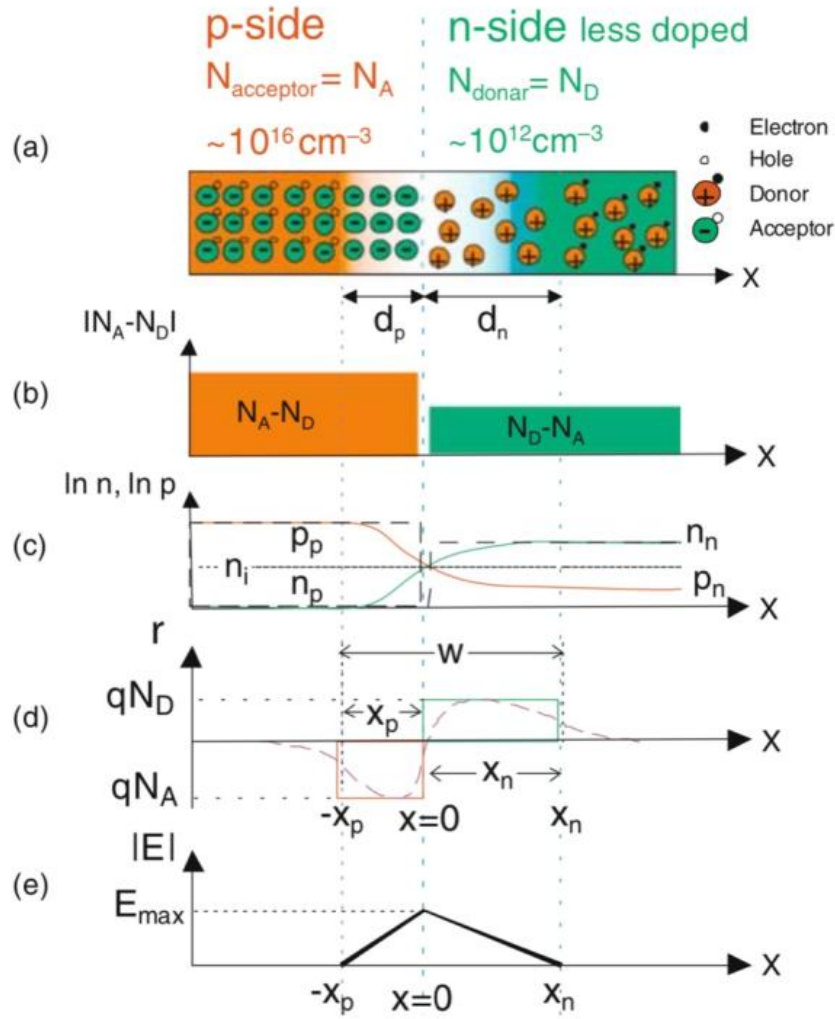


Figure 2.2: Sketch of p^+n junction (a), doping concentration profile (b), free charge carriers profile (c), space charge density profile (d), build-in electric field profile (e). The sketch is taken from [14].

2.2 Energy Loss in Silicon

When a charged particle passes through a matter, it loses energy and ionises the atoms. In semiconductors, the ionisation of atoms results in the creation of electron-hole pairs, which are used as signals of incoming particles. The mechanism in which charged particles lose energy in a medium depends on factors such as mass, charge, energy of the particles, density, and the atomic number of the medium. "Bethe-formula" describes the mean energy loss of relativistic charged particles as follows:

$$\left\langle -\frac{dE}{dx} \right\rangle = K z^2 \frac{Z}{A} \frac{1}{\beta^2} \left[\frac{1}{2} \ln \frac{2m_e c^2 \beta^2 \gamma^2 W_{\text{max}}}{I^2} - \beta^2 - \frac{\delta(\beta\gamma)}{2} \right] \quad (2.4)$$

In this formula:

- I : mean excitation energy in eV

2 Silicon Sensors

- Z : atomic number of the medium
- A : atomic mass of the medium
- z : charge of the incoming particle
- $\beta = v/c$ where v is the velocity of the incoming particle
- $\gamma = \frac{1}{\sqrt{1-\beta^2}}$: Lorentz factor
- W_{max} : maximum energy transfer in a single collision
- $\delta(\beta\gamma)$: the density effect correction
- $m_e c^2$: mass of the electron 0.511 MeV
- $K = 0.307 \text{ MeV mol}^{-1} \text{ cm}^2$

The Bethe formula describes the mean energy loss or stopping power in the energy range of $0.1 < \beta\gamma < 1000$. In Fig. 2.3, the mean stopping power, $\langle -\frac{dE}{dx} \rangle$, of anti-muons in copper is shown. One sees that at high energies above $E_{\mu c}$, most of the energy-loss is in the form of radiative processes such as Bremsstrahlung and pair-production.

In this work, silicon sensors with a thickness of 150 μm are studied with an electron beam with an energy of 5.2 GeV. For electrons with this range of energy, radiative processes must be considered. However, most produced photons are hard and escape the sensor without interactions. Therefore, the effect of radiative losses is minimal [15]. In Fig. 2.3, a broad minimum is seen at $\beta\gamma \approx 3$. A particle with a minimum energy loss is called a Minimum Ionising Particle (MIP). Particle detectors are usually characterised by the smallest possible signal using MIP.

The mean value of the energy loss is weighted by rare events with large single-collision energy transfer and therefore is subject to large fluctuations. The fluctuations are due to the number of collisions and the energy transfer per collision. The Most Probable Value (MPV) of energy loss distribution is considerably lower than its mean values calculated by Fig. 2.3[16]. MPV is a better quantity to describe the energy loss by single particles. Estimated energy loss for electrons with an energy of 5 GeV in 5 mm of silicon is 40.8 keV. The mean ionisation energy in silicon is 3.67 eV from [17] which translates to a signal with 11.1 ke. In the depleted region of a p-n junction, this signal is well above the intrinsic free charge carriers and can be easily detected.

It should be noted that the ionisation energy in silicon (3.67 eV) is more than three times higher than the band gap energy (1.12 eV). This difference is due to the "indirect band gap" of silicon, which means the maximum of the valence band and minimum of the conduction band is offset. Therefore, to excite an electron from the valence to the conduction band, it must transfer energy and momentum simultaneously. At energies higher than 50 eV, the additional constraint of momentum conservation becomes significant and

the ionisation energy is around 3.6 eV [18]. For this work, the ionisation energy of 3.6 eV is used.

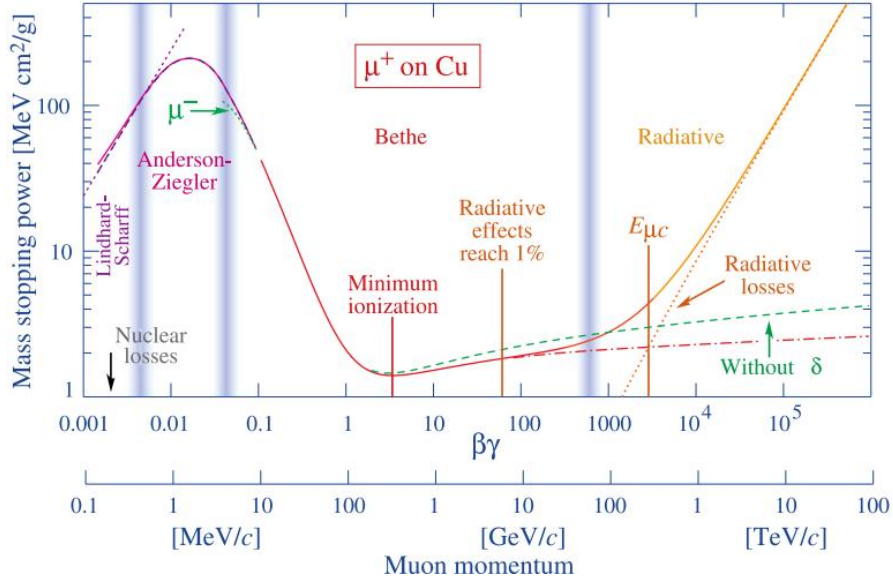


Figure 2.3: Mean stopping power of anti-muons in copper as a function of $\beta\gamma$. The solid line shows the total stopping powers. The plot is taken from [16].

2.3 Signal Formation in Silicon Sensors

Ionising radiation produces free charge carriers, i.e. electron-hole pairs, as they are passing a silicon sensor. As discussed in Section 2.1, an electric field is obtained by applying an external bias voltage to the p-n junction. The produced electron-hole pairs in the sensor start to drift in the electric field towards electrodes as shown in Fig. 2.4. In this example, electrons and holes drift to the n^+ and p^+ implants, respectively. According to Ramo's theorem [19], the drift of a charge carrier, q , induces a current in the electrodes:

$$I = q\vec{E}_w \cdot \vec{v} \quad (2.5)$$

In this relationship, \vec{E}_w is the weighting field of the sensor and \vec{v} is the velocity of the charge carrier, q , in the sensor. The drift velocity of charge carriers in an electric field of $\vec{E}(x)$ can be calculated as:

$$\vec{v}_{e,h}(x) = \mu_{e,h}(\vec{E}(x)) \cdot \vec{E}(x) \quad (2.6)$$

Where $\mu_{e,h}(\vec{E}(x))$ is the mobility of electrons and holes and is a function of the electric field itself. Here x is defined in the direction perpendicular to the electrodes. As indicated in Eq. (2.6), velocity and charge carrier are position-dependent quantities.

The weighting field, \vec{E}_w , determines the coupling of a charge drift to the electrodes. For a pad diode, the weighting field is simply $1/d$ where d is the thickness of the diode. For

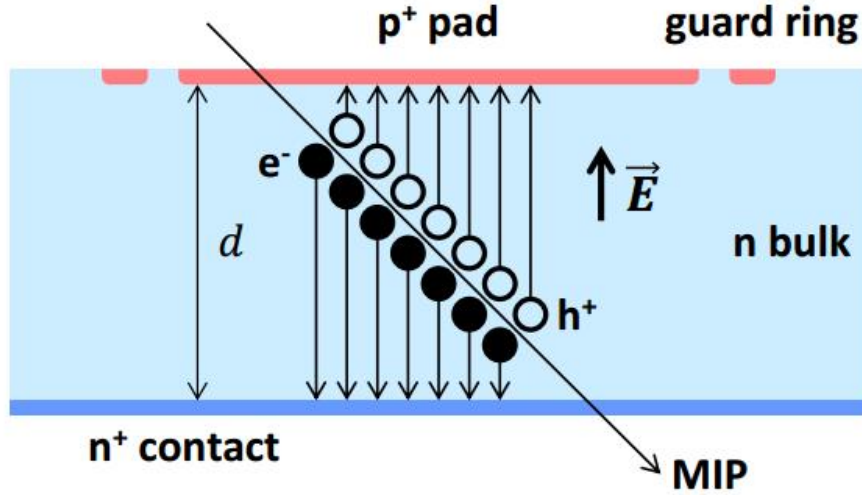


Figure 2.4: Drift of charge carriers produced by MIP inside a pad diode biased at a reverse bias voltage (p^+ to the negative and n^+ to the positive polarity). The sketch is taken from [20].

strip and pixel sensors, E_w is position-dependent and can be calculated from the weighting potential, Φ_w , as:

$$\vec{E}_w(x, z) = \nabla \Phi_w(x, z) \quad (2.7)$$

In this notation, x and z are directions perpendicular and parallel to the electrodes, respectively. For calculation of the weighting potential for a strip or pixel sensor, it is assumed that the considered electrode is connected to 1 V and all other electrodes are connected to 0 V. One calculates the weighting potential by solving the Poisson equation for this configuration. It is noted that this potential is purely geometrical and does not depend on the properties of the sensor. In [21], the weighting field was calculated for strip and pixel sensors with a thickness of 300 μm . Fig. 2.5 shows the results of this calculation for a few examples.

Charge carriers' motion inside a silicon sensor is also due to diffusion, caused by a gradient in the concentration of electrons and holes. The diffusion current per unit area for electrons and holes is given by [22]:

$$\begin{aligned} \vec{j}_e &= -D_e \nabla n \\ \vec{j}_h &= -D_h \nabla p \end{aligned} \quad (2.8)$$

Where D_e and D_h are the diffusion constants, and ∇n and ∇p are the gradients in concentrations of electrons and holes, respectively. The diffusion constant is calculated from the Einstein equation:

$$D_{e,h} = \mu_{e,h} \frac{k_B T}{e} \quad (2.9)$$

$\mu_{e,h}$ is the mobility of electrons and holes, respectively. Without an electric field, diffusion

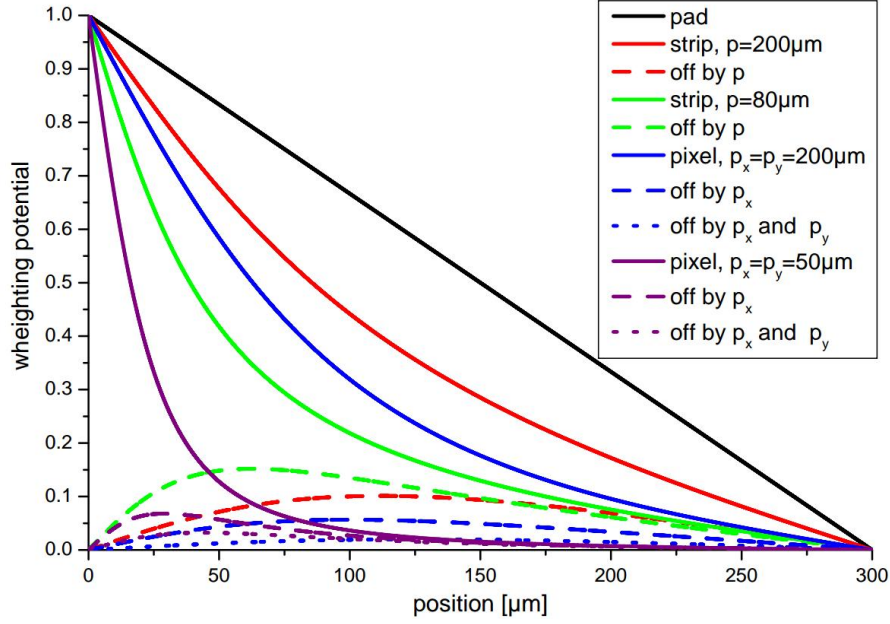


Figure 2.5: Calculated weighting potential for pad diodes, strip, and pixel sensors with different pitch sizes. The calculations are done for sensors with a thickness of the sensors are $300\mu\text{m}$. Dashed lines indicate the same geometry as the solid lines but show the weighting potential for charges centred beneath the neighbour electrode. Dotted lines show the weighting potential for charges centred beneath the electrode, which touches the pixel at the corner. The plot and explanations are taken from [21].

leads to a spread in the charge distribution. The spread can be characterised by a Gaussian distribution with a standard deviation given by:

$$\sigma_{e,h} = \sqrt{2D_{e,h}t} \quad (2.10)$$

Where t is the elapsed time. Diffusion causes a spread in the charge carriers' arrival time to the electrodes. For pixel sensors, this effect causes charge sharing between neighbouring pixels. As shown in Chapter 6, the charge sharing can be useful for reconstructing hits and improving spatial resolution.

Drift of charge carriers changes in the presence of a magnetic field. The following relation characterises the deflection:

$$\tan(\theta_L) = r_H\mu(|\vec{E}|)B_{\perp} \quad (2.11)$$

Where θ_L is the Lorentz angle, r_H is the Hall factor, and B_{\perp} is the magnetic field component perpendicular to the electric field in the sensor [22].

2.4 Hybrid Pixel Sensor

Silicon sensors are an excellent choice for a tracking detector because they can be segmented with high granularity. In high-energy physics experiments, hybrid pixel sensors have been used as tracking detectors[23]. This type of sensor sketch is shown in Fig. 2.6. For hybrid pixel detectors, the sensor and readout chip is processed separately and connected in a bump-bonding process. The bumps are made of $\approx 25\ \mu\text{m}$ thick tin-silver (Sn-Ag) material.

For this work, sensors with configurations of n^+pp^+ have been studied (more details in Section 3.4.1). A negative bias voltage is applied to the p^+ -side to deplete the sensor. As explained in Section 2.3, drifting of electron-hole pairs produced by ionising radiation induces a signal in the electrodes. For these sensors, electrons and holes drift towards n^+ and p^+ implants, respectively. The sensors were bump bonded to the RD53A chip (more details in Section 3.2.1). The bump bonds are on the n^+ -side so that the electrons move towards the readout electronics. As it is shown in Fig. 2.5, the weighting potential is maximum close to the readout electrode (around position = $0\ \mu\text{m}$) and smaller in the bulk region. Therefore, the charge carriers drifting towards the readout electrode (electrons for sensors in this work) have the highest contribution to the induced signal.

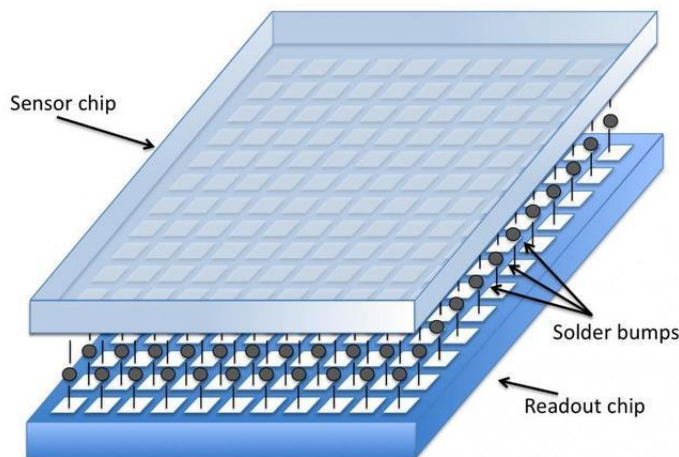


Figure 2.6: Sketch of a hybrid pixel sensor. The sketch is taken from [23].

The fact that a single particle can induce a signal in more than one pixel is called charge sharing and can be changed as a function of track angle, magnetic field, diffusion, and weighting field. Charge sharing significantly affects the spatial resolution of a pixel sensor. In the simplest case, when the cluster size is one, the hit is reconstructed at the

centre of the pixel. In this case, for a pixel size of p , the position resolution is given by:

$$\sigma_{bin} = \frac{p}{\sqrt{12}} \quad (2.12)$$

σ_{bin} is also called the binary resolution. For fresh sensors before irradiation, the cluster size is usually above 1, even for tracks at vertical incidence. This is due to tracks hitting the boundaries between two pixels and producing charge in two pixels. If the width of region with cluster size 2 is s , the resolution in the region with cluster size 1 is $(p-s)/\sqrt{12}$ and in the region with cluster size 2 is $s/\sqrt{12}$ [22].

2.5 Radiation Damage in Silicon

Hybrid pixel sensors are designed to work in the IT, which is the innermost part of the detector and the closest region to the interaction point. Therefore, this part of the detector receives the highest radiation fluence. The properties of silicon change after irradiation which leads to degradation of the sensor's performance. In general, radiation damage effects can be categorised into surface damage due to ionising energy loss and bulk damage due to the Non-Ionising Energy Loss (NIEL) of particles.

As mentioned in Section 2.3, ionising energy loss of particles is the main mechanism for signal formation in a silicon sensor. Ionisation in the sensor's bulk region produces charges with high mobility, which are either collected or recombined if produced in the depleted or non-depleted parts of the sensor, respectively. However, ionisation can create oxide charges with low mobility and long relaxation time at the SiO_2 layer. These slow positive charges are accumulated in the oxide layer. To counterbalance the charges in the oxide layer, fast electrons are accumulated in the Si-SiO₂ interface. This electron accumulation layer can short the neighbouring n^+ implants and reduce the detection efficiency. More about the surface damage effects can be found in [24, 25].

Bulk damage is due to the interaction of incoming particles with the nuclei of silicon atoms in the crystal. If the energy transfer in this interaction is above the threshold energy, around 25 eV for silicon, the atom can be removed from the lattice [26]. The pair of vacancy and interstitial defects is called a Frankel pair and is a point defect. The vacancy in the Frankel pair can become a trapping site for free-charge carriers. If the transferred energy is high enough (in the order of 10 keV), a cluster of point defects can be formed through the secondary interactions of the displaced atom. Fig. 2.7 shows the results of simulated vacancies produced by protons (10 MeV and 23 GeV) and neutrons (1 MeV).

The type of vacancy defects depends on the particle type and energy. In order to compare the radiation damage by different types of particles with different energy, the damage function, $D(E)$, is normalised to the damage of 1 MeV neutrons: $D_n(1 \text{ MeV}) = 95 \text{ MeVmb}$. Fig. 2.8 shows the normalised damage functions for different types of particle

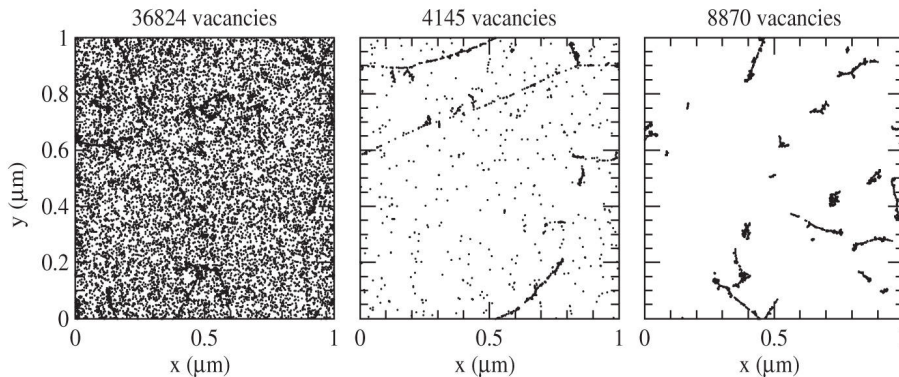


Figure 2.7: Simulated vacancies produced by 10 MeV protons (left), 24 GeV protons (middle) and 1 MeV neutrons (left). The irradiation fluence is $1 \times 10^{14} \text{ cm}^{-2}$ for each case. The plot is taken from [27].

as a function of particle energy in silicon.

The hardness factor, κ , is defined as the ratio of damage by a given particle type and energy to the damage of 1 MeV neutrons [28]:

$$\kappa = \frac{\int D(E)\phi(E)dE}{D_n(1 \text{ MeV}) \cdot \langle \phi \rangle} \quad (2.13)$$

Where $\phi(E)$ is the energy spectrum of the radiation field and $\langle \phi \rangle = \int \phi(E)dE$. By using κ , one can define the 1 MeV neutron-equivalent fluence as:

$$\phi_{eq} = \kappa \langle \phi \rangle \quad (2.14)$$

All quoted fluences in this thesis are expressed in terms of the 1 MeV neutron-equivalent fluence. It should be noted that the fact that different particles produce defects with different uniformity, as shown in Fig. 2.7, is not considered in this normalisation.

Point defects created after the irradiation can be electrically active and introduce additional energy levels in the silicon band gap. These additional levels change the macroscopic properties of silicon. To characterise these macroscopic changes, one must know the defects' properties: introduction rate, capture cross-section for electrons and holes, energy levels, and type of defects (donor/acceptor). Experimental methods such as Thermally Stimulated Current (TSC) and Deep Level Transition Spectroscopy (DLTS) can be used to extract the parameters of defects [30, 31]. Table 2.1 lists the properties of irradiation-induced defects.

Depending on the energy levels and capture cross-sections of defects, they have different effects on the macroscopic properties of silicon. Shallow defects with energy levels close to E_C and E_V , act as donor and acceptor, respectively. These defects change the doping profile of the bulk region, which can alter the electric field profile [33] and full depletion voltage. Defects with energy levels close to the middle of the band-gap or deep defects act

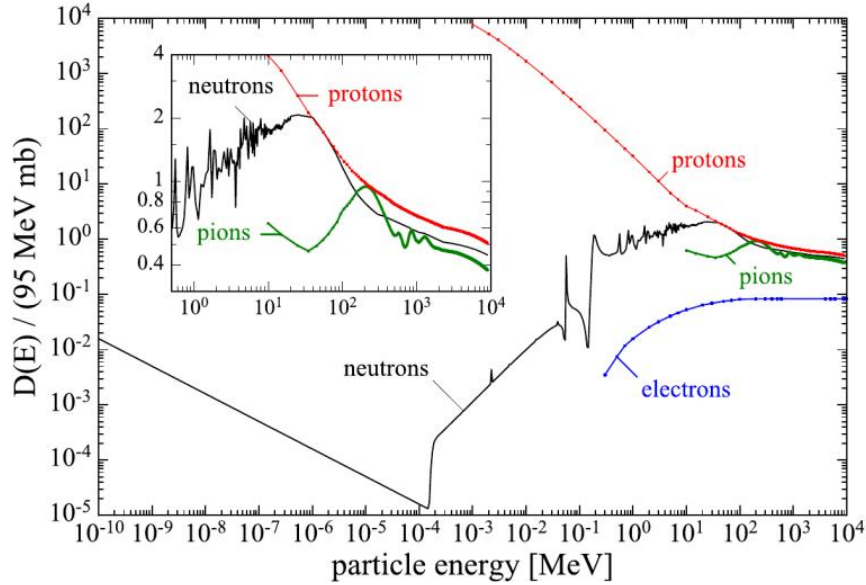


Figure 2.8: Normalised Damage function calculated for protons, neutrons, pions and electrons as a function of energy. The plot is taken from [29].

as recombination/generation centres. These defects increase the free charge carriers in the depleted region, hence the leakage current. These defects can also be trapping centres for free-charge carriers produced by incoming particles. Traps reduce the measured charge by the sensor. This charge loss reduces the hit detection efficiency for pixel sensors, which is discussed in Chapter 6. For pad diodes, this means reducing the charge collection efficiency, as discussed in Chapters 4 and 5.

2.6 CMS Detector

CMS is one of the four experiments running in LHC, along with ATLAS, ALICE, and LHCb. The CMS detector is positioned at LHC Point 5, one of the interaction points designed to deliver high luminosity. A sketch of the detector is shown in Fig. 2.9. Given the cylindrical shape of the detector, the cylindrical coordinates (r, ϕ, z) can be used for description, where the interaction point is the origin. r is the radial distance from the interaction point, z is in the direction of the beam, and ϕ is the azimuthal angle.

CMS detector includes the following sub-detectors:

- **Tracking System:** this detector is divided into two sub-detectors called inner and outer trackers. The IT is the closest element to the interaction point and comprises 3 barrel layers and two disc layers of pixel sensors. The outer tracker includes 10 barrel layers and 12 disc layers of strip sensor. The main task of the tracker is the reconstruction of the trajectory of charged particles and finding the primary and secondary vertices.

Defect	type	Energy Level	g_{int} [cm^{-1}]	σ_e [cm^{-2}]	σ_h [cm^{-2}]
$(V - O)$	Acceptor	$E_C - 0.176 \text{ eV}$	1.1	1.4×10^{-14}	—
$(V - V)^{-2}$	Acceptor	$E_C - 0.224 \text{ eV}$	1.5	7.0×10^{-16}	—
$(V - V)^{-}$	Acceptor	$E_C - 0.424 \text{ eV}$	1.5	2.0×10^{-15}	—
—	Acceptor	$E_C - 0.4 \text{ eV}$	1.5	—	—
—	e-trap	$E_C - 0.52 \text{ eV}$	0.03	—	—
$(C_i - O_i)$	Donor	$E_V + 0.36 \text{ eV}$	1.1	2.1×10^{-18}	2.5×10^{-15}
—	h-trap	$E_V + 0.36 \text{ eV}$	2.3	—	1.2×10^{-15}
—	h-trap	$E_V + 0.48 \text{ eV}$	0.08	$> 6.0 \times 10^{-16}$	5.5×10^{-15}
—	h-trap	$E_V + 0.53 \text{ eV}$	0.08	—	3.0×10^{-14}
—	h-trap	$E_V + 0.51 \text{ eV}$	0.03	—	1.0×10^{-14}

Table 2.1: Parameters of radiation-induced defects extracted from TSC, DLTS, and TCT measurements. E_C and E_V notes the energy levels of conduction and valence bands respectively. The data is collected in [32].

- Electromagnetic Calorimeter: this detector measures the energy of photons and electrons by lead tungsten scintillating crystals, which are read out with photodetectors [34]. This detector includes barrel layers in the cylindrical part and disk layers in the end cap.
- Hadronic Calorimeter: this detector measures the energy of hadrons and jets. This calorimeter is a sampling type which includes brass absorbers and plastic scintillators.
- Muon System: This detector is the outermost part of the CMS detector and detects muon final states. The system includes gaseous detectors, drift tubes and cathode strip chambers.

As it is shown in Fig. 2.9, CMS detector has a superconducting solenoid which provides a 4 T magnetic field. The yoke surrounds the tracker, electromagnetic and hadronic calorimeters. The purpose of this magnetic field is to bend the trajectory of charged particles to measure their curvatures and determine their momenta.

In LHC, particles are accelerated in bunches with a time difference of 25 ns. This translate to a collision rate of 40 MHz. Reading out and storing the signals from all detector channels at this rate is impractical. A trigger system with two levels has been developed to reduce the event rate. The Level-1 trigger is a hardware trigger that uses the sub-detector information and reduces the data rate to 100 kHz. The High-Level trigger applies physics algorithm selections to find the most interesting physics events [36]. After this trigger level, the data rate is reduced to 100 Hz.

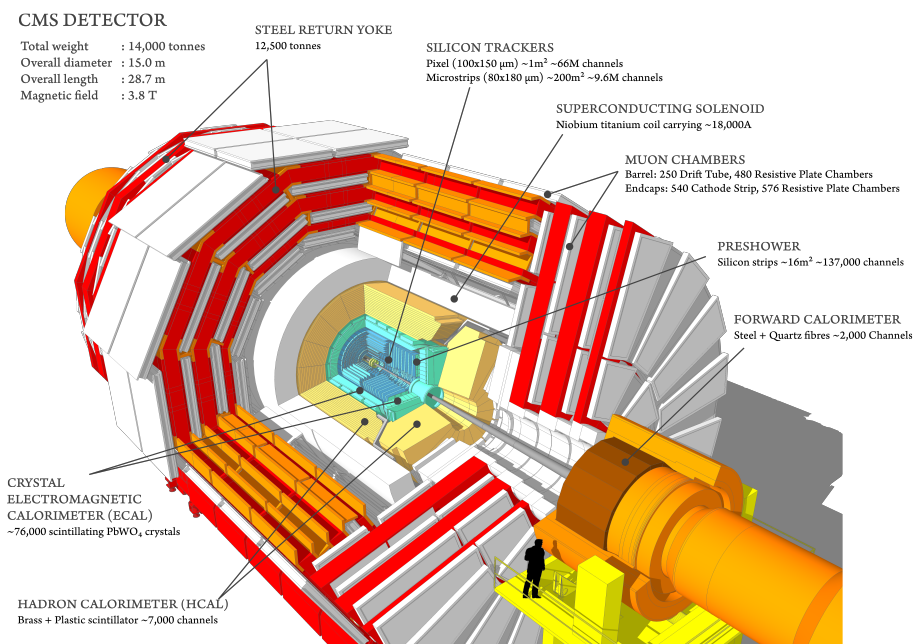


Figure 2.9: Sketch of the CMS detector, taken from [35].

2.7 Inner Tracker of the CMS Detector

The IT of the CMS detector consists of multiple layers of pixel sensors in the barrel and forward regions, named as Barrel Pixel Detector (BPIX) and Forward Pixel Detector (FPix), respectively. For the phase-1 upgrade, one layer was added to the BPIX and three layers were added to FPix. In addition, the distance between the first layer of the BPIX to the beam pipe was reduced from 44 mm to 29 mm in this upgrade [37, 38].

The Phase-2 upgrade is planned in mid 2020s in the Long Shutdown (LS)₃ for the data taking in HL-LHC. In HL-LHC phase, an instantaneous luminosity of $7.5 \times 10^{34} \text{ cm}^{-2} \text{ s}^{-1}$ is expected in the ultimate scenario [39]. This results in a total luminosity of 4000 fb^{-1} after ten years of operation. For the CMS detector, the number of interactions per bunch crossing or pile up is expected to be 200 in HL-LHC phase. For comparison, the pile-up for the phase-1 is around 34.

This condition introduces a few challenges for the detectors, especially for the IT. Increasing the pile up by a factor of ≈ 5 increases the detector's occupancy. In addition, higher luminosity means higher irradiation fluence for the detector. Fig. 2.10 shows the simulated 1 MeV neutron-equivalent fluence map of the CMS tracker after an integrated luminosity of 3000 fb^{-1} . As discussed in Section 2.5, the radiation damage in the silicon is scaled with the radiation fluence.

To keep the performance of the IT in the harsh environment of HL-LHC at least at the same level as phase-1, an upgrade of the detector is planned. Three key changes to the IT for the Phase-2 upgrade are introduced below:

- To keep the occupancy of the detector at an acceptable level at the HL-LHC envi-

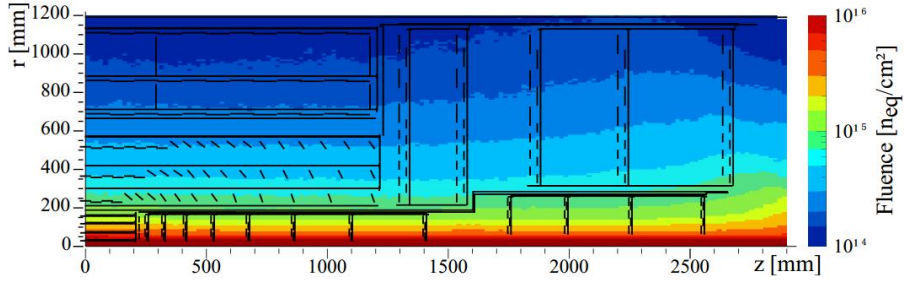


Figure 2.10: Simulated 1 MeV neutron-equivalent fluence map for IT of the CMS detector after integrated luminosity of 3000 fb^{-1} of proton-proton collisions at the centre of mass energy of $\sqrt{s} = 14 \text{ TeV}$. The plot is taken from [40].

ronment with the high pile up, the pixel size will be reduced from $100 \times 150 \mu\text{m}^2$ to $25 \times 100 \mu\text{m}^2$ or $50 \times 50 \mu\text{m}^2$.

- The thickness of the sensor will be reduced from $285 \mu\text{m}$ *n*-type to $150 \mu\text{m}$ *p*-type. Thinning down the sensor minimises the charge loss due to the trapping effects.
- The readout chip will be changed from PSI46dig and CROC600 to a chip based on the RD53A prototype chip produced by 65 nm CMOS technology.

In addition, the number of layers in FPIX will be increased from 4 to 12. Fig. 2.11 shows a schematic of the tracking system of the CMS detector for the Phase-2 upgrade.

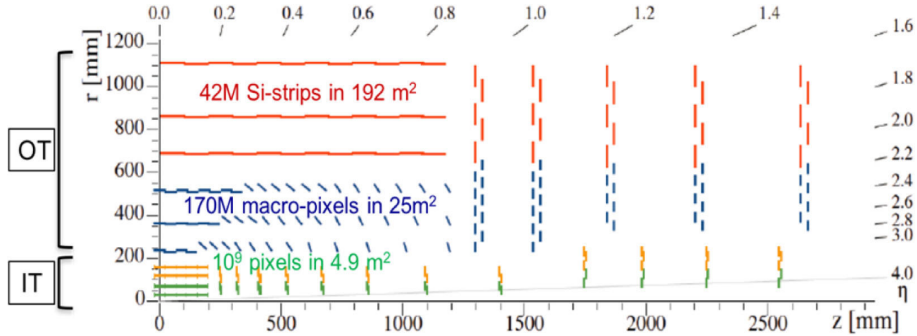


Figure 2.11: Sketch of one-quarter of the tracking system of the CMS detector for the Phase-2 upgrade in (r, z) view. The IT is shown with the green and yellow lines, which represent pixel modules with two and four readout chips, respectively. The sketch is taken from [40].

A set of requirements have been defined for parameters of pixel modules designed for the Phase-2 upgrade. Table 2.2 shows these requirements before and after irradiation. It should be noted that the fluences of $1 \times 10^{16} \text{ cm}^{-2}$ is roughly equal to the expected fluences of layer 1 after half time of the operation. The sensors in layer 1 are expected to be replaced after the first half of operation. $5 \times 10^{15} \text{ cm}^{-2}$ is roughly equal to the expected fluences of layer 2 after full operation. These fluences are estimated assuming an integrated luminosity of 3000 fb^{-1} .

Parameter Name	Parameter Value	Fluence (cm^{-2})	Measurement Conditions
Breakdown voltage	300 V	0	—
Breakdown voltage	800 V	5×10^{15}	—
Leakage current	$0.75 \mu\text{A cm}^{-2}$	0	at $V_{FL} + 50 \text{ V}$
Leakage current	$45 \mu\text{A cm}^{-2}$	5×10^{15}	at 600 V
Hit efficiency	0.99	0	at $V_{FL} + 50 \text{ V}$
Hit efficiency	0.99	5×10^{15}	at 800 V, -20°C
Hit efficiency	0.98	1×10^{16}	at 800 V, -20°C

Table 2.2: Requirements for pixel sensors designed for the Phase-2 upgrade of the CMS IT. V_{FL} stands for the full depletion voltage of the sensors. Hit efficiency is defined in Section 6.4. Quoted fluences are in the 1 MeV neutron-equivalent unit. The numbers are taken from [41].

To ensure the pixel module meets these requirements, they are characterised in the test-beam before and after irradiation. In Chapter 6, the results of these characterisations are shown for planar pixels sensors. In addition to planar sensors, 3D sensors are considered for the innermost layer of BPIX, as well. In 3D sensors, the implants are in forms of columns perpendicular to the surface of modules [42]. This design reduce the drift distances of charge carriers and trapping effects. Moreover, the full depletion voltage and leakage current of 3D sensors is much lower than planar sensors. However, the production yield of these sensors is lower due to more complex fabrication process.

3 Experimental setup for Test-Beam Measurements

A large fraction of the measurements for this thesis was performed at the Deutsches Elektronen-Synchrotron (DESY) II test-beam facility. In this chapter, information about the experimental setup in the test-beam measurement for both pad diodes and pixel sensors is presented. The specifications of the sensors are described in the last part of the chapter.

3.1 An Overview of Test-Beam Infrastructures

In this part, an overview of common infrastructures which are required for test-beam measurements of pixel sensors and pad diodes is given.

3.1.1 DESY II Beam Line

Tracking detectors for high energy physics can be characterised in a test-beam facility. The idea is to measure the response of the detectors using particles with an energy loss close to MIP. This can serve two purposes: the effect of Coulomb multiple scattering is minimised and the performance of the detectors with smallest signal can be studied.

The DESY II test-beam facility provides electron and positron beams with momenta up to 6.3 GeV/c [43]. Initially, the generation of the test-beam starts with electrons/positrons in the DESY II synchrotron which produce Bremsstrahlung photons in a primary target. These photons hit a secondary target and produce electron/positron pairs. This secondary target is made of aluminium or copper and is available in different thicknesses between 1 mm to 5 mm. To choose the type and momentum of the particles which reach the test-beam areas, electron/positron pairs are directed through a dipole magnet. The selected particles pass the primary collimator before reaching the beam areas. There are three beam areas called Test-Beam 21 (TB21), Test-Beam 22 (TB22) and Test-Beam 24 (TB24) available for users. In each area can change the target material and beam momentum, independently. Fig. 3.1 shows an overview of team beam in DESY II test-beam facility.

Most of the studies in this thesis were performed in TB21 area with a beam momentum of 5.2 GeV/c, unless it is mentioned otherwise. A secondary collimator is available inside

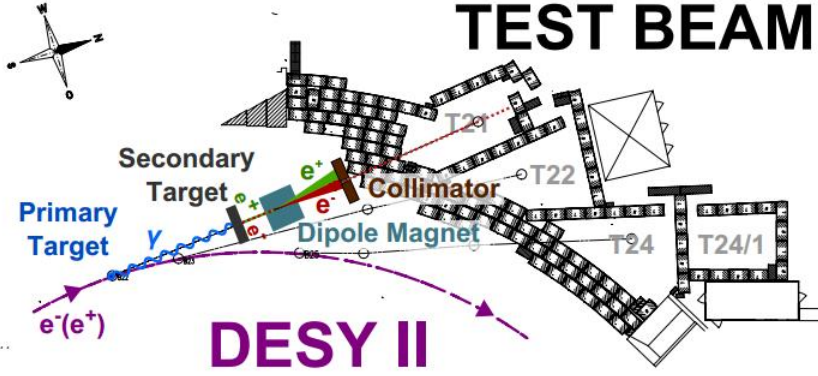


Figure 3.1: Test-beam at the DESY II facility. The picture is taken from [43].

the area where user can choose different openings. The beam rate and uncertainty of the beam momentum depends on the width of the primary and the secondary collimators.

Inside the area, further infrastructures needed for the measurements such as telescope, triggering scintillators, mechanical stages and etc. The user can control the beam shutter which is connected to an interlock system, in order to have access inside the beam area.

3.1.2 Telescope

For track reconstruction with a few micrometer precision, a beam telescope called "DATURA" was used in the TB21 area. The DATURA telescope is a detector developed within EU-DET project with 6 planes. Each plane is equipped with a MIMOSA 26 sensor which is a Monolithic Active Pixel Sensor (MAPS) with pixel size of $18.4 \times 18.4 \mu\text{m}^2$ and a thickness of $54.5 \pm 3.6 \mu\text{m}$ [44]. Each sensor has 1152 columns and 576 rows which cover an area of $21.2 \times 10.6 \text{mm}^2$. The readout of the sensors is done using the rolling shutter method with an integration time of $115.2 \mu\text{s}$. The readout of pixels is binary. The threshold was set at the a level which corresponds to 6 times the pixel noise. The intrinsic spatial resolution of each plane is $3.2 \pm 0.9 \mu\text{m}$ at vertical incidence.

Fig. 3.2 shows a schematic of a measurement set up with the DATURA telescope. As it is shown, each three planes are placed at equal distance around the Device Under Test (DUT). Each three planes of the telescope forms a triplet and is placed upstream and downstream with respect to the position of the DUT. The tracks reconstructed by two arms are extrapolated to the DUT to calculate the intersection.

The performance of DATURA has been studied in [45]. It has been shown that the single-hit resolution of the telescope is a function of material budget between two arms (ϵ_{DUT}), beam momentum (p), the spacing of the telescope planes dz , and the distance between telescope and the DUT surface (dz_{DUT}). Fig. 3.3 shows calculated track resolution as a function of telescope-to-DUT distance, i.e. dz_{DUT} , and the DUT material budget, i.e. ϵ_{DUT} . As expected, the resolution deteriorates as the material budget and telescope-to-DUT distance increase. This can be understood by considering the effect of the Coulomb scattering. This effect causes an angular deflection in the trajectory of charged particles

3 Experimental setup for Test-Beam Measurements

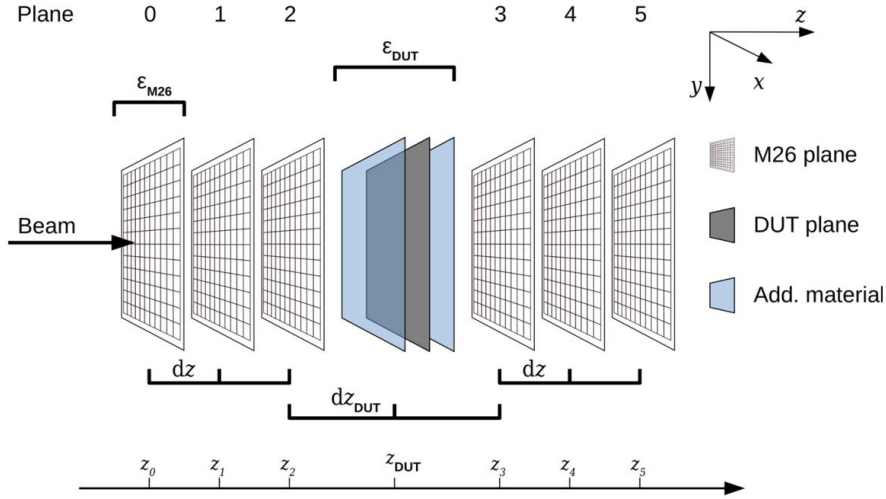


Figure 3.2: Schematic of a test-beam setup including MIMOSA sensor planes and DUT. The sketch is taken from [45].

as they travel through a medium. The rms of the angular distribution of the beam for a medium with a material budget of ϵ is given by the following relationship [46]:

$$\theta_0^{rms} = \frac{13.6 \text{ MeV}}{\beta c p} z \sqrt{\epsilon} \left[1 + 0.038 \ln\left(\frac{\epsilon z^2}{\beta^2}\right) \right] \quad (3.1)$$

In this relationship, p , βc , and z are the momentum, velocity and atomic number of the incident particle, respectively. ϵ is the thickness of the medium with a thickness of x in terms of the radiation length defined as $\frac{x}{x_0}$. From this relation, one can note that the rms value of the angular distribution is proportional to the thickness of the medium.

Another observation from Fig. 3.3 is that the track resolution for spacing of $dz = 150$ mm is typically better than $dz = 20$ mm for similar values of dz_{DUT} and ϵ_{DUT} .

In this work, the telescope spacing was chosen to be 120 mm. The electron beam energy was set at 5.2 GeV unless it is stated otherwise.

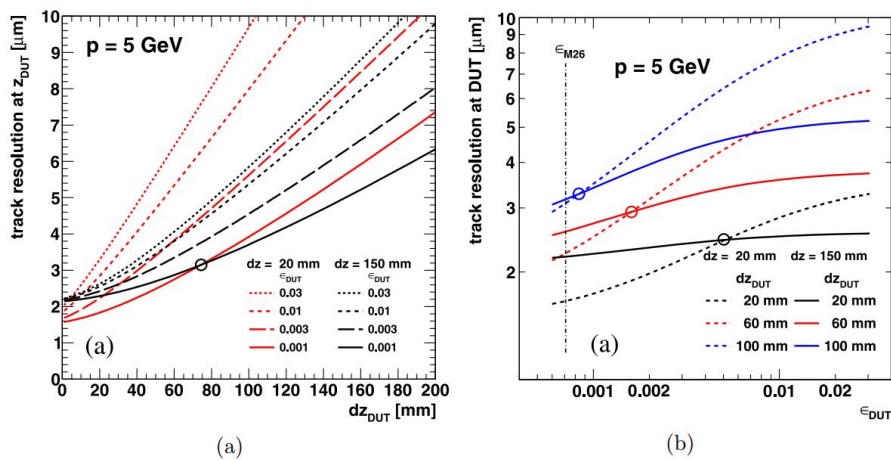


Figure 3.3: Telescope resolution as a function of dz_{DUT} (a) and ϵ_{DUT} (b) for different telescope spacing dz . The values are calculated using the General Broken Lines algorithm. The plots are taken from [45].

3.1.3 Trigger Unit

The trigger for data taking in the test-beam was provided by the coincidence signal between two scintillators. These scintillators were wrapped light-tight and coupled to Photo Multiplier Tube (PMT). They were placed before the first plane of the telescope (plane 0 in Fig. 3.2).

The outputs of the PMT signals were connected to a Trigger Logic Unit (TLU). A schematic of the TLU front panel is shown in Fig. 3.4. The most important functions of the TLU is listed below:

- Four output channels to provide the bias voltage for the PMTs (LV-Out in the sketch),
- Four input channels to read out PMT signals (PM-in in the sketch),
- AND/OR logic units to provide trigger masks from four input channels,
- NIM and TTL outputs for issuing the trigger signal according to the chosen logic mask (Trig0-3 and RJ45 DUT interface in the sketch),
- Four input channels from the DUT which can veto the trigger signal while DUT is busy (BUSY0-3 in the sketch).

For most of the measurements in this work, the AND signal between two PMT input channels was used as trigger. For measurement with pixel sensors, a BUSY signal was also provided from the DUT. In all cases, the MIMOSA telescope also send a BUSY signal to the TLU.

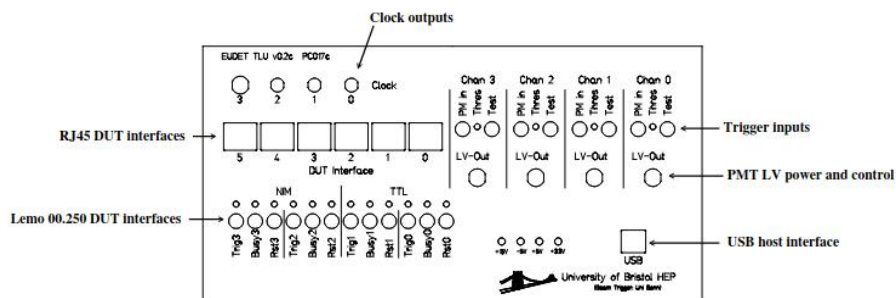
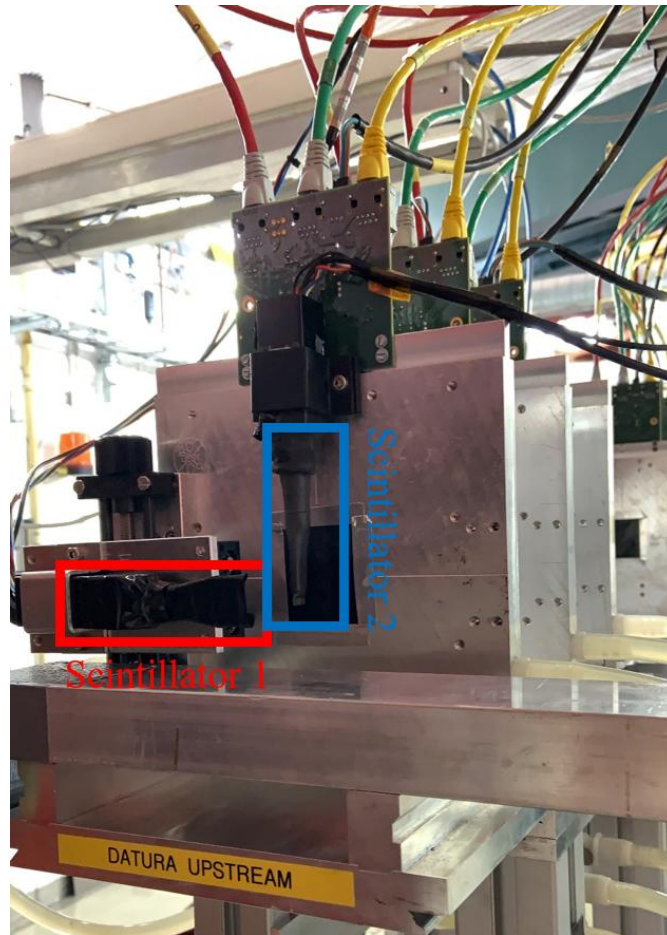


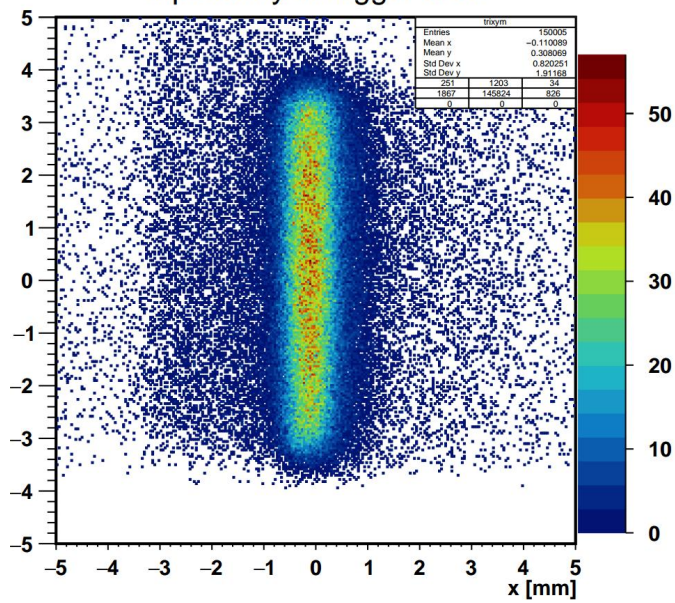
Figure 3.4: Front panel of the TLU. The sketch is taken from [47].

Depending on the size of DUT, the area covered by two scintillators was adjusted to gain the maximum acceptance of tracks. This was done by mounting the scintillator-PMT assembly on a movable manual stage. Fig. 3.5a shows an example of the positioning of scintillators for an edge-on measurements with a diode. For the setup shown in Fig. 3.5a, the diode had a cross section size of 0.150×5.0 mm. The hit map of the trigger area for this setup is shown in Fig. 3.5b. One recognises a rectangular shape with a size of 1.0×8.0 mm which translate to an acceptance of around 9 % for the DUT.

3 Experimental setup for Test-Beam Measurements



(a) Orientation of two scintillators for edge-on measurements with diode triplets x-y in trigger area



(b) Hit map of tracks within the triggering area for the setup shown in (a).

Figure 3.5: Trigger for the edge-on measurements

3.1.4 Timing Reference Module

As it was discussed earlier, one readout frame of the MIMOSA sensors of the telescope is 115.2 μs . The integration time of DUTs (pixel sensors and diodes), however, is typically less than 1 μs . Several tracks pass the setup during one readout cycle of the telescope. Therefore, a timing reference module is required to select the subset of the tracks which are in-time with the readout cycle of the DUT.

To provide the timing reference, a CMS Phase-1 pixel module was used. The sensor has a pixel size of $150 \times 100 \mu\text{m}^2$ and a thickness of 285 μm [38]. The sensor was read out by a PSI46dig readout chip with 52×80 pixels. The threshold of the readout chip was set at $1500 e^-$ with 8 bit digitisation of the charge. The depletion voltage of the sensor was 70 V, and it was operated at 150 V. The module was placed behind the triggering scintillators with an inclination angle around 18° ($\approx \text{atan}(\frac{100 \mu\text{m}}{285 \mu\text{m}})$) to gain cluster size 2 in the 100 μm direction. A Digital Test Board (DTB) was used for data acquisition of this module.

The readout frequency of the module is 40 MHz which is asynchronous with the DESY bunch. Therefore, the delay between trigger and the readout of the chip had to be adjusted to optimise the efficiency. This was done using both software and hardware delays. The efficiency of the reference module varied in the range of 60 % to 80 % depending on the delay.

3.1.5 Other Components of the Experimental Setup

In order to carry out measurements in the test-beam, additional equipment was required. A summary of these tools is presented in the following.

Irradiated sensors usually have high leakage currents on the bias line. Therefore, it is necessary to cool down the DUT while it is being operated. This was done using a combination of a water circulation chiller and two Peltier elements. Initially, the chiller cooled down a copper bridge. In the second stage, Peltier elements operating at power of $\approx 5 \text{ W}$ cooled down the Printed Circuit Board (PCB) which holds the DUT. The temperature of the chiller liquid was set to -35°C and -20°C for pixel sensors and pad diodes, respectively. The temperature of the DUT was not directly measured. To provide the thermal isolation, the copper bridge and the DUT were placed inside a so called "Cold Box". The box was isolated using an ArmaFlex insulation and flushed with dry air to avoid condensation.

The position of the DUT with respect to the telescope planes and triggering scintillators was adjusted using two linear stages perpendicular to the direction of the beam, i.e. x- and y-directions. These stages can be controlled with a sub-millimeter precision. In addition, the DUT can be rotated with a precision of 0.01° using a third stage.

The DUT bias voltage was provided by an ISEG SHQ high-voltage power supply. The unit was placed inside the control room so one can control the bias voltage without having

to break the interlock of the beam area. This unit also logged the leakage current on the bias line during the data taking.

As it was discussed earlier, the delay between the trigger and readout of the timing reference module needed to be adjusted. This was done using a NIM crate which provides NIM discriminator, NIM-to-TTL converter, and delay units.

3.2 Measurement Setup for Pixel Sensors

For the Phase-2 upgrade of the CMS IT, hybrid pixel modules have been investigated. These modules consist of a silicon pixel sensor which is bump bonded to a ReadOut Chip (ROC). Ionising tracks generate electron-hole pairs inside the sensor. By applying an electric field to the sensor, the produced charges drift in the sensor and induce a signal. The signal is then amplified and digitised by the ROC. The RD53A chip is the first prototype as the ROC for the Phase-2 upgrade of the CMS IT.

In the following parts, an overview of the RD53A chip and test-beam setup for the pixel sensors is presented.

3.2.1 RD53A Readout Chip

The RD53A chip is produced with 65 nm CMOS technology. Some of important requirements of the chip are [48]:

- Radiation tolerant
- Tunable and stable low threshold
- 4 bit digitisation of the charge using Time-over-Threshold (ToT) counter
- High readout bandwidth

The RD53A chip matrix has 192 rows and 400 columns with a physical size of $20 \times 11.6 \text{ mm}^2$. The size of the pixels in the chip matrix is $50 \times 50 \mu\text{m}^2$. The chip contains three analog front ends called Differential, Linear, and Synchronous. The top view of the chip layout including these front end is shown in Fig. 3.6.

By CMS, the Linear Front End (LFE) has been chosen for the final chip. As it is shown in Fig. 3.6, LFE has 192 rows and 136 columns. This front end includes a Charge Sensitive Amplifier (CSA) with Krummenacher feedback to comply with the high leakage current of the irradiated sensors. A schematic of the LFE is shown in Fig. 3.7. The output signal of the CSA is fed into a high-speed comparator which provides a threshold for the ROC. The pixel-to-pixel dispersion of the threshold is compensated using a 4 bit of Threshold DAC (TDAC) which generates the current I_{DAC} . The signal is digitised with a 4 bit ToT counter.

3 Experimental setup for Test-Beam Measurements

SCC to the BDAQ53 base board via a display port cable.

A more detailed discussion about the tuning procedure of the RD53A chip will be given in the following chapters.

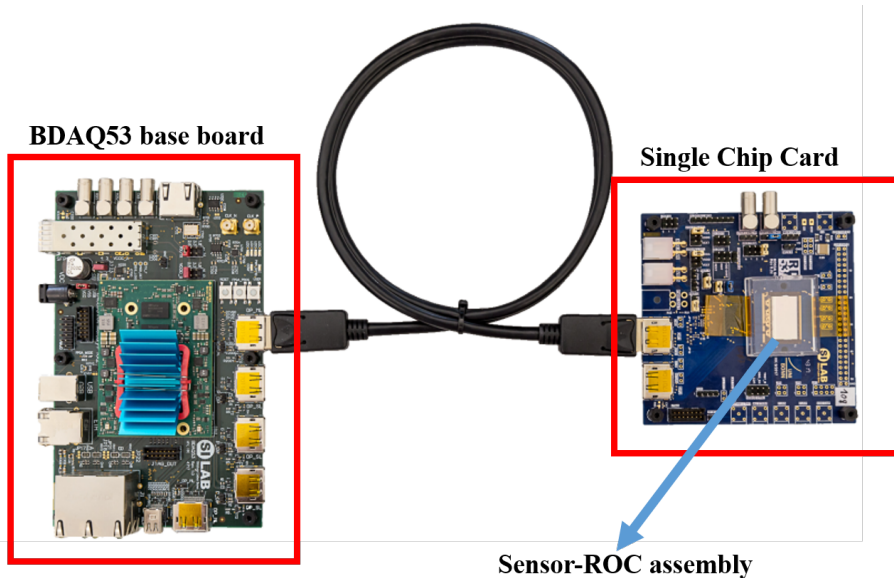


Figure 3.8: Connection of SCC to BDAQ53 base board. The picture is taken from [50].

3.2.2 Setup for Pixel Sensor Measurements

The measurement setup at the test-beam for pixel sensors was provided by the infrastructures explained in Section 3.1. Fig. 3.9 shows a schematic of a typical test-beam setup for measurement with RD53A modules.

For the non-irradiated modules was slightly different and the module was installed outside of the cold box (see Fig. 3.10). Therefore, all six planes of the telescope were used for track reconstruction. For irradiated modules only the upstream triplet could be used for the track reconstruction due to the scattering from the cold box. The module was installed on a rotation stage to enable measurements at different angles of incidence.

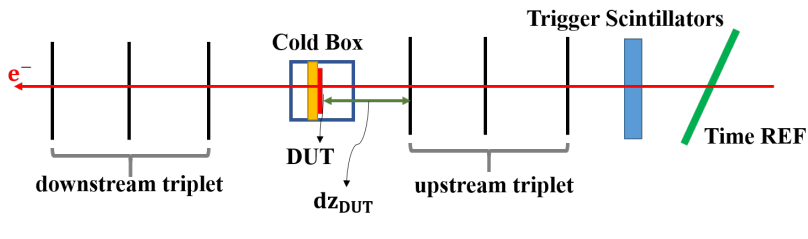


Figure 3.9: Schematic of the test-beam setup for measurement of RD53A modules.

The cabling diagram of the test-beam measurements for pixel sensor is shown in Fig. 3.11. In this diagram, arrows show the cables between devices. For data acquisition, three computers are required, one for each detector (DUT, timing reference module, and telescope).

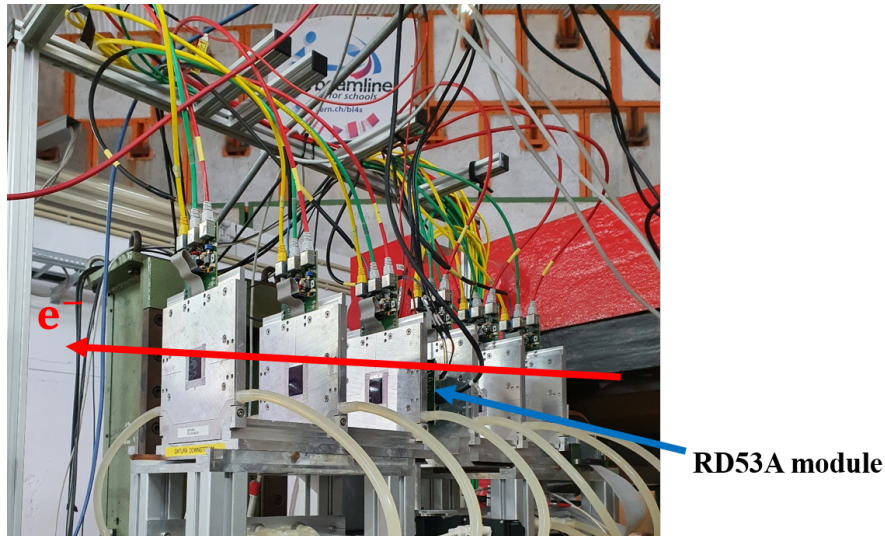


Figure 3.10: Test-beam setup for measurement of non-irradiated pixel sensors.

The TLU provides the readout trigger for all detectors and receive Busy signals from the BDAQ53 and the telescope.

The acquisition computers were accessible through a network connection. The data collector for the telescope and the RD53A module was the same and the reference module had a separate data collector. For each run two single file were produced: one file containing the telescope and RD53A module data and a second file containing the data for the reference module.

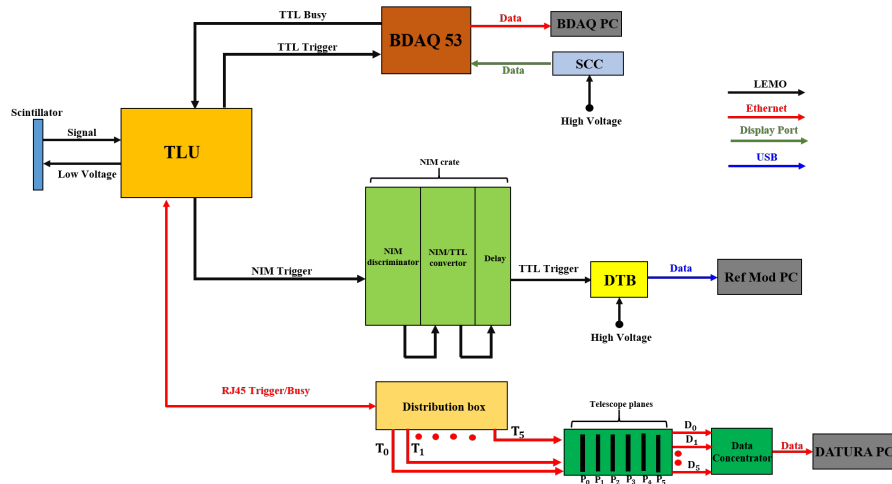


Figure 3.11: Cabling diagram of test-beam setup for pixel sensors. The colour of arrows represent their types, as it is shown in the figure.

3.3 Measurement Setup for Pad Diodes

To obtain the charge collection profile of pad diodes, they were measured with electron beam at the test-beam. A schematic of the setup for edge-on measurements with pad

3 Experimental setup for Test-Beam Measurements

diodes is shown in Fig. 3.12. For the edge-on measurements, only the upstream telescope planes were used for track reconstruction.

Both irradiated and non-irradiated pad diodes were placed inside the cold box. The box was only cooled down for measuring the irradiated diodes. The box was mounted on the rotation stage which can turn with a precision of 0.01° . This was an important feature for the in-situ alignment procedure, as it will be discussed in the following chapter. Fig. 3.13 shows a photo of the test-beam setup.

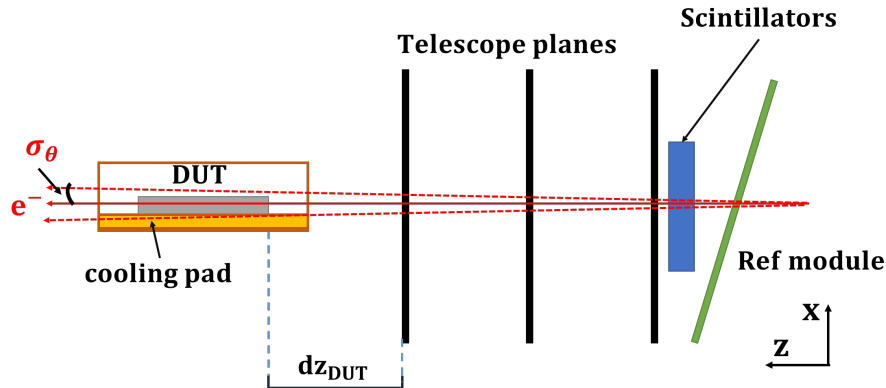


Figure 3.12: Test-beam setup for edge-on measurements with diodes. In this sketch, σ_θ is the divergence of the beam and dz_{DUT} is distance between DUT and third plane of telescope. The sketch is taken from [51].



Figure 3.13: Test-beam setup for edge-on measurements with diodes.

To record transient of pad diodes, a Rohde & Schwarz oscilloscope with an analog bandwidth of 4 GHz and a sampling rate of 20 GS/s was used. The oscilloscope was able to buffer up to 200,000 transients without a dead time. The amplitude and time

stamp of each transient was saved in a binary file for the offline analysis. To ensure the synchronisation between the oscilloscope and TLU, the time difference between two consecutive events was calculated using timestamps of each device (Δt_{RS} and Δt_{TLU}). The distribution of the difference between two devices, i.e. $\Delta t_{RS} - \Delta t_{TLU}$ is shown in Fig. 3.14. From this plot, one sees that the oscilloscope and TLU were synced in 100 ns range.

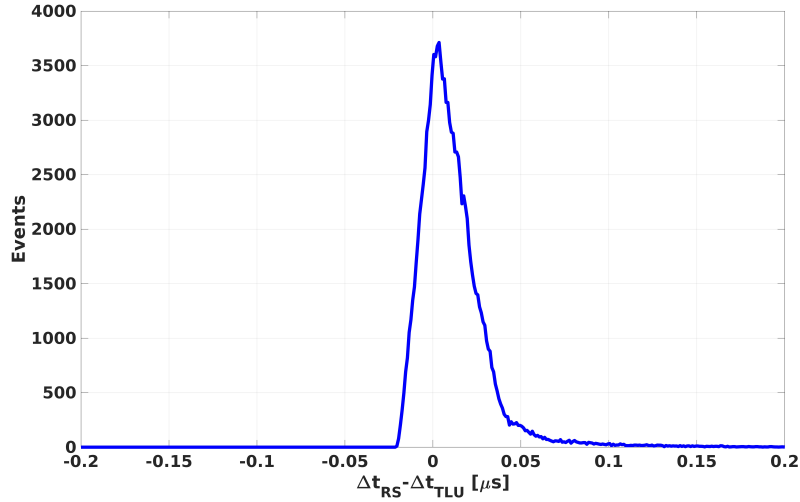


Figure 3.14: Distribution of time difference between oscilloscope and TLU, $\Delta t_{RS} - \Delta t_{TLU}$.

The transients of the pad diodes were amplified through a Femto HSA-X-40 amplifier with a bandwidth of 2.0 GHz and a nominal gain of 100 [52]. The trigger of the oscilloscope was provided through the TLU. The triggering area was adjusted as it was discussed in Section 3.1.3. Fig. 3.15 shows the cabling diagram for the diode measurements.

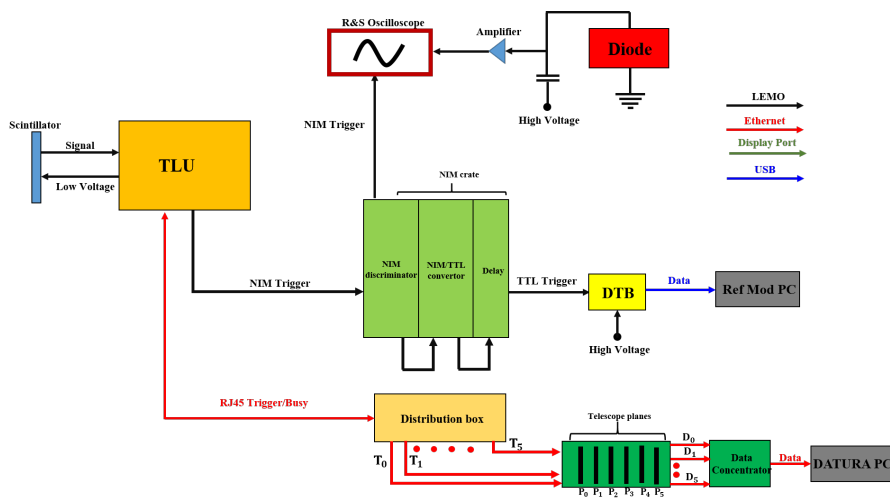


Figure 3.15: Cabling diagram of test-beam setup used for edge-on measurements.

To measure the transients, the diode is mounted on a PCB which provides the electrical connectors. The parallel beam produces showers inside the PCB. These showers can produce particles which deposit energy in the DUT. To cancel the effects of these showers

on the response of the diode, two spacers are inserted between the diode and the PCB. These spacer are metal bars with a width of $w = 1$ mm and a thickness of $d = 0.5$ mm. Fig. 3.16 shows how the spacer were inserted between the diode and the PCB.

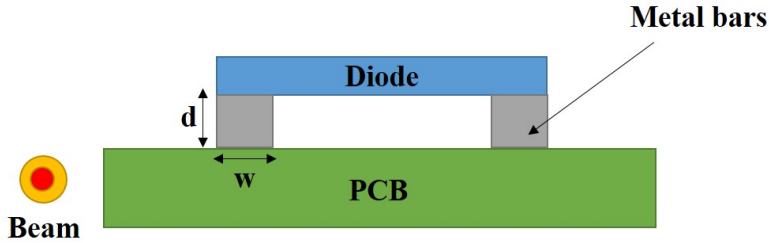


Figure 3.16: The metal spacers inserted between diode and PCB.

3.4 Specifications of Sensors

In this work, two type of silicon detectors are studied: planar pixel sensors and pad diodes. Both types of sensors are produced by the Hamamatsu Photonics K.K. (HPK) [53]. The base material or substrate of the sensors is the same, therefore quantities such as physical thickness, doping profile, oxygen concentration, and etc are similar for both types sensors. In following, a summary of specifications for each type of sensor is given.

3.4.1 Planar Pixel Sensors

To optimize the design of the planar pixel sensors a prototype submission with HPK was done in 2017. In [54], an overview of the first production of the HPK sensors (2017 submission) is given. In that submission, n^+p sensors with an active thickness of $150 \mu\text{m}$ were produced on 6 inch wafers. The wafers had resistivity of $1 \text{ k}\Omega \cdot \text{cm}$ to $5 \text{ k}\Omega \cdot \text{cm}$ and an oxygen concentration of $1 \times 10^{16} \text{ cm}^{-3}$ to $6.5 \times 10^{17} \text{ cm}^{-3}$ [55]. The submission included Flotzone THinned (FTH), Flotzone Direct Bonded (FDB) and Flotzone Deep Diffused (FDD) substrates. The sensors were produced to match different readout chips including ROC4SENS and RD53A.

From Capacitance-Voltage measurements, the doping concentration of the bulk region was determined to be $4.5 \times 10^{12} \text{ cm}^{-3}$ and $3.3 \times 10^{12} \text{ cm}^{-3}$ for FTH and FDB wafers, respectively. The full depletion voltage was found to be between 55 V to 75 V . The active thickness of the FTH sensors was estimated to be $148.0 \pm 1.0 \mu\text{m}$ from edge-on measurements with pad diodes (see Chapter 5). This value is in agreement with the value obtained from the edge-on measurements with pixel sensors presented in [56].

In this work, the sensors produced in the 2019 submission are studied. Theses sensors are compatible with RD53A or CMS Readout Chip (CROC). These Sensors have pitch sizes of $25 \times 100 \mu\text{m}^2$ and $50 \times 50 \mu\text{m}^2$. Only FDB and FTH wafers were produced. FDD

wafers were discarded for the 2019 submission as it turned out that the active thickness of the FDD wafers was around $175\ \mu\text{m}$ and the doping profile was not uniform.

Fig. 3.17 shows the top view and cross-section of the pixel layout for the pitch size of $25 \times 100\ \mu\text{m}^2$. The presence of a positive charge carriers in the oxide layer causes an accumulation layer of electrons in the region between the readout implants. Since electrons are the majority charge carriers in the n^+ implant, this accumulation layer would short the implant of two adjacent pixels. For inter-pixel isolation, p-stop technology was used. In this approach, an additional p^+ implant was introduced between pixels, as it is shown in Fig. 3.17b.

The pitch size of the RD53A chip is $50 \times 50\ \mu\text{m}^2$. Therefore, the opening of the passivation is not directly above the pixel's implant and is coupled to the implant of the pixel in the adjacent row, as it is shown in Fig. 3.17a. This coupling causes a "cross-talk" between the readout of two pixels in adjacent rows and can bias the hit position reconstruction in the sensor. To reduce this effect, the implant is slightly chipped in the new submission. This design is called "Bitten Implant". In Chapter 7, a systematic comparison between the cross-talk of these different designs is given.

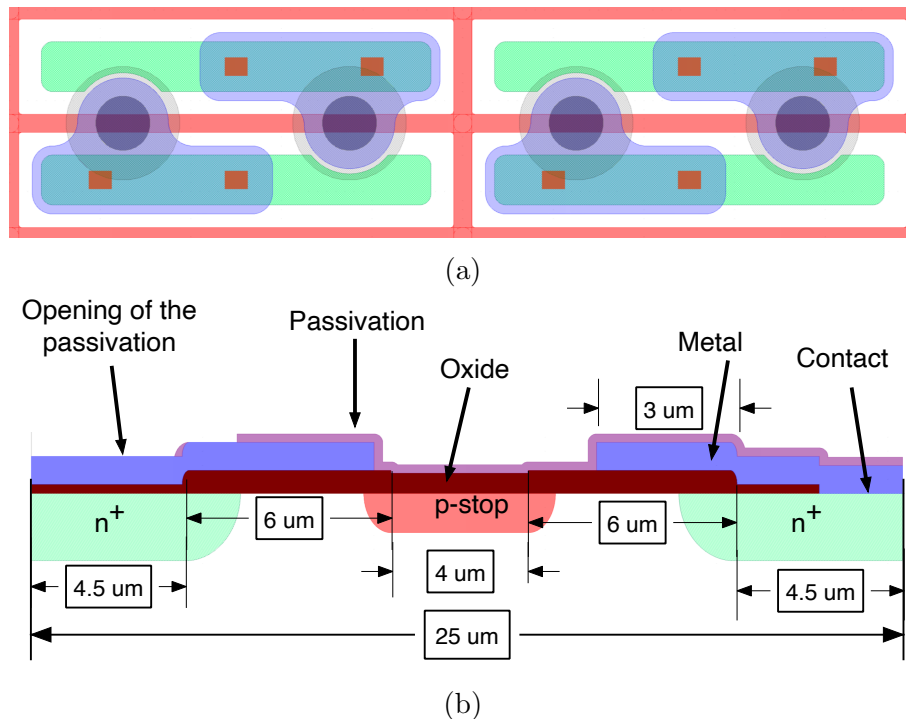


Figure 3.17: Top (a) and cross section (b) views of pixel sensors layout with pitch size of $25 \times 100\ \mu\text{m}^2$. Purple circles show the opening for passivation, and orange squares are the contact. The other colours are similar between the two figures.

In addition to the pixel layout shown in Fig. 3.17a, a few other designs were included in the 2019 submission. Fig. 3.18 shows these layouts:

- Bias dot: A common punch-through or bias dot connects group of 4 pixels to a biasing rail in this design. One can use this feature to bias the sensor as test before

3 Experimental setup for Test-Beam Measurements

bump bonding. The disadvantage is the reduced charge collection in the region around the bias dot which reduces the overall hit efficiency of the sensor, especially after irradiation.

- Bricked: Pixels in the odd rows are shifted by a half pitch size ($50\ \mu\text{m}$) compared to the even rows. This feature improves the resolution in the long direction and redistributes the cross-talk between two pixels (see Chapter 7).
- $50 \times 50\ \mu\text{m}^2$: This design is compatible with the pixel size of the RD53A chip and therefore the effect of the cross-talk is negligible. For the tracks with large angles, the collected charge is proportional to the pitch size rather than the thickness. Therefore, the collected charge of this design is lower than for the design with the pixel size of $25 \times 100\ \mu\text{m}^2$ in the barrel region.

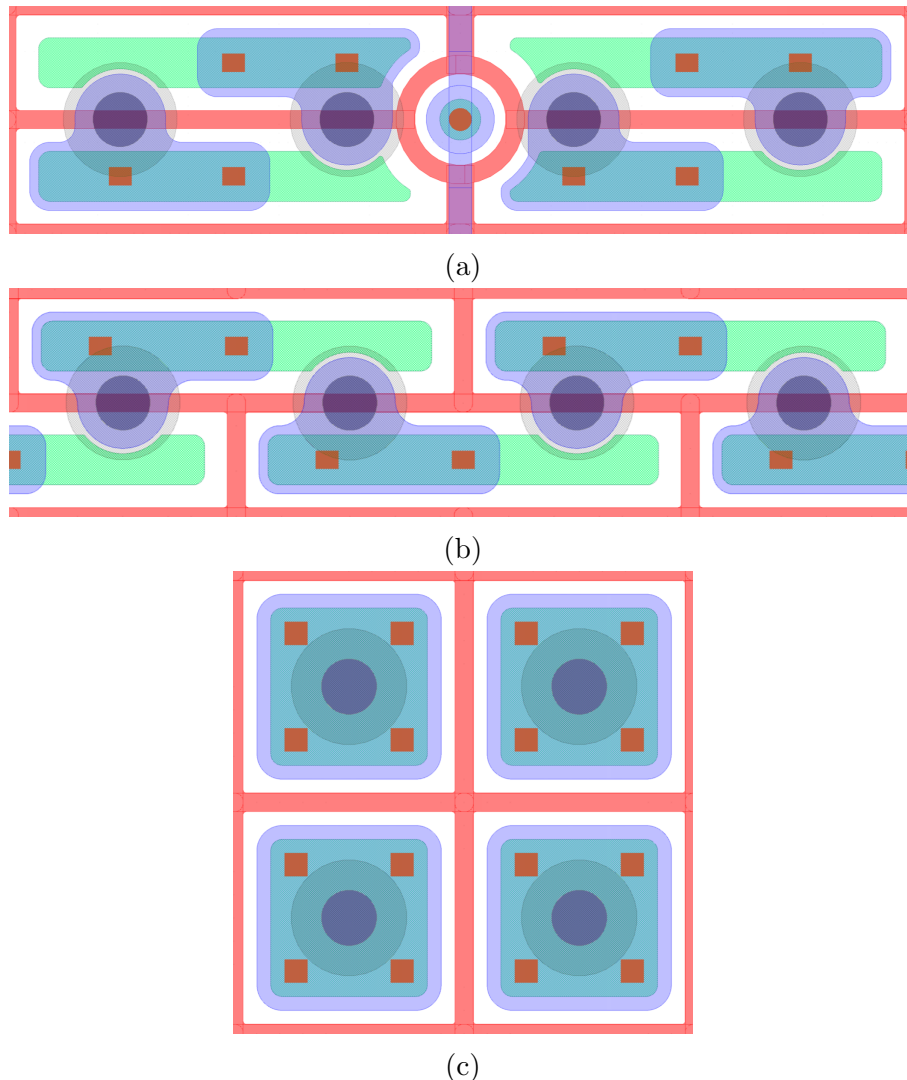


Figure 3.18: Pixel sensors designs included in 2019 HPK submission: (a) Bias dot, (b) Bricked, and (c) $50 \times 50\ \mu\text{m}^2$. Explanation about designs is given in the text.

Table 3.1 shows the list of the pixel sensors which were characterised in the test-beam for this work. The sensors were bump bonded to the RD53A readout chip at the Fraunhofer

Institut für Zuverlässigkeit und Mikrointegration [57]. For irradiation, sensor-readout modules were irradiated with 23 MeV protons at Zyklotron AG [58]. To calculate the 1 MeV neutron-equivalent fluence, a hardness factor of $\kappa = 2.2$ is used [59]. The estimated error on the irradiation fluence is 10%. The online threshold of the modules during the test-beam measurements (as defined in Section 6.1.2) are listed in the last column of the table.

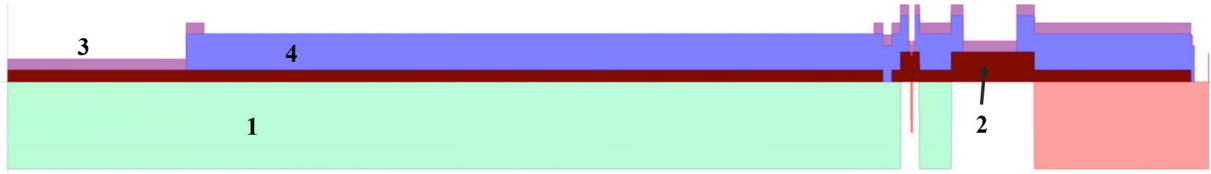
Module ID	Pitch Size (μm^2)	Fluence (cm^{-2})	Sensor Design	Threshold
M599	25×100	0	Bitten with bias dot	771 ± 96
M605	50×50	0	Without bias dot	815 ± 67
M606	25×100	0	Bricked without bias dot	859 ± 66
M612	25×100	0	Bitten without bias dot	741 ± 67
M595	25×100	0.86×10^{16}	Bitten without bias dot	1150
M596	25×100	1.2×10^{16}	Bitten without bias dot	1250
M598	25×100	1.2×10^{16}	Bricked without bias dot	1308 ± 73
M608	25×100	0.95×10^{16}	Bitten with bias dot	1210 ± 177
M613	25×100	2.0×10^{16}	Bitten without bias dot	1241 ± 138

Table 3.1: List of modules in this work. Irradiation fluences are quoted in 1 MeV neutron-equivalence unit. Threshold is quoted in electrons as defined in Section 6.1.2.

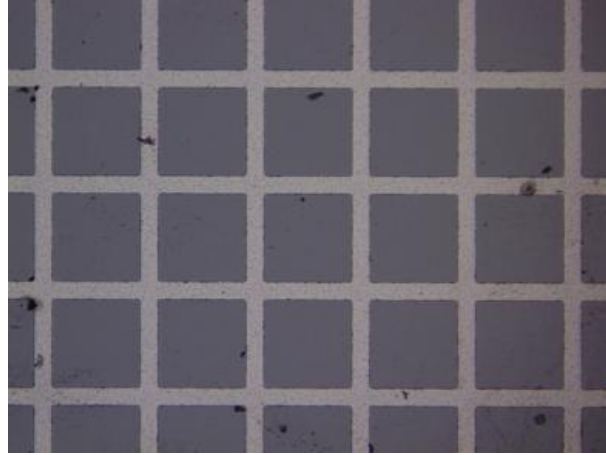
3.4.2 Pad Diodes

The diodes studied in this work are p-type (n^+pp^+ configuration) produced by HPK. They have a nominal thickness of $150 \mu\text{m}$ and area of $5 \times 5 \text{mm}^2$ and $2.5 \times 2.5 \text{mm}^2$. Fig. 3.19a shows a cross-section view of the diodes in n^+p region. Thickness of each layer was measured using a Keyence laser microscope [60]. Fig. 3.19b shows a microscope image of the grid structure in the rear-side of the diode. The thickness of different layers are presented in Table 3.2.

3 Experimental setup for Test-Beam Measurements



- (a) Cross-section view of the diode in the n^+p region (front-side). Each region is shown with a different colour and number: 1. n^+ implant, 2. SiO_2 layer, 3. passivation layer (SiO_2), 4. Aluminum layer. The sketch shows half of the diode cross-section.



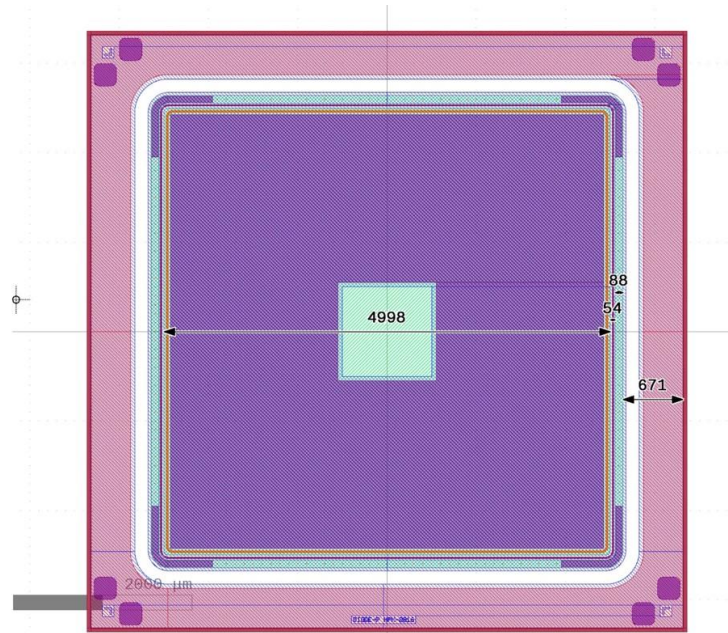
- (b) Grid structure in the p^+p region (rear-side): p^+ implant is visible with the dark squares and Aluminum grid is visible with the light grid.

Figure 3.19: Layers of the diode in n^+p and p^+p regions.

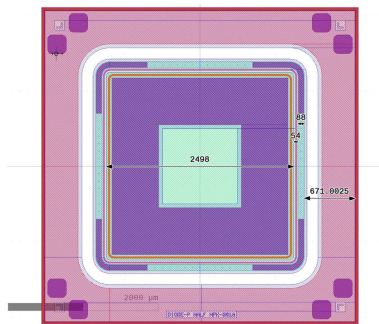
Parameter	Symbol	Value
Active thickness	d	150 μm
Aluminum front-side	$t_{Al,front}$	1.1 μm
Aluminum rear-side	$t_{Al,rear}$	1.2 μm
SiO_2	t_{SiO_2}	0.35 μm
n^+ depth	t_{n^+}	2.2 μm
p^+ depth	t_{p^+}	0.4 μm
Rear-side grid	—	50 μm Aluminum, 250 μm pitch size

Table 3.2: Specifications of the diode studied in this work.

Fig. 3.20 show the top view of the pad diodes. Four diodes were irradiated with 23 MeV protons to 1 MeV neutron-equivalent fluences Φ_{eq} of 2, 4, 8, and $12 \times 10^{15} \text{ cm}^{-2}$. For the calculation of Φ_{eq} , a hardness factor $\kappa = 2.2$ is used [59]. From the capacitance-voltage measurement, the depletion voltage of the non-irradiated diode is determined to be around 75 V and the doping density of the bulk region $4.5 \times 10^{12} \text{ cm}^{-3}$. The guard ring of the diodes is floating during the measurement.



(a) size of $5.0 \times 5.0 \text{ mm}^2$



(b) size of $2.5 \times 2.5 \text{ mm}^2$

Figure 3.20: Top view of pad diodes. Dimensions are given in μm .

4 TCT measurements with pad diodes

TCT has been used to extract the lifetimes of charge carriers, electrons and holes in silicon sensors. This method records the transient current generated by light or ionising particles with a known energy-loss distribution in silicon. By integrating this current, one calculates the collected charge. Trapping times for each charge carrier, τ_e and τ_h , can be determined separately because the charge carriers are produced close to the surface of the diode, and only one type of the charge carrier induces the transient current. Knowledge of the charge collection close to the junction is necessary to understand the results.

In this chapter the results of the TCT measurements using α -particles and red-light is presented. The chapter is organised in the following way: an overview of the previous studies for TCT measurement and dead-layer determination for semiconductor detectors is given in Section 4.1, the experimental setup is introduced in Section 4.2, the results for the non-irradiated diode are presented in Section 4.3, the results for two irradiated diodes are presented in Section 4.4, and in Section 4.5 a summary of the findings in this chapter is given.

List of own contributions

- Conducting the initial TCT measurements with alpha particle and red-light laser and establishing the procedure
- Analysing the raw data from measurements
- Developing an empirical model to describe the observations

The experimental results shown in this chapter were taken by Oscar Murzewitz in a format of a bachelor thesis [61].

4.1 Literature Review

In [62], p^+n pad sensors of 300 μm thickness fabricated on high-ohmic silicon were irradiated by neutrons to a 1 MeV neutron-equivalent fluence, Φ_{eq} , up to $3 \times 10^{13} \text{ cm}^{-2}$. Both p^+n and n^+n sides of the sensor were measured with α -particles from ^{244}Cm , and the current transients were recorded. The range of these α -particles in silicon is about 20 μm . It has been found that $\tau_e < \tau_h$, and as expected $1/\tau_e$ and $1/\tau_h$ are proportional to Φ_{eq} . In [63], similar p^+n pad diodes were irradiated by 1 MeV neutrons and 300 MeV

π -mesons to Φ_{eq} up to $3 \times 10^{14} \text{ cm}^{-2}$. The transients for α -particles and electrons from a ^{90}Sr source were recorded. To describe the data, bias-voltage-dependent lifetimes had to be introduced. For $\Phi_{\text{eq}} = 3 \times 10^{14} \text{ cm}^{-2}$ and a bias voltage 20 V above full depletion, $\tau_e = 3 \text{ ns}$ and $\tau_h = 7 \text{ ns}$ have been determined. It was also found that the lifetime of electrons is longer than holes at high bias voltages.

In [64] p^+n pad diodes fabricated on silicon crystals with resistivities between $1 \text{ k}\Omega \cdot \text{cm}$ to $15 \text{ k}\Omega \cdot \text{cm}$ and different oxygen concentrations were irradiated by reactor neutrons up to $\Phi_{\text{eq}} = 2 \times 10^{14} \text{ cm}^{-2}$. The current transients generated by a sub-nanosecond laser with a wavelength of 660 nm (absorption length $3.8 \mu\text{m}$ at 20°C [65]) which illuminated the diode from both sides were recorded. In the analysis, the transients were multiplied by e^{t-t_0/τ_i} for $t > t_0$, where t_0 is the time of the laser pulse and τ_i is the trapping time of the respective charge carrier. The values of the charge-carrier lifetimes, τ_i , were obtained by requiring that the integral of the transient above full depletion is independent of the bias voltage. It was found that trapping rates are proportional to Φ_{eq} and independent of the initial resistivity and oxygen concentration. Different to the results discussed above, the trapping rate for holes is larger than for electrons: $1/\tau_h \approx 1.4 \times 1/\tau_e$.

So far, this discrepancy is not resolved. One reason is that close to the two surfaces of the diode CCE is reduced. Possible causes discussed in [66]: An insufficient field strength as a result of the doping profile, accumulation layers at the highly-doped contacts, positive oxide charges at the Si-SiO₂ interface, and crystal lattice defects caused by radiation damage from the ion implantation or irradiations. As a reduced CCE is highly relevant for measuring low-energy ions, electrons, and X-rays, numerous studies are reported in the literature.

The standard method for determining inactive-layer thicknesses uses an α source [67, 68]. As a function of the angle of incidence, θ , the induced charge is measured, from which $E(\theta)$, the energy deposited in the active region of the detector, is obtained. Assuming $CCE = 0$ in the inactive region, the energy lost there, ΔE_{inact} , is obtained from the measured energy deficit: $E(\theta = 90^\circ) - E(\theta) = \Delta E_{\text{inact}}/\cos\theta$ and the thickness of the inactive layer is: $d_{\text{inact}} = \Delta E_{\text{inact}}/[\Delta E/dx(\theta = 90^\circ)]$.

This method is used in [69] for determining the inactive layer in an 1.5 mm thick p^+n detector produced by Micron Semiconductors with 1.95 mm wide orthogonal strips on both sides. The detector was exposed in vacuum to a point source of α -particles positioned 3.2 mm from the strip detector with energies of 6.062 MeV and 8.785 MeV from the decay of ^{212}Bi and ^{212}Po , respectively. From the position reconstructed in the strip sensor, the angles of the incident, α -particles were obtained. A silicon dead layer (inactive layer assuming $CCE = 0$) of thickness 610 nm was determined.

In [70] the energy deficit for α -particles from a ^{224}Cm source for p^+n pad detectors as a function of reverse voltage and incident angle has been measured. The detectors were fabricated by J. Kemmer with different boron implant densities and heat treatments, to find the parameters for minimal charge-collection losses at the p^+ implant. In the analysis,

in addition to the dead layer, charge-carrier lifetimes, surface-recombination velocities, and the plasma effect have been taken into account. Dead-layer depths between 20 nm and 300 nm were observed, and the technological parameters for minimal charge losses were determined.

In [71] monoenergetic electrons with energies of 12.6, 15.6, and 18.6 keV were used to investigate the CCE close to the surface of the p^+n pixel detector of the KATRIN experiment. From the comparison of the measured energy spectra, which show a characteristic low-energy tail, with a detailed simulation of the energy loss and the charge collection by drift and diffusion, and an inactive layer of 155.4 ± 0.2 nm and a CCE from this layer of 46 % were determined.

In [72] it was found that for non-irradiated n^+p diodes, field-free regions of 1 μm to 2 μm depth have to be introduced close to the surfaces to describe the transients: The charge carriers which diffuse into the high-field regions change the transients.

For this thesis, the charge collection of p -type pad diodes close to the n^+ and p^+ implants before and after irradiation are measured in the TCT setup using red-light laser and α -particles. The average transients were recorded for different bias voltages, and the collected charge was calculated by integrating these transients. The results suggest there is an inactive region in the n^+p implant with a reduced CCE compared to the CCE of the bulk region. A model was developed to estimate the width and CCE of this inactive region.

4.2 Experimental Setup

The specification of pad diodes for this study is given in Section 3.4.2. Three diodes were measured for this study: a non-irradiated diode and two irradiated diodes at 1 MeV neutron-equivalent fluences of $2 \times 10^{15} \text{ cm}^{-2}$ and $8 \times 10^{15} \text{ cm}^{-2}$. The pad size of all three diodes is $5.0 \times 5.0 \text{ mm}^2$.

Fig. 4.1 shows the setup used for the illumination of the n^+p and p^+p region. More details can be found in [61]. An LDH-series laser diode with a wavelength of 660 nm and the sub-nanosecond pulse width was used as a light source, which was operated at 1 kHz. An optical system could focus the light beam to a spot size of $\omega = 6.7 \mu\text{m}$. The ^{241}Am source, which emits 5.4 MeV α -particles, had a diameter of 5 mm, and an activity of 320 kBq. For the front and rear sides illumination, the minimum source-to-diode distance was 14.1 mm and 12.5 mm, respectively. To change the energy of α -particles, the Am-source was moved in the z -direction with steps of 500 μm .

The non-irradiated diode were measured at the room temperature and -20°C and irradiated diodes were only measured at -20°C . The cooling system includes a liquid chiller and a Peltier element. The temperature was controlled using a PT-100 sensor connected to the PCB where the diode is connected. A dry air flow was flushed into the copper box to avoid condensation.

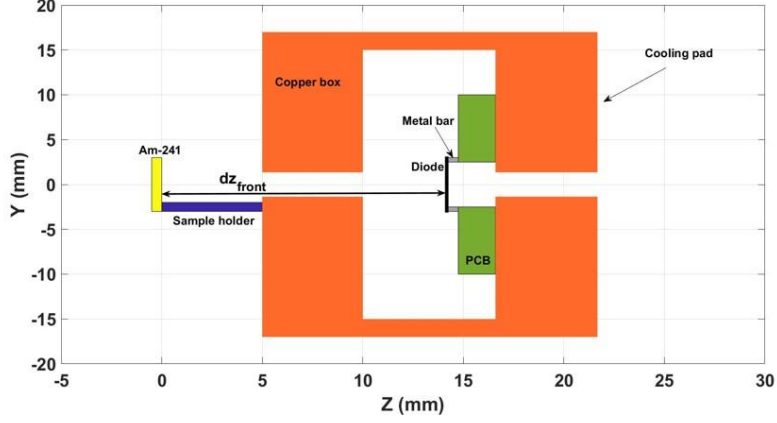
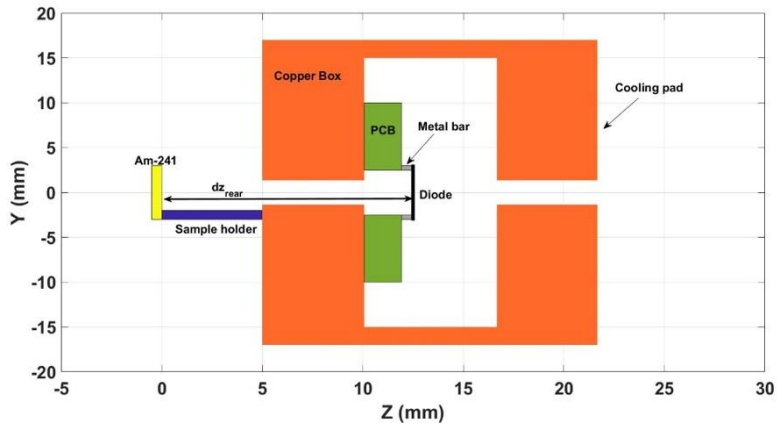
(a) Sketch of the setup for illumination of the n^+p implant (front-side).(b) Sketch of the setup for illumination of the p^+p implant (rear-side).

Figure 4.1: TCT setup used for this work.

A Tektronix oscilloscope with an analogue bandwidth of 2.5 GHz and a sampling rate of 40 GS/s was used to record the transients. The transients of the pad diodes were amplified through a Femto HSA-X-40 amplifier with a bandwidth of 2.0 GHz and a nominal gain of 100 [52]. For the alpha measurements, the trigger was provided with a threshold of 20 mV on the transient. For the laser measurements, the trigger came from the laser driver.

For each data point, the average of 512 transients was recorded. The gate width for calculating the charge is 20 ns. Before integrating the pulse, an average of the prepulse region is calculated and subtracted from the pulse. The diode transient measured by the oscilloscope is used to calculate the collected charge as:

$$Q = \int_{t_0}^{t_1} \frac{U(t)}{G \cdot R_L} dt \quad (4.1)$$

$U(t)$ is the average voltage transient after the baseline correction, R_L is the load resistor (50Ω), and G is the gain of the amplifier (100). Fig. 4.2 shows a transient measured with the non-irradiated diode illuminated with the laser light before and after the baseline correction along with the integration window.

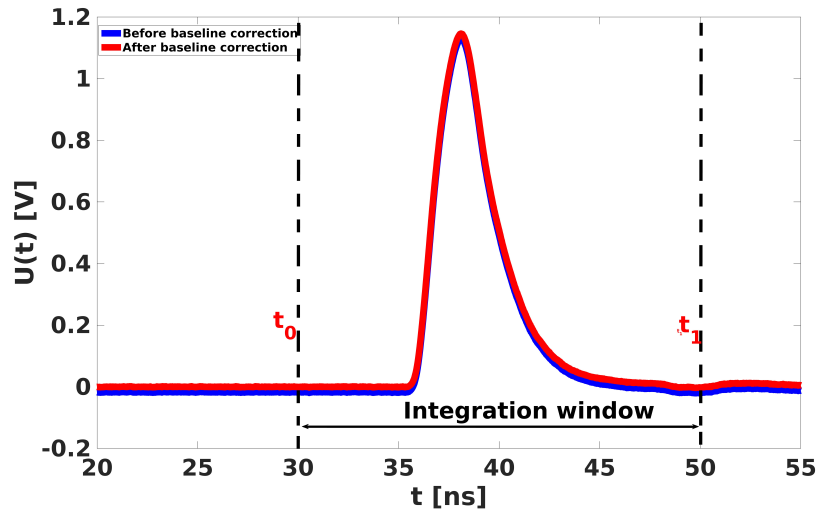


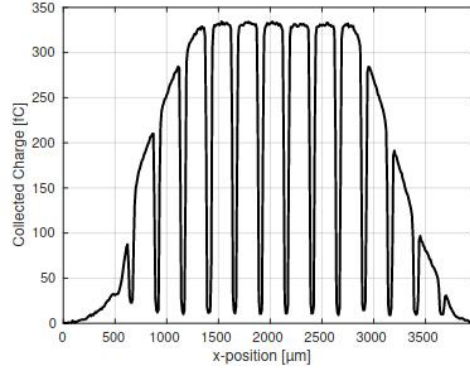
Figure 4.2: Average voltage transient of the non-irradiated diode before and after pedestal subtraction. The data was taken at room temperature by illuminating the diode from n^+ implant using red-light laser.

4.3 Results for Non-Irradiated Diode

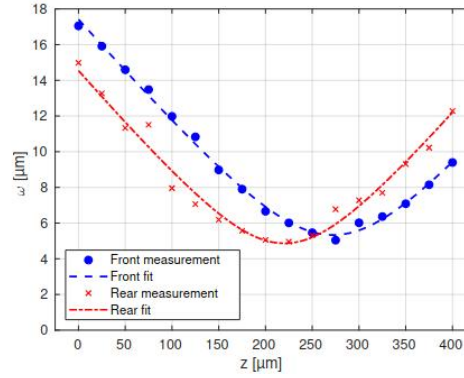
4.3.1 Geometrical Measurements

For the data measured by the laser, it has to be assured that the light beam passes through the opening of the front side and the Al-grid of the rear side. The focusing of the light beam on the surface of the diode uses a scan over the Al patterns of the diode in the x - and y - direction for different z - positions of the optical system. The width of the laser beam focus in x - and y - direction is equal, $\omega = 6.7 \mu\text{m}$. In Fig. 4.3a, an x scan of the rear side of the pad diode is shown. The pattern of the $50 \mu\text{m}$ wide Al-strips with the pitch of $250 \mu\text{m}$ can be seen. From the flat distribution of the signals at the maxima and the depth of the minima, it can be concluded that the focused light beam fits well in between two strips.

The precise knowledge of the distance between the Am-source and the diode surface for both front and rear side illumination is required for determining the charge collection efficiency: the energy loss in 1 mm of air is approximately equal to the energy loss of $0.5 \mu\text{m}$ in silicon, and precision for the air path of $200 \mu\text{m}$ is required for a $0.1 \mu\text{m}$ precision of a possible inactive layer. The calliper measurement has an estimated uncertainty of $500 \mu\text{m}$. As shown in Fig. 4.3b, a more precise determination of the difference of the z offset for front and rear is possible by measuring the z dependence of the width of the light spot, $\omega(z)$, for front and rear illumination. The z scale in the figure has been corrected for the mechanically measured difference in the distances between the entrance to the collimator and the illuminated face of the DUT for the front and rear sides. The z positions of the foci differ by approximately $60 \mu\text{m}$ which is well within the uncertainty of the calliper measurement and satisfies the requirements.



(a)



(b)

Figure 4.3: (a) Measured charge as function of horizontal position, x , of light spot on pad diode for rear-side illumination. (b) Spot size, $\omega(z)$, as function of z position of laser head for front and rear side illuminations. Plots are taken from [61].

4.3.2 Energy Calibration

In this section, the mean energy of α -particles at the surface of the Am sample, E_0 , and the calibration constant, K , or the ratio between the collected charge and the energy deposited by the α -particles in the active region of the pad diode E_α , is determined:

$$Q_\alpha = K \cdot E_\alpha \quad (4.2)$$

For the calibration, data from a non-irradiated diode exposed to α -particles from the front and rear sides are used. Fig. 4.4a shows $Q(z)$, where z is the distance between α -source and the outer surface of the diode (SiO_2 layer in Fig. 3.19a), for the data taken at 120 V bias and 20 °C. Because of the asymmetry of the setup (Fig. 4.1), the z ranges for front and rear differ by 1.65 mm. It is seen that $Q(z)$ for front and rear are similar at the same distance (z). Moreover, with increasing z , $Q(z)$ decreases because of the energy loss of the α -particles in air. E_α can be calculated from the literature values of stopping powers using the following equation:

$$E_\alpha(z) = E_0 - \Delta E_{air}(z) - \Delta E_{Al} - \Delta E_{\text{SiO}_2} - \Delta E_{inact} \quad (4.3)$$

4 TCT measurements with pad diodes

where:

E_0 : the α -particles energy at the source,

$\Delta E_{air}(z)$: the energy loss in air (front, rear),

$\Delta E_{Al}(z)$: the energy loss in an Al layer (front, rear),

$\Delta E_{SiO_2}(z)$: the energy loss in an $SiO_2(z)$ layer (only front),

$\Delta E_{inact}(z)$: the energy loss in a possible inactive layer (front, rear).

The energy loss for the different layers i is calculated as $\Delta E_i = \int_0^{t_i} (\rho_i \cdot dE/dz) dz$ where dE/dz is the energy-dependent total stopping powers of each layer in units of MeV cm²/g taken from [73] and t_i is the thickness of the layer i taken from Table 3.2. ρ_i is the specific weight of each layer. For the air density at 20 °C, $\rho_{air} = 1.204 \times 10^{-3}$ g cm⁻³ is used. ΔE_{inact} is introduced for a possible inactive layer of thickness, d_{inact} , in the silicon close to one of its surfaces. It is assumed that for the non-irradiated pad diode the charge-collection efficiency is 100 % in the active and zero in the inactive region. After calculation of E_α from Eq. (4.3), one can obtain the expected collected charge from Eq. (4.2). By taking E_0 , K , and d_{inact} as free parameters, the following function was minimised:

$$D_{\Phi=0}^2 = \sum_k (Q_m^{front}(z_k) - Q_\alpha^{front}(z_k))^2 + (Q_m^{rear}(z_k) - Q_\alpha^{rear}(z_k))^2 \quad (4.4)$$

In Eq. (4.4), Q_m and Q_α are the measured and calculated charge, respectively. z_k is the source-to-diode distance: for the front-side $z_k = (14.1 + k \times 0.5)$ mm and for the rear-side $z_k = (12.4 + k \times 0.5)$ mm.

The model results are shown in Fig. 4.4b with a black line. One can see that at lower charge values, the data start to deviate from the model. This can be understood by taking into account the effect of the trigger threshold. The energy spectrum of α -particles is well above the threshold level at high energies, and the effect of the threshold on the average transient is negligible. At lower energies, the spectrum falls below the threshold level, and only the pulses with amplitude higher than the threshold are recorded. The average transient at these lower energies is biased towards higher values. Therefore, the collected charge is higher than the values from the model, as is seen in Fig. 4.4b.

From the minimisation of Eq. (4.4), the following results for the free parameters are obtained:

$$E_0 = 4.75 \pm 0.01 \text{ MeV}$$

$$K = 41.4 \pm 0.1 \text{ fC/MeV}$$

$$d_{inact} = 1.0 \pm 0.1 \text{ }\mu\text{m, for the rear-side}$$

The value of E_0 is smaller than the 5.48 MeV which is expected from α -particle energy of the ^{241}Am source. The difference is ascribed to the self-absorption effect in the source. The value of K is close to the estimate of 43.6 fC/MeV for a value of 3.67 eV [17] for the average energy required to generate an electron-hole pair.

The value of about $1\ \mu\text{m}$ for $d_{inact, rear}$ is surprising. However, it is in agreement with the results of the measurements with red-light laser. At a bias voltage of 200 V and a temperature of $20\ ^\circ\text{C}$, the ratio of the collected charge of the non-irradiated diode for front-side, Q_L^{front} , and the rear-side, Q_L^{rear} , illumination was measured to be $R_m = \frac{Q_L^{front}}{Q_L^{rear}} = 1.69$. From Fresnel's law, the transmission of light between two layers is $Tr = 4 \cdot n_1 n_2 / (n_1 + n_2)^2$ where n_1 and n_2 are the refractive indices of two layers. For wavelength of 660 nm, the refractive index of Si, SiO_2 , and air is equal to 3.82, 1.45, and 1.00, respectively [65]. Using these values, the transmission of light from air to silicon (rear-side) is $Tr^{front} = 0.65$. The total transmission of light from air to SiO_2 and from SiO_2 to silicon (front-side) is $Tr^{rear} = 0.77$. The ratio between the light transmission in front to rear side is $R_{Tr} = Tr^{front}/Tr^{rear} = 1.18$ which is much smaller than measured value of R_m . Assuming an inactive region with a thickness of $\approx 1.4\ \mu\text{m}$ in the rear-side would justify the measured ratio:

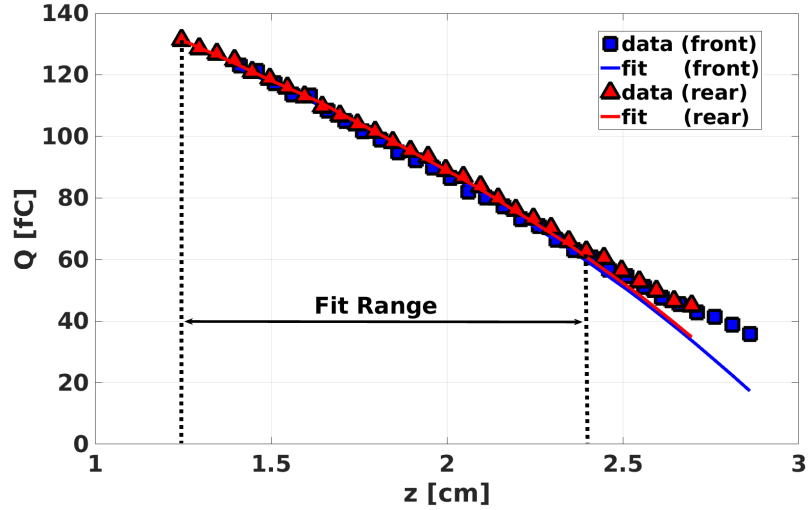
$$R = R_{Tr} \times e^{\frac{d_{inact}}{x_0}} = 1.18 \times e^{\frac{1.4\ \mu\text{m}}{3.8\ \mu\text{m}}} = 1.69 \quad (4.5)$$

The exponential term in Eq. (4.5) takes into account the charge loss in the assumed inactive region where $x_0 = 3.8\ \mu\text{m}$ is the absorption length of the light with a wavelength of 660 nm in silicon at $20\ ^\circ\text{C}$.

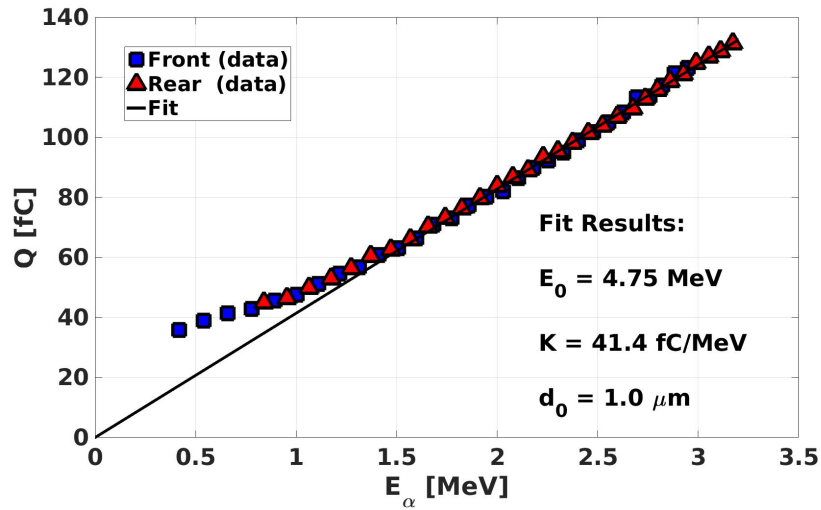
4.3.3 Results Taken at Cold Temperature

Air density increases as its temperature decreases, which changes the energy loss of alpha particles and the absorption length of light in silicon. Therefore, for the calculation of CCE of irradiated diodes, it is necessary to measure the non-irradiated diode at the cold temperature ($-20\ ^\circ\text{C}$) as well. Fig. 4.5 shows the results of the bias scan for the non-irradiated diode measured at $-20\ ^\circ\text{C}$ with α -particles and red-light laser. For both measurements, the collected charge becomes independent of the bias voltage for $V_{bias} > 100\ \text{V}$. The quoted energy in Fig. 4.5a, are calculated by dividing the collected charge by the calibration factor of $K = 41.4\ \text{fC/MeV}$ from Section 4.3.2.

The slight decrease of Q for front below $V_{bias} = 120\ \text{V}$ is caused by the slow drift of the holes in the low field at the rear side so that only part of the signal is integrated by the gate. Below the depletion voltage, the electric field at the rear side is zero, and CCE drops to zero for the rear.

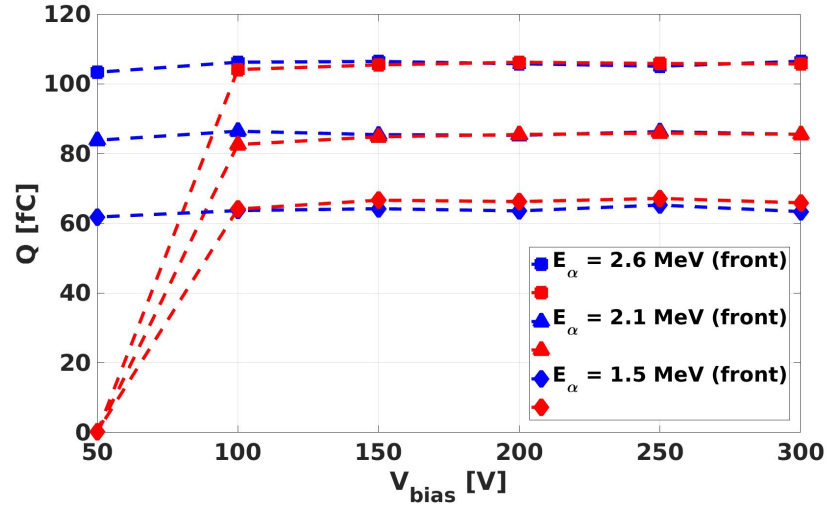


(a)

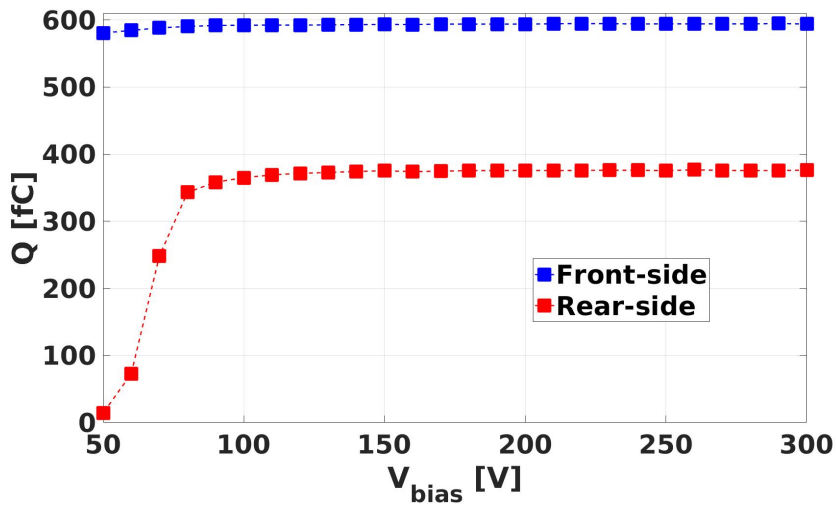


(b)

Figure 4.4: (a) Measured charge, $Q(z)$, as a function of z , the distance between the α -source and surface of the pad diode, at 20 °C for front and rear sides irradiation. The results of the model, which is described in the text, are shown as lines of the same colour. (b) $Q(E_\alpha)$ as a function of E_α , obtained from the data of (a) and the model. The slope of the linear curve is the calibration constant K . The deviation of the data from the model curve at low E_α is caused by the trigger threshold required for the α -particles measurements.



(a)



(b)

Figure 4.5: Results of the bias scan for the non-irradiated diode measured by α -particles for front-side (blue) and rear-side (red)(a) and red-light laser (b). The measurement was done at -20°C .

4.4 Results for Irradiated Diodes

4.4.1 Voltage-Dependent Charge Collection Efficiency

Voltage transients of two irradiated diodes were measured, and the collected charge was calculated as a function of bias voltage. Charge Collection Efficiency of the irradiated diodes measured with α -particles and red-light laser, $CCE_{\Phi,\alpha}$ and $CCE_{\Phi,L}$, are defined

4 TCT measurements with pad diodes

as:

$$CCE_{\Phi,\alpha} = \frac{Q_{\Phi,\alpha}}{Q_{0,\alpha}} \quad (4.6)$$

$$CCE_{\Phi,L} = \frac{Q_{\Phi,L}}{Q_{0,L}}$$

Where $Q_{0,\alpha}$ and $Q_{0,L}$ are the average of the collected charge of the non-irradiated diode for the bias voltage 300 V measured with α -particles and red-light laser, respectively.

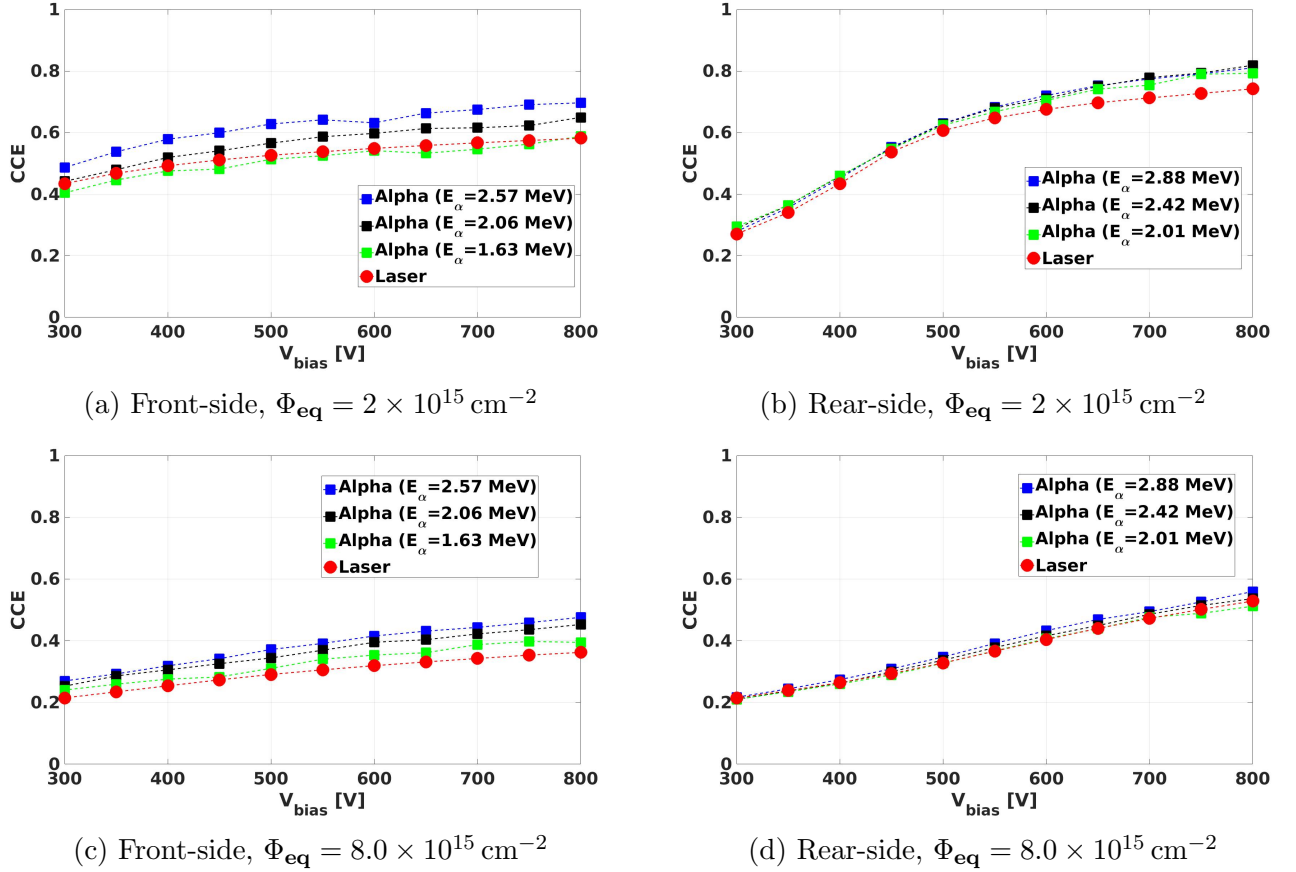


Figure 4.6: CCE of irradiated sensors for illumination with light and α -particles of different energies for front-side (a,c) and rear-side (b,d) illumination.

Fig. 4.6 shows the voltage dependence of $CCE_{\Phi,L}$ and $CCE_{\Phi,\alpha}$ for three E_α values and two irradiation fluences. It is noted:

- As expected, CCE increases with bias voltage and decreases with irradiation fluence.
- For rear-side, $CCE_{\Phi,\alpha}$ is approximately independent of E_α , and CCE for α -particles and for light are similar.
- For front-side, $CCE_{\Phi,\alpha}$ depends on E_α : By increasing E_α from 1.6 MeV to 2.6 MeV, $CCE_{\Phi,\alpha}$ increases by 25% and 18% for fluences of 2 and $8 \times 10^{15} \text{ cm}^{-2}$, respectively.

The third observation can be interpreted as evidence of an inactive layer on the front side, which changes with Φ_{eq} . This is qualitatively explained with the help of Fig. 4.7, which

shows the deposited energy profiles of α -particles for three values of E_α and light with 660 nm wavelength at -20°C in silicon (with $4.5\ \mu\text{m}$ absorption length at this temperature). An inactive layer at the implant causes an E_α -dependent reduction of $CCE_{\Phi,\alpha}$ and, given the different shape of the profile for light, a different reduction of $CCE_{\Phi,L}$. In the next section, a model for calculation of the thickness of the inactive layer (d_{inact}), CCE in the inactive layer (CCE_{inact}), and CCE in the active region (CCE_{active}) is introduced.

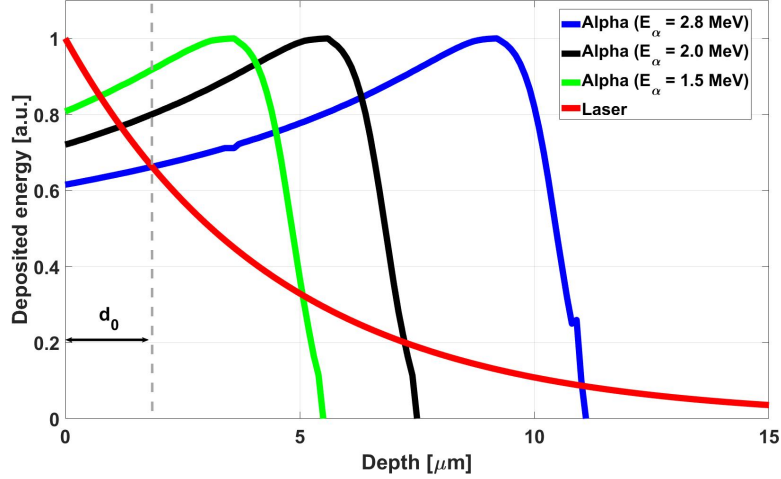


Figure 4.7: Stopping power profiles of α -particles, $dE/dx(x)$ in silicon for three E_α values. Intensity of the red-light (660 nm) as a function of depth in silicon. The curves are normalised to their maximum value. For the laser, the curve is plotted for an absorption length of $4.5\ \mu\text{m}$.

4.4.2 A Model for Characterisation of the Inactive Layer

A model for charge collection close to implants is proposed to characterise the observations in the last part. A sketch of the model is shown in Fig. 4.8. In this model, E_α is the energy of α -particles at the surface of the diode which is given by $Q_{\alpha,\Phi=0}^{T=-20^\circ\text{C}}/K$ and ΔE_{inact} is the energy deposited in the inactive region with a width of d_{inact} .

For measurements with α -particles, the expected charge from both inactive and active regions is given by:

$$Q_\alpha^{model}(z) = K \cdot (\Delta E_{inact}(z) \cdot CCE_{inact} + (E_\alpha(z) - \Delta E_{inact}(z)) \cdot CCE_{act}) \quad (4.7)$$

For the measurements with the laser light, the expected charge from both inactive and active regions is given by:

$$Q_L^{model} = Q_{L,\Phi=0} \cdot ((1 - e^{-d_{inact}/\lambda_L}) \cdot CCE_{inact} + e^{-d_{inact}/\lambda_L} \cdot CCE_{act}) \quad (4.8)$$

Where, λ_L is the absorption length of the red-light (660 nm) in silicon. By taking CCE_{act} , CCE_{inact} and d_{inact} as free parameters, the following function was minimised:

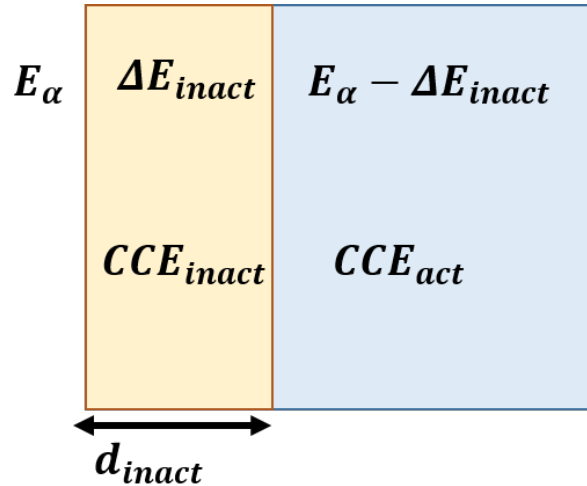


Figure 4.8: The model used for quantification of the measured CCE.

$$D_\Phi^2 = w_a \cdot \sum_k (Q_\alpha^{model}(z_k) - Q_\alpha^{meas}(z_k))^2 + w_L \cdot (Q_L^{model} - Q_L^{meas})^2 \quad (4.9)$$

This function is minimised separately for every bias voltage, fluence and illumination side (front/rear). For the weights, $w_\alpha = 1$ and $w_L = 5$ are chosen. The results are not sensitive to the choice of w_α and w_L . z_k is defined similar to Eq. (4.4) for front and rear sides.

Fig. 4.9 compares the measured to the z -dependence of the charge from the model for front and rear sides illumination with α -particles for bias voltages of 300 V and 800 V for two irradiation fluences. In Fig. 4.9e and Fig. 4.9f, a comparison between the voltage dependence of the charge for front and rear sides illumination with laser light is shown. Similar to the non-irradiated diode (Fig. 4.4a), the minimisation is only performed for low z values, which correspond to high E_α values, which are not affected by the trigger threshold.

The results of the minimisation for three free parameters of the model, i.e. CCE_{active} , CCE_{inact} and d_{inact} , is shown in Fig. 4.10. For the front-side at $\Phi_{eq} = 2 \times 10^{15} \text{ cm}^{-2}$ an inactive layer with $CCE_{inact} = 0.38$ is observed, which decreases from $3 \mu\text{m}$ at 300 V to $2.5 \mu\text{m}$ at 800 V. For the front-side at $\Phi_{eq} = 8 \times 10^{15} \text{ cm}^{-2}$, similar value for d_{inact} is observed at 800 V but CCE_{inact} is less than 0.05. From Fig. 4.10a, one can see that the CCE_{active} is significantly higher than measured CCE shown in Fig. 4.6a and Fig. 4.6c. Therefore, ignoring the charge loss in the inactive layer, when determining charge-carrier lifetimes from CCE using α -particles or light with short absorption length, results in too low life-time values.

For the rear-side, an inactive layer of about $1 \mu\text{m}$ for an assumed $CCE_{inact} = 0$ is observed already for the non-irradiated diode, as it is discussed in Section 4.3.2. The results obtained for the irradiated diodes (Fig. 4.10f) are relative to d_{inact} before irradiation. The values obtained for d_{inact} is small compared to the front-side. One can see that

CCE_{active} (Fig. 4.10b) is close to the measured value of CCE for the rear side (Fig. 4.6b) and Fig. 4.6d).

As it appears from Figs. 4.9a and 4.9c, at the bias voltage of 300 V, the deviation of the model from the data is more significant due to the effect of threshold. Therefore, the uncertainties of fit parameters for low bias voltages are higher. To understand the effect of the threshold on results, one needs to repeat the measurements by recording individual transients rather than the average transient and obtain the charge spectrum.

4.5 Summary and Conclusion

In this chapter, the results of charge collection measurements for pad diodes close to their implants (n^+p and pp^+) are shown before and after irradiation. The charge carriers are produced either by pulsed light with an absorption length of $4.5\ \mu\text{m}$ (at $-20\ ^\circ\text{C}$), or by α -particles with energies between 1.5 MeV to 2.8 MeV, with a range of $5\ \mu\text{m}$ and $10\ \mu\text{m}$, respectively.

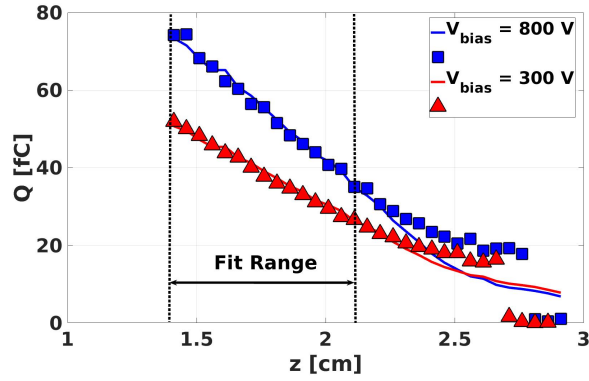
By assuming a 100% CCE for the non-irradiated diode, the calibration constant (K) for α -particles with a unit of fC/MeV is calculated. In addition, it is concluded that there is a dead layer of $1\ \mu\text{m}$ at the pp^+ side of the diode before irradiation.

The CCE results in the n^+p region after irradiation show higher values for measurements with α -particles with E_α than red-light laser. It is observed that as E_α increases, the measured CCE decreases and approaches the value measured by the laser. A model that assumes an inactive layer close to the implant is proposed to understand these results.

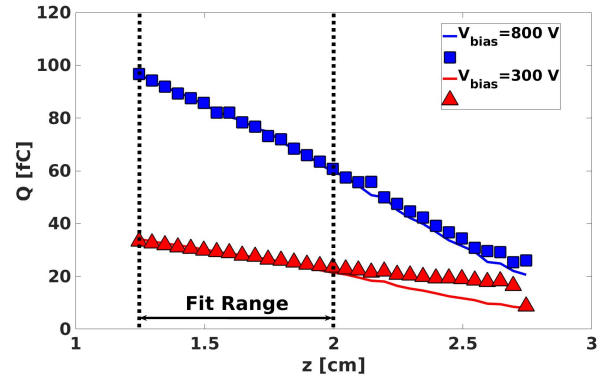
By fitting the model to data, it is revealed that there is an inactive region with a thickness around $2.5\ \mu\text{m}$ close to the n^+p implant. It is concluded that after excluding the effect of the inactive region, the CCE in the active region of the diode is significantly higher than the measured CCE. Ignoring the effect of this inactive region when one determines the lifetimes of holes results in too low values.

The effect of having a $2.5\ \mu\text{m}$ inactive thickness is significant when the incoming particles have a short absorption length in silicon. For radiation with long absorption length, such as MIP or IR light, this effect is small.

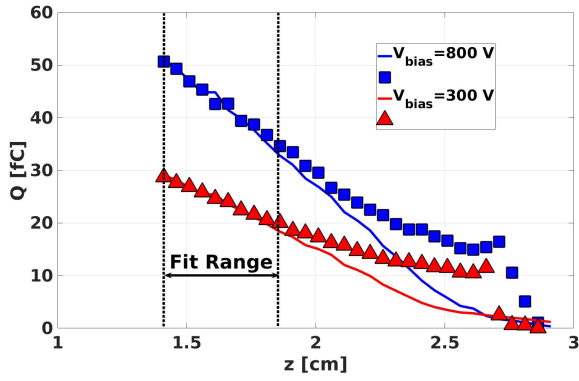
In this chapter, the effect of the non-active region on the estimated trapping times of electrons and holes is not quantified. One needs to know the electric field profile in the irradiated diodes, and this information cannot be retrieved from Top-TCT measurements.



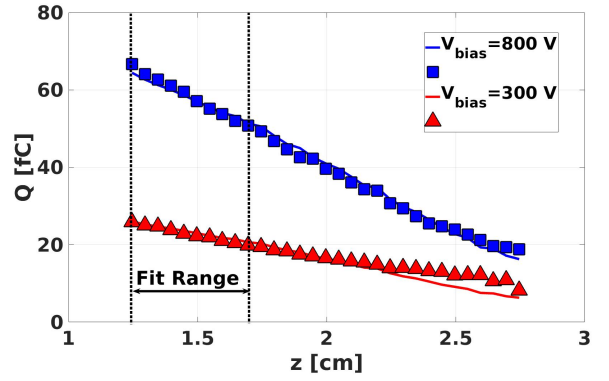
(a) Front-side, $\Phi_{\text{eq}} = 2 \times 10^{15} \text{ cm}^{-2}$



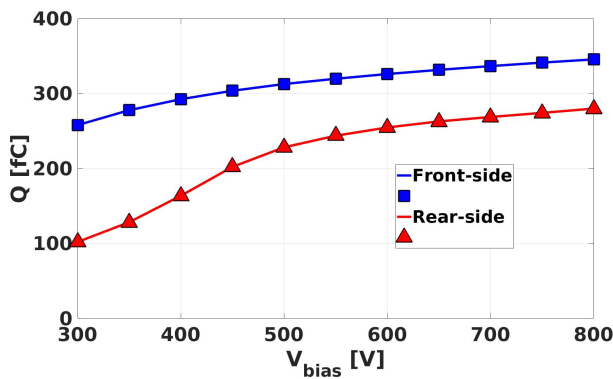
(b) Rear-side, $\Phi_{\text{eq}} = 2 \times 10^{15} \text{ cm}^{-2}$



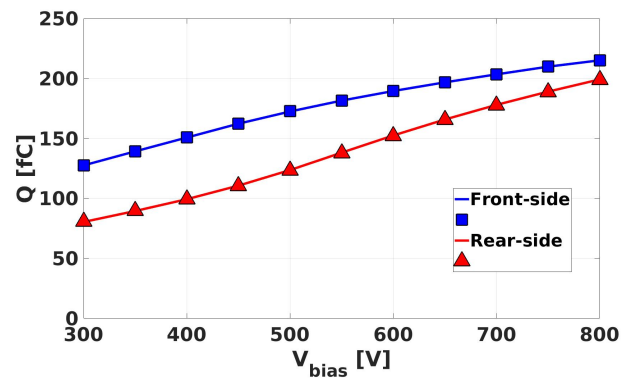
(c) Front-side, $\Phi_{\text{eq}} = 8 \times 10^{15} \text{ cm}^{-2}$



(d) Rear-side, $\Phi_{\text{eq}} = 8 \times 10^{15} \text{ cm}^{-2}$

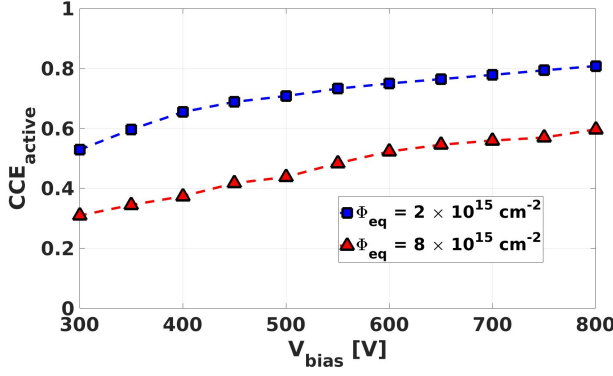


(e) $\Phi_{\text{eq}} = 2 \times 10^{15} \text{ cm}^{-2}$

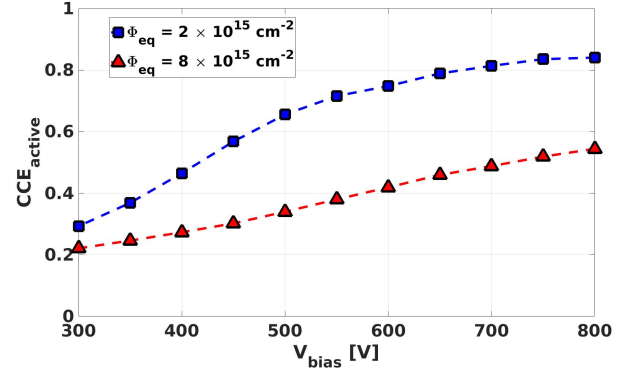


(f) $\Phi_{\text{eq}} = 8 \times 10^{15} \text{ cm}^{-2}$

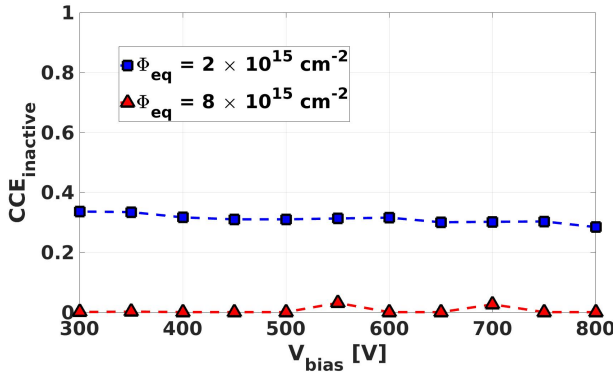
Figure 4.9: Comparison of between model and measured z dependence of charge for α -particles (a-d) and bias voltage dependence for laser (e-f). The results of the model are shown with solid lines and measured data are shown with shapes.



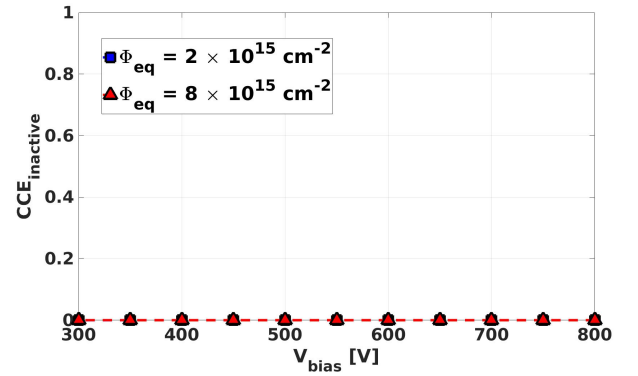
(a) Front-side



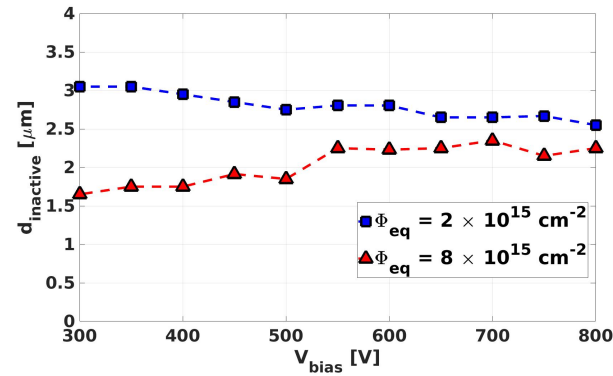
(b) Rear-side



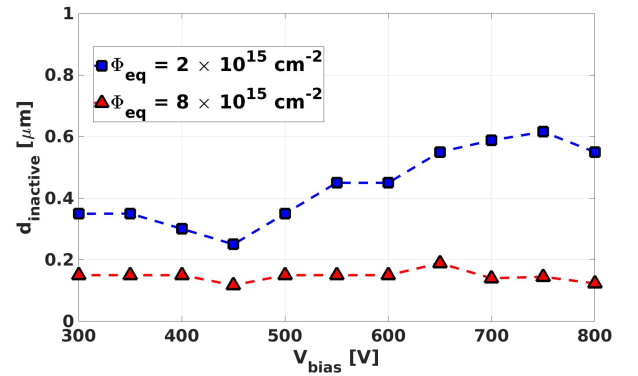
(c) Front-side



(d) Rear-side



(e) Front-side



(f) Rear-side

Figure 4.10: Results of the model: Voltage dependence of the depth of the inactive layer, d_{inact} , the CCE of the inactive layer, CCE_{inact} , and the CCE of the active layer, CCE_{act} , for the front-side (a,c,e) and the rear-side (b,d,f).

5 Edge-on Measurements with Pad Diodes

This chapter describes the development of an edge-on method for studying pad diodes with an electron. A motivation for this technique is given in Section 5.1. The symbols used in the chapter are defined in Section 5.2. The in-situ alignment procedure to find the minimum angle between the electron beam and the surface of the pad diode is introduced in Section 5.3. The measured charge collection profiles for the irradiated and non-irradiated diodes are shown in Section 5.4. A comparison between measured and simulated charge collection profiles using three radiation damage models is shown in Section 5.5. In Section 5.6, the measured collected charge profiles are unfolded to obtain CCE profiles of irradiated and non-irradiated diodes. A summary and conclusion of the chapter is given in Section 5.7.

List of own contributions

- Preparation of experimental tools for taking data
- Developing and testing the procedure for in-situ alignment
- Analysing the raw data taken at test-beam
- Simulation of charge collection profiles using radiation damage models
- Unfolding the measured charge collection profiles and extract CCE profiles

Some contents of this chapter has been published in [51]. The analysis code for the telescope alignment and DUT readout was provided by Dr Daniel Pitzl [74].

5.1 Motivation

TCT is an experimental method to study irradiated silicon sensors. In one flavour of this technique so-called Top-TCT, the DUT is illuminated by α -particles [75, 64, 76] or red light and IR laser [62, 63, 77], and the induced current transient is recorded. One can determine the collected charge by integrating this transient. The result of this measurement is CCE defined as the ratio between the collected charge by the electrodes and the produced charge inside the sensor.

Due to short absorption depths of α -particles and red light in silicon, all electron-hole pairs are generated close to the surface of the diode. Therefore, only one of the charge carrier types (electrons or holes) is drifting through the bulk region while the other is collected immediately at the implant. The induced signal in the electrodes of the diode is dominated by the charge carrier type, which is drifting through the entire bulk and the other type has a minor contribution to the signal. As a result, one can study the trapping times of electrons and holes separately using this technique for irradiated sensors. One can obtain the overall CCE of irradiated samples with contribution from both electrons and holes using IR light.

Top-TCT with alpha particle, and the red-light laser is limited for studying highly irradiated pad diodes. The estimated CCE values from these measurements are very sensitive to possible inactive layers in the sensor implants. There is a field-free region in the diode implant where the generated electron-hole pairs can be trapped before they diffuse to the active region of the diode (the region with a non-zero electric field) [72, 20]. Simulation of a non-irradiated diode shows that this region remains field-free, independent of the applied voltage. As a result, the measured CCE values with the Top-TCT method using alpha-particles or red light underestimate the actual CCE in the active region of irradiated diodes and are affected by the change of the thickness of the non-active layer, depending on the irradiation fluence. This effect is discussed in detail in Chapter 4.

In another flavour of this technique called "edge-TCT" or E-TCT, the sensor is illuminated by focused IR laser light from the edge [78]. By scanning the light along the edge, one can obtain information on the charge collection as a function of depth. This method has been used to study strip sensors to extract their charge, and electric field profiles [79, 80, 33]. An issue with this technique is that the waist radius of the light spot changes as it travels through the sensor, and the beam becomes defocused. As a result, it can only be used for segmented sensors (strips and pixels) where the charge produced below a narrow strip is collected and read out. This technique cannot be used for measuring pad diodes with only one readout electrode. Another issue is that it is not straightforward to normalise E-TCT measured charges to an absolute value, as the exact number of electron-hole pairs generated by light in the sensor is unknown. In addition, it has been shown that the absorption length of IR light changes after irradiation [81]. Therefore, a direct comparison between irradiated and non-irradiated detectors is not straightforward.

After considering the limits of the existing experimental methods, a new edge-on technique was developed for this thesis. In this method, a pad diode is illuminated with an electron beam from the side. Fig. 5.1 shows a concept of this technique.

The advantages of this technique compared to the Edge-TCT with IR light are:

- Radius and direction of the beam do not change as it travels through the sensor. The estimated deflection angle of an electron beam with an energy of 5.2 GeV after travelling in 5.0 mm of silicon is 0.53 mrad from Eq. (3.1). This number is well

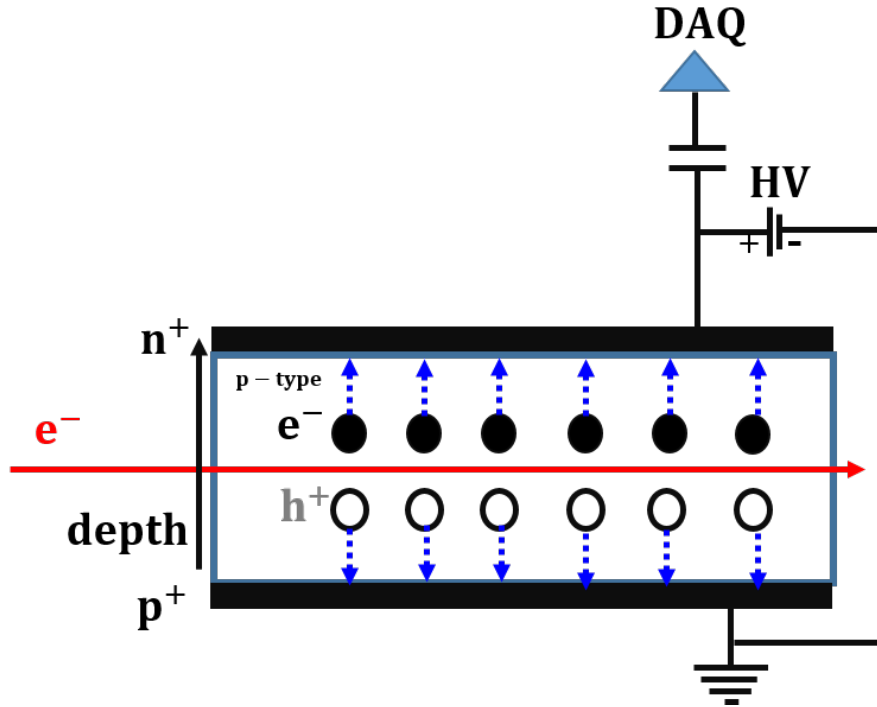


Figure 5.1: Edge-on measurements for pad diodes using an electron beam.

within the uncertainty of the measurements. Therefore, the method can be used to study pad diodes.

- An absolute normalisation is possible as the energy loss of the beam in the sensor, i.e. average dE/dx , is well known.
- The energy loss of the electron beam by charge deposition does not change after irradiation. Therefore, one can directly compare the results of the non-irradiated and irradiated diodes together.

The disadvantages of this technique are:

- Due to the large capacitance of pad diodes, the rise times of induced signals on the electrodes are in the order of a few nanoseconds. As a result, it is not straightforward to extract information about charge carrier velocity and electric field from the transients.
- The alignment procedure proposed in this paper is limited for highly irradiated sensors where the charge collection profile is not uniform as a function of depth.

Charge collection profiles as a function of depth have been measured for pixel detector at grazing angles [82] and edge-on [83, 56]. For pad diodes, the edge-on method was introduced in [84]. In that work, pions with the energy of 120 GeV were used to study 300 μm thick pad diodes. However, no results about the charge collection of the studied

diode were shown in that paper. Moreover, the required alignment accuracy was not discussed, and no alignment procedure was presented.

In this work, a procedure is introduced to align the diode with respect to the electron beam. The uncertainty of the procedure is estimated in Section 5.3.

5.2 Definitions

The measurements are performed at the DESY test-beam facility. The details about the experiment setup can be found in Section 3.3. The specifications of diodes are given in Section 3.4.2. In total six pad diodes were measured for this study: two non-irradiated diodes with pad sizes of $5 \times 5 \text{ mm}^2$ and $2.5 \times 2.5 \text{ mm}^2$, and four irradiated diodes at 1 MeV neutron-equivalent fluences of $2 \times 10^{15} \text{ cm}^{-2}$ and $4 \times 10^{15} \text{ cm}^{-2}$ with a pad size of $5.0 \times 5.0 \text{ mm}^2$, and $8 \times 10^{15} \text{ cm}^{-2}$ and $12 \times 10^{15} \text{ cm}^{-2}$ with a pad size of $2.5 \times 2.5 \text{ mm}^2$.

Transients were integrated in a time window (gate) to calculate the collected charge. The charge is calculated as:

$$Q_{meas}(x_k) = \int_{t_0}^{t_1} \frac{U(x_k, t)}{G \cdot R_L} dt \quad (5.1)$$

$U(x_k, t)$ is the voltage transient after the baseline correction at a position of x_k (in the test-beam coordinates). R_L is the input impedance of the oscilloscope (50Ω) and G is the nominal gain of the amplifier (100). For this study, a gate width of 30 ns was chosen. Fig. 5.2 shows an average transient for the non-irradiated diode biased at 100 V for the events with amplitude higher than 20 mV.

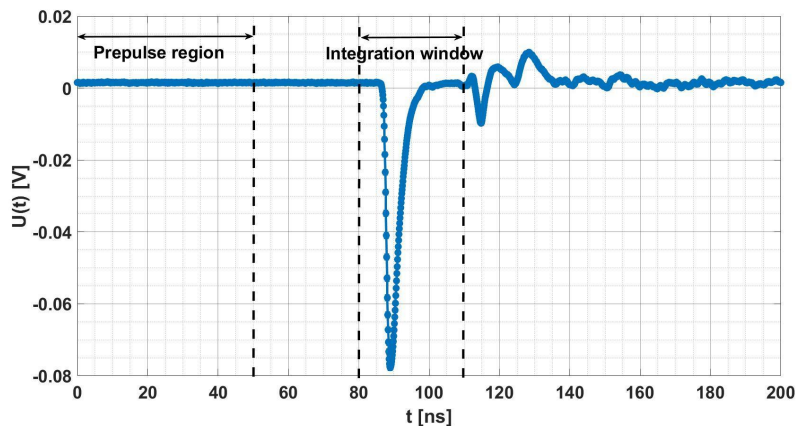


Figure 5.2: Average transient of the non-irradiated diode for all events with an amplitude higher than 20 mV. The bias voltage for this measurement was set at 100 V.

The following symbols are used throughout this section:

d : thickness of the diode,

x : distance from the n^+ implant extends from $-d/2$ (n^+p implant) to $+d/2$ (p^+p implant) in sensor coordinates,

$Q_{meas}(x_k)$: measured collected charge profile as a function of x_k (in test-beam coordinates),

$CCE_e(x)$ and $CCE_h(x)$: Charge Collection Efficiency of electrons and holes as a function of x using $\lambda_{e,h}$ values (Eq. (5.7)),

$CCE_{tot}(x)$: total Charge Collection Efficiency as a function of x ($CCE_e(x) + CCE_h(x)$),

$Q_{sim}(x)$: simulated collected charge profile using parameters from radiation damage models (Eq. (5.8)),

CCE_{x_i} : assumed Charge Collection Efficiency at a depth of i used for unfolding,

$CCE_{spl}(x)$: calculated Charge Collection Efficiency by spline interpolation between CCE_{x_i} values,

$Q_{sm}(x)$: calculated collected charge profile used for unfolding (Eq. (5.9))

It should be noted that the measured charge profiles, i.e. Q_{meas} , are shown as a function of x_k in test-beam coordinates in the paper. The simulated and calculated charge profiles, i.e. Q_{sim} and Q_{sm} , are expressed as a function of x in the sensor coordinates, as defined above.

5.3 In-situ Alignment

The method proposed in this paper only works if tracks are parallel to the diode surface. An "online alignment" procedure is used to ensure this condition before data takes. It is important to point out that this procedure has to be done online before one can start taking data and cannot be corrected offline.

In this procedure, the mean collected charge is measured as a function of angle with fine steps of 0.1° or ≈ 1.7 mrad. The minimum or "zero" angle is defined as the angle where the measured charge is maximum. If tracks and diode surface are not parallel, a part of the tracks leaves the diode through the top or bottom plane and therefore deposits less charge than tracks that cross the whole diode (5 mm). As a result, the average charge is maximal when the angle between the tracks and the diode is minimal. Fig. 5.3 shows how the angle scan was done to minimise θ . The important assumption in this procedure is that the collected charge is uniform as a function of depth.

In the following, a short discussion about the angular spread of the beam, i.e. σ_θ , and the required precision of angle scan, i.e. $\Delta\theta$, is given.

The uncertainty of the position reconstruction due to the angular spread of the beam (σ_θ) is given by $d \cdot \sigma_\theta$, where d is the length of the diode which is 5 mm for this study. This quantity should be smaller than the resolution $\sigma_{x,beam}$. The uncertainty due to the

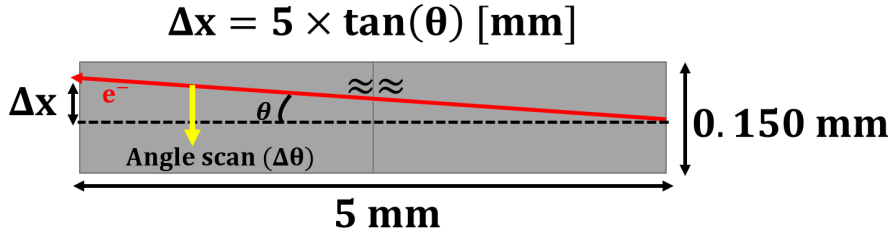


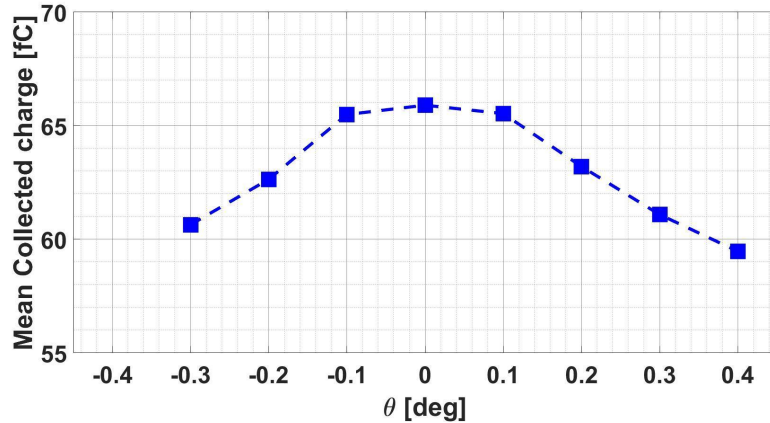
Figure 5.3: Sketch of the angle scan measurement to find the minimal value for θ for a pad diode with area of $5 \times 5 \text{ mm}^2$. The sketch is not to scale.

step size of the angle scan ($\Delta\theta$), which is given by $d \cdot \Delta\theta$, should be smaller than the resolution $\sigma_{x,beam}$ as well.

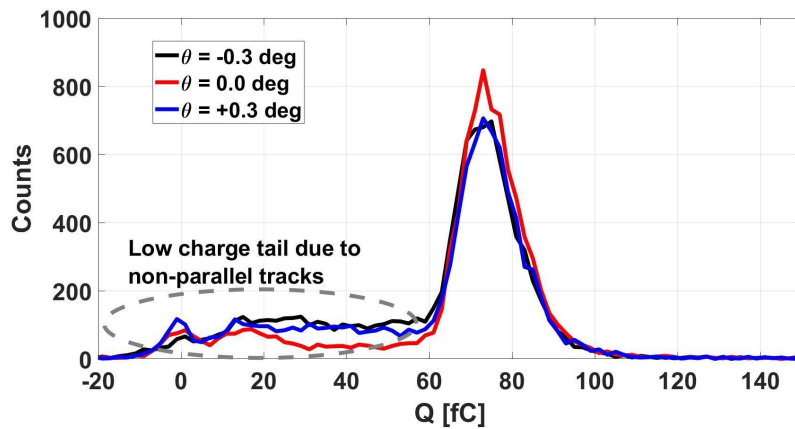
In [45], the telescope resolution was calculated as a function of the DUT-to-telescope distance. By assuming a resolution around $10 \mu\text{m}$, the maximum value for σ_θ and $\Delta\theta$ is estimated to be 2.0 mrad.

In the offline analysis, a cut is applied on the slope of the reconstructed track to select the ones with a slope less than $\pm 1 \text{ mrad}$ to fulfil the requirement on σ_θ . The step size of the angle scan is chosen 0.1° or 1.7 mrad to fulfil the second requirement.

Fig. 5.4a shows the mean collected charge of the non-irradiated diode as a function of angle (θ). The measurement is done at a bias voltage of 120 V and room temperature. For each angle, 20,000 triggers are collected. To obtain this plot, an offline threshold of 20 mV is applied to the recorded transients. Fig. 5.4b shows the charge distributions for three angles. One can notice, for non-zero angles, the charge distributions show a tail below the peak around 75 fC towards the lower charges. This tail corresponds to the tracks that partially crossed the diode, which is minimal when θ is minimal.



(a) Mean collected charge as a function of the angle (θ) for the non-irradiated diode. The plot is obtained for transients with amplitude higher than 20 mV.



(b) Collected charge distributions at three angles for non-irradiated diode.

Figure 5.4: Results of the online alignment procedure needed to adjust the angle of the diode w.r.t. the beam before starting data taking. As a result of the scan, the angle for which the mean collected charge is maximum, was defined to be $\theta = 0^\circ$. The measurement was taken at 120 V.

Based on Fig. 5.4b plot, one can define a ratio between the number of events in peak of charge distribution, i.e. $Q > 60$ fC, and number of events in the tail, i.e. $Q < 60$ fC. It is expected that at a minimum angle, this ratio is maximal. Fig. 5.5 shows this ratio as a function of angle. One can see the results are compatible with Fig. 5.4a. The advantage of using this quantity instead of the mean charge is its higher sensitivity to changes in the angle.

The procedure exploits a simple geometrical relation between the track length inside the DUT and the angle of incidence. The advantage of using this procedure is that no track reconstruction was required. This procedure had to be repeated once the diode was changed or the cooling box was dismantled.

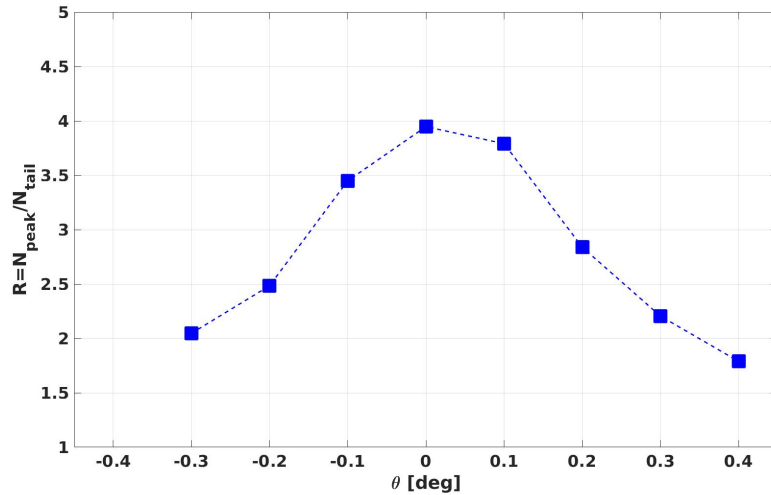
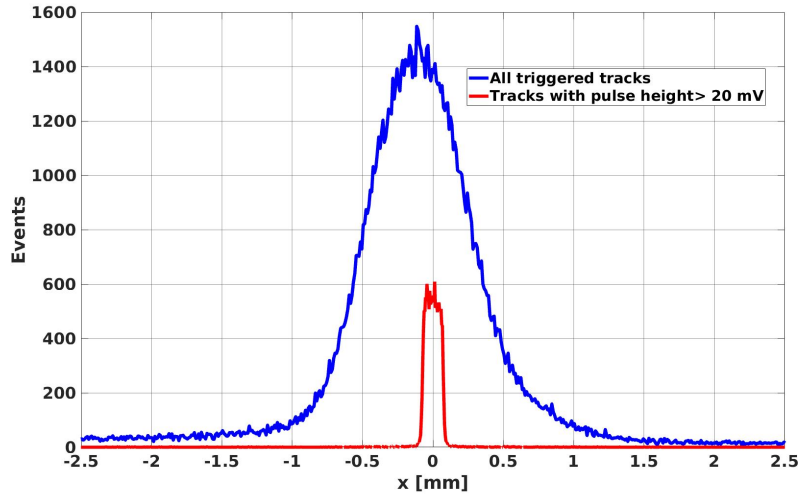
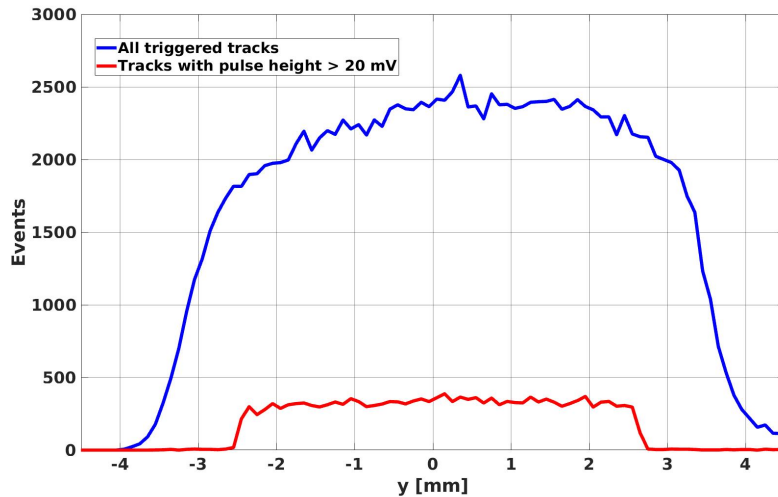


Figure 5.5: Ratio of number of events in peak of charge distribution ($Q > 60$ fC) to number of events in tail ($Q < 60$ fC) as a function of angle (θ).

After finding the minimum angle between tracks and surface of the pad diode, the alignment of DUT with respect to the triggering area was checked. In the offline analysis, this was done by reconstructing the track at the DUT surface. An offline threshold of 20 mV was applied to the diode transients to select a track which produces a pulse amplitude above the noise level. Fig. 5.6 shows all triggered tracks and tracks which a pulse height higher than 20 mV in x - (0.150 mm) and y - (5.0 mm) directions. From these plots, one can see the diode is centred inside the triggering area.



(a) All triggered tracks and tracks with a pulse height higher than 20 mV in x -direction (0.150 mm).



(b) All triggered tracks and tracks with a pulse height higher than 20 mV in y -direction (5.0 mm).

Figure 5.6: Alignment of DUT in x - and y - directions with respect to triggering area.

5.4 Charge Collection Profiles

In this section the results of the edge-on measurements for non-irradiated and irradiated diode are presented.

5.4.1 Non-Irradiated Diodes

Fig. 5.7 shows the charge profile as a function of depth for the non-irradiated diode with a size of $5 \times 5 \text{ mm}^2$ at a bias voltage of 120 V and room temperature. The assumed position of n^+ and p^+ implants at $x_k = \pm 75 \mu\text{m}$ is shown with dot lines in the figure. For comparison, the measurement was repeated at a lower beam energy of 4.2 GeV and different diode-to-telescope distance (dz_{dut}). By increasing E_{beam} and decreasing dz_{dut} ,

the profile at the edges becomes sharper, and the spatial resolution of the measurement improves.

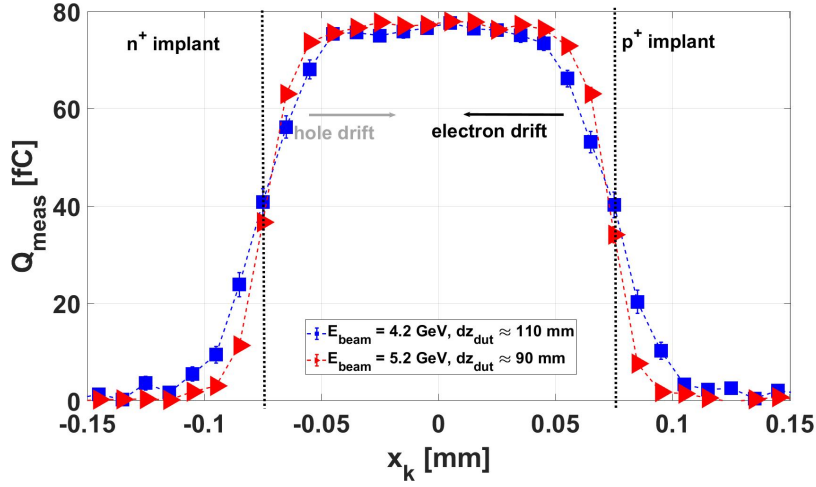


Figure 5.7: Charge profiles of non-irradiated diode with a size of $5 \times 5 \text{ mm}^2$ at bias voltage of 120 V at two different settings (E_{beam} and dz_{dut}).

As expected for the non-irradiated diode, the profile is uniform in the central region of the diode, i.e. $-0.05 \text{ mm} < x_k < 0.05 \text{ mm}$ with an average value around 77 fC. At the edges, the collected charge is slightly less due to two effects: 1. the smearing effect due to the limited spatial resolution, 2. loss at the edges due to the non-uniform energy deposition of the electron beam. To better understand the loss at the edge, the mean energy deposition as a function of depth was simulated using the GEANT4 code [85].

Fig. 5.8 shows the result of the simulation of a 5.2 GeV electron track inside 5 mm of silicon. For this simulation, *PENELOPE* physics list was used [86]. One can see that the maximum energy deposition is at the centre ($x = 0 \text{ }\mu\text{m}$), and less energy is deposited near edges ($x = \pm 75 \text{ }\mu\text{m}$). The reason is that Bremsstrahlung photons and pair-produced electrons and positrons have a higher chance of reaching out of the diode if the electron beam is close to the face of the diode.

Each data point shown in Fig. 5.7 is a mean value of a distribution. Fig. 5.9 shows the charge distribution for a central bin ($x_k = -5.0 \text{ }\mu\text{m}$) and a bin at the edge ($x_k = -65.0 \text{ }\mu\text{m}$). The distribution at $x_k = -5.0 \text{ }\mu\text{m}$ shows a peak around $\approx 77 \text{ fC}$ which corresponds to tracks pass the 5.0 mm of the diode. The distribution at $x_k = -65.0 \text{ }\mu\text{m}$ shows the same peak and an additional peak around 0 fC. These events correspond to tracks which did not pass the DUT but were reconstructed in the DUT because of the limited spatial resolution.

Another observation from this plot comes from a comparison between the mean values of two peaks around 77 fC. One sees the peak at $x_k = -65.0 \text{ }\mu\text{m}$ has slightly lower mean than the peak at $x_k = -5 \text{ }\mu\text{m}$. This is due to the edge losses shown in Fig. 5.8.

The measurements were repeated for a pad diode with a size of $2.5 \times 2.5 \text{ mm}^2$. Fig. 5.10 shows the results for both diodes. The measurements were taken at room temperature.

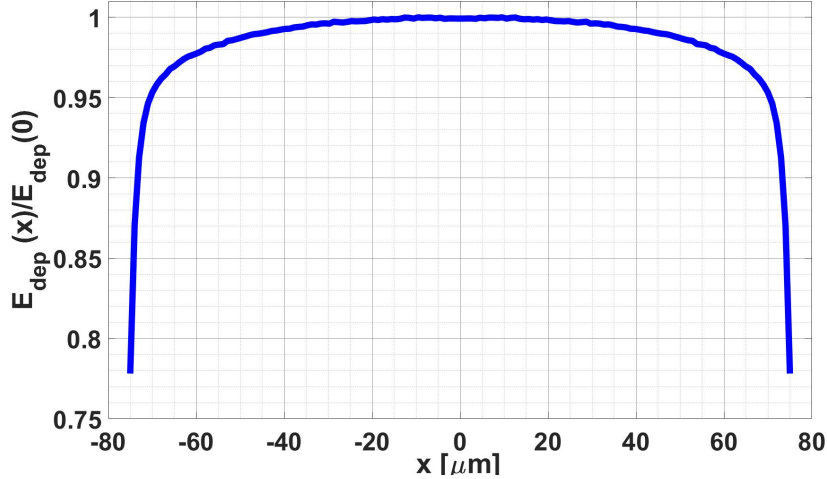


Figure 5.8: GEANT4 simulation of the relative energy deposition profile of 5.0 GeV electron beam in silicon. The profile is normalised to its maximum value.

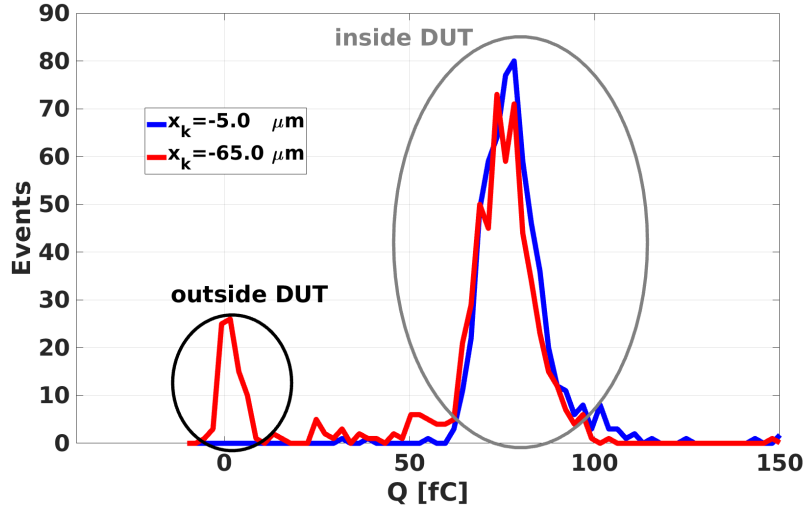


Figure 5.9: Charge distributions of data points in Fig. 5.7 in two bins with $x_k = -5.0 \mu\text{m}$ and $x_k = -65.0 \mu\text{m}$.

To estimate the collected charge and the thickness of the diodes, the data is fitted with the following equation:

$$F(x) = \frac{A}{2} \cdot \left(\operatorname{erf}\left(\frac{x - \mu_1}{\sqrt{2} \cdot \sigma}\right) - \operatorname{erf}\left(\frac{x - \mu_2}{\sqrt{2} \cdot \sigma}\right) \right) \quad (5.2)$$

The free parameters of the fit are A , σ , μ_1 and μ_2 . A gives scaling of the charge collection profile which corresponds to the collected charge of the diode, μ_1 and μ_2 are position of the diode faces in test-beam coordinates, and σ is the rms width of the position resolution of the beam telescope. The results of the fit to the data is shown in Fig. 5.10 with solid lines. The fit is done in the range of $-0.075 \mu\text{m}$ to $0.075 \mu\text{m}$. The thickness of the diode is estimated as $\mu_2 - \mu_1$. The results for the $5 \times 5 \text{ mm}^2$ and the $2.5 \times 2.5 \text{ mm}^2$ diodes are $147.6 \pm 0.4 \mu\text{m}$ and $148.9 \pm 0.6 \mu\text{m}$. The rms of deviation between fit and data

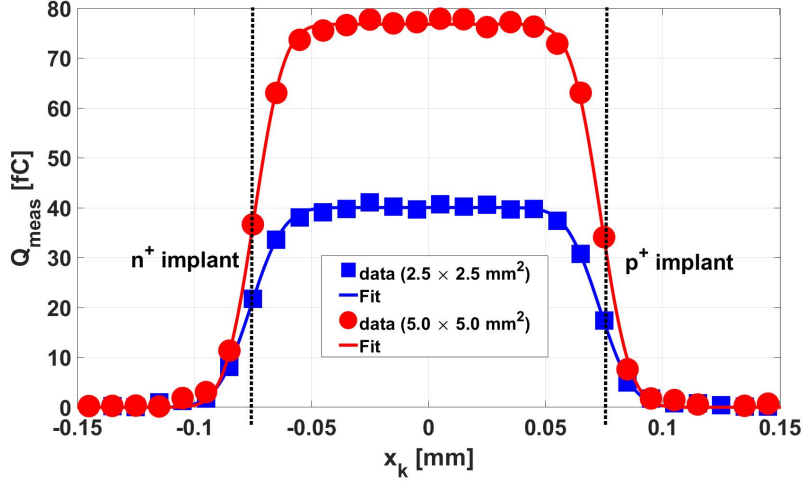


Figure 5.10: Charge collection profile of non-irradiated pad diodes as a function of depth at a bias voltage of 120 V and room temperature.

is 0.74 fC and 0.37 fC for large and small diodes, respectively. The spatial resolution of the beam telescope corresponds to σ values which are $10.6 \pm 0.2 \mu\text{m}$ and $11.6 \mu\text{m}$, for the large and the small diodes, respectively.

The ratio between the collected charge of each diode from the fit, i.e. A , is given by:

$$\frac{A_{small}}{A_{large}} = \frac{40.0 \pm 0.2 \text{ fC}}{76.8 \pm 0.3 \text{ fC}} = 0.521 \pm 0.003$$

Where A_{small} and A_{large} are the values obtained from the fit to the data for $2.5 \times 2.5 \text{ mm}^2$ and $5.0 \times 5.0 \text{ mm}^2$ diodes, respectively. This ratio is slightly higher than 0.50, which is the ratio of the implants. To check this number, one can estimate the width of the diodes from charge collection profiles in the y -direction shown in Fig. 5.11. Since the diodes are square-shaped in the yz -plane, the path length of the electron beam in the diode (z -direction) should be the same as the width of the diode (y -direction). Therefore, the ratio between the collected charges and the widths of the two diodes should be the same. The profiles of Fig. 5.11 are fitted with the formula given in Eq. (5.2) and the width of diodes is determined as $\mu_2 - \mu_1$. The ratio between width of two diodes (W_{small} and W_{large}) is:

$$\frac{W_{small}}{W_{large}} = \frac{2.640 \pm 0.008 \text{ mm}}{5.120 \pm 0.004 \text{ mm}} = 0.515 \pm 0.001$$

The results are compatible with the ratio A_{small}/A_{large} . One sees that the estimated widths for both diodes are higher than the nominal values by $\approx 130 \mu\text{m}$. This could be because the guard ring was floating during the measurements. Therefore, the charge is collected over a larger area than the pad area.

The measurements were repeated at different bias voltages. Fig. 5.12 show the collected charge profiles for two pad diodes. The profile remains unchanged for bias voltage above

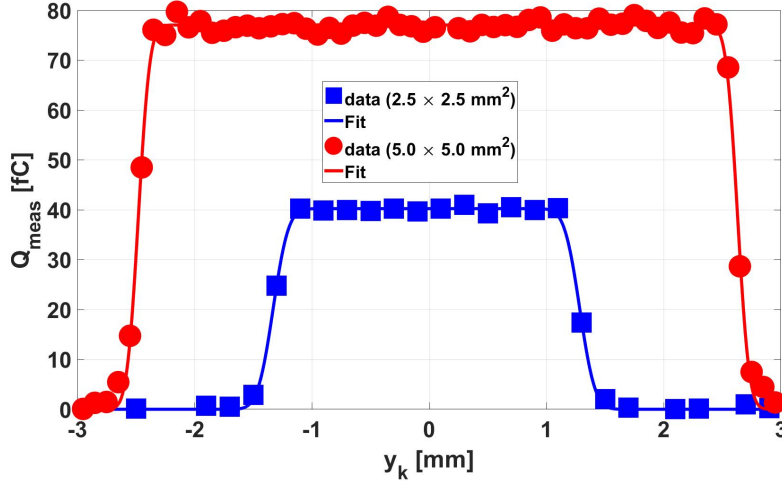


Figure 5.11: Charge collection profile of non-irradiated pad diodes as a function of width.

full depletion, i.e. 75 V. At bias voltage of 40 V and 20 V, the charge collection is zero in the region near the p^+ implant. This can be explained by the fact that the electric field expands from the n^+ to the p^+ implant. At bias voltages below the full depletion voltage, the electric field is zero near the p^+ region, resulting in a region with zero charge collection.

The depletion depth of the diode at a bias voltage of V_{bias} can be calculated using Eq. (2.2). The doping concentration of bulk region from the CV measurements is estimated ($4.5 \times 10^{12} \text{ cm}^{-3}$). The calculated depletion depth at bias voltages of 40 V and 20 V is 107 μm and 76 μm , respectively. From the plots shown in Fig. 5.12, the full width of half maximum of the profiles is around 120 μm and 90 μm for 40 V and 20 V, respectively. These values are higher than the estimated depletion thickness from Eq. (2.2). This can be explained by taking into account the effect of the diffusion of charge carriers from the non-depleted region to the active region. Due to this effect, the thickness of the region with non-zero charge collection is larger than the depletion depth.

One of the advantages of this method is the possibility of an absolute normalisation of the measurements as the energy loss of the beam in the sensor, dE/dx , is known. To examine this assumption, the average energy loss of a 5.2 GeV electron beam in 5.12 mm was simulated with GEANT4. The deposited energy was converted to deposited charge using the following relation:

$$Q_{deposited} = E_{deposited} \cdot \frac{1.6 \times 10^{-4} \text{ fC/eh}}{3.6 \text{ eV/eh}} \quad (5.3)$$

Fig. 5.13 shows the comparison between data and simulation results. The measurement charge spectrum shown in this figure is taken for the diode with the size of $5 \times 5 \text{ mm}^2$ at a bias voltage of 120 V.

One sees that the mean value of the simulated spectrum is $\approx 3\%$ higher than the data. This can be explained by the charge losses in the cables. In calculating the collected

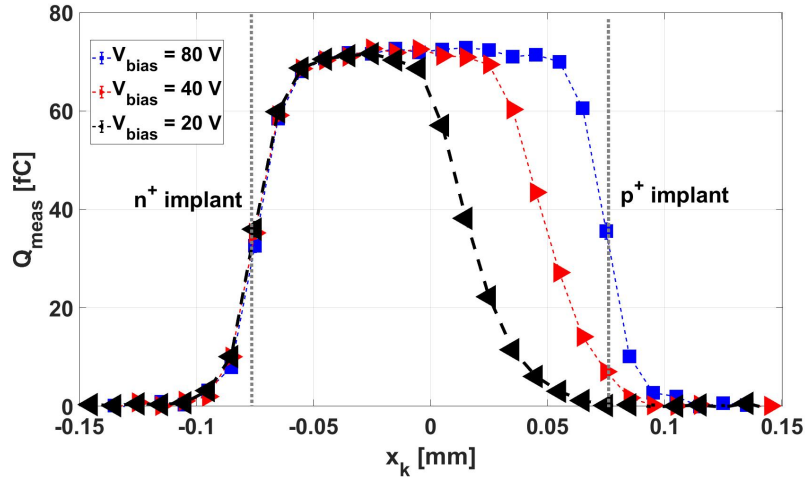
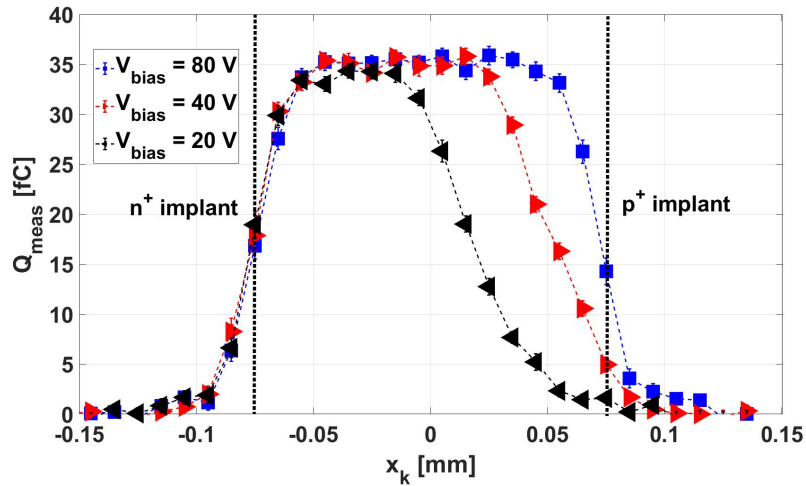
(a) Pad size: $5.0 \times 5.0 \text{ mm}^2$ (b) Pad size: $2.5 \times 2.5 \text{ mm}^2$

Figure 5.12: Charge collection of non-irradiated pad diodes at several bias voltages

charge using Eq. (5.1), the gain of the amplifier was assumed to be 100. However, this nominal value has not yet been verified with an experimental result.

5.4.2 Irradiated Diodes

The measurements were repeated for four irradiated diodes. Irradiated diodes at fluences of $2 \times 10^{15} \text{ cm}^{-2}$ and $4 \times 10^{15} \text{ cm}^{-2}$ had a size of $5.0 \times 5.0 \text{ mm}^2$ and diodes with fluences of $8 \times 10^{15} \text{ cm}^{-2}$ and $12 \times 10^{15} \text{ cm}^{-2}$ had a size of $2.5 \times 2.5 \text{ mm}^2$. To take this data, the cold box was cooled down using a circulation chiller (operating at -20°C) and two Peltier elements. For each diode, the measurements were taken at bias voltage between 100 V to 800 V. The in-situ alignment explained in Section 5.3 were done at 800 V for each diode.

The results of measurements with irradiated diodes are shown in Section 5.4.2. For each irradiated diode, the charge collection profile of the non-irradiated with the same pad size taken at a bias voltage of 120 V is shown for comparison.

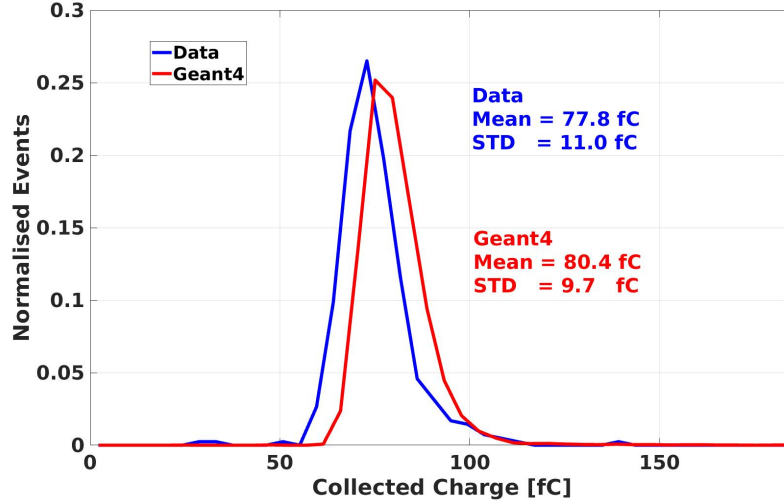


Figure 5.13: Collected charge spectrum from data and GEANT4 simulation. The data is shown for the diode with a pad size of $5 \times 5 \text{ mm}^2$ biased at 120 V and a central bin with $x_k = -5.0 \mu\text{m}$. Both distributions are normalised to their number of entries for a better comparison.

- the collected charge decreases at lower bias voltages and higher irradiation fluences.
- at high bias voltages, the charge profiles are uniform.
- at low bias voltages, the charge profiles are non-uniform, and the region close to the n^+ implant has a higher charge collection than the region close to the p^+ implant with a minimum in the central region.

These results are similar to previously published results on velocity and electric field profiles of irradiated strip sensors [87, 33]. In these references, one can see high electric fields near n^+p and pp^+ implants and a lower electric field in the centre of the sensor. Moreover, one can see a more uniform electric field at high bias voltages, which agrees with the measured, collected charge profile presented in this paper. At the highest bias voltage, a reduced CCE is seen, which is a consequence of the trapping of charge carriers.

One can calculate CCE of irradiated diode at a given bias voltage of V_{bias} by following relationship:

$$CCE(V_{bias}, \Phi) = \frac{\sum_{x_k=-0.150 \text{ mm}}^{0.150 \text{ mm}} Q_{V_{bias}, \Phi}[x_k]}{\sum_{x_k=-0.150 \text{ mm}}^{0.150 \text{ mm}} Q_0[x_k]} \quad (5.4)$$

In this relationship, $Q_{V_{bias}, \Phi}$ is the charge collection profile of the pad diode at measured a bias voltage and irradiated at a fluence of Φ and Q_0 is the charge collection of the non-irradiated diode. Q_0 is the charge collection profile of the non-irradiated diode at the bias voltage of 120 V.

Fig. 5.15 shows the CCE as a function of bias voltage for four irradiated diode. One sees that at the lowest fluences, the CCE curve shows a kink around 500 V and stays constant at higher bias voltages. At higher fluences, the kink disappears, and CCE increases

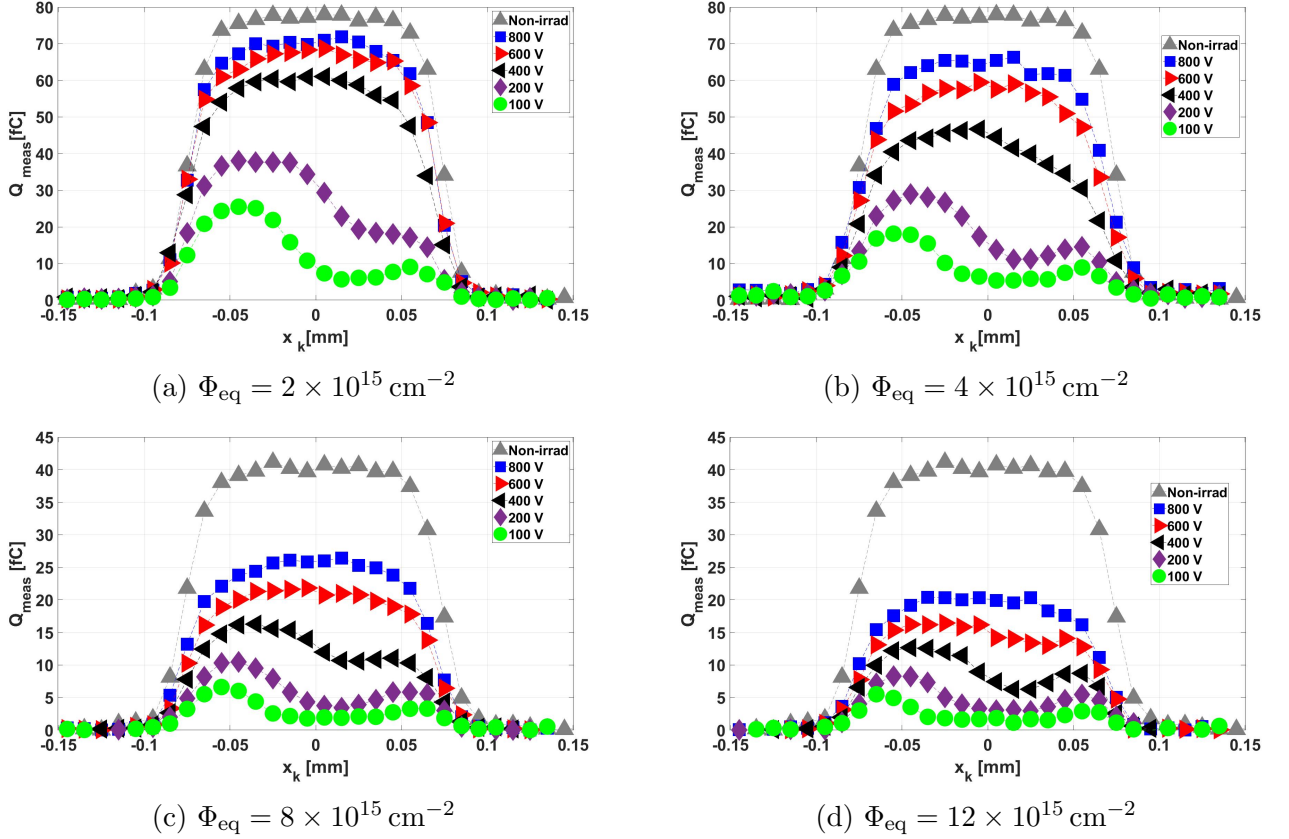


Figure 5.14: Charge collection profiles of irradiated pad diodes at four different fluences. For each irradiated diode, the charge collection profile of the non-irradiated with the same pad size taken at bias voltage of 120 V is also shown.

monotonically up to 800 V. These results are in agreement with previously published results on CCE of irradiated pad diodes using TCT with IR light [88, 20].

5.5 Comparison of the Data with TCAD Simulation

In this section, the simulation results of the charge collection profiles with Technology Computer-Aided Design (TCAD) device simulator using Hamburg Penta Trap Model (HPTM) and two Perugia models are presented. The first part gives an overview of HPTM and two Perugia models and their parameters. The simulation procedure to obtain the charge collection profile is explained in the second part. The comparison between simulation results and data is presented in the final part.

5.5.1 Hamburg Pent Trap Model

HPTM is a result of an attempt for simulation of irradiated pad diodes using the optimiser of Synopsys TCAD [89]. One challenge of using TCAD for device simulation is implementation of satisfactory radiation damage model. At high radiation fluences, using experimental techniques such as Thermally Stimulated Current to extract microscopic

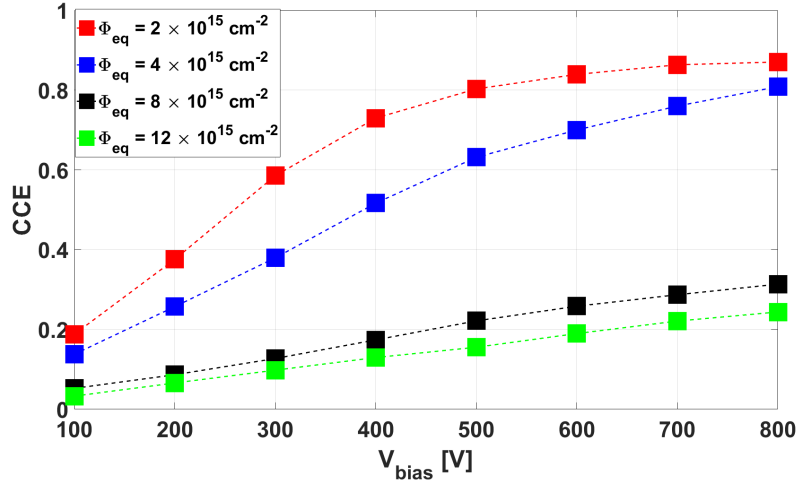


Figure 5.15: CCE as a function of bias voltage for four irradiated diodes.

defects is not possible. Moreover, implementation of cluster defects in TCAD simulation is not possible. An approach to overcome these challenges is using "effective models" by assuming a number of point defect levels and tuning the parameters to reproduce the macroscopic results.

HPTM was introduced in [90] to reproduce the experimental results on irradiated pad diodes. For that study, p -type diodes with 200 μm thickness were irradiated at the CERN PS with 24 GeV/c protons at various fluences in the range of $0.3 \times 10^{15} \text{ cm}^{-2}$ to $13 \times 10^{15} \text{ cm}^{-2}$. Current-Voltage (I-V), Capacitance-Voltage (C-V) and CCE measurements with IR light were used for tuning the model by minimising the following function:

$$F = \sum_{i,j} w_{i,j}^i \int_{V_{min}}^{V_{max}} \left(1 - \frac{Q_{i,sim}^j}{Q_{i,meas}^j} \right)^2 dV \quad (5.5)$$

In this function, i and j run over fluences and measurement types and $Q_{i,sim}^j$ and $Q_{i,meas}^j$ are simulated and measurement values, respectively. $w_{i,j}^i$ are the weighting factors of different measurements. The CCE measurements with IR light traversing the diode normal to the implants where no information as a function of depth could be obtained

HPTM assumes 5 type of defects in the silicon band gap after irradiation. The parameters of these traps after optimisation are listed in Table 5.1. In this table, g_{int}^k is the introduction rate of defect with the type k , so that the trap concentration at the fluence of Φ_{eq} is given by $N^k = g_{int}^k \cdot \Phi_{eq}$. σ_e^k and σ_h^k are the cross section of each trap for electrons and holes, respectively. For optimisation of the model, g_{int} , σ_e and σ_h were considered as free parameters. The type and energy of defects were fixed for the optimisation.

Defect	type	Energy	g_{int} [cm ⁻¹]	σ_e [cm ⁻²]	σ_h [cm ⁻²]
E30K	Donor	$E_C - 0.1$ eV	0.0497	2.300E-14	2.920E-16
V ₃	Acceptor	$E_C - 0.458$ eV	0.6447	2.551E-14	1.511E-13
I _p	Acceptor	$E_C - 0.545$ eV	0.4335	4.478E-15	6.709E-15
H220	Donor	$E_V + 0.48$ eV	0.5978	4.166E-15	1.965E-16
C _i O _i	Donor	$E_V + 0.36$ eV	0.3780	3.230E-17	2.036E-14

Table 5.1: Parameters of HPTM

5.5.2 Perugia Models

The "new Perugia Model" was introduced in [91]. After irradiation, the model assumes three defect levels (two acceptors and one donor) in the silicon band-gap. For modelling the bulk damage, the model was compared with the results of charge collection for irradiated PiN diodes and strip sensors. Charge collection of irradiated strip sensors up to the equivalent fluence of 2.3×10^{16} cm⁻² were measured with electrons from a ⁹⁰Sr source at a bias voltage of 900 V [92]. PiN diodes were measured with the IR pulsed laser, and the results were normalised to the collected charge of the non-irradiated diode [93]. A more recent version of the Perugia model was presented in [94]. The model parameters were optimised using CV and IV measurements of PiN and Low Gain Avalanche Diodes (LGAD).

5.5.3 Simulation of Charge Collection Profile

From each model using the optimised parameters, the position-dependent trapping times, $\tau_e(x)$ and $\tau_h(x)$, and drift velocities $v_e(x)$ and $v_h(x)$ are obtained. The Charge Collection Length (λ_e, λ_h) of each charge carrier type is calculated as:

$$\lambda_{e,h}(x) = v_{e,h}(x) \cdot \tau_{e,h}(x) \quad (5.6)$$

Charge Collection Efficiency of electrons and holes as a function of depth, x :

$$\begin{aligned} CCE_e(x) &= \int_{-d/2}^x E_w(y) \cdot \exp\left(\int_x^y \frac{dy'}{\lambda_e(y')}\right) dy \\ CCE_h(x) &= \int_x^{+d/2} E_w(y) \cdot \exp\left(\int_x^y \frac{-dy'}{\lambda_h(y')}\right) dy \end{aligned} \quad (5.7)$$

$E_w(y)$ is the weighting field which is $1/d$ for a pad diode with a thickness of d [95]. The total CCE as a function of depth is the sum of electron and hole components, i.e. $CCE_{tot}(x) = CCE_e(x) + CCE_h(x)$. To compare the simulation to the measured data, $CCE_{tot}(x)$ has to be corrected for the charge leakage, the position resolution of the tele-

scope and the normalisation as follows:

$$Q_{sim}(x) = A \cdot \left(CCE_{tot}(x) \cdot \frac{E_{dep}(x)}{E_{dep}(0)} \right) * \text{Gauss}(x, 0, \sigma) \quad (5.8)$$

In this relation, $\frac{E_{dep}(x)}{E_{dep}(0)}$ is the profile shown in Fig. 5.8 and takes into account the leakage effect, convolution with $\text{Gauss}(x, 0, \sigma)$ takes into account the limited spatial resolution of the beam telescope, and multiplication with A scales the CCE profile. The value for σ is assumed $10 \mu\text{m}$ and the scaling factors, A , for the $2.5 \times 2.5 \text{ mm}^2$ and $5.0 \times 5.0 \text{ mm}^2$ diodes are 40.0 fC and 76.8 fC , respectively (see Section 5.4.1). In Eq. (5.8), \cdot and $*$ are the multiplication and convolution operators, respectively. Fig. 5.16 shows an example the simulated CCE profiles at different steps. The profiles are shown for $\lambda_{e,h}$ from the HPTM at the fluence of $2 \times 10^{15} \text{ cm}^{-2}$ and bias voltage of 800 V .

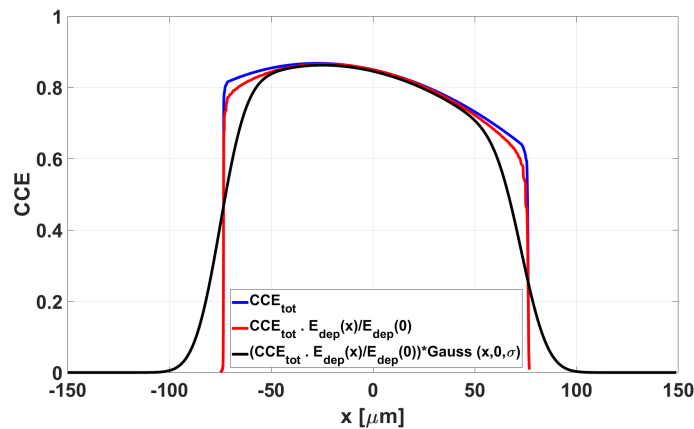


Figure 5.16: CCE profile as a function of x using the HPTM simulation. The results are shown for irradiation fluence of $2 \times 10^{15} \text{ cm}^{-2}$ and bias voltage of 800 V .

The irradiation fluence quoted in Section 5.2 has $\pm 10\%$ uncertainty. To take this uncertainty into account in simulation, $\lambda_{e,h}$ were calculated from HPTM at $\pm 10\%$ with respect to the nominal fluence.

5.5.4 Comparison Between Data and HPTM

In Fig. 5.17 a comparison between simulated using HPTM and measured charge collection profile is shown. For each simulated profile, a band is shown, taking into account the irradiation fluence's error. From the comparison between data and simulation, the following observations are made:

- At high bias voltages ($V_{bias} < 800 \text{ V}$), simulation results are lower than data.
- At low bias voltages, simulation results are higher than data.
- Qualitatively, the shape of simulated profiles are similar to data.

5.5 Comparison of the Data with TCAD Simulation

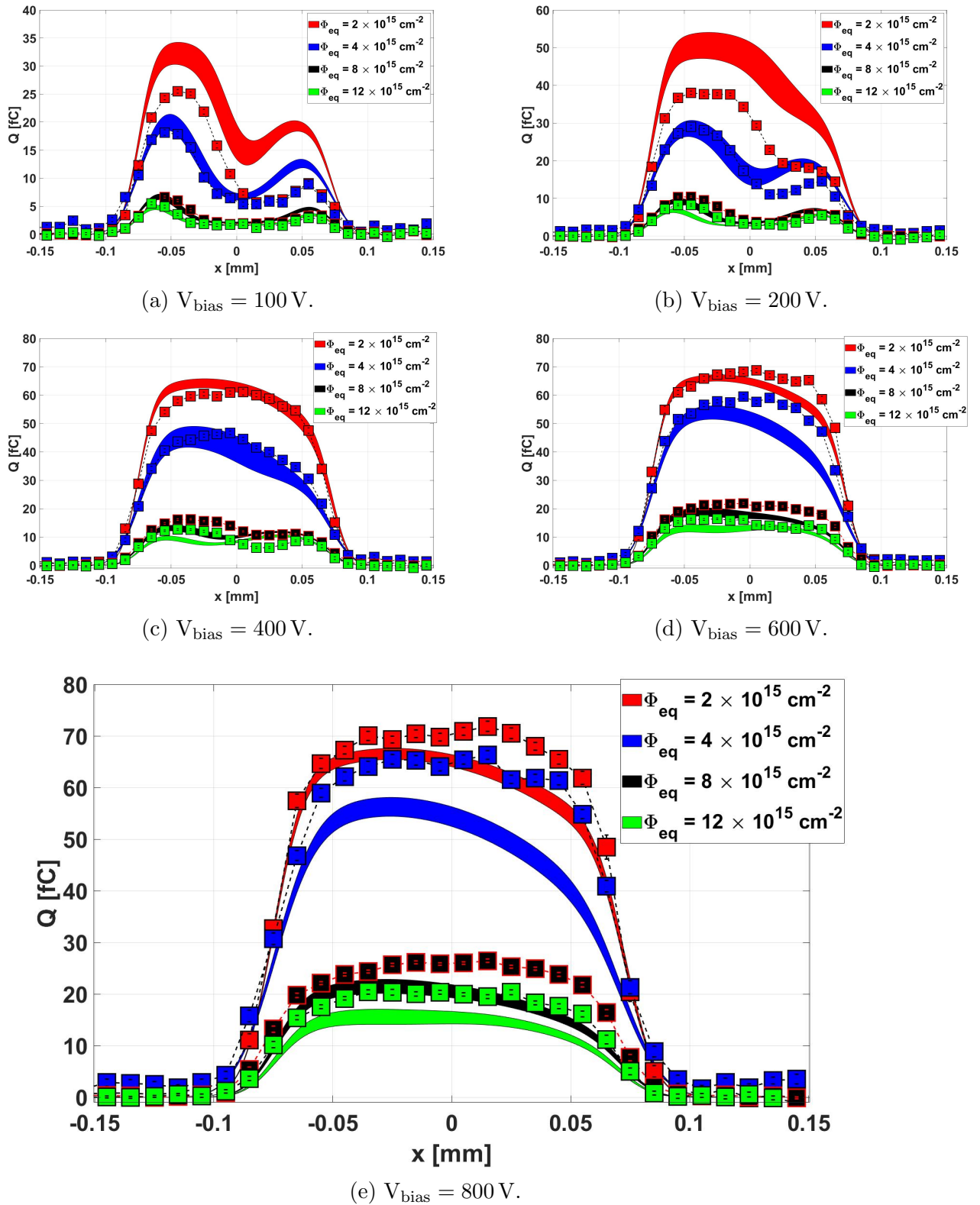


Figure 5.17: Comparison between simulated using HPTM and measured charge collection profile at different bias voltage and fluences. For simulated profiles, $\pm 10\%$ uncertainty of the irradiation fluence is shown with bands.

Using Eq. (5.4), the overall CCE of simulated profiles were calculated. Fig. 5.18 shows the simulated and measured CCE as a function of bias for four irradiation fluences. These CCE results are similar to what is shown in [90]. Fig. 5.19 shows the comparison between HPTM simulation and data. As mentioned before, CCE was measured with IR at -20°C in that work. One can see the simulated CCE at high bias voltage is lower than data which is similar to the results shown in this work (Fig. 5.18).

Furthermore, it should be noted that HPTM was tuned to reproduce the irradiated diodes with 24 GeV/ protons. While, the diodes in this work were irradiated with 23 MeV protons. In [96], it was shown CCE of irradiated diode with 23 MeV is higher than the diode irradiated with 24 GeV at a similar fluence.

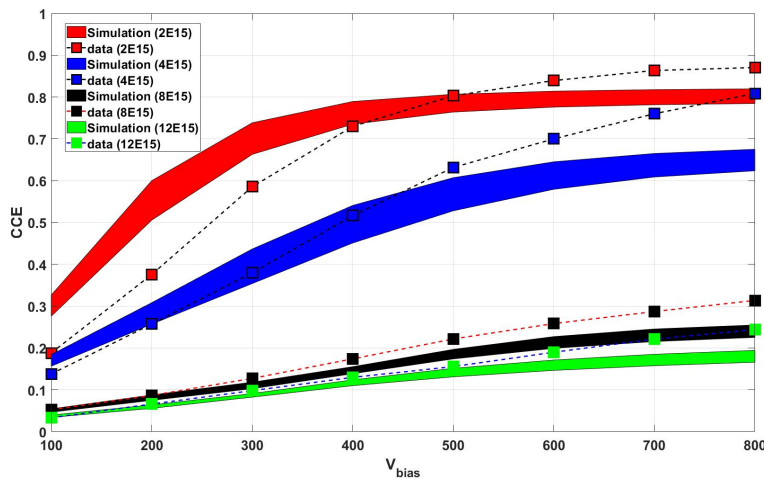


Figure 5.18: Simulated (with HPTM) and measured CCE as a function of bias voltage for four irradiation fluences. For simulated values, $\pm 10\%$ uncertainty of the irradiation fluence is shown with bands.

5.5.5 Comparison Between Data and Perugia Models

In Fig. 5.20 a comparison between simulated and measured charge collection profiles is shown. Three simulated profiles from HPTM and two Perugia models (2019 and 2022) are shown for each measured profile.

The voltage-dependence and shapes of charge collection profiles from the two Perugia models are not in good agreement with the data. Especially at low bias voltage, the agreement of two Perugia models to the data is worse than the HPTM.

It is noted that none of the models can describe the observed voltage and fluence dependence of the charge collection. This is not too surprising, as the models have been tuned using silicon sensors irradiated with different types of particles. However, the study demonstrates that the precise measurement of depth profiles provides stringent tests of models for the radiation damage of silicon detectors.

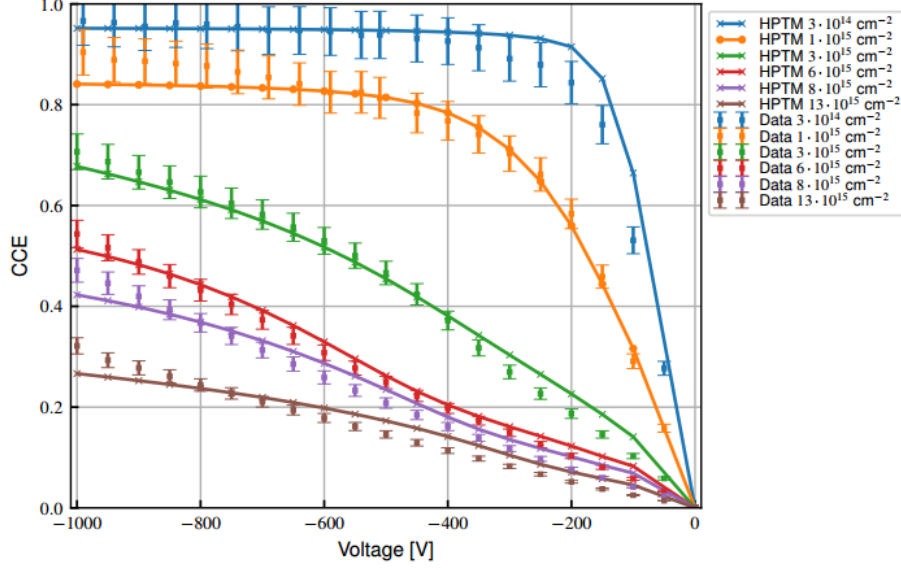


Figure 5.19: Simulated and measured CCE as a function of bias voltage. The data was taken using IR laser as explained in the text. The plot is taken from [90].

5.6 Extracting CCE Profile from Data

The limited spatial resolution and the loss at the sensor edges affect the measured charge collection profiles. One can extract the CCE profile of pad diodes by unfolding the profiles.

The unfolding procedure assumes CCE_{x_i} values at 7 depth values of -65 , -45 , -25 , -5 , 15 , 35 , $55 \mu\text{m}$ as free parameters. $CCE_{spl}(x)$ is calculated by spline interpolation between CCE_{x_i} values. For the interpolation, the "cubic spline interpolation" and the "not-a-knot" boundary condition were used. This condition means the third derivative of the interpolation function is continuous at the end points. For this calculation, MATLAB2019a was used ([97]). $CCE(x)$ is multiplied with the energy deposition profile, $\frac{E_{dep}(x)}{E_{dep}(0)}$ shown in Fig. 5.8, convolved with a Gauss function with a standard deviation of σ and scaled with a factor of A_{scale} calculated from the fit of non-irradiated diode profiles with Eq. (5.2) (see Eq. (5.8)). These steps can be written as a single formulae:

$$Q_{sm}(x) = A \cdot \left(CCE_{spl}(x) \cdot \frac{E_{dep}(x)}{E_{dep}(0)} \right) * \text{Gauss}(x, 0, \sigma) \quad (5.9)$$

The values of CCE_i is obtained by minimising the following function:

$$D^2 = \sum_{k=1}^{n_k} (Q_{meas}(x_k) - Q_{sm}(x_k + \Delta x_{tr}))^2 + w_{pen} \sum_{i=2}^6 \left(\frac{0.5 \cdot (CCE_{i-1} + CCE_{i+1}) - CCE_i}{\Delta x} \right)^2 \quad (5.10)$$

In this function, $Q_{meas}(x_k)$ and $Q_{sm}(x_k)$ are the measured and calculated charge at x_k , respectively. It should be noted that the measured charge values, $Q_{meas}(x_k)$, are

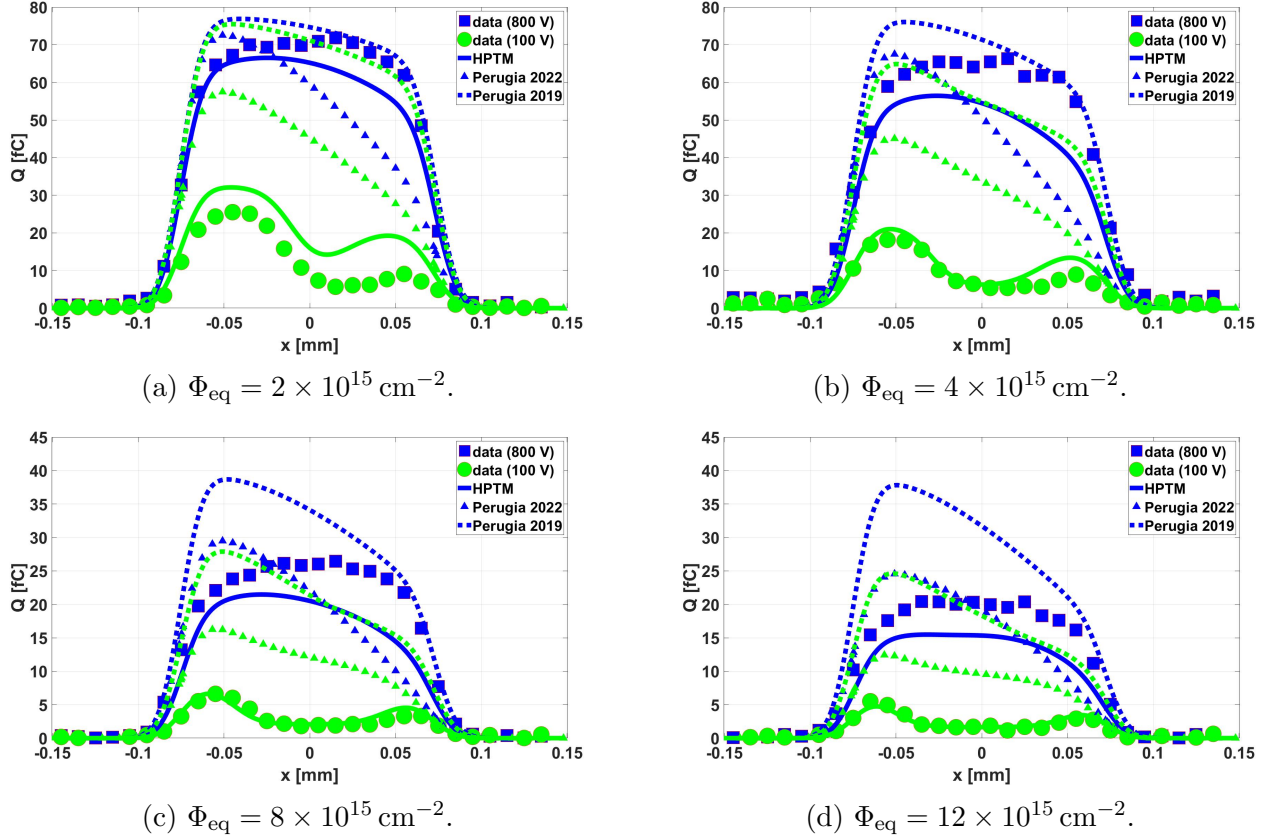


Figure 5.20: Comparison between measured and simulated charge collection profiles at bias voltages of 800 and 100 V for each fluence. The data are shown with squares (800 V), and circles (100 V). Simulations are show with line (HPTM), triangles (Perugia 2022) and squares (Perugia 2019).

a function of test-beam coordinates, and the calculated charge values, $Q_{sm}(x_k)$, are a function of the sensor coordinates. Δx_{tr} parameter takes into account the shift from the sensor to test-beam coordinates. Δx is the distance between two x_i points, i.e. 20 μm .

The first term in the above function minimises the differences between the data and the model for the n_k measurements. The second term is the second derivative of the CCE_{x_i} values. By minimising this term, the CCE_{x_i} profile is smoothed. The penalty weight, w_{pen} , is adjusted for each profile separately.

In this procedure, the value of σ is adjusted for each profile separately. For each profile, σ is changed manually in steps of 0.5 μm in the range of 9.0 μm to 11.0 μm to find the minimum value for D^2 . The same is done for the value of Δx_{tr} with steps of 1 μm . The fit range is set at $-75 \mu\text{m}$ to 75 μm . The thickness of the diodes is assumed 150 μm .

Fig. 5.21 shows the comparison between data and model for four irradiated and two non-irradiated diodes. The obtained CCE profiles from the fits are shown in Fig. 5.22.

The difference between data and fit is shown in Fig. 5.23. The fit values are in agreement with the data in the range of 2 fC to 3 fC. In the fit range, no systematic difference between data and the fit is seen.

As expected, for non-irradiated diodes, CCE_{x_i} profile is uniform with values around 1

and deviations not exceeding 2.5% compatible with the statistical fluctuations of the data. For irradiated diodes, the shape of the CCE_{x_i} profiles depends on the bias voltage. At high bias voltages ($V_{\text{bias}} > 600 \text{ V}$), the maximum CCE_{x_i} is close the centre of the diode, i.e. ($-10 \mu\text{m} < x < 10 \mu\text{m}$). At low bias voltage ($V_{\text{bias}} < 400 \text{ V}$), CCE_{x_i} is maximal at the region close to the n^+ implant and decreases towards the p^+ implant.

As mentioned, the assumed thickness of the diode is $150 \mu\text{m}$ for these calculations. To check this assumption, the procedure is repeated for a thickness of $148 \mu\text{m}$. The extracted CCE_{x_i} values for two assumed thickness are found to be similar in one percent level for $x_k > -65 \mu\text{m}$. At $x_k = -65 \mu\text{m}$, the extracted CCE is $\approx 4\%$ higher when the thickness is assumed $148 \mu\text{m}$.

A qualitative discussion of the CCE profiles which are shown in Fig. 5.21 follows. From Eq. (5.7), it is noted that CCE is a geometrical quantity. If λ_e and λ_h are large compared to the diode thickness, d , $CCE_{\text{tot}}(x) = 1$. In this case the CCE of electrons and holes as a function of x is given by:

$$\begin{aligned} CCE_e(x) &= 1/2 + x/d \\ CCE_h(x) &= 1/2 - x/d \end{aligned}$$

For finite charge-carrier-absorption lengths larger than d , from a symmetric $CCE_{\text{tot}}(x)$ profile peaking in the centre, one can conclude that $\lambda_e \approx \lambda_h$. This appears to be the case for the irradiated diode at high voltages ($V_{\text{bias}} > 600 \text{ V}$).

A small asymmetry, as observed at somewhat lower voltages, indicates a difference between λ_e and λ_h : If the $CCE_{\text{tot}}(x)$ is smaller at negative x , $\lambda_h < \lambda_e$, and $\lambda_h > \lambda_e$ for the opposite case. The first case is observed for intermediate voltages.

A flat $CCE_{\text{tot}}(x)$ minimum in the centre means that both λ_e and λ_h are small there, that the charges are trapped, and charges entering or generated in this region will not leave it. In this case, the $CCE_{\text{tot}}(x)$ is given by the distance between the average position at which the holes are trapped and the position at which electrons are trapped divided by d . Thus, for the $CCE_{\text{tot}}(x)$ in the flat regions which are observed at low voltages $CCE_{\text{tot}}(x) \approx (\lambda_e + \lambda_h)/d$.

In spite of these constraints, the determination of the position dependencies of $\lambda_e(x)$ and $\lambda_h(x)$ has not been achieved. The reasons are that Eq. (5.7), which relates $CCE_{\text{tot}}(x)$ to $\lambda_e(x)$ and $\lambda_h(x)$ is an integral equation and that from a single measured function, $CCE_{\text{tot}}(x)$, it appears impossible to determine two functions, $\lambda_e(x)$ and $\lambda_h(x)$.

5.7 Summary and Conclusion

In this chapter, a new method for characterising pad diodes was introduced. In this method, the charge collection profiles of pad diodes as a function of depth are measured by an electron beam. An in-situ alignment procedure was introduced to find the minimum

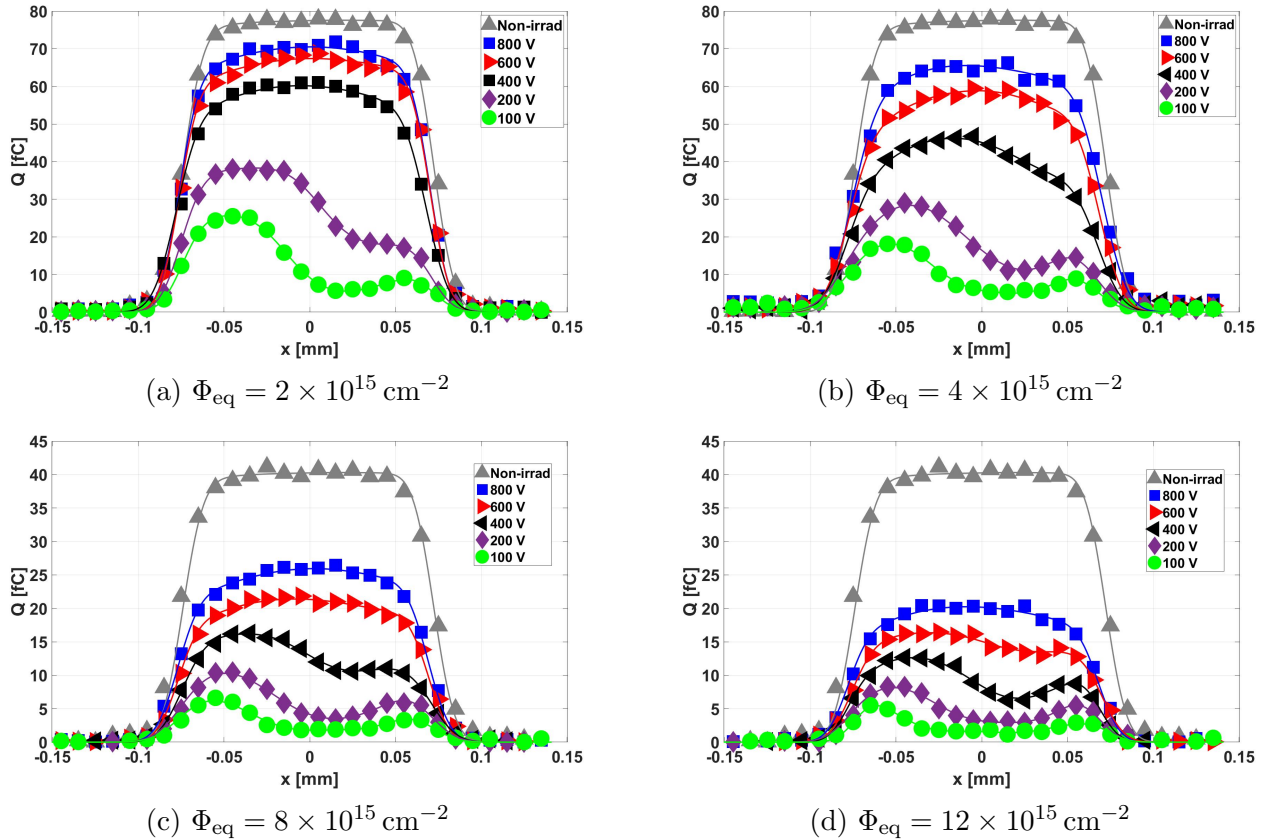


Figure 5.21: Comparison between data and fit for irradiated and non-irradiated diodes at different fluences. Data are shown with shapes and fits are shown with lines.

angle between the DUT and the electron beam. The results of the measurements with non-irradiated diodes show that the charge collection profiles are uniform as a function of depth and scale with the pad size. The active thickness of the diodes was estimated and found to agree with the physical thickness provided by the manufacturer.

The results of the measurements with irradiated diodes at high bias voltages ($V_{\text{bias}} > 600$ V) show uniform profiles with reduced CCE values. At lower bias voltages ($V_{\text{bias}} < 400$ V), the profiles show a non-uniform shape with enhanced peaks close to the n^+ and p^+ implants.

The results of the irradiated diodes were compared with simulation using HPTM and two Perugia models. The comparison reveals that simulated charge collection profiles are lower at high bias voltages than the data. This observation was found to agree with previously published results on comparison between HPTM and data. At low bias voltages, the shape of measured profiles is similar to the simulation.

In the last part of this section, the measured charge collection profiles were unfolded by taking into account the effects of limited spatial resolution and non-uniform energy deposition profile. The results of the unfolding give the CCE profiles as a function of depth. These profiles can be used for tuning simulation models.

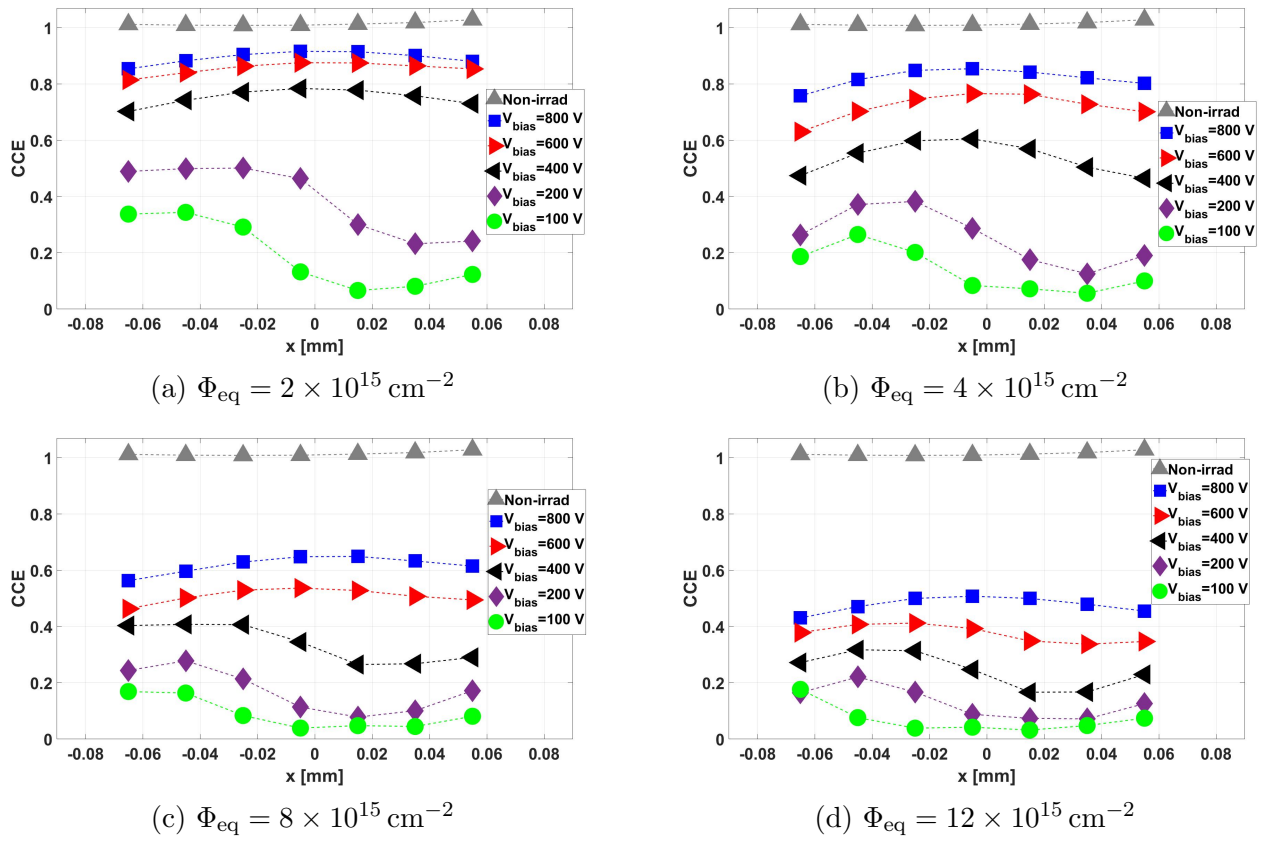
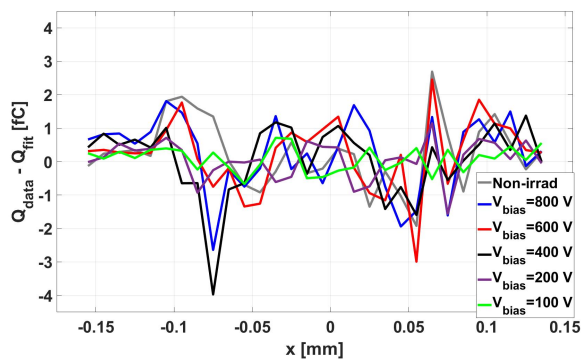
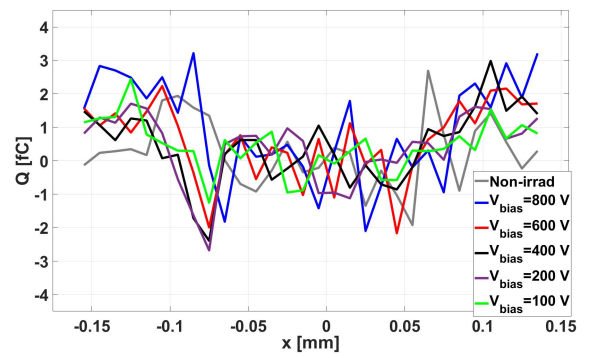


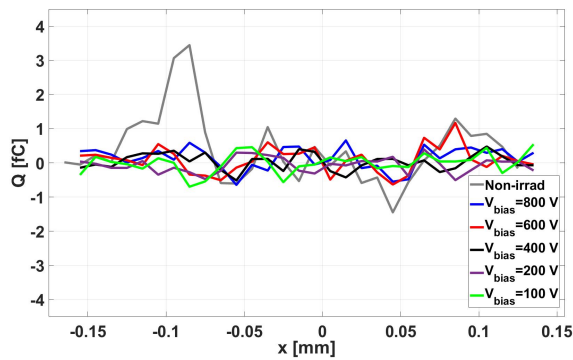
Figure 5.22: CCE profiles as a function of depth for irradiated and non-irradiated diodes. The profiles are extracted from the fit.



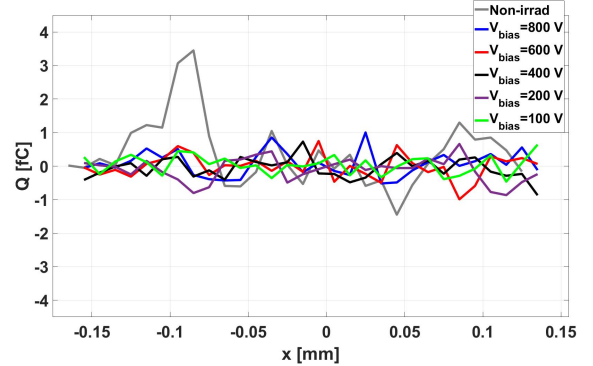
(a) $\Phi_{\text{eq}} = 2 \times 10^{15} \text{ cm}^{-2}$



(b) $\Phi_{\text{eq}} = 4 \times 10^{15} \text{ cm}^{-2}$



(c) $\Phi_{\text{eq}} = 8 \times 10^{15} \text{ cm}^{-2}$



(d) $\Phi_{\text{eq}} = 12 \times 10^{15} \text{ cm}^{-2}$

Figure 5.23: Difference between the data and fit for profiles shown in Fig. 5.21

6 Characterisation of Planar Pixel Modules in Test-Beam

As introduced in Chapter 2, a hybrid pixels module includes a sensor layer which is bump bonded to a readout chip. For this work, planar sensors with pixel sizes of $25 \times 100 \mu\text{m}^2$ and $50 \times 50 \mu\text{m}^2$ are investigated where the readout electrodes are parallel to the surface of the sensor. The readout chip is the RD53A chip with a pixel size of $50 \times 50 \mu\text{m}^2$. The characterisations are done with respect to the requirements for the Phase-2 upgrade of the CMS IT.

As a part of this thesis, irradiated and non-irradiated planar pixel modules were characterised in the DESY II test-beam facility. The measurement setup and specifications of the planar pixel sensors are given in Section 3.4.1. The specifications of the RD53A chip are discussed in Section 3.2.1.

In this chapter, tuning and trimming the readout chip for the test-beam measurements are explained in Section 6.1. A summary of the module's installation in the test-beam and online monitoring is given in Section 6.2. The procedure used to analyse the measured data is explained in Section 6.3. The observables for characterisation of pixel sensors are defined in Section 6.4. The selection cuts for the offline analysis are defined in Section 6.5. The results of the measurements are presented in Section 6.7.

List of own contributions

- Preparation and installing of modules for data taking in test-beam
- Analysis of the data and extraction of key parameters
- Modifying the existing analysis code and implementing all the selection cuts

The analysis code for the telescope and DUT alignments was provided by Dr. Daniel Pitzl [74].

6.1 Tuning and Trimming of Readout Chip

As discussed in Chapter 3, the LFE of the RD53A chip has been chosen for the final chip in the CMS IT. The front end contains Digital-to-Analog Converters (DAC) that are used

for the chip configuration. The RD53A chip is powered by a low voltage power supply. Before performing the measurements in the test-beam, the chip needs to be trimmed and tuned. In this context, trimming means setting the low voltages and currents of the chip, and tuning means setting the value of DAC, as listed in Section 6.1.3.

6.1.1 Trimming of Readout Chip

RD53A chip is designed to operate with single supply serial powering [48]. It is still possible to bypass the internal regulators of the chip and supply the voltage rail directly. This mode is called "Direct Powering" and was used for measurements in this work.

For powering the chip, there are two voltage rails named "VDDA" and "VDDD" for analogue and digital parts, respectively. The target values for VDDA and VDDD are 1.2V and 1.3V, respectively. For some irradiated modules, VDDA and VDDD have to be supplied from a single channel on the power supply.

The reference current, I_{REF} , is another important parameter of the chip. This current provides a global master reference for the DAC in the chip. The optimal value of this current is $4\mu\text{A}$. This current can be adjusted using 4 bits "IREF_TRIM" to compensate for process variations. One can access these 4 bits using four pins on the card, as shown in Fig. 6.1.

Fig. 6.1 shows the single-chip card with a wire bonded RD53A module. The corresponding pins for measuring VDDA and VDDD and trimming I_{REF} are shown.

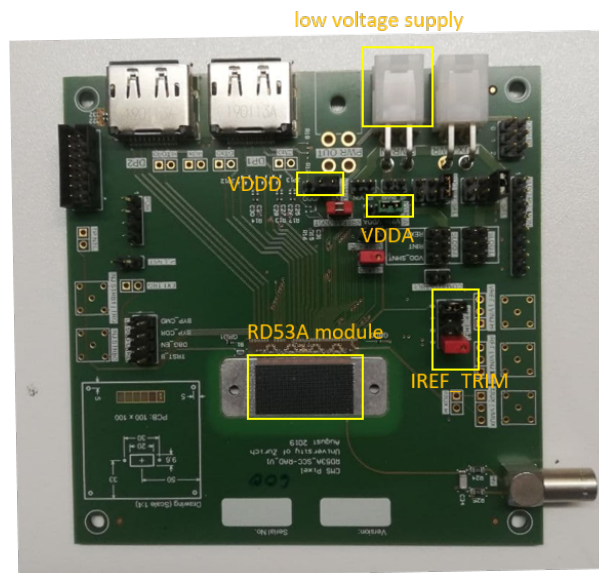


Figure 6.1: Single Chip Card for the RD53A module.

6.1.2 Tuning of Threshold

As mentioned in Chapter 3, the RD53A chip has a stable and tunable threshold. Two parameters determine the threshold of each pixel. First, is the global threshold called

Vthreshold-LIN. Second, the 4 bit of an in-pixel TDAC (see Fig. 3.7). Vthreshold-LIN sets the coarse threshold of the chip, and the in-pixel TDAC compensates for pixel-to-pixel dispersion. This feature minimises the chip's threshold dispersion by setting the correct values for TDAC, referred to as threshold tuning

For tuning the chip, the pixel sensor should be biased at a voltage above the full depletion to have the total capacitance between the sensor and the readout chip. For this work, non-irradiated modules were tuned at a bias voltage of 120 V and irradiated modules were tuned at 300 V.

To determine the threshold of the chip, the "charge injection" method is used. Each pixel is equipped with an injection circuit. Each pixel is injected with a certain amount of charge Q in this method, and the pixel output is measured. The measurement is repeated 100 times. The occupancy of each pixel with an injected charge of Q is defined as:

$$O(Q) = \begin{cases} 1 & \text{if ToT} > 0 \\ 0 & \text{if ToT} = 0 \end{cases} \quad (6.1)$$

The procedure is repeated for different values of Q . If the pixel does not have noise, one would expect zero occupancies for Q values below the threshold and occupancy of 1 for Q values above the threshold. The occupancy versus Q plot would look like a step function in this case.

Adding Gaussian distributed noise to the pixel charge smears the step function to an error function or an "S-Curve". The S-Curve's mid point is given the pixel's threshold, and the width (σ) gives its noise. Fig. 6.2 shows a typical plot of occupancy as a function of injected charge for one pixel. The data is fitted with the following function:

$$Y(Q) = \frac{A}{2} \left(\operatorname{erf} \left(\frac{Q - \mu}{\sqrt{2} \cdot \sigma} \right) + 1 \right) \quad (6.2)$$

The free parameters of the fit are μ and σ . A is fixed to the number of injections (100). The error for each data point is calculated from the Binomial distribution:

$$\delta_O(Q) = \sqrt{O(Q) \left(1 - \frac{O(Q)}{100} \right)} \quad (6.3)$$

For this particular pixel, the threshold, μ in Eq. (6.2), is determined as $116 \Delta V_{\text{cal}}$ and the noise (σ) is $9 \Delta V_{\text{cal}}$.

A differential circuit generates the injection voltage in the chip with two registers at potentials of $V_{\text{CAL}_{\text{MED}}}$ and $V_{\text{CAL}_{\text{HIGH}}}$. The ΔV_{cal} unit is defined as the difference between these two potentials [98, 48]. To convert from the ΔV_{cal} unit to electrons, the chip designers propose the following relationship:

$$Q(\text{electrons}) = Q(\Delta V_{\text{cal}}) \times 10.02 \left(\frac{\text{electrons}}{\Delta V_{\text{cal}}} \right) + 64 \text{ electrons} \quad (6.4)$$

There are two caveats to using this formula. First, it was found that the calibration factor proposed in Eq. (6.4) is only correct for specific settings on the chip. For some of the measurements presented in this work, the chip settings were different, which resulted in a slightly (5% to 10%) higher threshold than quoted values in Table 3.1. Second, the conversion factor in Eq. (6.4) comes from testing a few chips and taking an average of the results. This factor can be different from one chip to another. Therefore, the threshold values quoted in electrons are only a rough estimation of the actual threshold.

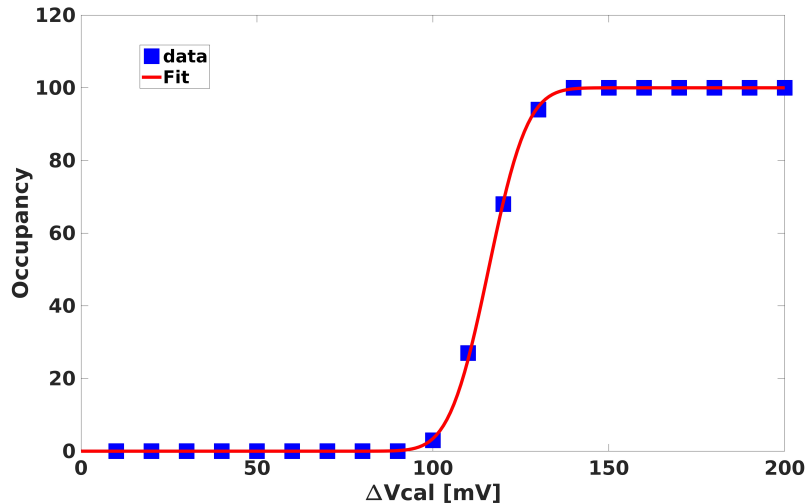


Figure 6.2: Occupancy of a pixel as a function injected charge. For each Q , charge is injected 100 times. Data is fitted with the function defined in Eq. (6.2).

The threshold and noise for this pixel are 1226 electrons and 154 electrons, respectively. This procedure is repeated for each pixel, and the threshold is estimated. Fig. 6.3 shows the S-Curve of all pixels in the LFE after tuning the chip. One sees some points with occupancy above the total number of injections or 100. These events are caused by noisy pixels in the chip. For this particular example, 20 noisy pixels are detected.

In Fig. 6.4a and Fig. 6.4b, the distributions of μ and σ extracted from the fit using Eq. (6.2) for all pixels are shown. The distributions are fitted with a Gaussian function, and the fit results are shown in the figures. From Fig. 6.4a, one sees that the threshold dispersion of this chip is around 62 electrons. The distribution in Fig. 6.4b shows a mean chip noise of 80 electrons which is in agreement with the result of the simulation presented in [48].

The occupancy plot shown in Fig. 6.4 is obtained after tuning the chip threshold. The tuning is done using 4 bit of in-pixel TDAC with an iterative algorithm. Fig. 6.5 shows a flowchart of this algorithm. This algorithm aims to find the TDAC value for each pixel, which gives the threshold closest to the target value. In this diagram, the first two steps are shown. Two more steps are required to cover the whole range of TDAC values, from 0 to 15,

Tuning of the threshold is done in two steps. First the chip is tuned at a relatively

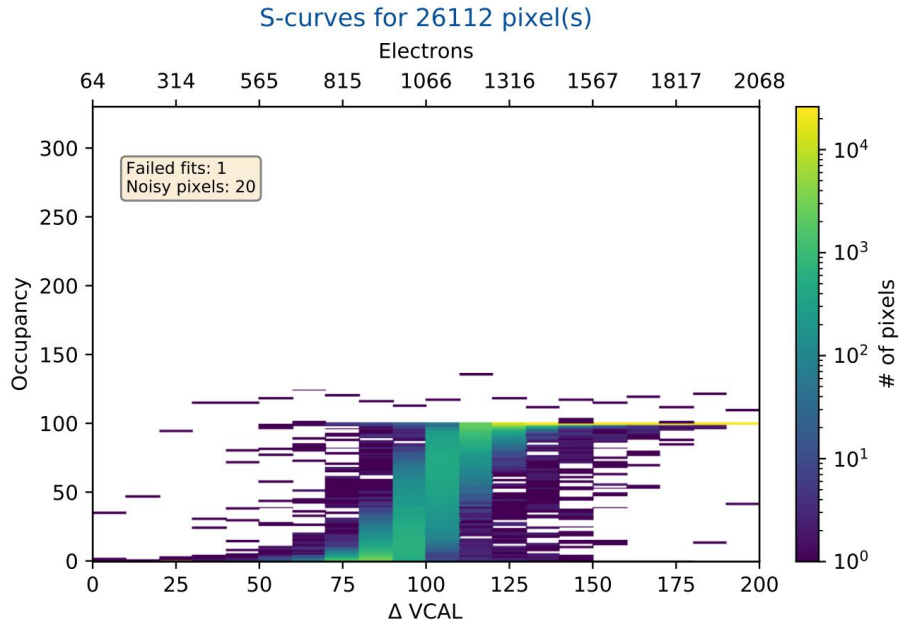
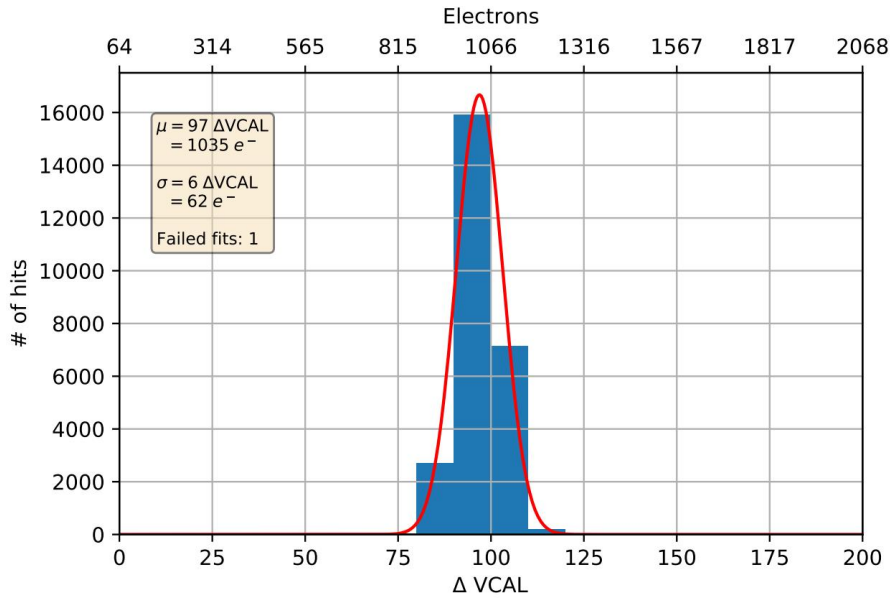
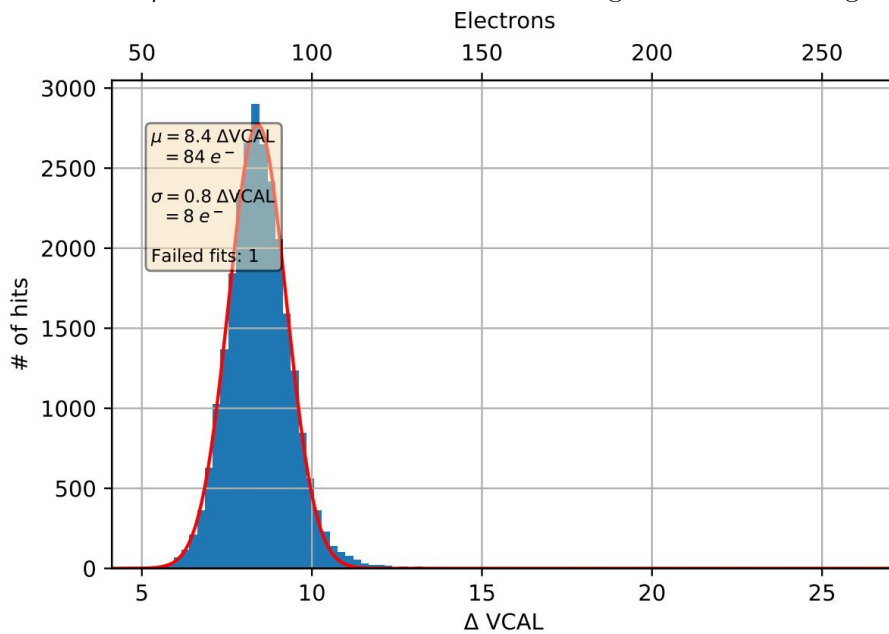


Figure 6.3: S-Curve of all pixels in LFE. DUT is a non-irradiated module biased at 120 V. S-Curve is shown after tuning the module as explained in the text.

high threshold (2500 electrons to 3000 electrons) and TDAC distribution is stored. In the second step, the chip is tuned at the target threshold around 1200 electrons using the TDAC distribution obtained in the first step. This approach is proven to improve the convergence of the tuning algorithm.



(a) Distribution of μ -value of distribution shown in Fig. 6.3 from fit using Eq. (6.2).



(b) Distribution of σ -value of distribution shown in Fig. 6.3 from the fit using Eq. (6.2).

Figure 6.4: Results of the charge injection for all pixels in the LFE.

DAC name	DAC value
Vthreshold-LIN	340-370 (depending on the chip)
KRUM-CURR-LIN	29
LDAC-LIN	130 (warm)/185 (cold)
FC-BIAS-LIN	20
COMP-LIN	110
PA-IN-BIAS-LIN	350
REF-KRUM-LIN	300

Table 6.1: DAC parameters of the RD53A chip and the values chosen for this work.

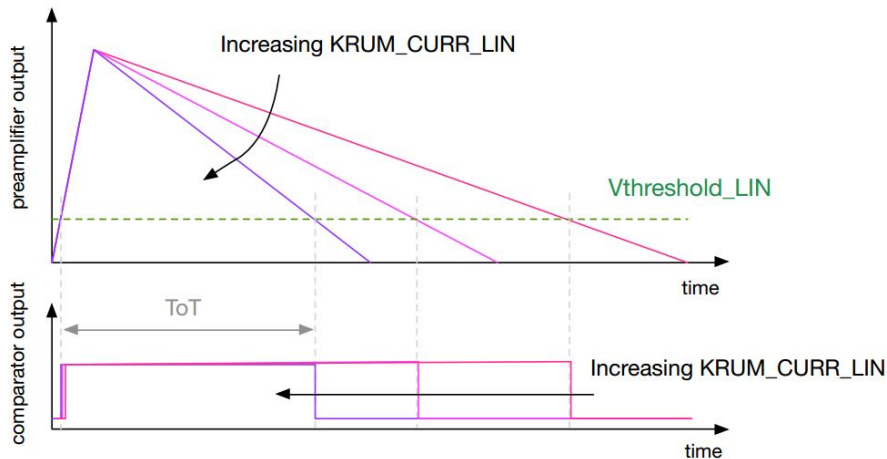


Figure 6.6: Effect of changing KRUM-CURR-LIN on output of preamplifier and comparator. The plot is taken from [99].

LDAC-LIN sets the dynamic range of TDAC. By increasing LDAC-LIN, the output range of the TDAC increases, making it possible to correct a more significant threshold dispersion. This feature is essential, especially for irradiated chips where an increased threshold dispersion is expected. Fig. 6.7 shows two distributions of the threshold for two values of LDAC-LIN. One sees that the outliers in the threshold distribution are reduced by increasing LDA-LIN. This value was increased when the chip was operated at a cold temperature.

6.2 Installation and Online Monitoring in Test-beam

The measurement setup for pixel sensors at the test-beam is introduced in Chapter 3. The module is installed on a movable stage which can shift it in two directions (x and y) and rotate it. Before acquiring data, a few adjustments are required. In the following, a summary of these adjustments is given.

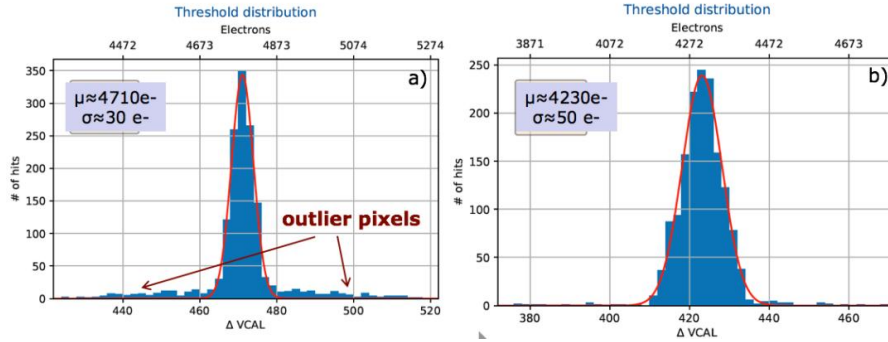


Figure 6.7: Threshold distributions for small (left) and increased (right) values for the LDAC-LIN. The plot is taken from [100].

6.2.1 Configuring the Readout Chip

Once the module is installed, and low voltages for the chip are supplied, the first test is communication with the readout chip. This test is usually done by running a so-called "Digital Scan" on the chip. Fig. 6.8 shows a typical result of the digital scan for the LFE. Each pixel in the LFE is injected and read 100 times. Therefore, one expects the total occupancy of $192 \times 136 \times 100 = 2611200$, as it is shown in Fig. 6.8. After this step, one can start trimming and tuning the readout chip as explained in Section 6.1.

For this work, the RD53A chip is configured in the following conditions:

- The online threshold was set to around 1200 electrons unless it is stated otherwise (see Section 6.3.1).
- All pixels in the LFE were read out without masking pixels online.
- For one trigger, the chip was read 31 times, with 25 ns between consecutive cycles. One cycle is referred to as one bunch crossing.

6.2.2 Online Monitoring

After configuring the readout chip, one can start taking data with the electron beam using the reference module and DATURA beam telescope as reference systems, as introduced in Chapter 3. Software for monitoring the raw data during the measurement has been developed named "EUDAQ" [101] to ensure the quality of the data taken in the test-beam.

A subset of plots is chosen for the online monitor. The raw data are read by DUT and the telescope without further analysis to make these plots.

The correlation distribution is one of the plots shown in the online monitor. This plot takes rows and columns of the pixels with a hit in the telescope planes and DUT for each trigger and fills them in a 2D histogram. Here, hit means the pixel has output over the threshold. By spotting a diagonal line, one can conclude that the data acquisition of two devices is synchronised in time.

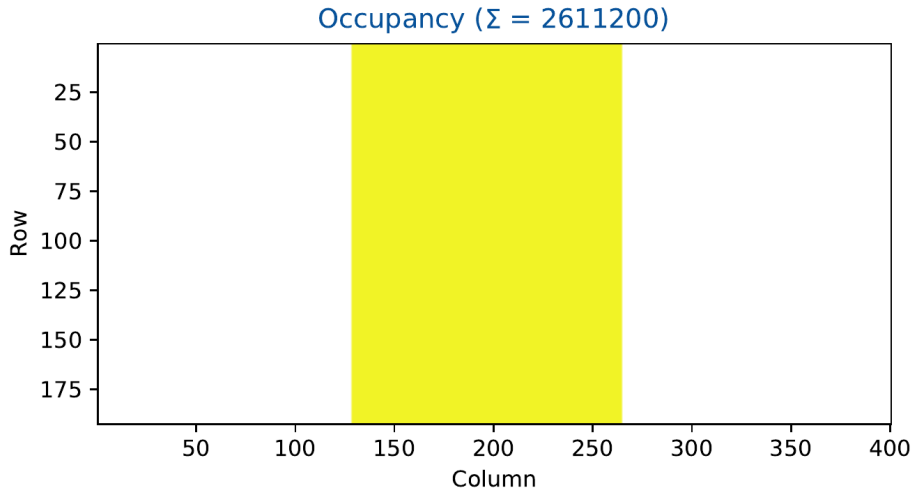


Figure 6.8: The results of the digital scan for the LFE. The total occupancy of 2611200 corresponds to the number of pixels in the LFE times 100 readings. The LFE columns are between 128 to 263 (see Fig. 3.6)

Fig. 6.9 shows a typical correlation plot between the rows of the third plane of the telescope (x -axis) and columns of the DUT (y -axis). The third plane is chosen because it is the closest detector to the DUT and the effect of the multiple scattering is minimal. One recognises a diagonal line in the plot caused by the correlated hits between the two devices. In this example, the DUT is installed 90° rotated with respect to the telescope planes. Therefore, the correlation is between rows of the DUT and columns of the telescope plane and vice versa. The horizontal and vertical lines in this plot are caused by the "noisy pixels" in the DUT and the telescope plane, respectively.

The correlation plot can also be used for checking the alignment of the DUT with respect to the telescope. From Fig. 6.9, one can see that 192 rows of the LFE are covered by the telescope plane columns between 300 to 800, and the DUT is within the range of acceptance of the telescope. The same plot can be made for the columns of the DUT versus rows of the telescope plane to check the alignment in the other direction.

6.3 Analysis of Test-Beam Data for Pixel Sensors

Hit efficiency and spatial resolution are two key parameters of a pixel sensor that can be obtained from the test-beam data. The analysis of the test-beam data for the calculation of the spatial resolution includes the following steps:

- Clustering and hit reconstruction by the telescope planes
- Track reconstruction for the telescope planes
- Clustering and hit reconstruction for the DUT
- Applying the selection cuts to the tracks

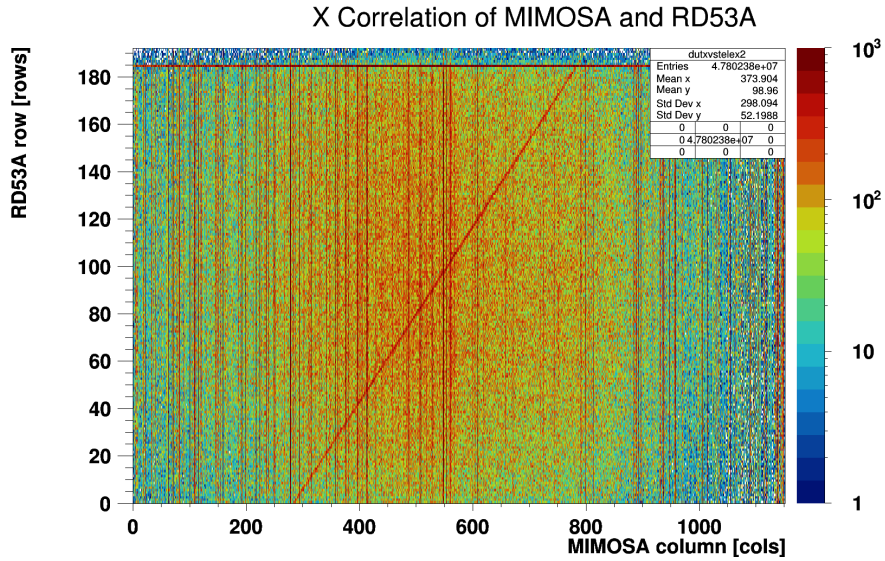


Figure 6.9: Correlation plot between the third plane of the telescope and DUT.

- Calculating the "residual distribution" of the DUT by comparing the expected and the measured hit position
- Extracting the width of the residual distribution and subtracting the telescope resolution

These steps in the analysis are described in the following.

6.3.1 Data Storage

An online threshold is applied to all three devices, i.e. the telescope, the timing reference module, and the DUT to limit the size of data stored at the test-beam. Only the response of the pixels with an output higher than the threshold is stored. The information stored for each device is as follows:

- Telescope: A threshold equivalent to 5 times the noise of an individual pixel is applied. For each plane, the row and column index of the pixels with outputs over the threshold are stored (binary readout).
- Timing reference module: A threshold of 1500 electrons is applied to the pixels response. The row, column, and charge of the pixels with output over the threshold are stored with 12 bit precision.
- RD53A module: As explained in Section 6.1.2, the online threshold is tuned to around 1200 electrons. For each pixel above the threshold row, column, charge in ToT unit (4 bit), and the Bunch Crossing ID (BCID) are stored.

6.3.2 Clustering Algorithm and Hit Reconstruction

Due to the charge sharing between pixels, a single particle can produce charges over the threshold in several pixels. The first step in the analysis is to find all the pixels associated with the same particle, and these pixels form a "cluster". The clustering algorithm used for this work starts with one pixel and continues until the cluster conditions are met. These conditions are defined as:

$$\begin{aligned} |\Delta i| &\leq 1 \\ |\Delta j| &\leq 1 \end{aligned} \quad (6.5)$$

Δi and Δj are the difference in the row and column index between two considered pixels. Fig. 6.10 shows an example of different cluster shapes and sizes. After clustering the

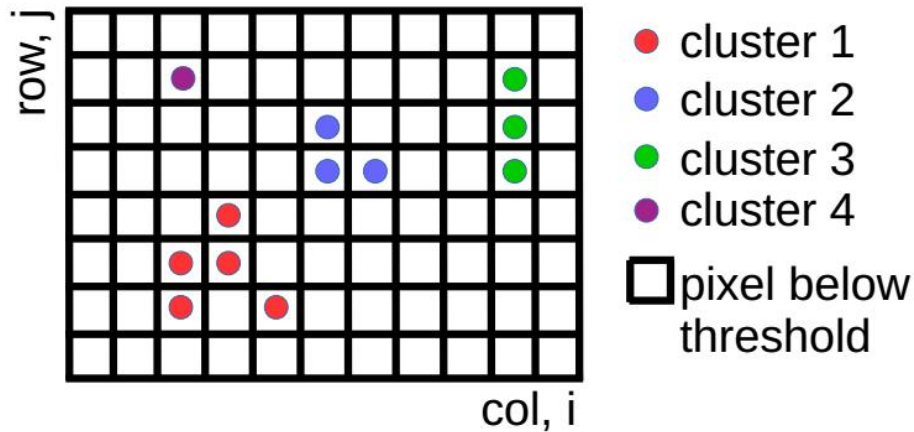


Figure 6.10: A few examples of cluster shapes and sizes. Sketch is taken from [55].

pixels, one can reconstruct the hit position using the Centre of Gravity (CoG) method [102]. The CoG is calculated as:

$$x_{cls} = p_x \frac{\sum_{k=1}^{n_{px}} Q_k \cdot i_k}{\sum_{k=1}^{n_{px}} Q_k} \quad (6.6)$$

In Eq. (6.6), n_{px} is the number of pixels in the cluster, p_x is the pitch sizes along the x -, i_k is the row index of a given pixel in the cluster and Q_k is the pixel charge in the ToT unit. The same relation can be written for y_{cls} . It should be mentioned that the 4 bits output of the ToT unit in the RD53A chip is stored with values between 0 to 15. To avoid a division to 0, in the analysis 1 unit is added to ToT values of all pixels. Therefore, the pixel charge unit is ToT'.

For the binary readout of the telescope planes, the reconstructed cluster position is the average of the row and column indices of the pixels in the cluster.

6.3.3 Track Reconstruction

After reconstruction of the cluster position in the individual planes of the telescope, a track is reconstructed with a combination of clusters in three planes called "triplet". The first step is the transformation from the local coordinates of the clusters (in the telescope plane) to the global coordinates. In the global coordinates, it is assumed that the centre of the telescope plane 0 (the first plane) is the origin of the coordinate system, and z -axis is parallel to the direction of the beam (see Fig. 3.9). The transformation is applied as follows:

$$\vec{x}_{glb} = (\vec{x}_{cls} + \vec{x}_{alg}) \cdot \bar{R}_z(\theta_{zp}) \quad (6.7)$$

$\bar{R}_z(\theta_{zp})$ is the rotation matrix which takes into account the rotation around the z -axis. The alignment vector, \vec{x}_{alg} , comes from the direct measurement of the position of planes.

After calculation of \vec{x}_{glb} , triplet candidates are reconstructed for the upstream and downstream arms of the telescope. A triplet candidate is a straight line between the two cluster positions. In Fig. 6.11, the procedure of triplet reconstruction is shown for two cluster points per plane. A triplet candidate is reconstructed from each cluster position in planes 0 and 2. There are four candidates for two clusters in each plane (for n clusters per plane, there are 2^n candidates). The following conditions are applied to select the "correct" triplet candidates:

- Triplets with an absolute slope, i.e. $|\frac{x_{glb,2} - x_{glb,0}}{dz_{02}}|$ and $|\frac{y_{glb,2} - y_{glb,0}}{dz_{02}}|$, of more than 5 mrad are rejected. Here $x_{glb,i}$ is defined as the global x -position of the cluster in the i plane of the telescope and dz_{02} is the distance between the first and third planes (240 mm in this work).
- The triplets are interpolated to the plane 1 and $(x_{i,1}, y_{i,1})$ pair is calculated. The candidates with residuals $|x_{glb,1} - x_{i,1} = \Delta x_{tri}| > 50 \mu\text{m}$ and $|y_{glb,1} - y_{i,1} = \Delta y_{tri}| > 50 \mu\text{m}$ are rejected.

The combinations which satisfy these two conditions are stored for further analysis. This

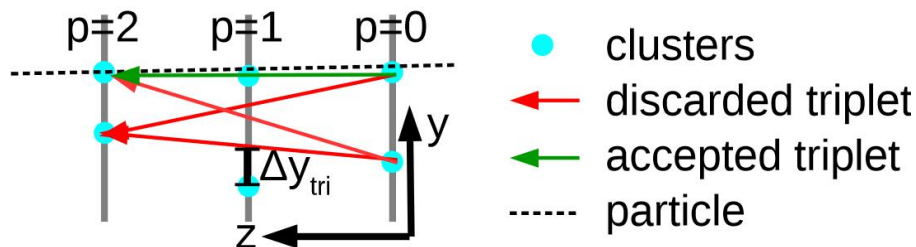


Figure 6.11: Criteria for selection the "correct" combination of triplets. In this example, 1 out of 4 candidates was selected. The sketch is taken from [55].

procedure is repeated for the downstream arm of the telescope using planes 3 to 5.

To reconstruct the trajectory of a particle with all six planes, triplets of upstream and downstream arms are extrapolated to the z -position of the DUT. This gives $(x_{utri}^{zDUT}, y_{utri}^{zDUT})$

and $(x_{dtri}^{zDUT}, y_{dtri}^{zDUT})$ for upstream and downstream triplets, respectively. The residuals are calculated as:

$$\begin{aligned}\Delta x_{TEL} &= x_{utri}^{zDUT} - x_{dtri}^{zDUT} \\ \Delta y_{TEL} &= y_{utri}^{zDUT} - y_{dtri}^{zDUT}\end{aligned}\quad (6.8)$$

A combination of the upstream and downstream triplet is defined as a "telescope track" if the following conditions are satisfied:

$$\begin{aligned}|\Delta x_{TEL}| &< 30 \mu\text{m} \\ |\Delta y_{TEL}| &< 30 \mu\text{m}\end{aligned}\quad (6.9)$$

These conditions are satisfied for the measurement of the non-irradiated modules without a cold box since the effect of the multiple scattering on an RD53A module is not significant (see Section 3.2). For measurement of irradiated modules, only the first arm of the telescope (upstream triplet in Fig. 3.9) could be used due to the multiple scattering on the copper bar in the cold box. The effect of the copper bar on the quality of reconstructed tracks can be seen in Fig. 6.12 where the distribution of Δx_{TEL} with and without the cold box is shown.

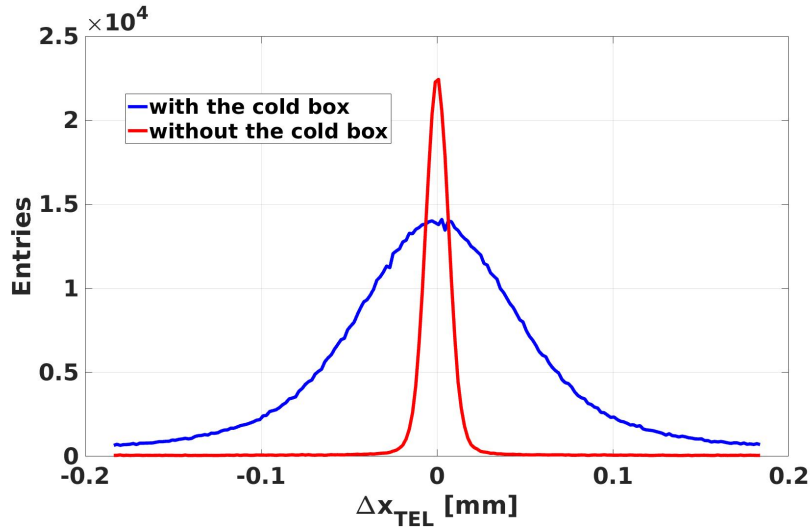


Figure 6.12: Δx_{TEL} distribution at the z -position of DUT with and without the cold box between two arms of the telescope.

6.3.4 Telescope Alignment

The required precision for the track reconstruction in the micrometre range is achieved through a recursive algorithm for the alignment of the telescope planes. Five parameters are defined for the alignment procedure for each plane: the shift in the x -, y - and z -directions (dx_{pl} , dy_{pl} , and dz_{pl}), rotation around x - and y -axis (θ_x^{pl} and θ_y^{pl}). The dz_{pl} parameter is only calculated for the third and sixth planes of the telescope.

To estimate the alignment parameters for each plane of the telescope, the residual distributions of each plane, i.e. Δx_{pl} and Δy_{pl} with respect to the second plane are calculated. The analysis is as follows:

- dx_{pl} and dy_{pl} : Δx_{pl} and Δy_{pl} are fitted with a sum of Gauss function and a constant. The mean value of the Gaussian from the fit gives dx_{pl} and dy_{pl} , respectively.
- θ_x^{pl} and θ_y^{pl} : The average value of Δx_{pl} as a function of y_{utri}^{zDUT} is calculated and fitted with a linear function. The slope of the line corresponds to θ_x^{pl} . For θ_y^{pl} , the average of Δy_{pl} as a function of x_{utri}^{zDUT} is calculated and the procedure is repeated.
- dz_{pl} : The average value of Δx_{pl} as a function of the slope of the corresponding track is calculated and fitted with a linear function. The slope of the line corresponds to dz_{pl} .

In the above analysis, the alignment parameters of the second plane are zero by definition.

6.3.5 Alignment of DUT

A similar procedure is used for finding the alignment parameters of the reference module and DUT. For the alignment of the DUT, the first step is the calculation of the intersection points between upstream and downstream triplets at the DUT plane (x_{utri}^{zDUT} , x_{dtri}^{zDUT}). The next step is the transformation of these points to the local coordinates of the DUT with a passive transformation (x_{TEL} , y_{TEL}). The DUT residual distributions are calculated as follows:

$$\begin{aligned}\Delta x_{DUT} &= x_{DUT} - x_{TEL} \\ \Delta y_{DUT} &= y_{DUT} - y_{TEL}\end{aligned}\tag{6.10}$$

Where x_{DUT} and y_{DUT} are the reconstructed cluster position in the DUT plane(Eq. (6.6)).

For the alignment of the DUT, 6 parameters are defined: shift in x - and y -directions (dx_{DUT} and dy_{DUT}), distance between the third plane of telescope and DUT (dz_{DUT}), rotation around x -, y -, and z -axes (θ_x , θ_y , θ_z). The shift parameters, i.e. dx_{DUT} , dy_{DUT} , dz_{DUT} , are estimated in a procedure similar to what was explained for the telescope alignment. For the calculation of θ_x , θ_y and θ_z , the following procedure is used:

- Tilt (θ_x): the average value of Δx_{DUT} as a function of x_{DUT} is calculated and fitted with a linear function. The slope of the line corresponds to θ_x .
- Turn(θ_y): the average value of Δy_{DUT} as a function of y_{DUT} is calculated and fitted with a linear function. The slope of the line corresponds to θ_y .

- Rotation (θ_z): the average value of Δx_{DUT} as a function of y_{DUT} is calculated and fitted with a linear function. The slope of the line corresponds to θ_z .

Fig. 6.13a shows an example of the DUT residual distribution before and after the alignment indicating a shift in the x -direction. In Fig. 6.13b, the average of Δx_{DUT} as a function of y_{TEL} is shown before and after the alignment. The slope of the curve before alignment indicates a rotation around the z -direction. The procedure for alignment of the reference module is similar, but only the upstream triplets are used for tracking.

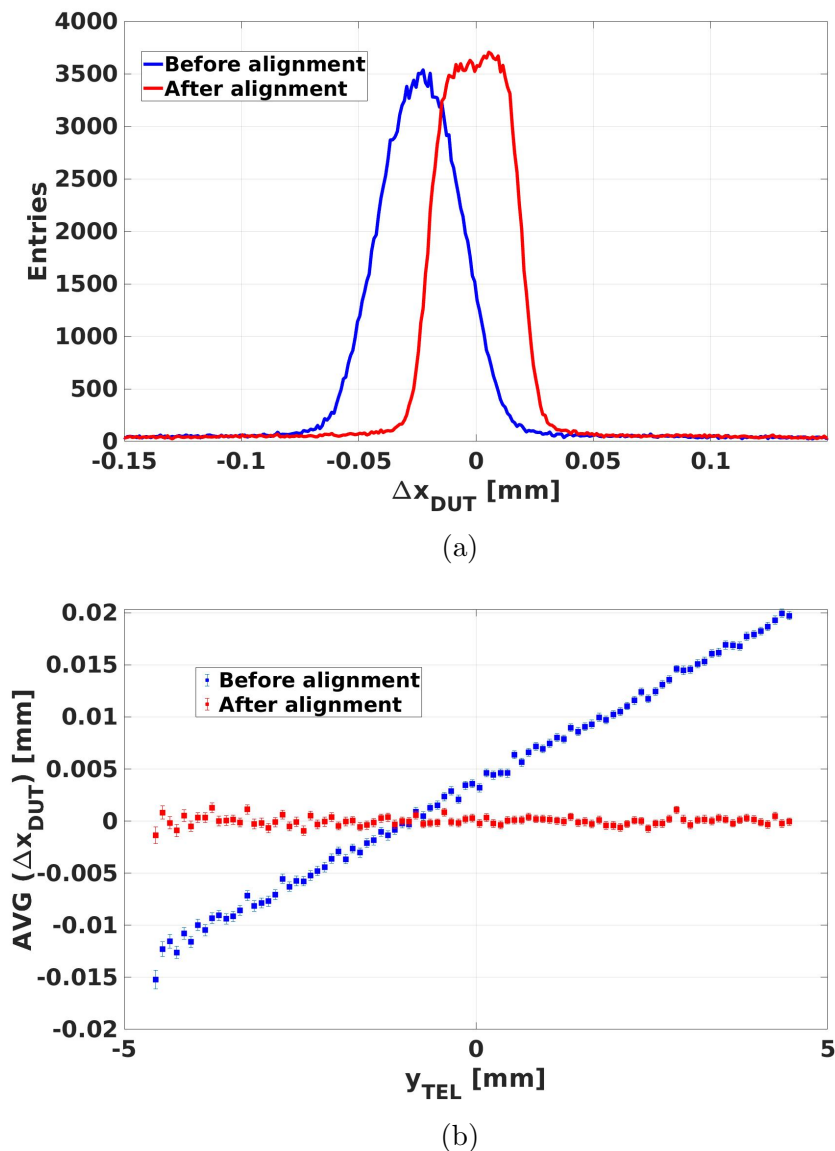


Figure 6.13: The residual distributions before and after the alignment where Δx_{DUT} distribution before the alignment indicates a shift in the x -direction (dx_{DUT}) (a). The mean of Δx_{DUT} as a function of y_{TEL} which indicates a rotation of the DUT around z -direction (θ_z) (b).

6.4 Definition of Observables

The key observables of a pixel sensor are defined in the following.

6.4.1 Hit Efficiency

The hit efficiency of the DUT is defined as:

$$\epsilon_{DUT} = \frac{N(\text{tracks with DUT hit})}{N(\text{tracks})} \quad (6.11)$$

Where $N(\text{tracks})$ is the number of tracks reconstructed in the beam telescope, and $N(\text{tracks with DUT hit})$ is the number of those tracks with a matched hit in the DUT. A series of cuts are applied to tracks for this calculation which are explained in the next section.

To find tracks with a matched hit in the DUT, the distance between the telescope track and the closest hit in the DUT is calculated as:

$$r_{min} = \sqrt{(x_{TEL} - x_{DUT}^{min})^2 + (y_{TEL} - y_{DUT}^{min})^2} \quad (6.12)$$

Where x_{DUT}^{min} and y_{DUT}^{min} are the position of the closest reconstructed hit in the DUT to the telescope tracking. A track has a matched hit in the DUT if $r_{min} < 500 \mu\text{m}$. Fig. 6.14 shows an example of hit efficiency as a function of r_{min} for an irradiated sensor. One can see the chosen cut for r_{min} is well above the step at low values of r_{min} . The low efficiency at $r_{min} < 0.06 \text{ mm}$ is due to the poor resolution of the reconstructed tracks and DUT.

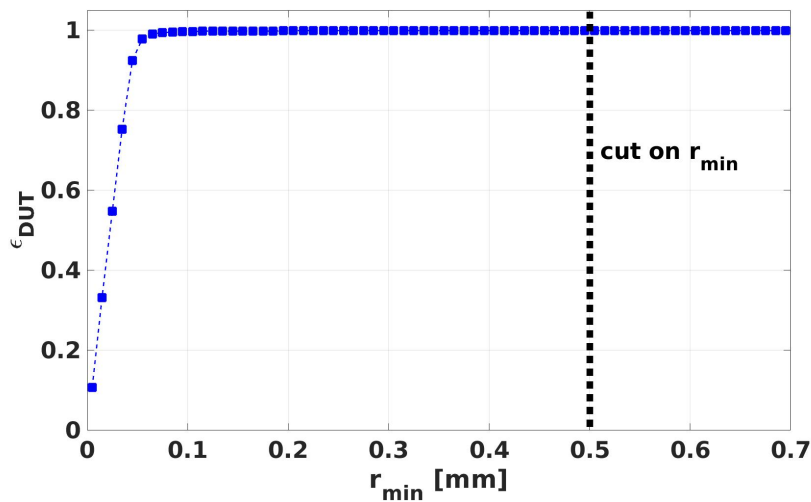


Figure 6.14: Hit efficiency as a function of r_{min} . The results are shown for the sensor with the bitten design irradiated at $\Phi_{eq} = 0.86 \times 10^{16} \text{ cm}^{-2}$ (M595) measured at 800 V at vertical incidence.

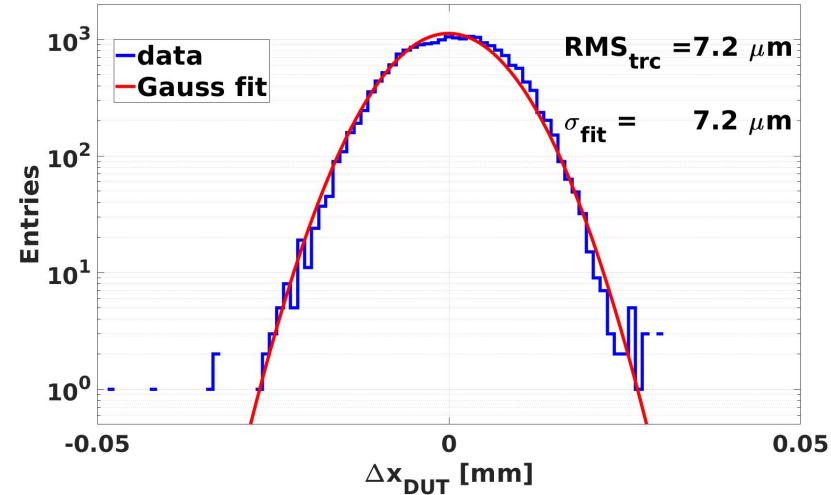
The error on the hit efficiency from a Binomial distribution is calculated as [103]:

$$\sigma_\epsilon = \frac{1}{\sqrt{N_{track}}} \cdot \sqrt{\epsilon(1-\epsilon)} \quad (6.13)$$

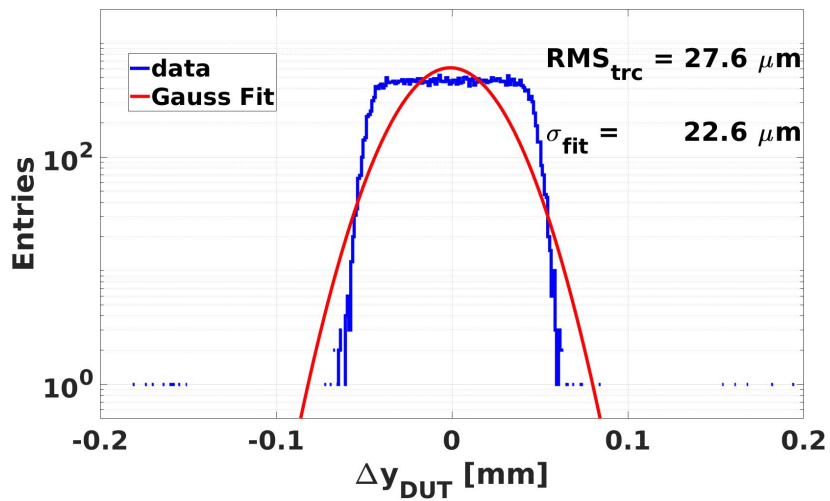
6.4.2 Spatial Resolution

The spatial resolution of a pixel sensor is the uncertainty of position measurement by the sensor. This quantity can be calculated by analysing the residual distributions of the DUT (see Eq. (6.10)) and extracting its width.

To calculate the width of residual distributions, several methods have been proposed in the literature. A comprehensive study of various methods is presented in [104]. For this work, the truncated RMS (RMS_{trc}) is used to extract the width of the residual distributions. In this method, the RMS of the residual distribution is calculated in an iterative approach within the $\pm 3 \cdot RMS_{trc}$ range. The residual distributions of a non-irradiated sensor with a pixel size of $25 \times 100 \mu\text{m}^2$ in x (short pitch) and y (long pitch) directions is shown in Fig. 6.15 to emphasise the impact of the characterisation method on the results, . Both distributions are fitted with a Gauss function, and the width extracted from the fit is reported as σ_{fit} . Although the results from the fit and RMS are compatible for the Δx_{DUT} distribution, they are very different for Δy_{DUT} and the fit fails to describe the box-shaped distribution.



(a)



(b)

Figure 6.15: DUT residual distributions in x -(a) and y -direction (b). The pitches are 25 and $100 \mu\text{m}$ respectively. DUT is a non-irradiated sensor with a bitten design operated at 120 V. The measurement was taken at vertical incidence ($\theta_y = 0^\circ$).

There are two uncertainties contributing to the width of the DUT residual distributions: the intrinsic DUT resolution, which we want to know and the telescope resolution. The uncertainty of the telescope, x_{TEL} and y_{TEL} , can be calculated from the residual distribution of the telescope at the z -position of the DUT in Eq. (6.8). A similar procedure as for the DUT residual is used to extract the width of the telescope residual distribution: after applying the selection cuts to the residual distribution, the truncated RMS, RMS_{trc} is calculated. The uncertainty of x_{TEL} is defined as:

$$\begin{aligned}\sigma_{x_{TEL}} &= \frac{\text{RMS}_{trc}(\Delta x_{TEL})}{2\cos(\theta_y)} \\ \sigma_{y_{TEL}} &= \frac{\text{RMS}_{trc}(\Delta y_{TEL})}{2\cos(\theta_x)}\end{aligned}\tag{6.14}$$

The full derivation of Eq. (6.14) is presented in [55]. The resolution of the DUT can now be calculated as:

$$\sigma_{x_{DUT}} = \sqrt{(\text{RMS}_{trc}(\Delta x_{DUT}))^2 - \sigma_{x_{TEL}}^2}\tag{6.15}$$

A similar expression can be defined for $\sigma_{y_{DUT}}$.

This procedure only works for the measurement of non-irradiated modules outside of the cold box. As shown in Fig. 6.12, when the cold box is placed between the upstream and downstream arms, the condition in Eq. (6.9) is not satisfied, and only the upstream arm of the telescope can be used for tracking. Under these circumstances, a direct estimation of $\sigma_{x_{TEL}}$ is not possible. Instead, a non-irradiated module with a known intrinsic resolution is placed inside the cold box to measure the track resolution using only the upstream arm of the telescope. The procedure is explained in the following.

First, the non-irradiated module is measured outside of the cold box and the DUT resolution, $\sigma_{x_{DUT}}$, is estimated using Eq. (6.15). Fig. 6.16 shows the residual distribution of a non-irradiated module with a pixel size of $25 \times 100 \mu\text{m}^2$ in the $25 \mu\text{m}$ direction (Δx_{DUT}) and the residual distribution of the telescope at the z -position of the DUT (Δx_{TEL}). From Eq. (6.15), the resolution of the DUT, $\sigma_{x_{DUT}}$, is calculated as $5.32 \pm 0.04 \mu\text{m}$. The error is calculated by propagating the statistical error of $\text{RMS}_{trc}(\Delta x_{DUT})$ and $\text{RMS}_{trc}(\Delta x_{TEL})$ in Eq. (6.15).

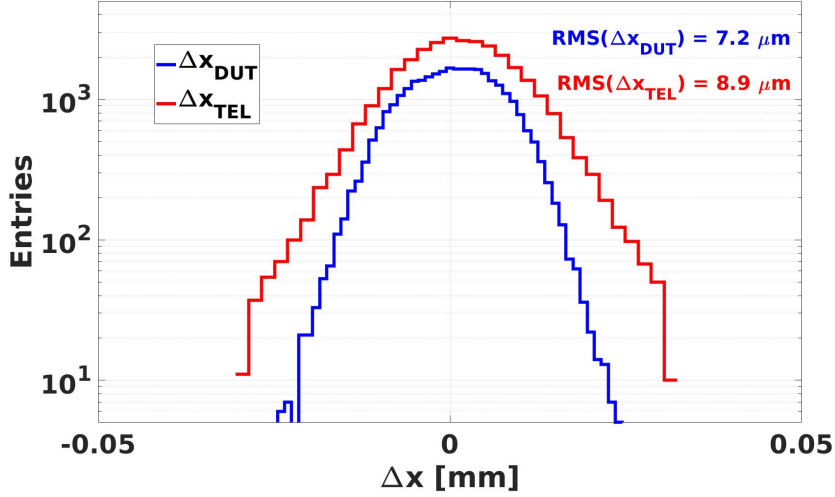


Figure 6.16: Residual distributions of the DUT (blue) and the telescope (red). DUT is a non-irradiated module with a pitch size of $25 \times 100 \mu\text{m}^2$ operated at 120 V outside the cold box. The measurement was taken at vertical incidence.

In the second step, the sensor is placed inside the cold box, and the measurement is repeated for the same condition (temperature, threshold, etc.). The residual of the DUT is calculated and its width, σ_{mDUT}^{box} , is extracted. The measurement is repeated at several values of dz_{DUT} . Fig. 6.17 shows the DUT residual distributions for three different dz_{DUT} values. One sees that the width of the measured residual distribution increases by increasing dz_{DUT} . Since the DUT resolution is independent of dz_{DUT} , this increase is due to an increase in the extrapolation error of telescope tracks to the plane of the DUT.

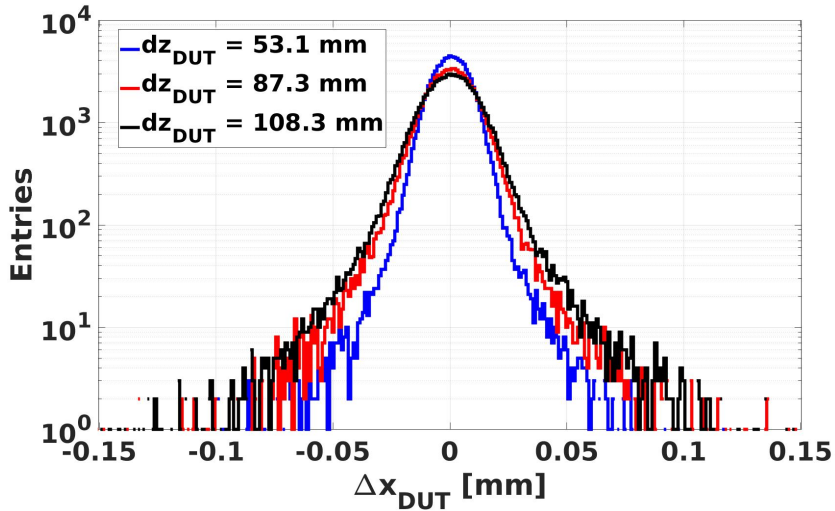


Figure 6.17: DUT residual distributions measured inside cold box at different dz_{DUT} .

The extrapolated telescope resolution from the upstream arm is estimated as:

$$\sigma_{TEL}^{urti}(dz_{DUT}) = \sqrt{(\sigma_{mDUT}^{box}(dz_{DUT}))^2 - (\sigma_{xDUT})^2} \quad (6.16)$$

Fig. 6.18 shows σ_{TEL}^{urti} as a function of dz_{DUT} for beam energies of 5.2 and 5.6 GeV. The data are fitted with a linear function. Results for both energies have a similar slope, but the intercept for the beam energy of 5.2 GeV is higher than the line for 5.6 GeV. This difference can be understood by considering the multiple scattering effects in Eq. (3.1) where the deflection angle is inversely proportional to the beam energy.

The result from the linear fit is used to calculate the telescope resolution for the irradiated modules in the cold box. For each module, dz_{DUT} is estimated as explained in Section 6.3.5 and expected uncertainty of the telescope, σ_{TEL}^{urti} is calculated from the linear fit shown in Fig. 6.18. The intrinsic resolution of the irradiated module measured inside the cold box is then calculated as:

$$\sigma_{xDUT} = \sqrt{(\text{RMS}_{trc}(\Delta x_{DUT}))^2 - (\sigma_{TEL}^{urti})^2} \quad (6.17)$$

There is a caveat to the values obtained from Eq. (6.17) for the pitch size of 25 μm . As shown in Fig. 6.18, the extrapolated telescope resolution, σ_{TEL}^{urti} , is in the range of 6 μm to 11 μm which is larger than the expected spatial resolution of the DUT in the 25 μm direction ($\approx 7 \mu\text{m}$ to $9 \mu\text{m}$). Therefore, the spatial resolution obtained for the irradiated sensors should be taken with a grain of salt.

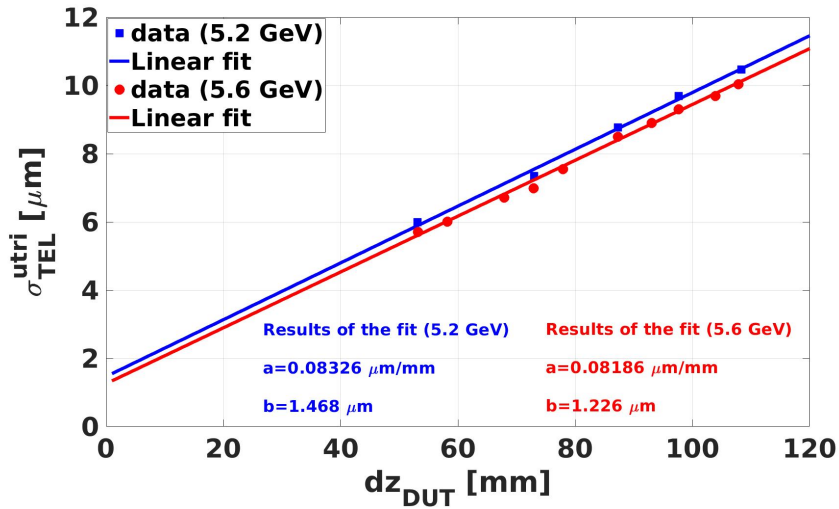


Figure 6.18: Calculated telescope resolution as a function of dz_{DUT} for beam energies of 5.2 and 5.6 GeV. The data is fitted with a linear function ($a \cdot dz_{DUT} + b$) and the fit parameters are given in the figure.

6.4.3 Cluster Size

A cluster is a group of neighbouring pixels with a charge above the threshold. The cluster size is an important quantity for the characterisation of pixel sensors and is an index of charge sharing between pixels. The cluster size is defined in three ways:

- projected cluster size in the x -direction: number of pixels in the cluster with different columns or n_{col} .
- projected cluster size in the y -direction: number of pixels in the cluster with different rows or n_{row} .
- total cluster size: total number of pixels in the cluster or n_{px} .

6.4.4 Noisy Pixels

After irradiation, the leakage of the sensors increases by several orders of magnitude. This effect increases the number of noisy pixels in the module. The noisy pixels usually have high occupancy. Here, occupancy is defined as the number of hits of a pixel divided by the number of triggers (or events). Pixels with outputs above the threshold in the LFE are read out during the measurements, and the noisy pixels are masked in the offline analysis.

For layer 1 of the CMS IT, pixels with occupancy higher than 2×10^{-5} are defined as noisy. This number is defined for one bunch crossing. However, for the measurements in this work, the DUT is read for 31 bunch crossings. Therefore, the maximum occupancy is re-defined as:

$$O_{max} = 2 \times 10^{-5} \times (31 - \Delta N_{BC}) \quad (6.18)$$

Where ΔN_{BC} is the range of bunch crossings containing a real particle hit (see Eq. (6.22)), for this work, ΔN_{BC} is usually around 5 to 7 which translates to the maximum occupancy of 4.8×10^{-4} to 5.2×10^{-4} . Fig. 6.19 shows an occupancy distribution for all pixels in an irradiated module. The analysis identifies pixels with an occupancy higher than the limit shown with the dotted line as noisy and masked.

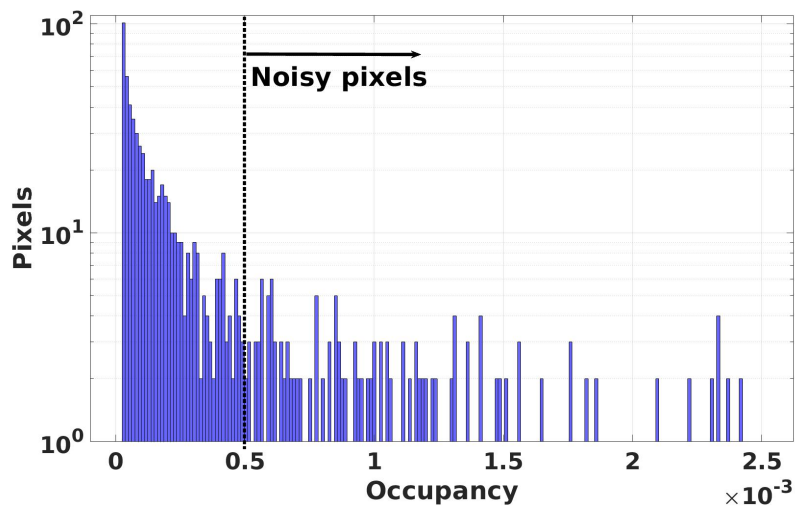


Figure 6.19: Occupancy distribution of all pixels in a RD53A module. DUT is a bitten design module irradiated at $\Phi_{eq} = 2.0 \times 10^{16} \text{ cm}^{-2}$ (M613) operated at 800 V. The limit for identifying noisy pixels is shown with a dotted line. For this example, 592 noisy pixels are identified.

6.5 Selection Cuts

The track reconstruction method and the alignment procedure can be affected by background processes. For example, as shown in Fig. 6.11, multiple clusters in each plane of the telescope cause fake track candidates. The same problem can arise with the noisy pixels in the DUT mimicking particle hits. Associating the telescope tracks to the noisy hits biases the DUT hit efficiency and residual distributions.

To reduce the effect of such processes on the reconstructed observables, eight selection cuts (C1 to C8) are applied to the data in the offline analysis. In the following, these selection cuts are defined. The first three cuts, C1 to C3 and C5, are applied to evaluate all quantities (hit efficiency, spatial resolution, cluster size). The rest of the cuts are only applied for studying the resolution and cluster size.

6.5.1 Cut 1: Link to Reference Module

As mentioned in Chapter 3, the readout frame of the telescope is long compared to the DUT readout cycle and the particle rate at DESY II test-beam. Therefore, several particles can pass the telescope during one readout frame and cause pile-up tracks.

To reduce the impact of these tracks, a timing reference module is used to select the in-time tracks. The specifications of this module are explained in Section 3.1.4. Telescope tracks are projected to the reference module and transformed to its local coordinate (x_{TEL}^{REF} , y_{TEL}^{REF}). Then, the residual distributions of the reference module are calculated between the track intersection and the cluster position in the reference module (x_{REF} , y_{REF}) as:

$$\begin{aligned}\Delta x_{REF} &= x_{TEL}^{REF} - x_{REF} \\ \Delta y_{REF} &= y_{TEL}^{REF} - y_{REF}\end{aligned}$$

A track has a link to the reference module if the following conditions are satisfied:

$$\begin{aligned}|\Delta x_{REF}| &\leq 150 \mu\text{m} \text{ and} \\ |\Delta y_{REF}| &\leq 100 \mu\text{m}\end{aligned}$$

6.5.2 Cut 2: Fiducial Region

To evaluate the hit efficiency of the DUT, only the telescope tracks that are pointing to the active region of the DUT can be used. The following cuts are applied to the telescope tracks at the DUT plane to ensure this:

$$\begin{aligned}-3.5 \text{ mm} &< x_{TEL}^{DUT} < 3.1 \text{ mm} \text{ and} \\ -4.7 \text{ mm} &< y_{TEL}^{DUT} < 4.7 \text{ mm}\end{aligned}\tag{6.19}$$

The specified region corresponds to the LFE of the RD53A chip, excluding two rows

and columns (100 μm) from each side of the chip. The pixels in the exclusion regions were found to be noisy, especially after the irradiation. If the module is rotated by 90° , the conditions in Eq. (6.19) are adjusted accordingly.

6.5.3 Cut 3: Track Isolation in Reference Module

The telescope can reconstruct several tracks for the same event. If the intersections of these tracks with the reference module are too close to each other, it is not clear which of the reconstructed tracks are in time with the readout cycle of the reference module. To prevent confusion, the radial distance between two telescope tracks in the reference module is calculated as:

$$d_{12} = \sqrt{(x_{TEL,1}^{REF} - x_{TEL,2}^{REF})^2 + (y_{TEL,1}^{REF} - y_{TEL,2}^{REF})^2} \quad (6.20)$$

This calculation is repeated for each pair of tracks (d_{13} , d_{23} , etc) and the minimum value is found, d_{min} . The isolation condition is defined as:

$$d_{min} \leq 600 \mu\text{m} \quad (6.21)$$

For this calculation, only the position information from the telescope is used.

6.5.4 Cut 4: Track Isolation in DUT

A similar procedure as for C3 is repeated for the DUT plane and d_{min} is calculated. The isolation condition is the same as Eq. (6.21).

6.5.5 Cut 5: Bunch Crossing ID of the DUT

As mentioned in Section 6.2.1, for each trigger, the chip is read out for 31 cycles known as bunch crossings. Each bunch crossing corresponds to 25 ns. The signal from the "real particles" usually appears in 1 or 2 bunch crossings. To select the hits associating with the signal, the largest and smallest BCID for each cluster in the DUT is found ($\max(\text{BCID})$ and $\min(\text{BCID})$) in the analysis and the following cuts are applied

$$\begin{aligned} \max(\text{BCID}) &\leq 12 \text{ and} \\ \min(\text{BCID}) &\geq 7 \end{aligned} \quad (6.22)$$

Fig. 6.20 shows the distributions of maximum and minimum BCID along with the selection cut. The entries outside the selection region are due to the activity of noisy pixels. The peak observed around BCID of 10 corresponds to the signal from real particles. If the delay time between the trigger signal and the DUT readout changes, this peak is shifted. Therefore, the range of the cut should be adjusted for each run separately.

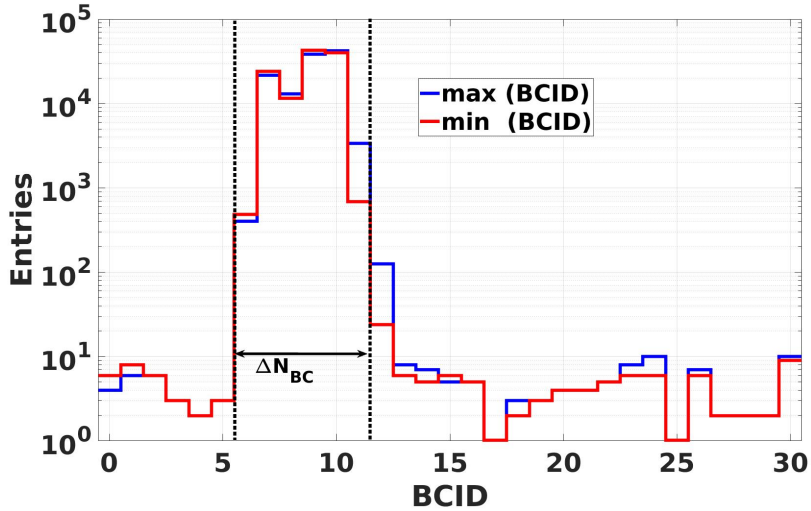


Figure 6.20: Distribution of maximum and minimum BCID. The DUT is a sensor with the bitten design irradiated at $\Phi_{eq} = 2.0 \times 10^{16} \text{ cm}^{-2}$ (M613) measured at 800 V at vertical incidence.

6.5.6 Cut 6: Residual Cut

As mentioned above, not all hits in the DUT are due to the real particles, and noise fluctuations can mimic a hit and bias the reconstruction. The following cuts are applied to the residual distributions of the DUT to reduce the effect of fake hits:

$$\begin{aligned} |\Delta x_{DUT}| &< \frac{2 \cdot p_x}{\sqrt{12}} \\ |\Delta y_{DUT}| &< \frac{2 \cdot p_y}{\sqrt{12}} \end{aligned} \quad (6.23)$$

Where p_x and p_y are the pixel pitch sizes in x and y direction, respectively. The cut on Δx_{DUT} is applied to study the Δy_{DUT} distribution and vice versa. The values for the cut limits were chosen to be consistent with [105, 55].

6.5.7 Cut 7: Charge Cut

As mentioned in Section 6.3.2, the CoG method is used to reconstruct the hit position. Particles with large energy deposition associated with δ -rays can shift the CoG of deposited charge and deteriorate the spatial resolution. This effect has been shown experimentally in [106]. A cut on the cluster charge is applied to exclude the effect of these events.

First, the cluster charge distribution is calculated. Then the cluster charge, which includes the 90% of total entries, $Q_{90\%}$, is found. The clusters with a charge higher than $Q_{90\%}$ are excluded. Fig. 6.21 shows the cluster charge distributions for three incident angles for a non-irradiated module and the corresponding limit for the cluster charge.

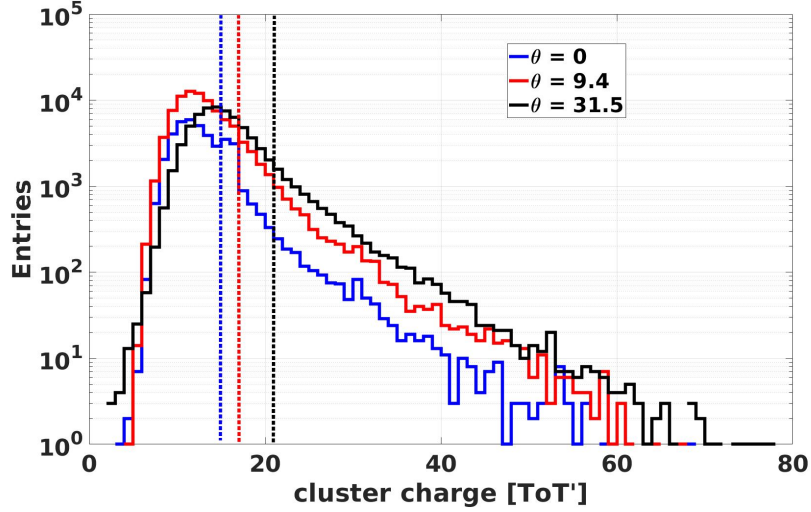


Figure 6.21: Cluster charge distribution for three angles of incidences. Dash lines represent limit with highest 10% of cluster charge with same colour. DUT is a non-irradiated module with a pixel size of $25 \times 100 \mu\text{m}^2$ operated at 120 V. Cluster charges are expressed in terms of ToT' as explained in Section 6.3.2.

6.5.8 Cut 8: Residual Pairing

To obtain the residual distribution using Eq. (6.10), the correct combination of hits in two devices, telescope, and DUT, must be found. This is a straightforward task when there is one hit per device. However, there will be ambiguous combinations with more than one hit per device. An algorithm was developed in [55] to find the "correct" pair of hits. The algorithm defines the following conditions to find the correct pair:

1. The hit j on device 1 is closest to hit k on device 2.
2. The hit k on device 2 is closest to hit j on device 1.

A sketch of this algorithm is shown in Fig. 6.22. The pair of events that pass the requirements are circled.

Two conditions stated above are not the same. This can be understood by looking at the three events in the square in Fig. 6.22. Although the first condition is met for both events in device 1, the second condition is only met for one of them. It should be noted that the "correct pair" means the combination of two events with the highest probability of originating from the same particle.

6.6 Results and Discussion

This section presents the results of the test-beam characterisation of pixel modules listed in Table 3.1. Two types of measurements were carried out in the test-beam: bias scan and turn scan (rotation around the long axis). Hit efficiency, spatial resolution, and cluster size are extracted from these measurements.

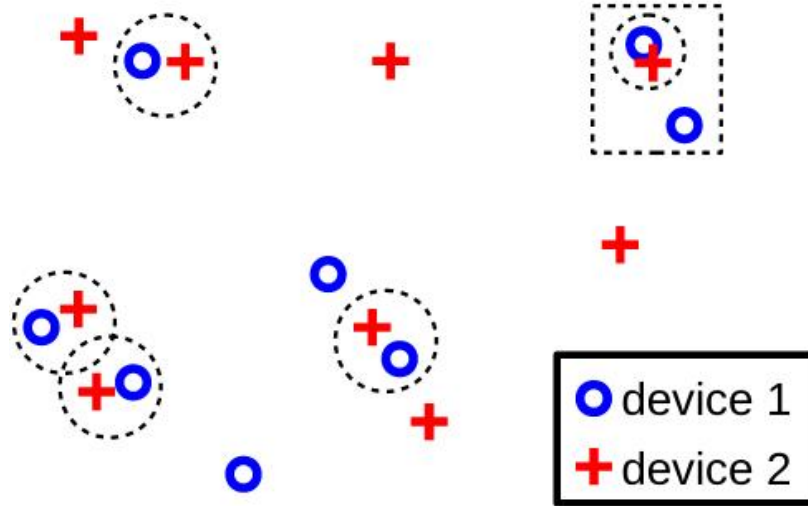


Figure 6.22: Sketch of pair finding algorithm for two devices. Events which meet requirements of algorithm are circled. In the case of three events in the dashed box: the first condition is met for two hits in device 1, but the second condition is only met for the pair of events in the circle. Sketch is taken from [55].

6.6.1 Results of Non-Irradiated Modules

The following results of the test-beam characterisation of four non-irradiated modules in Table 3.1 are presented. All measurements were done at room temperature. The modules were tuned to the lowest possible threshold in the range of 700 electrons to 900 electrons (see Table 3.1).

Hit Efficiency

The hit efficiency as a function of bias voltage for non-irradiated modules is shown in Fig. 6.23. All modules are fully efficient (> 0.99) at bias voltages above 30 V. The statistical error on the efficiency using Eq. (6.13) is found to be between 10^{-5} to 10^{-4} . The leakage current of sensors was monitored during measurements in the range of few μA without any signs of breakdown. The number of noisy pixels (as defined in Section 6.4.4) was found to be less than 10 in the whole LFE.

For the bias dot design, it is observed that the efficiency decreases slightly for bias voltages above 120 V. The loss of efficiency is observed at the position of the bias. This loss can be seen in Fig. 6.24, which shows the in-pixel efficiency of the bias dot design at bias voltages of 120 V and 400 V. The in-pixel efficiency is calculated by mapping the efficiency of the whole sensor in one pixel. The inefficiency at the bias dot position increases at higher bias voltage. This is because the diffusion of charge carriers decreases at higher bias voltages. Therefore charge loss at the position of the bias dot increases, which in turn increases the inefficiency in this region.

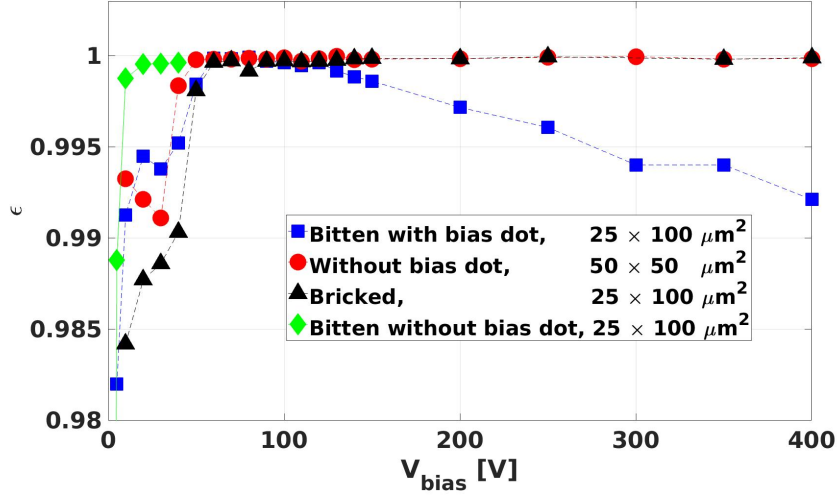


Figure 6.23: The hit efficiency as a function of bias voltage for non-irradiated modules. All measurements were performed at the room temperature and online threshold in the range of 700 – 900 electrons (see Table 3.1).

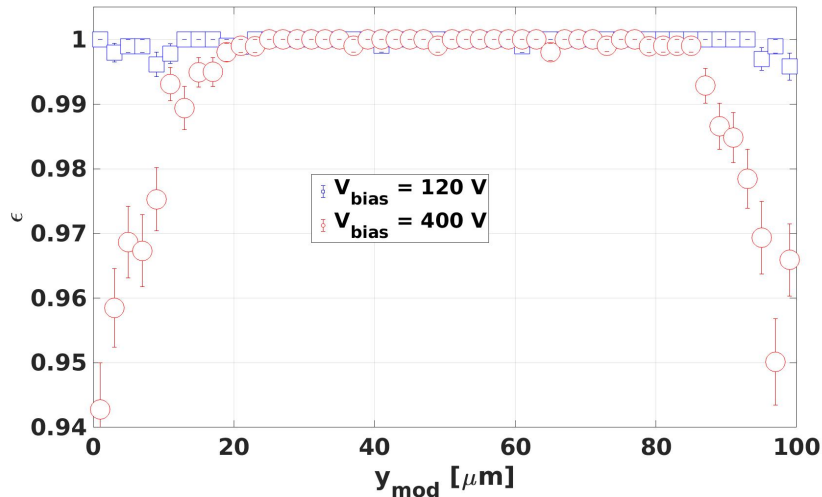


Figure 6.24: In-pixel hit efficiency of the non-irradiated module with the bias dot (M599) at bias voltages of 120 V and 400 V. The bias dot positions are at $y_{mod} = 0 \mu\text{m}$ and $y_{mod} = 100 \mu\text{m}$.

Spatial resolution

The CoG algorithm is used for the hit reconstruction in DUT. Using this algorithm, one expects a better spatial resolution for increased charge sharing between pixels. The amount of charge sharing depends on various factors such as the magnetic field, diffusion, electric field, track angle, and cross-talk. In this work, the resolution was studied as a function of the track angle.

The spatial resolution of the modules was measured as a function of the angle of incidence (θ_y). The modules were rotated around the long axis ($100 \mu\text{m}$), which resulted in

a charge sharing between pixels along the short axis ($25\ \mu\text{m}$) for modules with the pixel size of $25 \times 100\ \mu\text{m}^2$. For these measurements, sensors were biased at 120 V.

Fig. 6.25 shows the results of the spatial resolution as a function of turn angle in two directions, where σ_{xDUT} and σ_{yDUT} are the spatial resolution along $25\ \mu\text{m}$ and $100\ \mu\text{m}$, respectively. The resolution was extracted from the DUT residual distribution as explained in Section 6.4.2. The telescope resolution was estimated from the Δx_{TEL} and Δy_{TEL} distributions (Eq. (6.8)) and subtracted from the measured resolution of the DUT using Eq. (6.15). The angle of incidence, θ_y , was estimated from the alignment procedure as explained in Section 6.3.5. The quoted error bars are only due to the statistical uncertainties.

For all modules, it is observed that the resolution at vertical incidence is better than binary resolution. As discussed in Section 2.4, a fraction of tracks hit the boundaries between two pixels and generate a signal over the threshold in both pixels. This results in a resolution better than binary.

It is seen that for all modules the best resolution in x -direction is obtained at optimal angle of $\arctan(\frac{\text{pitch}}{\text{thickness}})$. At this angle, the average cluster size is two, considering the geometry of the pixel. For the pitch size of $25\ \mu\text{m}$ and $50\ \mu\text{m}$, the best resolution of $2.15 \pm 0.05\ \mu\text{m}$ and $3.56 \pm 0.03\ \mu\text{m}$ is obtained respectively. At angles larger than optimal angle, resolution degrades for all sensors. At these angles, deposited charge by tracks is spread over more pixels, and the signal-to-noise ratio is reduced.

In y -direction, the resolution of three sensors with the non-bricked design stays constant as a function of turn angle. This is expected as the turn angle does not affect charge sharing in this direction. For the sensor with the bricked design, σ_{yDUT} reaches to $11.70 \pm 0.02\ \mu\text{m}$ which is equal to the resolution of the sensor with the pitch size of $50\ \mu\text{m}$. In other words, the module with bricked design shows an "effective pitch size" of $50\ \mu\text{m}$ in the $100\ \mu\text{m}$ direction.

To better understand the spatial resolution of the sensor with the bricked design, the DUT residual distribution of two sensors with and without the bricked design are shown in Fig. 6.26 for different angles of incidence. In the x -direction, both sensors show a similar distribution. In the y -direction, the bricked sensor shows a better resolution even at $\theta_y = 0^\circ$. At $\theta_y = 17.2^\circ$, the width of residual distribution for the bricked sensor is approximately two times smaller than for the non-bricked design.

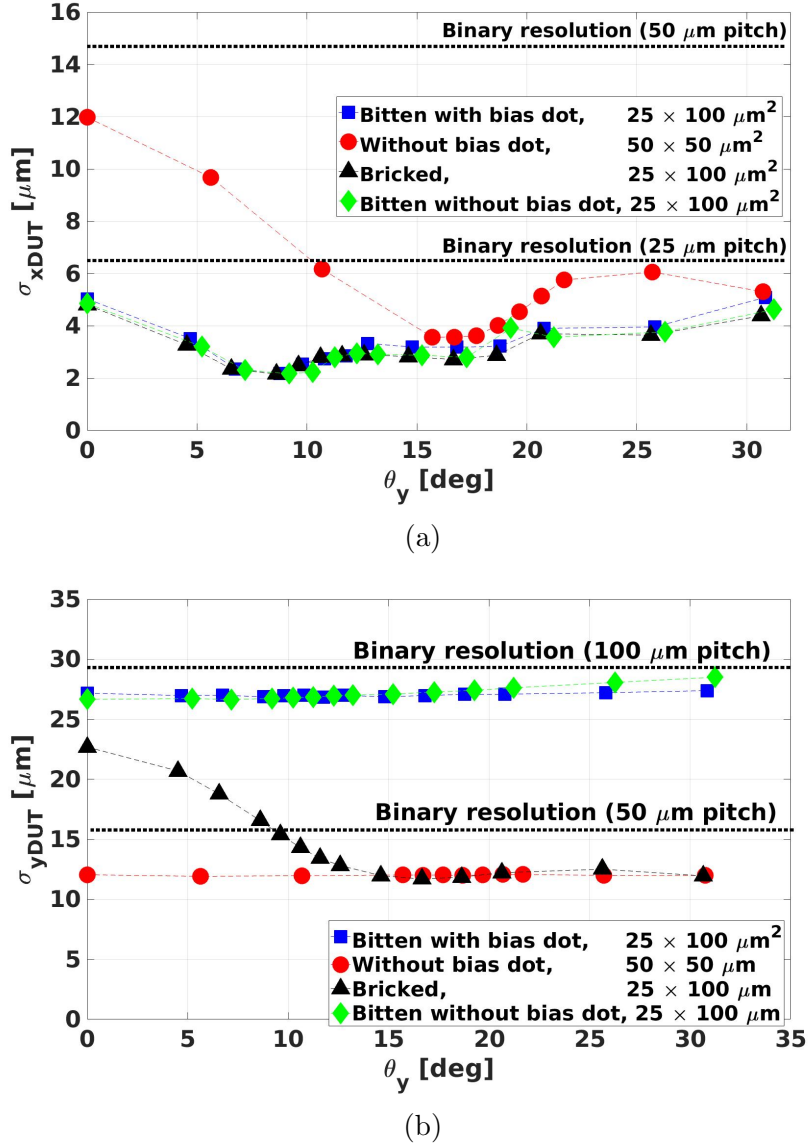


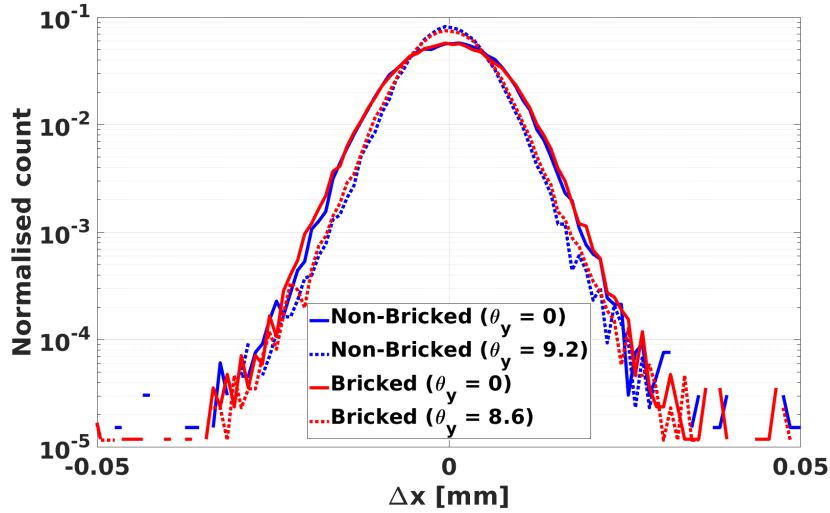
Figure 6.25: Spatial resolution of non-irradiated modules in short (a) and long (b) axes as a function of turn angle.

Cluster size

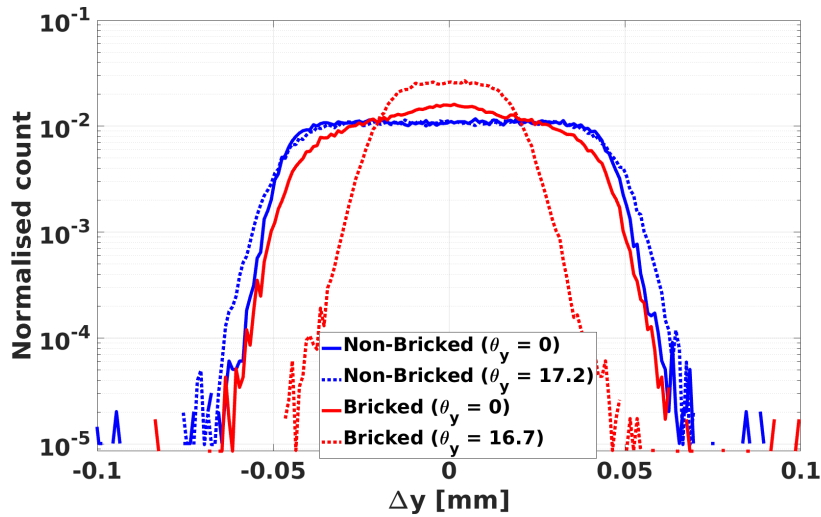
Fig. 6.27 shows the mean projected cluster size in x and y directions, i.e. n_{row} and n_{col} , as a function of turn angle (θ_y) for the non-irradiated modules. The same selection cuts for the spatial resolution are applied to reconstruct this quantity.

It is seen that a cluster size of 2 is obtained at optimal for all modules. The projected cluster size, n_{row} , at vertical incidence is higher than 1, as explained in the previous part. Moreover, n_{row} is higher for the sensors with the pitch size of $25\ \mu\text{m}$ than $50\ \mu\text{m}$. For smaller pitch sizes, the effect of charge diffusion of charge carriers is more significant. In addition, the cross-talk effect is much more significant for the pixel size of $25 \times 100\ \mu\text{m}^2$. Cross-talk is discussed in more detail in Chapter 7.

Similar to the resolution results, the projected cluster size in y -direction, n_{col} , stays



(a)

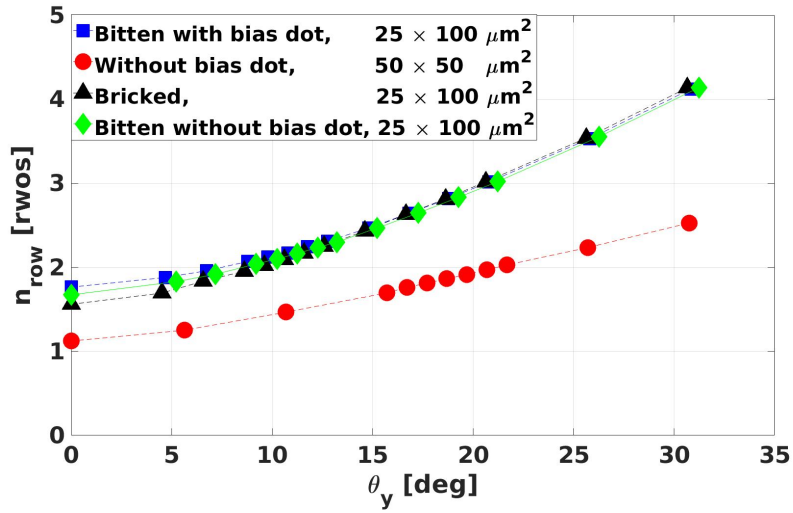


(b)

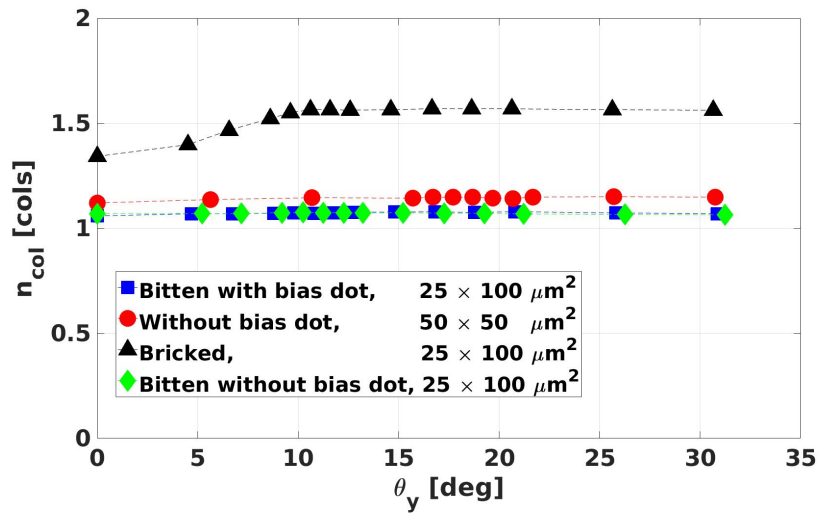
Figure 6.26: DUT residual distributions in x (a) and y (b) directions measured for two non-irradiated sensors with bricked and non-bricked designs. Each distribution is normalised to its number of entries for better comparison.

constant as a function of turn angle for the modules with non-bricked design as the charge sharing does not change in this direction. For the bricked design, n_{col} increases to 1.56.

In Fig. 6.28, the total cluster size as a function of in-pixel position is shown for sensors of different designs. The data was taken at the vertical incidence. One recognises the pixel layout of each design. For the sensor with the pitch size of $50 \times 50 \mu\text{m}^2$, the cluster size is around 1 at the centre of the pixel and reaches 2.4 in the boundaries of pixels. For the sensor with the pitch size of $25 \times 100 \mu\text{m}^2$, the cluster is around 1.8 at the centre and increases to 2.5 in the boundaries between pixels. The higher cluster size in the centre of the pixel is due to the higher diffusion of charge carriers and cross talk for this pitch size.



(a)



(b)

Figure 6.27: Mean projected cluster size in x (a) and y (b) directions as a function of turn angle (θ_y) for non-irradiated modules.

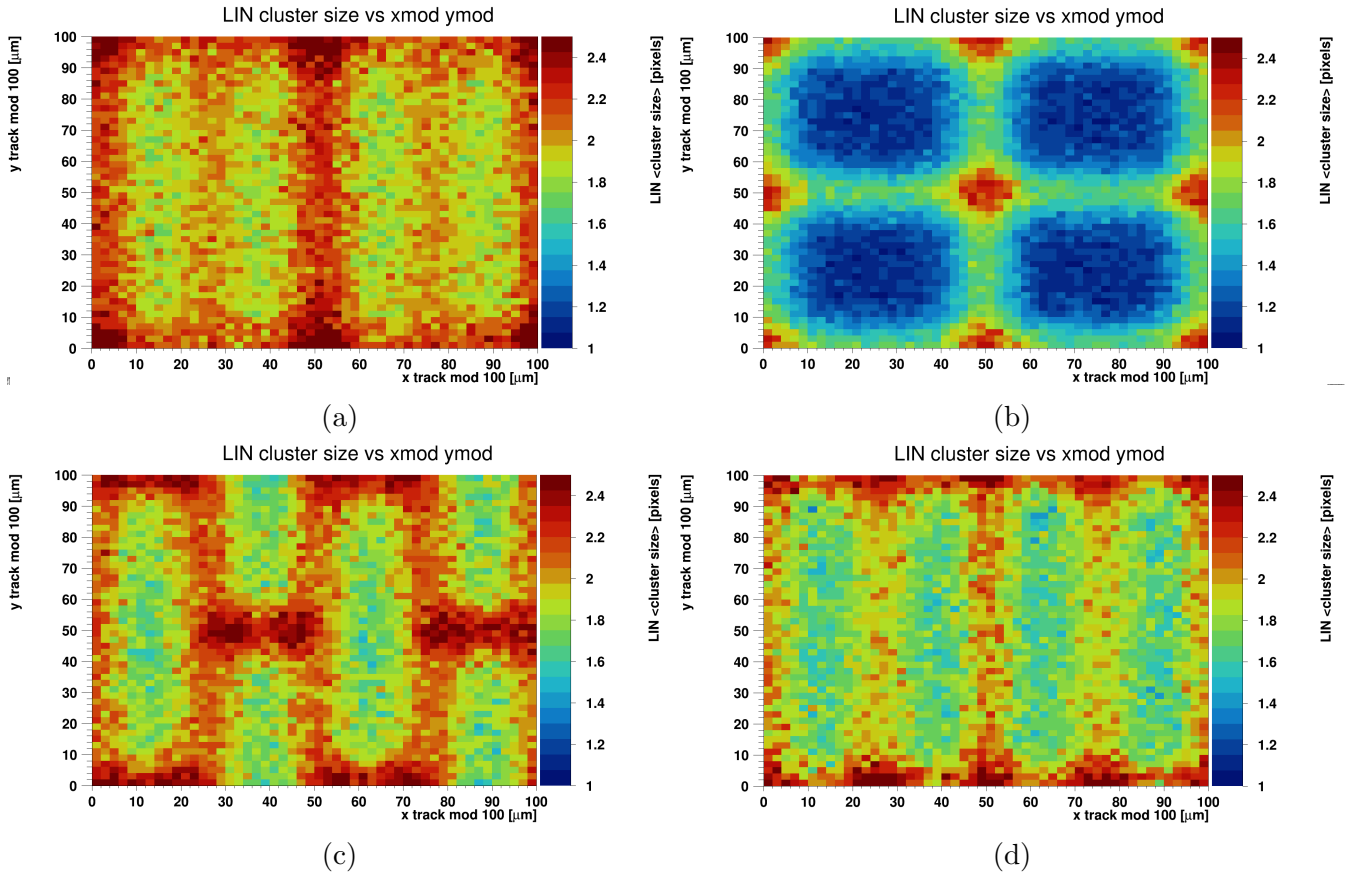


Figure 6.28: Total cluster size for non-irradiated modules : $25 \times 100 \mu\text{m}^2$ bitten with bias dot (a), $50 \times 50 \mu\text{m}^2$ without bias dot (b), $25 \times 100 \mu\text{m}^2$ bricked (c), and $25 \times 100 \mu\text{m}^2$ bitten without bias dot (d). This data was taken at vertical incidence and a bias voltage of 120 V.

6.6.2 Results of Irradiated Modules

As mentioned in Section 3.4.1, five modules were irradiated with 23 MeV protons (see Table 3.1). These modules were characterised in the test-beam. The modules were put in the cold box. Only the upstream arm of the telescope was used for the tracking. The sensors were biased up to a bias voltage of 800 V. The online threshold of the modules was tuned in the range of 1100 electrons to 1300 electrons. To study resolution as a function of angle of incidence, the cold box was rotated up to a turn angle of 15° . Turning to higher angles was not possible due to mechanical constraints.

In the following, the hit efficiency, spatial resolution, and cluster size for the irradiated modules are presented. In the analysis, the selection cuts explained in Section 6.5 are applied to reconstruct these quantities.

Hit Efficiency

The hit efficiency of the irradiated modules as a function of the bias voltage is shown in Fig. 6.29. All the measurements shown in Fig. 6.29 were taken at vertical incidence. The

irradiated modules up to the fluences of $1.2 \times 10^{16} \text{ cm}^{-2}$, except the one with the bias dot, reach 0.99 hit efficiency at a bias voltage below 800 V. The irradiated module at the highest fluence, $2.0 \times 10^{16} \text{ cm}^{-2}$ reach 0.985 hit efficiency at the bias voltage of 800 V.

It should be noted that the requirements for hit efficiency depend on the irradiation fluence: 0.99 hit efficiency for fluences up to $0.5 \times 10^{16} \text{ cm}^{-2}$ and 0.98 hit efficiency for fluences up to $1.0 \times 10^{16} \text{ cm}^{-2}$ (see Table 2.2). Therefore, all investigated modules, except the one with bias-dot, fulfills the requirements for the Phase-2 upgrade of IT of the CMS detector.

The voltage needed to reach 0.98 efficiency increases with the irradiation fluence. The reason can be understood with the results presented in Chapters 4 and 5 for pad diodes, where it was shown that the CCE of irradiated pad diodes is reduced after irradiation and increases by the bias voltage. The same happens to the pixel sensors after irradiation. Therefore, the sensor bias voltage has to be increased to have a charge above the threshold and detect a hit for irradiated sensors.

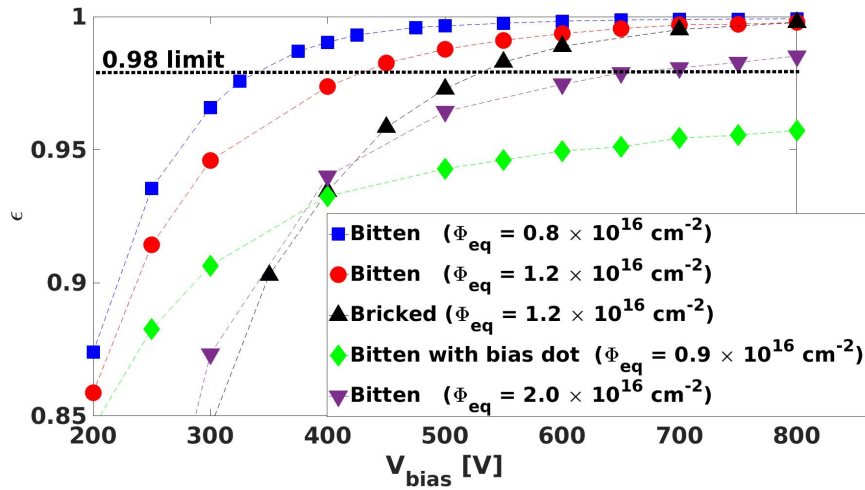


Figure 6.29: Hit efficiency of irradiated sensors as a function of bias voltage. All the sensors have a pitch size of $25 \times 100 \mu\text{m}^2$. The data were taken at vertical incidence.

For the sensor with the bias dot, the efficiency reaches 0.95 at the highest bias voltage. The loss of efficiency is due to the charge loss at the position of the bias dot. This can be seen in Fig. 6.30 which shows the in-pixel efficiency for two sensors with and without the bias dot. One sees that at the centre of the pixels, both sensors have a similar efficiency above 0.99. At the corners, however, the efficiency of the sensor with the bias dot drops to 0.8.

It is noted that the hit efficiency for the sensors with bitten and bricked designs at the similar fluence, $1.2 \times 10^{16} \text{ cm}^{-2}$, is different. This could be ascribed to the different online thresholds for two modules: 1250 ± 60 electrons and 1308 ± 70 electrons for sensors with the bitten and bricked designs, respectively.

As explained in Section 6.4.4, the pixels with high occupancy are masked during the

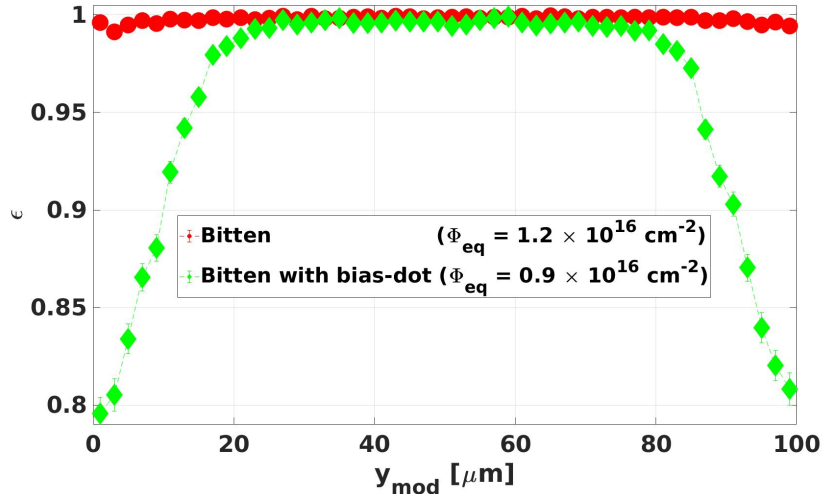


Figure 6.30: Hit efficiency as a function of in-pixel position for two sensors without the bias dot (red) and with the bias dot (green). The results are shown for the bias voltage of 800 V and vertical incidence. The bias dot is positioned at $y_{mod} = 0 \mu\text{m}$ and $y_{mod} = 100 \mu\text{m}$. Note that two sensors are irradiated to different fluences.

offline analysis. In Fig. 6.31, the number of masked pixels as a function of the bias voltage is shown for three irradiated sensors with the bitten designs. One sees the number of masked pixels increase with irradiation fluence. The number of masked pixels stays below 3% of the total number of pixels in the LFE. These pixels are not taken into account for the calculation of hit efficiencies shown in Fig. 6.29.

It should be noted that the number of noisy pixels shown in Fig. 6.31 is for the whole LFE which includes outside the fiducial region defined in Section 6.5.2. The purpose of this work is focused on the performance of the sensors after irradiation. The issue of noisy pixels in the RD53A readout chip after irradiation is still being investigated at the time of writing this thesis.

Spatial resolution

The spatial resolution of the irradiated modules was measured at various turn angles (θ_y). The distance between the DUT-to-telescope, dz_{DUT} , is taken from the alignment procedure. The telescope resolution at a given dz_{DUT} is calculated from the fit result shown in Fig. 6.18 for beam energy of 5.2 GeV. The calculated values for the telescope resolution are in the range of 10.5 μm to 11.1 μm and 6.8 μm to 8.2 μm for the bitten and bricked designs, respectively.

The results for spatial resolution as a function of turn scan for two irradiated modules are shown in Fig. 6.32. The results for the non-irradiated sensor with the bricked design are included for comparison. As mentioned in Section 6.4.2, there is a higher uncertainty on the values obtained for the resolution in the short axis, i.e. σ_{xDUT} , for irradiated modules since the telescope resolution is at the level of the expected resolution for DUTs

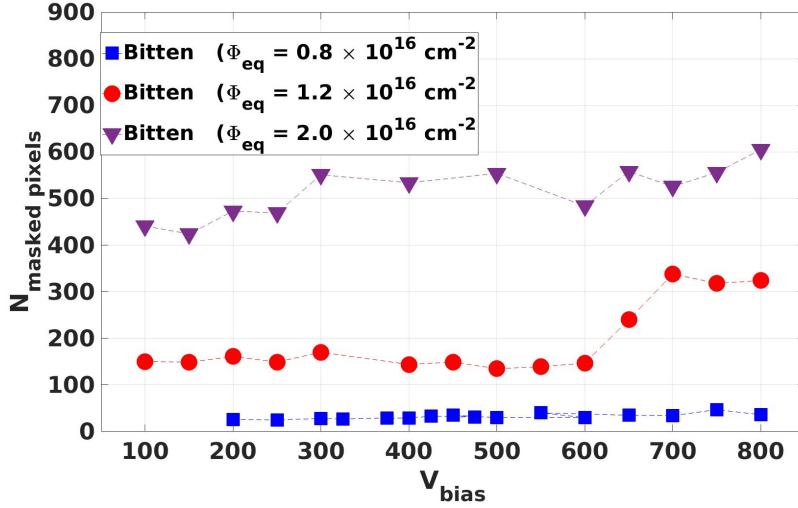


Figure 6.31: Number of masked pixels as a function of bias voltage for three irradiated sensors with the bitten designs and different irradiation fluences. The criteria for masking pixels are described in Section 6.4.4.

or even larger. From Fig. 6.32b one can see that the resolution of the two irradiated sensors in the short axis degrades compared to the non-irradiated module. The best resolution achieved for two irradiated sensors in the short axis, σ_{xDUT} is:

$$4.2 \pm 0.3 \mu\text{m} \quad \text{for sensor with bitten design} \quad (6.24)$$

$$4.9 \pm 0.2 \mu\text{m} \quad \text{for sensor with bricked design} \quad (6.25)$$

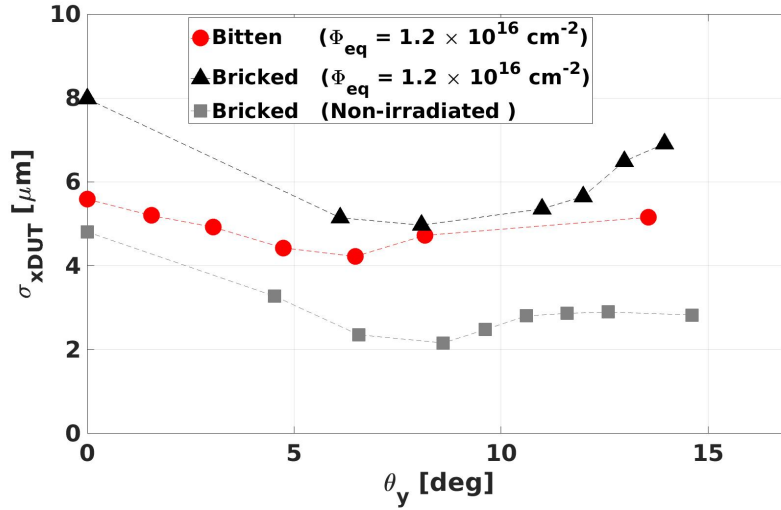
The error bars are calculated by assuming an error of $0.1 \mu\text{m}$ on the calculated telescope resolution. The resolution degradation after irradiation is expected: due to the bulk damage, the CCE of the irradiated sensors is reduced, and therefore the signal-to-noise ratio and the fraction of charge sharing between pixels or the cluster size decreases.

For the long axis, σ_{yDUT} does not change as a function of θ_y for the bitten design and stays at the level of $28.0 \mu\text{m}$ which is similar to the results of the non-irradiated sensor with the same design (Fig. 6.25b). For the irradiated sensor with the bricked design, the resolution in the long direction improves as a function of θ_y and reaches around $22.1 \mu\text{m}$ at an angle of 14° . Compared to the non-irradiated sensor, the resolution in this direction is approximately $10 \mu\text{m}$ worse.

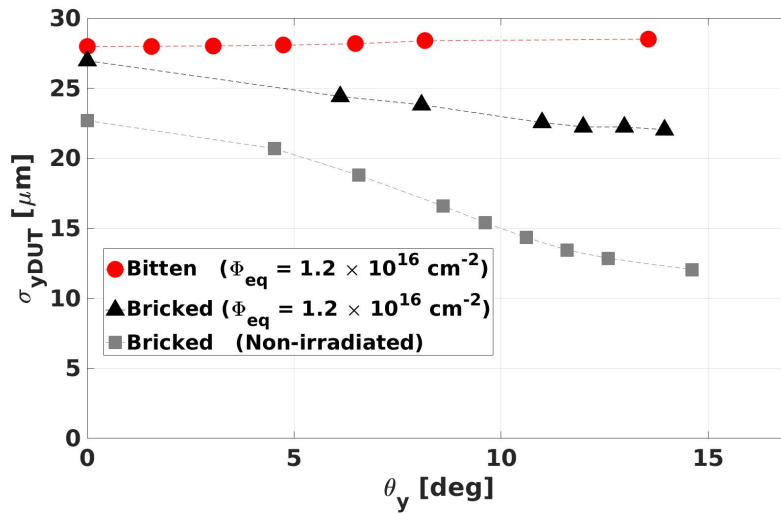
Cluster size

The projected cluster sizes give an insight into the physics of the charge sharing between pixels after irradiation. The mean projected cluster sizes in x - and y -directions for two irradiated sensors as a turn angle are shown in Fig. 6.33.

In the short axis (n_{row}), both sensors show a similar projected cluster size as a function of turn angle. Mean n_{row} for both irradiated sensors is reduced by $\approx 35\%$ compared to



(a)



(b)

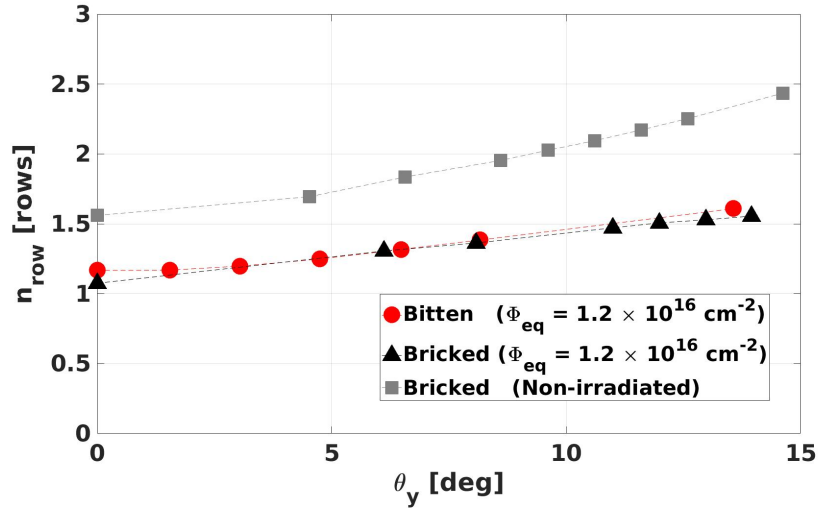
Figure 6.32: Resolution of two irradiated modules in short (a) and long (b) axes. Both irradiated sensors were biased at 800 V. For comparison, the results of a non-irradiated module with the bricked design is plotted.

the non-irradiated sensors and does not reach 2.

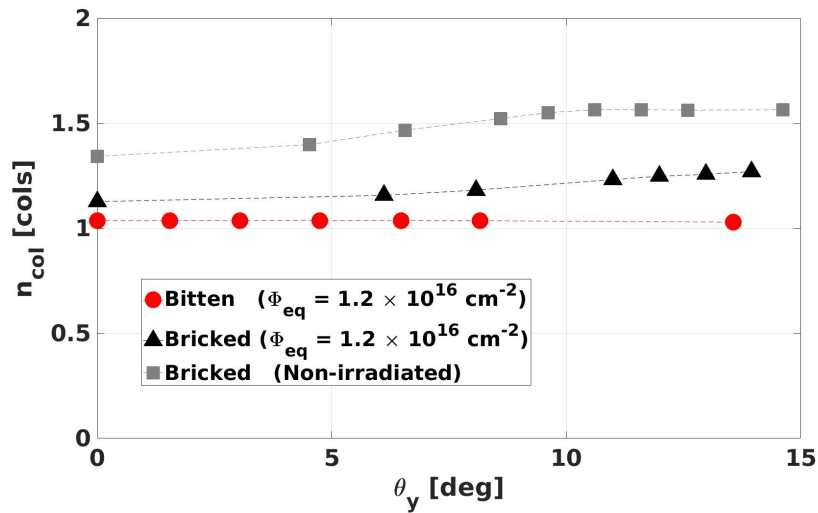
In the long axis (n_{col}), the cluster size of the sensor with the bitten design does not change as a function of θ_y and stays at a level of 1.03, which is similar to the results of the non-irradiated sensors with a similar design (Fig. 6.27b). For the bricked design, mean n_{col} increases to 1.27 at the turn angle of 14° . Compared to the non-irradiated sensor with the bricked design, n_{col} is reduced by 23%.

6.7 Summary and Conclusion

In this chapter, an overview of the test-beam characterisation of the planar pixel modules designed for the IT of the CMS experiment is presented. In this chapter's final section,



(a)



(b)

Figure 6.33: Mean projected cluster size in x (a) and y (b) directions as a function of turn angle (θ_y) for two irradiated sensors. For comparison, also the results of a non-irradiated module with the bricked design is plotted.

the test-beam characterisation results of four non-irradiated and five proton-irradiated modules are presented. The following conclusion is drawn from the measurements of the non-irradiated sensors:

- Four investigated sensors reach hit efficiency of 0.99 at a bias voltage of 30 V. The sensors are tested up to a bias voltage of 400 V without any signs of a breakdown.
- The hit efficiency of the sensor with bias dot slightly decreases for bias voltages above 120 V. The efficiency loss is due to the charge loss at the bias dot. The charge loss becomes more prominent at higher bias voltage due to the reduced diffusion of charge carriers.
- For the three sensors with a pixel size of $25 \times 100 \mu\text{m}^2$, the best spatial resolution

of $2.15 \pm 0.05 \mu\text{m}$ is achieved at the optimal angle of 9.4° . At this angle, the mean projected cluster size reaches 2 for all three sensors.

- For the sensor with the pixel size of $50 \times 50 \mu\text{m}^2$, the best spatial resolution of $3.56 \pm 0.03 \mu\text{m}$ is achieved at the optimal angle of 18.8° . The mean projected cluster size reaches two at this angle.
- For the sensor with the bricked design, the spatial resolution in the long direction improves as a function of turn angle and reaches $11.70 \pm 0.02 \mu\text{m}$ at a turn angle of 15° . This value is at the level of expected resolution for binary readout and a pitch size of $50 \mu\text{m}$ ($\frac{50 \mu\text{m}}{\sqrt{12}}$).

The following conclusion is drawn from the measurements of proton irradiated sensors:

- All sensors, except the sensor with the bias dot, reach 0.98 hit efficiency at a bias voltage below 800 V at vertical incidence. The voltage needed to reach the hit efficiency of 0.98 increases with the irradiation fluence. For the sensor with a bias dot, the hit efficiency only reaches 0.95 at the bias voltage of 800 V. The charge loss at the position of the bias dot is the main reason for the inefficiency.
- In the $25 \mu\text{m}$ direction, the spatial resolution of irradiated sensors is degraded by more than $2 \mu\text{m}$. The mean projected cluster size is reduced by $\approx 35\%$ and does not reach two.
- In the $100 \mu\text{m}$ direction, the spatial resolution of the irradiated sensor with the bitten design is $28.0 \mu\text{m}$ which is similar to the value obtained for the non-irradiated sensor. In the same direction, the spatial resolution of the irradiated sensor with the bricked design improves as a function of turn angle and reaches $22.1 \mu\text{m}$ at a turn angle of 14° . Compared to the non-irradiated sensor, the improvement is $10 \mu\text{m}$ less which is because of reeducation of the charge sharing between pixels after irradiation.

It is found that the number of noisy pixels in the readout chip after irradiation is correlated to the radiation fluence and reaches 3% of the total number of pixels in LFE. These pixels are masked during the analysis and not considered for calculating the hit efficiency. The issue of the noisy pixels in the readout chip is still under investigation at the time of writing this thesis.

In general, the presented results in this chapter show the planar pixel sensor is qualified for the Phase-2 upgrade of the CMS IT, based on the hit efficiency requirements defined in Table 2.2. The sensor with the bias dot show inefficiency of 5% even at the highest bias voltage and should be discarded. For the final decision on the sensor type, one should consider other factors such as power dissipation, yield production, and leakage current.

Other detectors at LHC will undergo an upgrade for the HL-LHC phase, as well. In LHCb, the Phase-2 upgrade is scheduled for 2030 in the LS4. The integrated luminosity

for this detector is expected to reach 300fb^{-1} by the end of HL-LHC phase, and the estimated pile-up is around 50. This luminosity leads to a maximum 1 MeV neutron-equivalent fluence of $3 \times 10^{15}\text{cm}^{-2}$ at the innermost edge of the silicon sensors. For the Phase-2 upgrade, the tracker of LHCb will use a mixed technology of scintillating fibres in the outer region and strip sensors in the inner region to cope with the radiation damage effects in fibres [107].

The expected integrated luminosity in ATLAS experiment is close to projection for the CMS detector, i.e. 4000fb^{-1} . The tracking system of the ATLAS detector includes pixel sensors and strip sensors in inner and outer trackers, similar to CMS. In ATLAS, there are five layers of pixel sensors in BPIX. For layer 0, ATLAS has decided to use 3D sensors with an active thickness of $150\mu\text{m}$. Planar sensors with active thickness of $100\mu\text{m}$ and $150\mu\text{m}$ are considered for layer 1 and layers 2 to 4, respectively.

Layers 0 and 1 are scheduled to be replaced after integrated luminosity of 2000fb^{-1} . For this luminosity, the expected 1 MeV neutron-equivalent fluences in layers 0 and 1 are $1.3 \times 10^{16}\text{cm}^{-2}$ and $3.8 \times 10^{15}\text{cm}^{-2}$, respectively [108]. For layer 0, 3D irradiated sensors at the fluence of $1 \times 10^{16}\text{cm}^{-2}$ have achieved a hit efficiency of 0.98 at bias voltage below 150 V [109]. For layer 1, irradiated planar sensors at the fluence of $5 \times 10^{15}\text{cm}^{-2}$ have reached hit efficiency of 0.98 [110].

7 Study of Cross-Talk with Charge Injection

7.1 Introduction

The RD53A chip has a non-staggered bump-bond pattern. Therefore, the opening of the passivation of a sensor pixel is not directly above its implant and routing is needed (see Fig. 7.1a). This increases a cross-talk between the two pixels in adjacent rows and can bias the hit position reconstruction in the sensor. It is important to quantify this effect and take it into account when the hit is reconstructed.

Every pixel in the RD53A chip is equipped with a charge injector circuit. One can use this circuit to inject a certain amount of charge to the pixel and read its occupancy. By measuring the occupancy as a function of injected charge, one estimates the cross-talk. This method measures the cross-talk due to the capacitive coupling between neighbouring pixels. In this chapter, the results of the cross-talk study for three different sensor designs are presented.

List of own contributions

- Preparation of modules for data taking in lab
- Performing cross-talk measurements on three modules
- Analysis of the data and extraction of occupancy as a function of injected charge
- Calculation of cross-talk from occupancy measurements

The scripts for measurement routines including tuning and charge injection were found in [111].

7.2 Sensor Designs

Fig. 7.1 shows the pixel cell of three designs which were studied for the cross-talk. The design with the non-bitten implant (Fig. 7.1a) was produced in the 2017 submission. After observing the issue of cross-talk, the implant was chipped away at the region close to the passivation opening in the new submission. The modules studied in this section are non-irradiated. The specification of the sensors can be found in Section 3.4.1.

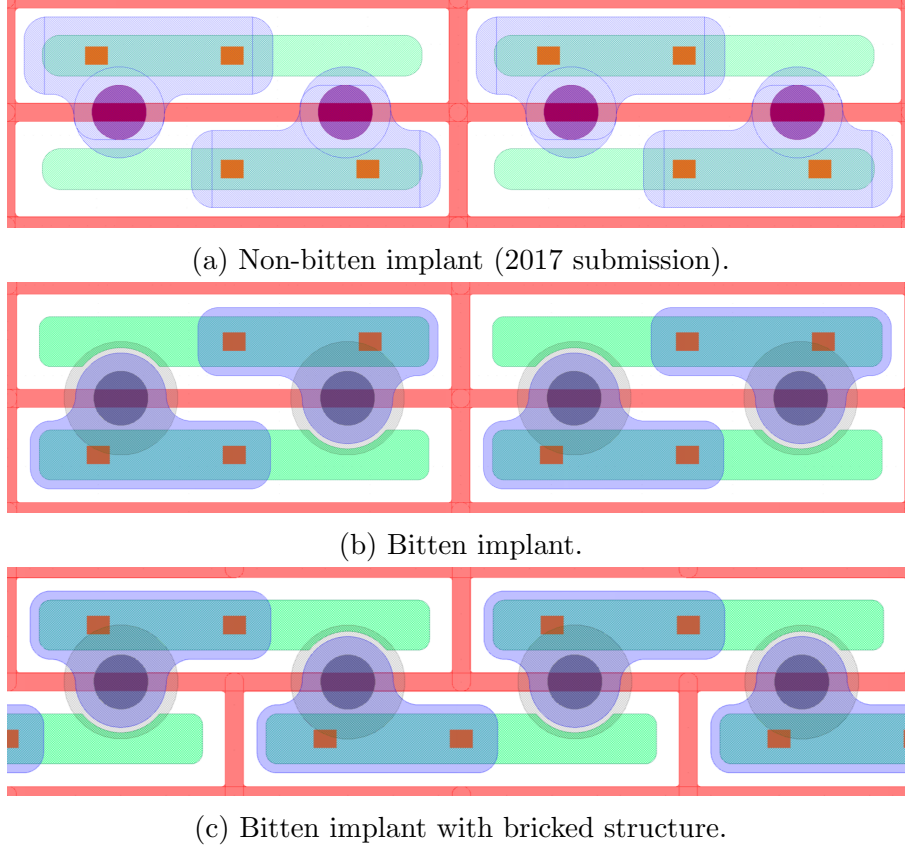


Figure 7.1: Pixel cell designs for cross-talk study. The mapping of the pixels in for the bitten implant (b) is mirrored with respect to the non-bitten pixel (a).

7.3 Definition of Cross-Talk

The cross-talk effect studied in this chapter is related to the capacitive coupling between pixels readout after generation of the charge in the pixel. This is the difference with the physical charge sharing between pixel due to the charge diffusion or track angle.

In Fig. 7.2a, a sketch of the pixel matrix for a planar sensor with the pitch size of $25 \times 100 \mu\text{m}^2$ with a non-bricked design is shown. In this sketch, the coordinates of the pixels in the sensor and the readout chip are shown in blue and yellow, respectively. Due to the coupling, there is a cross-talk between pixels in the same row of the readout chip. In terms of the pixel coordinates, the cross-talk effect is between following pairs of pixels: $[(0, 0), (1, 0)]$, $[(2, 0), (3, 0)]$, $[(0, 1), (1, 1)]$, $[(2, 1), (3, 1)]$, and etc.

In the case of the pixel pair in the first row, the cross-talk is defined as a fraction of charge produced in the pixel at the coordinate of $(0, 0)$ transferred to the pixel at the coordinates of $(1, 0)$ and vice versa. If $Q_{0,0}^i$ and $Q_{1,0}^i$ are the injected charge to the pixels at the coordinates of $(0, 0)$ and $(1, 0)$, the measured charge in the pixels is calculated as:

$$\begin{bmatrix} Q_{0,0}^m \\ Q_{1,0}^m \end{bmatrix} = \begin{bmatrix} 1 - XT & XT \\ XT & 1 - XT \end{bmatrix} \times \begin{bmatrix} Q_{0,0}^i \\ Q_{1,0}^i \end{bmatrix}$$

$Q_{0,0}^m$ and $Q_{1,0}^m$ are the measured charges by pixels at coordinates of $(0, 0)$ and $(1, 0)$,

7 Study of Cross-Talk with Charge Injection

respectively. XT , as defined above, is the fraction of the charge which is transferred to the neighbouring pixel due to the cross-talk effect.

For the sensor with the bricked design, Fig. 7.2b, the cross-talk is between three pixels. In this sensor, the cross-talk effect is between following group of pixels: $[(0, 0), (1, 0), (1, 1)]$, $[(0, 1), (1, 1), (1, 2)]$, $[(2, 0), (3, 0), (3, 1)]$, $[(3, 1), (2, 0), (2, 1)]$ and etc.

To measure the cross-talk, the charge injection method was used as explained in Section 7.5.

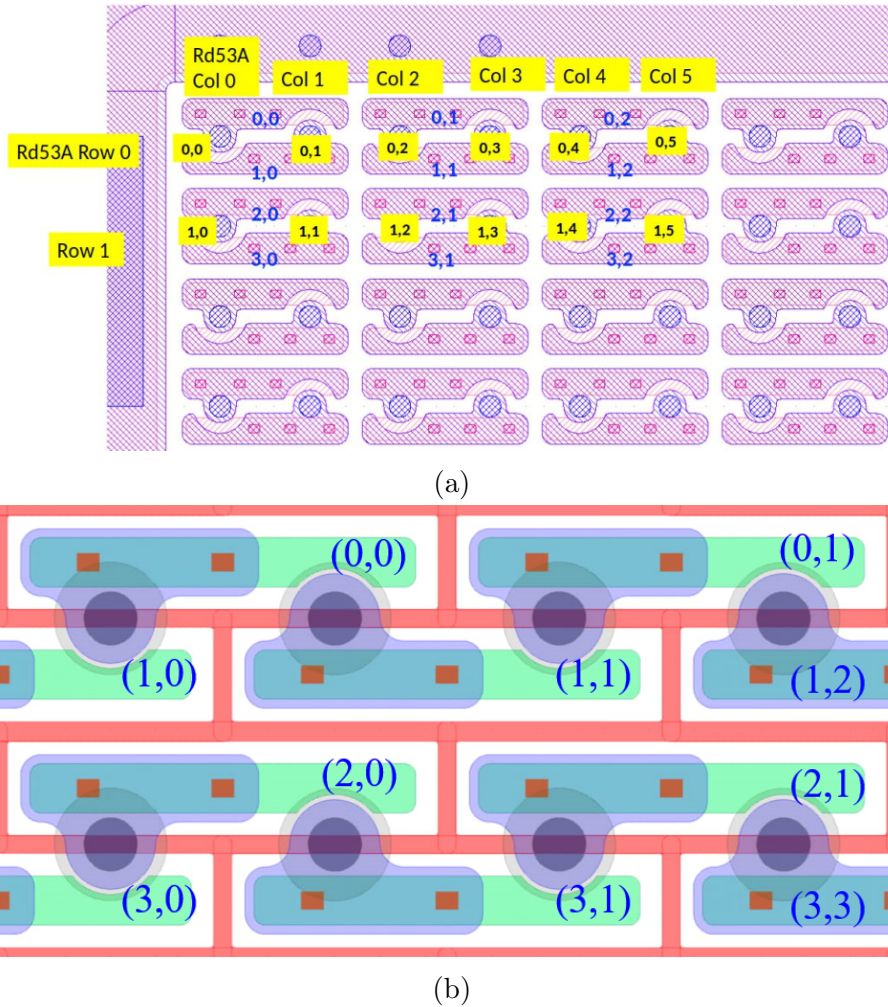


Figure 7.2: Pixel matrix for a planar sensor with the pitch size of $25 \times 100 \mu\text{m}^2$ with the non-bricked (a) and bricked (b) designs.

7.4 Tuning of ROC

The first step of the measurement is tuning the RD53A chip for three modules. The chosen values for DAC registers are presented in Table 6.1. The sensor bias was set at 120 V and the data was taken at room temperature. The charge was injected in the range of $0 \Delta V_{\text{cal}}$ to $200 \Delta V_{\text{cal}}$ with steps of $10 \Delta V_{\text{cal}}$ in each pixel. For each step, the charge is injected 100 times into the pixel and the occupancy is read. Occupancy is defined as

the number of detected hits in the chip per injection per pixel. Since the injection is 100 times, one expects occupancy of 100 in the chip when the injected charge is above the threshold of the pixel.

Using the value of $V_{\text{threshold-LIN}}$, all three modules were tuned at a threshold around $105 \Delta\text{Vcal}$. Fig. 7.3a shows the average S-curve of all pixels in the LFE for three modules. S-curve of each pixel was fitted with Eq. (6.2). The distribution of extracted μ^{50} -value from the fit is shown in Fig. 7.3b. The mean value of μ -distribution for three modules are:

$$\begin{aligned}\bar{\mu}_{\text{non-bitten}}^{50} &= 103.70 \pm 0.04 \Delta\text{Vcal} \\ \bar{\mu}_{\text{bitten}}^{50} &= 107.00 \pm 0.03 \Delta\text{Vcal} \\ \bar{\mu}_{\text{bricked}}^{50} &= 104.80 \pm 0.04 \Delta\text{Vcal}\end{aligned}$$

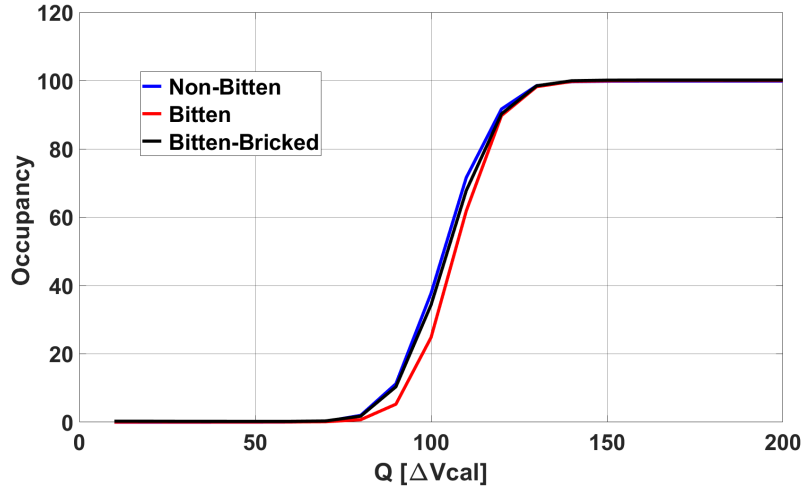
The quoted error is the standard deviation of the distribution divided to the square root of number of pixels ($\sigma/\sqrt{n_{\text{pixels}}}$). These values show three modules have a similar threshold within $\pm 2 \Delta\text{Vcal}$ units.

7.5 Cross-talk Measurement Results

To study the cross-talk, the occupancy of the chip was measured as a function of injected charge in the pixel, Q . The measurements were done at the same condition explained in Section 7.4. The charge was injected in the range of $0 \Delta\text{Vcal}$ to $3000 \Delta\text{Vcal}$ with steps of $20 \Delta\text{Vcal}$. At high values of Q , the occupancy reaches 200 or 300. This means that with 1 charge injection into a pixel, 2 or 3 hits are detected. The extra 1 or 2 hits are due to the cross-talk. Fig. 7.4 shows the S-curve of all pixels for three modules. From these plots, the following observations are made:

- For non-bitten and bitten designs, the occupancy increases from 100 to 200 by increasing Q .
- For the bricked design, occupancy of most pixels increases from 100 to 300 by increasing Q . The maximum occupancy of a fraction of pixels stays at 200 even at high values of Q .

The occupancy of 200 for the bitten and non-bitten designs is due to the cross-talk between two rows of pixels, as explained in Section 7.3. For the bricked design, the occupancy increases to 300 because there is a cross-talk between three pixels in this design. The maximum occupancy of 380 pixels in the bricked design stays at 200. These pixels correspond to the first and last rows ($\approx 2 \times 192$) of the LFE where there is a cross-talk between two pixels due to the shape of the chip matrix.



(a) Average S-curve of all pixels in the LFE for three modules.

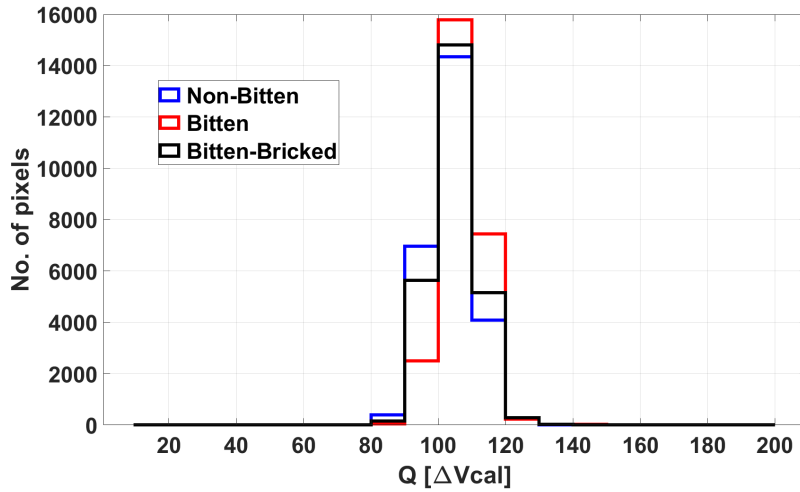

 (b) Distribution of extracted μ -value from the fit.

Figure 7.3: Results of the threshold tuning for three modules.

7.6 Analysis of Data

The first step to extracting the cross-talk from S-curve is to fit the data with the following function:

$$F(Q) = \begin{cases} A \cdot \operatorname{erf}\left(\frac{Q-\mu_{150}}{\sqrt{2}\cdot\sigma}\right) + 150 & \text{if } F(Q)_{max} = 200 \pm 10 \\ A \cdot \operatorname{erf}\left(\frac{Q-\mu_{200}}{\sqrt{2}\cdot\sigma}\right) + 200 & \text{if } F(Q)_{max} = 300 \pm 10 \end{cases} \quad (7.1)$$

In Eq. (7.1), μ_{150} and μ_{200} correspond to the charge where the occupancy reaches 150 and 200, respectively. The fit is done in the range where occupancy is 100 to 200 for the non-bitten and the bitten designs and 200 to 300 for the bricked design. The distribution of extracted μ_{150} and μ_{250} values from the fit is shown in Fig. 7.5. The mean value of the

distribution for three modules is:

$$\begin{aligned}\bar{\mu}_{non-bitten}^{150} &= 721.3 \pm 0.4 \Delta\text{Vcal} \\ \bar{\mu}_{bitten}^{150} &= 1347.5 \pm 0.9 \Delta\text{Vcal} \\ \bar{\mu}_{bricked}^{200} &= 1702.6 \pm 0.7 \Delta\text{Vcal}\end{aligned}$$

For the bricked design, the fit is done separately for the first and last rows with $F(Q)_{max} = 200 \pm 10$ and the rest of rows with $F(Q)_{max} = 300 \pm 10$ and only the latter is shown in Fig. 7.5. To estimate cross-talk, the following relationship is used:

$$\overline{XT} = \begin{cases} \frac{r}{r+1}, & r = \frac{\bar{\mu}_{50}}{\bar{\mu}_{150}}, \text{ if } F(Q)_{max} = 200 \pm 10 \\ \frac{r}{2r+1}, & r = \frac{\bar{\mu}_{50}}{\bar{\mu}_{200}}, \text{ if } F(Q)_{max} = 300 \pm 10 \end{cases} \quad (7.2)$$

The average cross-talk in three designs are as follows:

$$\begin{aligned}\overline{XT}_{non-bitten} &= 0.125 \\ \overline{XT}_{bitten} &= 0.073 \\ \overline{XT}_{bricked} &= 0.055\end{aligned}$$

From these results, one sees that the cross-talk is reduced significantly in the module with the bitten implant compared to the non-bitten. For the bricked design, the cross-talk is "redistributed" between two pixels instead.

To understand the effect of cross-talk in the first and last rows (edge pixels) of the bricked designs, S-curve of those pixels are fitted with Eq. (7.1) with $F(Q)_{max} = 200$. Fig. 7.6 shows extracted μ -values for all pixels in the bricked module. From this plot, one reads:

$$\begin{aligned}\bar{\mu}_{bricked}^{200} &= 1702.6 \pm 0.7 \Delta\text{Vcal} \\ \bar{\mu}_{bricked}^{150} &= 1704.9 \pm 7.8 \Delta\text{Vcal}\end{aligned}$$

Using Eq. (7.2), the average cross-talk for the central and edge pixels is 0.055 and 0.058, respectively. The difference between cross-talk for pixels in the edge and central parts of the matrix is small.

7.7 Summary

Because of the non-staggered bump-bond pattern in the RD53A chip, the opening for passivation of a sensor pixel is not directly above its implant and routing is required. This routing increases the cross-talk between two pixels in adjacent rows. Cross-talk biases the hit reconstruction in the sensor and deteriorates the spatial resolution. Therefore, this

effect should be quantified and taken into account when the hit is reconstructed.

The standard procedure for the characterisation of the cross-talk is done by measuring the occupancy as a function of the injected charge. Due to the cross-talk, the occupancy of the chip reaches 200 or 300. The ratio between the threshold of the module and the mean charge required for occupancy of 150 or 200 corresponds to the cross-talk.

In this chapter, the results of cross-talk characterisation for three non-irradiated HPK planar sensors were shown. For the standard (non-bricked) modules, a relatively large cross-talk of 0.125 was observed. It was found that by chipping away the implant in the region close to the passivation opening (bitten-implant design), cross-talk is reduced to 0.073. For the bricked module, a cross-talk between three pixels was observed for the pixel in the central part of the matrix but the overall cross-talk has been reduced to 0.055.

To obtain the spatial resolution of the sensors presented in Chapter 6, the effect of cross-talk on the reconstruction of hit position was not taken into account. The correction can be done by inverting the cross-talk matrix in Section 7.3 and calculating the injected charge, for sensors with non-bricked designs.

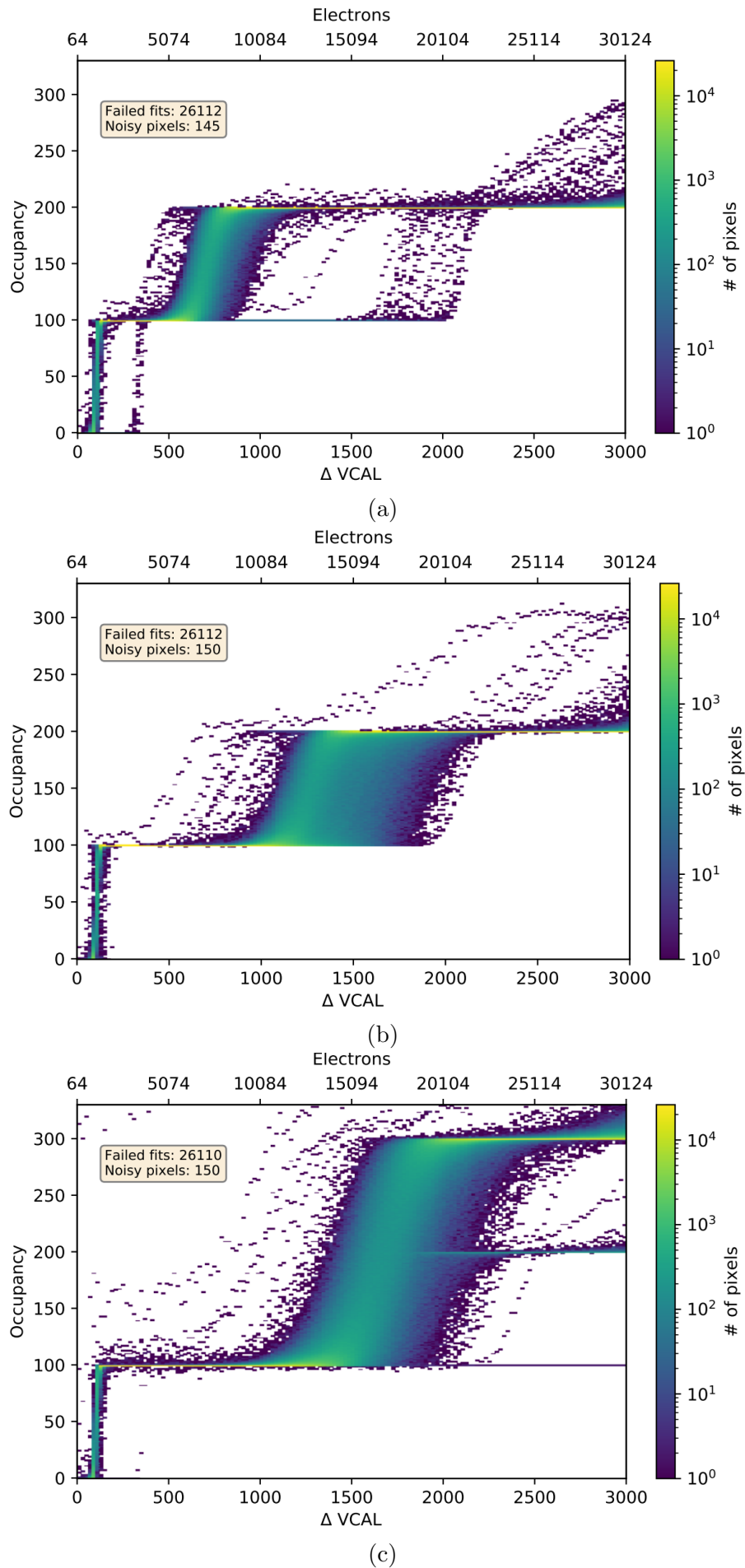


Figure 7.4: S-curve of pixels for non-bitten (a), bitten (b), and bricked (c) designs.

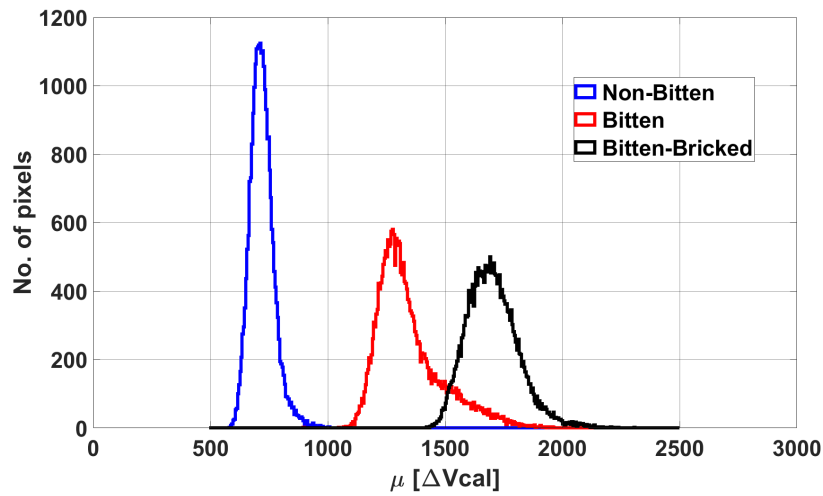


Figure 7.5: Distribution of extracted μ_{150} and μ_{200} values from the fit using Eq. (7.1). For the bricked design, the results for pixels with maximum occupancy of 300 ± 10 , i.e. μ^{200} are shown.

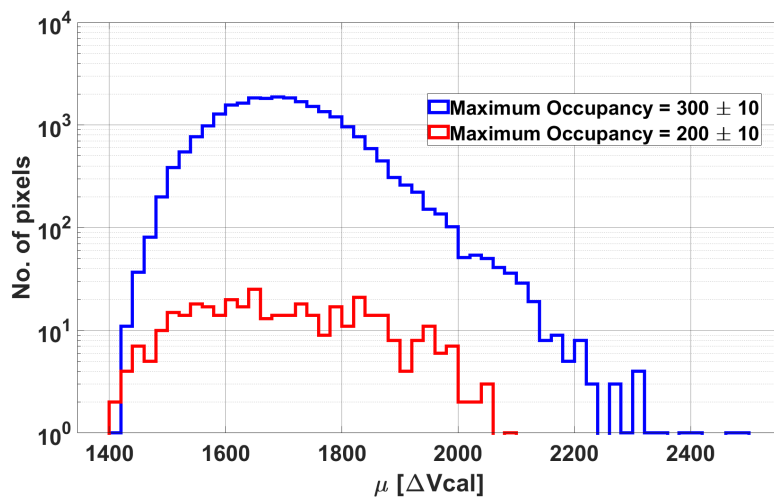


Figure 7.6: Distribution of extracted μ -values for central (blue) and edge (red) pixels in the bricked design.

8 Summary and Conclusion

For the HL-LHC phase, the CMS detector will undergo a major upgrade. The IT of the CMS detector is made up multiple layers of silicon pixel sensors. The current tracker will be replaced entirely for the HL-LHC phase to cope with the high track density and radiation fluence. The focus of this thesis is understanding the charge collection in irradiated silicon sensors and characterisation of hybrid planar sensor designed for the Phase-2 upgrade of the IT.

In the first part of this thesis, pad diodes are characterised in the TCT lab and test-beam. In Chapter 4, the results of TCT measurements using alpha-particles and red-light are presented for two irradiated diodes. CCE measured by alpha-particles shows higher values than red-light laser for both diodes. The difference decreases at lower energies of alpha-particles. An empirical model is developed to understand these results, which assumes a non-active region with a reduced CCE close to the implant. Applying the model to experimental results reveals a non-active region with a width of $\approx 2.5 \mu\text{m}$ at the n^+ implant. The calculated CCE in this region is significantly lower than the CCE in the bulk region. Not taking into account the effect of the non-active region results in too low values for estimated CCE, hence, the lifetimes of holes for investigated diodes in this work. To estimate the trapping times of electrons and holes, additional information about the electric field profile is required which was not studied in this work. The impact of having a $2.5 \mu\text{m}$ non-active region is significant for radiation with short absorption length in silicon, such as alpha particles and red light. However, the effect becomes much smaller when the illumination source is a MIP, and the charge is deposited uniformly at the $150 \mu\text{m}$ of the bulk region.

In Chapter 5, an edge-on method using an electron beam for characterising pad diodes is introduced. The technique requires an in-situ alignment procedure to find the minimal angle between the diode surface and the electron beam. This procedure is presented. The charge collection profile of pad diodes as a function of depth is measured. For non-irradiated diodes, the profile is uniform in the central region of the diodes with a value similar to the simulation result. For irradiated diodes, the shape of profiles depends on the irradiation fluence and the bias voltage. The procedure to compare the results of measurements with radiation damage models is described and shown for three models. By taking into account the beam resolution and ionisation profile, the measured collected charge profiles are unfolded to obtain the CCE profiles of irradiated and non-irradiated diodes. At the highest fluence, i.e. $12 \times 10^{15} \text{cm}^{-2}$, the CCE profile is uniform around

the value of 0.5 at the bias voltage of 800 V. These CCE profiles are independent of the experimental conditions and can directly be used for tuning radiation damage models.

The second part of the thesis is on the characterisation of planar pixel sensors in the test-beam and the lab. In Chapter 6, the results of the test-beam characterisation of pixel sensors, including hit efficiency, spatial resolution, and cluster size, are presented. The results are shown as a function of the sensor bias voltage and beam incidence angle for non-irradiated and proton-irradiated sensors. Non-irradiated sensors are fully efficient (> 0.99) for bias voltages above 30 V and tested without a break-down up to 400 V. The spatial resolution of the non-irradiated sensors with pitch sizes of 25 μm and 50 μm reach 2.2 μm and 3.6 μm , respectively at the optimal angle where the average cluster size is 2. The sensor with the bricked design shows a better resolution than the ones with the regular design in the 100 μm direction. In this direction, the resolution reaches 11.7 μm for the sensor with the bricked design, which is better than the sensor with the regular design by a factor of 2.3.

After irradiation, higher bias voltages are required to reach the efficiency benchmark of 0.98. All investigated modules, except the one with the bias-dot, meet the hit efficiency requirements for the Phase-2 upgrade IT of the CMS detector. The bias voltage needed to reach the hit efficiency of 0.98 increases as a function of irradiation fluence. The spatial resolution of irradiated modules is degraded. This degradation is due to the trapping effects in irradiated sensors, which reduce the charge sharing between neighbouring pixels and hence, the cluster size. Nevertheless, for the irradiated sensor with bricked design, the resolution in the 100 μm direction is still better than the sensor with the regular design.

In Chapter 7, the result of the cross-talk characterisation for sensors with three different designs is presented. It is found that chipping away a part of the sensor implant close to the bump bond connection reduces the cross-talk between two pixels significantly.

In conclusion, the planar pixel sensors are qualified for the Phase-2 upgrade of the IT in CMS detector. The investigated hybrid modules in this work meet the hit efficiency requirements for layers 1 and 2. For the final decision on the sensor type, other considerations such as power dissipation, leakage current, and production yield of the sensors should be taken into account.

List of Figures

2.1	Different types of material	5
2.2	p-n junction	7
2.3	Energy loss in silicon	9
2.4	Signal formation in pad diode	10
2.5	Weighting potentials for different sensors	11
2.6	Hybrid pixel sensor	12
2.7	Vacancy distribution	14
2.8	Damage function	15
2.9	CMS detector	17
2.10	Fluence map	18
2.11	Phase-2 upgrade of inner tracker	18
3.1	DESYII test-beam	21
3.2	DATURA telescope	22
3.3	Telescope resolution	22
3.4	TLU front panel	23
3.5	Trigger for edge-on measurements	24
3.6	RD53A chip	27
3.7	LFE schematic	27
3.8	SCC connection to BDAQ53	28
3.9	Sketch of test-beam setup for pixel sensors	28
3.10	Photo of test-beam setup for pixel sensors	29
3.11	Cabling diagram in test-beam for pixel sensors	29
3.12	Sketch of test-beam setup for diodes	30
3.13	Photo of test-beam setup for diodes	30
3.14	Time difference between TLU and oscilloscope	31
3.15	Cabling diagram in test-beam for diodes	31
3.16	Spacers between diode and PCB	32
3.17	Sensor prototype design	33
3.18	Pixel sensor designs	34
3.19	Different layers in pad diodes	36
3.20	Top view of pad diodes	37
4.1	TCT setup	41

List of Figures

4.2	Pulse shape of pad diodes	42
4.3	Results of position scans	43
4.4	Charge as a function distance	46
4.5	Bias scan results for non-irradiated diode	47
4.6	CCE results as a function of bias	48
4.7	Stopping power of alpha particles and attenuation of red-light in silicon . .	49
4.8	Model with inactive layer	50
4.9	Comparison between model and data	52
4.10	Results of model	53
5.1	Edge-on measurements with diodes	56
5.2	Average transient of diode	57
5.3	Angle scan measurement	59
5.4	Charge as a function of angle	60
5.5	Peak to tail ratio as a function of angle	61
5.6	Alignment of diode in x and y directions	62
5.7	Charge profiles for two beam energies	63
5.8	Energy deposition profile	64
5.9	Charge distributions at two depths	64
5.10	Charge collection profiles of non-irradiated diodes	65
5.11	Charge collection profile as a function of width	66
5.12	Charge collection profiles at different bias voltages	67
5.13	Comparison between GEANT4 simulation and data	68
5.14	Charge collection profiles of irradiated diodes	69
5.15	CCE as a function of bias voltage	70
5.16	Simulated CCE profile using HPTM	72
5.17	Comparison between measured and simulated charge collection profiles . .	73
5.18	Comparison between measured and simulated CCE	74
5.19	Comparison between measured and simulated CCE using IR	75
5.20	Comparison between measured and simulated charge collection profile . . .	76
5.21	Comparison between data and fit	78
5.22	CCE profile as a function of depth	79
5.23	Difference between data and fit	80
6.1	Single Chip Card	82
6.2	Occupancy as a function of injected charge	84
6.3	S-curve of all pixels in LFE	85
6.4	Charge injection results for all pixels in LFE	86
6.5	Flowchart of threshold tuning	87
6.6	Different Krummenacher settings	88
6.7	Different LDAC-LIN settings	89

6.8	Results of a digital scan	90
6.9	Correlation between DUT and telescope	91
6.10	Different cluster shapes	92
6.11	Selection of correct triplets	93
6.12	Telescope residuals with and without cold box	94
6.13	Alignment of DUT	96
6.14	Hit efficiency as a function of r_{min}	97
6.15	DUT residual distributions	99
6.16	DUT and telescope residual distributions	101
6.17	DUT residual distributions at different dz_{DUT}	101
6.18	Estimated telescope resolution as a function of dz_{DUT}	102
6.19	Occupancy distribution of all pixels in LFE	103
6.20	BCID distributions	106
6.21	Cluster charge distributions for different angles of incidence	107
6.22	Pair finding algorithm	108
6.23	Hit efficiency as a function of bias voltage	109
6.24	In-pixel hit efficiency	109
6.25	Spatial resolution of non-irradiated modules as a function of turn angle	111
6.26	DUT residual distributions for bricked and non-bricked designs	112
6.27	Projected cluster size of non-irradiated modules as a function of turn angle	113
6.28	Cluster size map of non-irradiated modules	114
6.29	Hit efficiency of irradiated modules as a function of bias voltage	115
6.30	In-pixel hit efficiency of irradiated module	116
6.31	Number of noisy pixels as a function of bias voltage	117
6.32	Spatial resolution of irradiated modules as a function of turn angle	118
6.33	Projected cluster size of irradiated modules as a function of turn angle	119
7.1	Pixel sensor designs	123
7.2	Pixel matrix for bricked and non-bricked designs	124
7.3	Results of the threshold tuning for three modules.	126
7.4	S-curves of all pixels in LFE for different designs	129
7.5	Distribution of μ_{150} and μ_{200} values	130
7.6	Distribution of μ_{150} and μ_{200} values in bricked design	130

List of Tables

2.1	Defect parameters	16
2.2	Requirements of pixel sensors designed for Phase-2 upgrade of CMS IT . . .	19
3.1	List of modules studied in this work	35
3.2	Thickness of different layers in pad diode	36
5.1	Parameters of HPTM	71
6.1	DAC settings	88
.1	Measured and calculated CCE values in n^+p -side	148
.2	Measured and calculated CCE values in p^+p -side	148
.3	CCE_{x_i} profiles of irradiated and non-irradiated diodes.	149

Acronyms

ALICE A Large Ion Collider Experiment. 15

ATLAS A Toroidal LHC ApparatuS. 15, 121

BCID Bunch Crossing ID. 91, 105, 106

BPIX Barrel Pixel Detector. 17, 19, 121

CCE Charge Collection Efficiency. 2, 39, 40, 45, 48–51, 53–55, 68–72, 74–79, 115, 117, 131, 132

CMS Compact Muon Solenoid. 1–4, 15–19, 25, 26, 81, 103, 115, 118, 120, 121, 131, 132

CoG Centre of Gravity. 92, 106, 109

CROC CMS Readout Chip. 32

DAC Digital-to-Analog Converters. 81, 82, 87, 88, 124

DESY Deutsches Elektronen-SYnchrotron. 20, 21, 25, 57, 81, 104

DLTS Deep Level Transition Spectroscopy. 14, 16

DTB Digital Test Board. 25

DUT Device Under Test. 21–23, 25, 28, 30, 31, 42, 54, 59–63, 78, 81, 85, 89–91, 93–107, 109, 110, 112, 116

FDB Flotzone Direct Bonded. 32

FDD Flotzone Deep Diffused. 32, 33

FPGA Field Programmable Gate Array. 27

FPIX Forward Pixel Detector. 17, 18

FTH Flotzone THinned. 32

HL-LHC High-Luminosity LHC. 1, 2, 17, 120, 121, 131

Acronyms

- HPK** Hamamatsu Photonics K.K.. 32, 34, 35, 128
- HPTM** Hamburg Penta Trap Model. 69–74, 76, 78
- IR** Infra-Red. 2, 51, 54, 55, 69–71, 74, 75
- IT** Inner Tracker. 1–4, 13, 15, 17–19, 26, 81, 103, 115, 118, 120, 131, 132
- LFE** Linear Front End. 26, 27, 81, 84–86, 89, 90, 103, 104, 108, 116, 120, 125, 126
- LGAD** Low Gain Avalanche Diodes. 71
- LHC** Large Hadron Collider. 1, 15, 16, 120
- LHCb** Large Hadron Collider beauty. 15, 120, 121
- LS** Long Shutdown. 17, 120
- MAPS** Monolithic Active Pixel Sensor. 21
- MIP** Minimum Ionising Particle. 8, 10, 20, 51, 131
- MPV** Most Probable Value. 8
- NIEL** Non-Ionising Energy Loss. 13
- PCB** Printed Circuit Board. 25, 31, 32, 40
- PMT** Photo Multiplier Tube. 23
- ROC** ReadOut Chip. 26, 27
- SCC** Single Chip Card. 27, 28
- SM** Standard Model of particle physics. 1
- TB21** Test-Beam 21. 20, 21
- TB22** Test-Beam 22. 20
- TB24** Test-Beam 24. 20
- TCAD** Technology Computer-Aided Design. 69, 70
- TCT** Transient Current Technique. 2, 16, 38, 40, 54, 55, 69, 131
- TDAC** Threshold DAC. 26, 83–85, 87, 88
- TLU** Trigger Logic Unit. 23, 29, 31
- ToT** Time-over-Threshold. 26, 27, 87, 91, 92
- TSC** Thermally Stimulated Current. 14, 16

Bibliography

- [1] M. Thomson, *Modern Particle Physics*, Cambridge University Press,, 2013.
- [2] ATLAS Collaboration, Observation of a new particle in the search for the Standard Model Higgs boson with the ATLAS detector at the LHC, *Physics Letters B* 716 (1) (2012) 1–29. doi:<https://doi.org/10.1016/j.physletb.2012.08.020>.
- [3] CMS Collaboration, Observation of a new boson at a mass of 125 GeV with the CMS experiment at the LHC, *Physics Letters B* 716 (1) (2012) 30–61. doi:<https://doi.org/10.1016/j.physletb.2012.08.021>.
- [4] *Recent Developments in Gauge Theories*. Proceedings, Nato Advanced Study Institute, Cargese, France, August 26 - September 8, 1979, Vol. 59. doi:10.1007/978-1-4684-7571-5.
- [5] S.P. Martin, A Supersymmetry primer, in: *Perspectives on Supersymmetry*, WORLD SCIENTIFIC, 1998, pp. 1–98. doi:10.1142/9789812839657_0001.
- [6] H. Georgi, S. L. Glashow, Unity of All Elementary-Particle Forces, *Phys. Rev. Lett.* 32 (1974) 438–441. doi:10.1103/PhysRevLett.32.438.
- [7] L. Evans and P. Bryant, LHC Machine, *Journal of Instrumentation* 3 (08) (aug 2008). doi:10.1088/1748-0221/3/08/s08001.
- [8] G. Apollinari et al., High-Luminosity Large Hadron Collider (HL-LHC): Technical Design Report V. 0.1, CERN Yellow Reports 4/2017 (2017). doi:10.23731/CYRM-2017-004.
- [9] CMS Collaboration, The CMS experiment at the CERN LHC, *Journal of Instrumentation* 3 (08) (2008) S08004–S08004. doi:10.1088/1748-0221/3/08/s08004.
- [10] D. Contardo et al., Technical Proposal for the Phase-II Upgrade of the CMS Detector, CERN-LHCC-2015-010, LHCC-P-008, CMS-TDR-15-02 (6 2015). URL <https://cds.cern.ch/record/2020886>
- [11] A.M. Sirunyan et al. , Particle-flow reconstruction and global event description with the CMS detector, *Journal of Instrumentation* 12 (10) (2017) P10003–P10003. doi:10.1088/1748-0221/12/10/p10003.

Bibliography

- [12] A.S. Grove, *Physics and Technology of Semiconductor Devices*, John Wiley & Sons, 1967.
- [13] S. M. Sze, *Physics of Semiconductor Devices*, John Wiley & Sons, 2006.
- [14] F. Hartmann, *Evolution of Silicon Sensor Technology in Particle Physics*, Springer, 2017. doi:10.1007/978-3-319-64436-3.
- [15] H. Bichsel, Straggling in thin silicon detectors, *Rev. Mod. Phys.* 60 (1988) 663–699. doi:10.1103/RevModPhys.60.663.
- [16] P. A. Zyla et al., *Review of Particle Physics*, PTEP (2020). doi:10.1093/ptep/ptaa104.
- [17] D. Groom et al., Temperature dependence of mean number of of eh pairs per eV of x-ray energy deposit (2004). doi:https://www-ccd.lbl.gov/wSi.pdf.
- [18] Helmuth Spieler, *Semiconductor Detector Systems*, Oxford University Press, 2005.
- [19] S. Ramo, Currents Induced by Electron Motion, *Proceedings of the IRE* 27 (9) (1939) 584–585. doi:10.1109/JRPROC.1939.228757.
- [20] Scharf, Christian, *Radiation damage of highly irradiated silicon sensors*, Ph.D. thesis, Universität Hamburg (2018).
- [21] Becker, Julian, *Signal development in silicon sensors used for radiation detection*, Ph.D. thesis, DESY (2010).
- [22] L. Rossi et al., *Pixel detectors: From fundamentals to applications*, Springer Science & Business Media, 2006.
- [23] L. Vigani et al., Study of prototypes of LFoundry active CMOS pixels sensors for the ATLAS detector, *Journal of Instrumentation* 13 (02) (feb 2018). doi:10.1088/1748-0221/13/02/c02021.
- [24] T. Poehlsen et al., Charge losses in segmented silicon sensors at the Si–SiO₂ interface, *Nucl. Instrum. Meth. A* 700 (2013) 22–39. doi:https://doi.org/10.1016/j.nima.2012.10.063.
- [25] J. Schwandt et al., Surface effects in segmented silicon sensors, *Nucl. Instrum. Meth. A* 845 (2017) 159–163. doi:https://doi.org/10.1016/j.nima.2016.06.032.
- [26] C. Leroy and P.-G. Rancoita, *Principles of Radiation Interaction in Matter and Detection*, WORLD SCIENTIFIC, 2016.

- [27] M. Huhtinen, Simulation of non-ionising energy loss and defect formation in silicon, *Nucl. Instrum. Meth. A* 491 (1) (2002) 194–215. doi:[https://doi.org/10.1016/S0168-9002\(02\)01227-5](https://doi.org/10.1016/S0168-9002(02)01227-5).
- [28] M. Moll, Radiation damage in silicon particle detectors: Microscopic defects and macroscopic properties, Ph.D. thesis, Hamburg U. (1999).
- [29] M. Moll, Displacement Damage in Silicon Detectors for High Energy Physics, *IEEE Transactions on Nuclear Science* 65 (8) (2018) 1561–1582. doi:[10.1109/TNS.2018.2819506](https://doi.org/10.1109/TNS.2018.2819506).
- [30] L. R. Weisberg and H. Schade, A Technique for Trap Determinations in Low-Resistivity Semiconductors, *Journal of Applied Physics* 39 (1968). doi:<https://doi.org/10.1063/1.1655936>.
- [31] D. V. Lang, Deep-level transient spectroscopy: A new method to characterize traps in semiconductors, *Journal of Applied Physics* 45 (1974). doi:<https://doi.org/10.1063/1.1663719>.
- [32] Z. L. V. Eremin, E. Verbitskaya, The origin of double peak electric field distribution in heavily irradiated silicon detectors, *Nucl. Instrum. Meth. A* 476 (3) (2002) 556–564. doi:[https://doi.org/10.1016/S0168-9002\(01\)01642-4](https://doi.org/10.1016/S0168-9002(01)01642-4).
- [33] R. Klanner et al., Determination of the electric field in highly-irradiated silicon sensors using edge-TCT measurements, *Nucl. Instrum. Meth. A* (2020). doi:<https://doi.org/10.1016/j.nima.2019.162987>.
- [34] K. Deiters et al., Double screening tests of the cms ecal avalanche photodiodes, *Nucl. Instrum. Meth. A* 543 (2005) 549–558. doi:<https://doi.org/10.1016/j.nima.2005.01.088>.
- [35] CMS detector, <https://cms.cern/detector>, Accessed: 2022 (2022).
- [36] Cittolin, Sergio and Rácz, Attila and Spiccas, Paris, CMS The TriDAS Project: Technical Design Report, Volume 2: Data Acquisition and High-Level Trigger. CMS trigger and data-acquisition project, Technical design report. CMS, CERN, Geneva, 2002.
URL <http://cds.cern.ch/record/578006>
- [37] A. Dominguez et al., CMS Technical Design Report for the Pixel Detector Upgrade, Tech. rep. (Sep 2012).
URL <https://cds.cern.ch/record/1481838>
- [38] W. Adam et al., The CMS phase-1 pixel detector upgrade, *Journal of Instrumentation* 16 (2021). doi:[10.1088/1748-0221/16/02/p02027](https://doi.org/10.1088/1748-0221/16/02/p02027).

Bibliography

- [39] Apollinari, G and Béjar Alonso, I and Brüning, O and Lamont, M and Rossi, L, High-Luminosity Large Hadron Collider (HL-LHC): Preliminary Design Report, CERN Yellow Reports: Monographs, CERN, Geneva, 2015. doi:[10.5170/CERN-2015-005](https://doi.org/10.5170/CERN-2015-005).
- [40] The Phase-2 Upgrade of the CMS Tracker, Tech. rep., CERN, Geneva (Jun 2017). doi:[10.17181/CERN.QZ28.FLHW](https://doi.org/10.17181/CERN.QZ28.FLHW).
- [41] G. Steinbrück, Development of planar pixel sensors for the CMS Inner Tracker at the High-Luminosity LHC, Nucl. Instrum. Meth. A 978 (2020) 164438. doi:<https://doi.org/10.1016/j.nima.2020.164438>.
- [42] E. Currás et al., Study of small-cell 3D silicon pixel detectors for the high luminosity LHC, Nucl. Instrum. Meth. A 931 (2019) 127–134. doi:<https://doi.org/10.1016/j.nima.2019.04.037>.
- [43] R. Diener et al., The DESY II test beam facility, Nucl. Instr. and Meth. A 922 (2019). doi:<https://doi.org/10.1016/j.nima.2018.11.133>.
- [44] C. Hu-Guo et al., First reticule size MAPS with digital output and integrated zero suppression for the EUDET-JRA1 beam telescope, Nucl. Instr. and Meth. A 623 (2010). doi:<https://doi.org/10.1016/j.nima.2010.03.043>.
- [45] H. Jansen et al., Performance of the EUDET-type beam telescopes, EPJ Techniques and Instrumentation 3 (2016). doi:[10.1140/epjti/s40485-016-0033-2](https://doi.org/10.1140/epjti/s40485-016-0033-2).
- [46] G. Lynch, O. Dahl, Approximations to multiple Coulomb scattering, Nucl. Instr. and Meth. A 58 (1991). doi:[https://doi.org/10.1016/0168-583X\(91\)95671-Y](https://doi.org/10.1016/0168-583X(91)95671-Y).
- [47] D. Cussans, Description of the JRA1 Trigger Logic Unit (TLU), v0.2c, Tech. rep., University of Bristol (2009).
- [48] M. Garcia-Sciveres, The RD53A Integrated Circuit, Tech. Rep. CERN-RD53-PUB-17-001, CERN, Geneva (Oct 2017).
URL <https://cds.cern.ch/record/2287593>
- [49] M. Vogt et al., Characterization and Verification Environment for the RD53A Pixel Readout Chip in 65 nm CMOS, PoS TWEPP-17 (2018) 084. doi:[10.22323/1.313.0084](https://doi.org/10.22323/1.313.0084).
- [50] M. Daas et al., BDAQ53, a versatile pixel detector readout and test system for the ATLAS and CMS HL-LHC upgrades, Nucl. Instr. and Meth. A 986 (2021) 164721. doi:<https://doi.org/10.1016/j.nima.2020.164721>.

- [51] M. Hajheidari et al., Depth-dependent charge collection profile of pad diodes, *Nucl. Instrum. Meth. A* 1025 (2022) 166177. doi:<https://doi.org/10.1016/j.nima.2021.166177>.
- [52] FEMTO Messtechnik GmbH, Klosterstrasse 64, 10179 Berlin, Germany, <http://www.femto.de/>, Accessed: 2021 (2021).
- [53] "Hamamatsu Photonics K.K.", <https://www.hamamatsu.com/jp/en.html>, accessed: 2022-03-03 (2022).
- [54] J. Schwandt, CMS Pixel detector development for the HL-LHC, *Nucl. Instrum. Meth. A* 924 (2019) 59–63. doi:<https://doi.org/10.1016/j.nima.2018.08.121>.
- [55] F. Feindt, Silicon Pixel Sensors in the Inner Tracking System of the CMS Experiment, Ph.D. thesis, Universität Hamburg (2021).
- [56] C. Niemeyer, Edge-on Measurements on Planar Pixel Sensors for the CMS Phase 2 Upgrade, Ph.D. thesis, Universität Hamburg (2021).
- [57] "Fraunhofer IZM", <https://www.izm.fraunhofer.de>, Accessed: 2022 (2022).
- [58] "Zyklotron AG", <https://www.zyklotron-ag.de/>, Accessed: 2022 (2022).
- [59] P. Allport et al., Experimental determination of proton hardness factors at several irradiation facilities, *Journal of Instrumentation* (2019). doi:[10.1088/1748-0221/14/12/P12004](https://doi.org/10.1088/1748-0221/14/12/P12004).
- [60] Keyence Laser microscope, <https://www.keyence.com/>, accessed: 2022-04-05 (2022).
- [61] O. W. Murzewitz, Dead layer determination in radiation-damaged silicon diodes, Bachelor's thesis, Universität Hamburg (2021).
- [62] HW. Kraner et al., The use of the signal current pulse shape to study the internal electric field profile and trapping effects in neutron damaged silicon detectors, *Nucl. Instrum. Meth. A* (1993). doi:[https://doi.org/10.1016/0168-9002\(93\)90376-S](https://doi.org/10.1016/0168-9002(93)90376-S).
- [63] L. Beattie et al., Carrier lifetimes in heavily irradiated silicon diodes, *Nucl. Instrum. Meth. A* (1999). doi:[https://doi.org/10.1016/S0168-9002\(98\)01229-7](https://doi.org/10.1016/S0168-9002(98)01229-7).
- [64] G. Kramberger et al., Determination of effective trapping times for electrons and holes in irradiated silicon, *Nucl. Instrum. Meth. A* (2002). doi:[https://doi.org/10.1016/S0168-9002\(01\)01653-9](https://doi.org/10.1016/S0168-9002(01)01653-9).

Bibliography

- [65] Green, Martin A, Self-consistent optical parameters of intrinsic silicon at 300 K including temperature coefficients, *Solar Energy Materials and Solar Cells* 92 (11) (2008) 1305–1310. doi:<https://doi.org/10.1016/j.solmat.2008.06.009>.
- [66] R. Hartmann et al., Low energy response of silicon pn-junction detector, *Nucl. Instrum. Meth. A* 377 (2-3) (1996) 191–196. doi:[https://doi.org/10.1016/0168-9002\(96\)00254-9](https://doi.org/10.1016/0168-9002(96)00254-9).
- [67] G.F.Knoll, *Radiation detection and measurement*, John Wiley & Sons, 2010.
- [68] S. Wagner, *IEEE Standard Test Procedures for Semiconductor Charged-Particle Detectors*, IEEE, 2006.
- [69] J. Manfredi et al., On determining dead layer and detector thicknesses for a position-sensitive silicon detector, *Nucl. Instrum. Meth. A* 888 (2018) 177–183. doi:<https://doi.org/10.1016/j.nima.2017.12.082>.
- [70] E. Verbitskaya et al., Physical aspects of precise spectrometry of α -particles with silicon pn-junction detectors, *Nucl. Instrum. Meth. B* 84 (1) (1994) 51–61. doi:[https://doi.org/10.1016/0168-583X\(94\)95703-7](https://doi.org/10.1016/0168-583X(94)95703-7).
- [71] B.L.Wall et al., Dead layer on silicon p-i-n diode charged-particle detectors, *Nucl. Instrum. Meth. A* 744 (2014) 73–79. doi:<https://doi.org/10.1016/j.nima.2013.12.048>.
- [72] C. Scharf, R. Klanner, Measurement of the drift velocities of electrons and holes in high-ohmic $< 100 >$ silicon, *Nucl. Instrum. Meth. A* (2015). doi:<https://doi.org/10.1016/j.nima.2015.07.057>.
- [73] M.J.Berger et al., *Stopping-power and range tables for electrons, protons, and helium ions*, NIST Physics Laboratory Gaithersburg, MD, 1998.
- [74] test beam pixel telescope analysis, <https://github.com/pitzl/tele-scope>, Accessed: 2022 (2022).
- [75] G. Kramberger et al., Effective trapping time of electrons and holes in different silicon materials irradiated with neutrons, protons and pions, *Nucl. Instrum. Meth. A* (2002). doi:[https://doi.org/10.1016/S0168-9002\(01\)01263-3](https://doi.org/10.1016/S0168-9002(01)01263-3).
- [76] T.J. Brodbeck et al., A new method of carrier trapping time measurement, *Nucl. Instrum. Meth. A* (2000). doi:[https://doi.org/10.1016/S0168-9002\(00\)00573-8](https://doi.org/10.1016/S0168-9002(00)00573-8).
- [77] J. Fink et al., Characterization of charge collection in CdTe and CZT using the transient current technique, *Nucl. Instrum. Meth. A* (2006). doi:<https://doi.org/10.1016/j.nima.2006.01.072>.

- [78] G. Kramberger et al., Investigation of Irradiated Silicon Detectors by Edge-TCT, *IEEE Trans. Nucl. Sci.* (2010). doi:10.1109/TNS.2010.2051957.
- [79] I. Mandić et al., Edge-TCT measurements with the laser beam directed parallel to the strips, *Journal of Instrumentation* (2015). doi:10.1088/1748-0221/10/08/P08004.
- [80] I. Mandić et al., TCT measurements of irradiated strip detectors with a focused laser beam, *Journal of Instrumentation* (2013). doi:10.1088/1748-0221/8/04/P04016.
- [81] C. Scharf, F. Feindt, R. Klanner, , *Nucl. Instrum. Meth. A* (2020). doi:https://doi.org/10.1016/j.nima.2020.163955.
- [82] V. Chiochia et al., Simulation of heavily irradiated silicon pixel sensors and comparison with test beam measurements, *IEEE transactions on nuclear science* (2005). doi:10.1109/TNS.2005.852748.
- [83] Savić, Natascha, Development of pixel detectors for the inner tracker upgrade of the ATLAS experiment, Ph.D. thesis, Universitätsbibliothek der Ludwig-Maximilians-Universität (2018).
- [84] A. Gorišek et al. , The edge transient-current technique (E-TCT) with high energy hadron beam, *Nucl. Instrum. Meth. A* (2016). doi:https://doi.org/10.1016/j.nima.2016.03.061.
- [85] S. Agostinelli et al., Geant4—a simulation toolkit, *Nucl. Instrum. Meth. A* 506 (3) (2003) 250–303. doi:https://doi.org/10.1016/S0168-9002(03)01368-8.
- [86] J. Sempau, J.M. Fernández-Varea, E. Acosta, F. Salvat, Experimental benchmarks of the Monte Carlo code PENELOPE, *Nucl. Instrum. Meth. B* 207 (2) (2003) 107–123. doi:https://doi.org/10.1016/S0168-583X(03)00453-1.
- [87] G. Kramberger et al., Modeling of electric field in silicon micro-strip detectors irradiated with neutrons and pions, *Journal of Instrumentation* (2014). doi:10.1088/1748-0221/9/10/P10016.
- [88] T. Pöhlson, Charge Losses in Silicon Sensors and Electric-Field Studies at the Si-SiO₂ Interface, Ph.D. thesis, U. Hamburg, Dept. Phys. (2013).
- [89] "Synopsys TCAD", <https://www.synopsys.com/>, accessed: 2022-02-03 (2022).
- [90] J. Schwandt et al., A new model for the TCAD simulation of the silicon damage by high fluence proton irradiation, in: 2018 IEEE Nuclear Science Symposium and Medical Imaging Conference Proceedings (NSS/MIC), 2018, pp. 1–3. doi:10.1109/NSSMIC.2018.8824412.

Bibliography

- [91] A. Morozzi et al., TCAD advanced radiation damage modelling in silicon detectors, Tech. rep. (2019).
- [92] A. Affolder, P. Allport, G. Casse, Charge collection efficiencies of planar silicon detectors after reactor neutron and proton doses up to $1.6 \times 10^{16} \text{ cm}^{-2}$, Nucl. Instrum. Meth. A 612 (2010) 470–473. doi:[10.1016/j.nima.2009.08.005](https://doi.org/10.1016/j.nima.2009.08.005).
- [93] M. Ferrero et al., Recent studies and characterization of UFSD sensors, in: 34th RD50 Workshop, 2019.
- [94] P. Asenov et al., Sensitivity analysis of parameters characterizing the bulk radiation damage on silicon devices, in: 17th Trento Workshop, 2022.
- [95] J. Schwandt R. Klanner, On the weighting field of irradiated silicon detectors, Nucl. Instrum. Meth. A 942 (2019) 162418. doi:<https://doi.org/10.1016/j.nima.2019.162418>.
- [96] C. Neubüser, Impact of Irradiations by Protons with different Energies on Silicon Sensors, Master’s thesis, Hamburg U. (2013).
- [97] MATLAB2019b, <https://de.mathworks.com/help/matlab/ref/spline.html>, Accessed: 2022 (2022).
- [98] M. Standke, Characterization of the Joined ATLAS and CMS RD53A Pixel Chip, Master’s thesis, Universität Bonn, presented 28 Feb 2019 (2019). doi:<https://cds.cern.ch/record/2717863>.
- [99] L.Gaioni, F.Loddo, CMS analog front-end: simulations and measurements, Tech. rep., CERN, Geneva (Dec 2020).
- [100] L.Gaioni, Linear Analog Front-end, Guidelines and Recommendations, Tech. rep., CERN, Geneva (218).
URL https://twiki.cern.ch/twiki/pub/RD53/RD53ATesting/LIN_AFE_guidelines.pdf
- [101] P.Ahlburg et al., EUDAQ-a data acquisition software framework for common beam telescopes, JINST 15 (01) (2020) P01038. arXiv:1909.13725, doi:[10.1088/1748-0221/15/01/P01038](https://doi.org/10.1088/1748-0221/15/01/P01038).
- [102] R. Turchetta, Spatial resolution of silicon microstrip detectors, Nucl. Instrum. Meth. A 335 (1) (1993) 44–58. doi:[https://doi.org/10.1016/0168-9002\(93\)90255-G](https://doi.org/10.1016/0168-9002(93)90255-G).
- [103] M. Paterno, Calculating efficiencies and their uncertainties, Tech. rep., FNAL (2004). doi:[10.2172/15017262](https://doi.org/10.2172/15017262).

- [104] I. Zoi et al., Position resolution with 25 μm pitch pixel sensors before and after irradiation, *Nucl. Instrum. Meth. A* 1021 (2022) 165933. doi:<https://doi.org/10.1016/j.nima.2021.165933>.
- [105] Zoi, Irene, Search for diboson resonances in the all jets final state with CMS at $\sqrt{s} = 13$ TeV and pixel sensors development for HL-LHC., Ph.D. thesis, Universität Hamburg (2021).
- [106] M. Boronat et al., Physical limitations to the spatial resolution of solid-state detectors, *IEEE Transactions on Nuclear Science* 62 (1) (2015) 381–386. doi:10.1109/TNS.2014.2376941.
- [107] LHCb Collaboration, Expression of Interest for a Phase-II LHCb Upgrade: Opportunities in flavour physics, and beyond, in the HL-LHC era, Tech. rep., CERN, Geneva (Feb 2017).
URL <https://cds.cern.ch/record/2244311>
- [108] ATLAS Collaboration, Technical Design Report for the ATLAS Inner Tracker Pixel Detector, Tech. rep., CERN (Sep 2017). doi:10.17181/CERN.FOZZ.ZP3Q.
- [109] S. T. et al., A new generation of radiation hard 3d pixel sensors for the atlas upgrade, *Nucl. Instrum. Meth. A* 982 (2020) 164587. doi:<https://doi.org/10.1016/j.nima.2020.164587>.
- [110] S. Terzo, Phase 2 Upgrade of the ATLAS Inner Tracker, in: 16th Vienna Conference on Instrumentation, 2022.
- [111] DAQ and test system for the RD53 readout chips, <https://gitlab.cern.ch/silab/bdaq53>, Accessed: 2022 (2022).

Appendix A

Table .1 and Table .2 show the Measured CCE values using α -particles (CCE_α) and red-light laser (CCE_L) and calculated CCE in the active region (CCE_{act}), non-active region (CCE_{inact}), and thickness of the inactive region (d_{inact}) using the model proposed in Section 4.4.2 for n^+p and p^+p sides.

fluence & bias voltage	$CCE_\alpha^{2.57 \text{ MeV}}$	$CCE_\alpha^{2.06 \text{ MeV}}$	$CCE_\alpha^{1.63 \text{ MeV}}$	CCE_L	CCE_{act}	CCE_{inact}	d_{inact}
$2 \times 10^{15} \text{ cm}^{-2}$, 800 V	0.69	0.65	0.58	0.58	0.81	0.28	2.5 μm
$2 \times 10^{15} \text{ cm}^{-2}$, 700 V	0.67	0.61	0.54	0.56	0.78	0.30	2.6 μm
$2 \times 10^{15} \text{ cm}^{-2}$, 600 V	0.63	0.59	0.55	0.55	0.75	0.31	2.8 μm
$2 \times 10^{15} \text{ cm}^{-2}$, 500 V	0.63	0.56	0.51	0.52	0.71	0.31	2.7 μm
$2 \times 10^{15} \text{ cm}^{-2}$, 400 V	0.58	0.52	0.47	0.49	0.65	0.31	2.9 μm
$2 \times 10^{15} \text{ cm}^{-2}$, 300 V	0.48	0.44	0.40	0.43	0.53	0.33	3.0 μm
$8 \times 10^{15} \text{ cm}^{-2}$, 800 V	0.47	0.45	0.39	0.36	0.59	0.0	2.2 μm
$8 \times 10^{15} \text{ cm}^{-2}$, 700 V	0.44	0.42	0.38	0.34	0.56	0.02	2.3 μm
$8 \times 10^{15} \text{ cm}^{-2}$, 600 V	0.41	0.39	0.35	0.32	0.52	0.02	2.2 μm
$8 \times 10^{15} \text{ cm}^{-2}$, 500 V	0.37	0.34	0.31	0.29	0.44	0.0	1.8 μm
$8 \times 10^{15} \text{ cm}^{-2}$, 400 V	0.31	0.30	0.27	0.25	0.37	0.0	1.7 μm
$8 \times 10^{15} \text{ cm}^{-2}$, 300 V	0.27	0.25	0.24	0.21	0.31	0.0	1.6 μm

Table .1: n^+p -side

fluence & bias voltage	$CCE_\alpha^{2.88 \text{ MeV}}$	$CCE_\alpha^{2.42 \text{ MeV}}$	$CCE_\alpha^{2.01 \text{ MeV}}$	CCE_L	CCE_{act}	CCE_{inact}	d_{inact}
$2 \times 10^{15} \text{ cm}^{-2}$, 800 V	0.81	0.82	0.79	0.74	0.84	0.0	0.5 μm
$2 \times 10^{15} \text{ cm}^{-2}$, 700 V	0.77	0.78	0.75	0.71	0.81	0.0	0.6 μm
$2 \times 10^{15} \text{ cm}^{-2}$, 600 V	0.72	0.71	0.70	0.67	0.75	0.0	0.4 μm
$2 \times 10^{15} \text{ cm}^{-2}$, 500 V	0.63	0.63	0.62	0.60	0.65	0.0	0.3 μm
$2 \times 10^{15} \text{ cm}^{-2}$, 400 V	0.45	0.46	0.46	0.43	0.46	0.0	0.3 μm
$2 \times 10^{15} \text{ cm}^{-2}$, 300 V	0.28	0.29	0.29	0.27	0.29	0.0	0.3 μm
$8 \times 10^{15} \text{ cm}^{-2}$, 800 V	0.56	0.53	0.51	0.53	0.54	0.0	0.1 μm
$8 \times 10^{15} \text{ cm}^{-2}$, 700 V	0.49	0.48	0.47	0.47	0.49	0.0	0.1 μm
$8 \times 10^{15} \text{ cm}^{-2}$, 600 V	0.43	0.41	0.40	0.40	0.42	0.0	0.1 μm
$8 \times 10^{15} \text{ cm}^{-2}$, 500 V	0.34	0.33	0.32	0.32	0.34	0.0	0.1 μm
$8 \times 10^{15} \text{ cm}^{-2}$, 400 V	0.27	0.26	0.26	0.26	0.27	0.0	0.1 μm
$8 \times 10^{15} \text{ cm}^{-2}$, 300 V	0.22	0.21	0.21	0.21	0.22	0.0	0.1 μm

Table .2: p^+p -side

Appendix B

In Section 5.6, CCE_{x_i} profiles of irradiated and non-irradiated diodes are extracted and shown in Fig. 5.22. These values are printed in Table .3.

CCE_{x_i}	-65 μm	-45 μm	-25 μm	-5 μm	15 μm	35 μm	55 μm
$\Phi_{eq} = 0 \times 10^{15} \text{ cm}^{-2}$ ($5.0 \times 5.0 \text{ mm}^2$)	0.9838	0.9951	1.0040	1.0085	1.0086	1.0055	1.0004
$\Phi_{eq} = 0 \times 10^{15} \text{ cm}^{-2}$ ($2.5 \times 2.5 \text{ mm}^2$)	1.0038	1.0047	1.0063	1.0075	1.0087	1.0092	1.0103
$\Phi_{eq} = 2 \times 10^{15} \text{ cm}^{-2}$, $V_{\text{bias}} = 800 \text{ V}$	0.8114	0.8808	0.9120	0.9216	0.9249	0.9064	0.8317
$\Phi_{eq} = 2 \times 10^{15} \text{ cm}^{-2}$, $V_{\text{bias}} = 600 \text{ V}$	0.7952	0.8308	0.8728	0.8922	0.8768	0.8628	0.8166
$\Phi_{eq} = 2 \times 10^{15} \text{ cm}^{-2}$, $V_{\text{bias}} = 400 \text{ V}$	0.6777	0.7491	0.7853	0.7963	0.7836	0.7589	0.6778
$\Phi_{eq} = 2 \times 10^{15} \text{ cm}^{-2}$, $V_{\text{bias}} = 200 \text{ V}$	0.4102	0.4994	0.4964	0.4749	0.3273	0.2402	0.2318
$\Phi_{eq} = 2 \times 10^{15} \text{ cm}^{-2}$, $V_{\text{bias}} = 100 \text{ V}$	0.3263	0.3460	0.2973	0.1397	0.0665	0.0802	0.1201
$\Phi_{eq} = 4 \times 10^{15} \text{ cm}^{-2}$, $V_{\text{bias}} = 800 \text{ V}$	0.7103	0.8021	0.8490	0.8576	0.8455	0.8245	0.7986
$\Phi_{eq} = 4 \times 10^{15} \text{ cm}^{-2}$, $V_{\text{bias}} = 600 \text{ V}$	0.6442	0.7072	0.7481	0.7673	0.7624	0.7324	0.6621
$\Phi_{eq} = 4 \times 10^{15} \text{ cm}^{-2}$, $V_{\text{bias}} = 400 \text{ V}$	0.4986	0.5679	0.5946	0.6148	0.5584	0.4998	0.4357
$\Phi_{eq} = 4 \times 10^{15} \text{ cm}^{-2}$, $V_{\text{bias}} = 200 \text{ V}$	0.3758	0.3832	0.3545	0.2307	0.1301	0.1628	0.2045
$\Phi_{eq} = 4 \times 10^{15} \text{ cm}^{-2}$, $V_{\text{bias}} = 100 \text{ V}$	0.2010	0.2581	0.1870	0.0826	0.0700	0.0676	0.0984
$\Phi_{eq} = 8 \times 10^{15} \text{ cm}^{-2}$, $V_{\text{bias}} = 800 \text{ V}$	0.5511	0.5920	0.6286	0.6499	0.6502	0.6338	0.6032
$\Phi_{eq} = 8 \times 10^{15} \text{ cm}^{-2}$, $V_{\text{bias}} = 600 \text{ V}$	0.4523	0.4975	0.5291	0.5388	0.5295	0.5082	0.4848
$\Phi_{eq} = 8 \times 10^{15} \text{ cm}^{-2}$, $V_{\text{bias}} = 400 \text{ V}$	0.3982	0.4050	0.3913	0.3469	0.2955	0.2703	0.2686
$\Phi_{eq} = 8 \times 10^{15} \text{ cm}^{-2}$, $V_{\text{bias}} = 200 \text{ V}$	0.2490	0.2682	0.2101	0.1199	0.0816	0.1048	0.1611
$\Phi_{eq} = 8 \times 10^{15} \text{ cm}^{-2}$, $V_{\text{bias}} = 100 \text{ V}$	0.1732	0.1552	0.0868	0.0435	0.0443	0.0485	0.0781
$\Phi_{eq} = 12 \times 10^{15} \text{ cm}^{-2}$, $V_{\text{bias}} = 800 \text{ V}$	0.4209	0.4671	0.4996	0.5095	0.5010	0.4807	0.4475
$\Phi_{eq} = 12 \times 10^{15} \text{ cm}^{-2}$, $V_{\text{bias}} = 600 \text{ V}$	0.4021	0.4070	0.4031	0.3865	0.3617	0.3446	0.3295
$\Phi_{eq} = 12 \times 10^{15} \text{ cm}^{-2}$, $V_{\text{bias}} = 400 \text{ V}$	0.2334	0.3109	0.3230	0.2649	0.1798	0.1559	0.2152
$\Phi_{eq} = 12 \times 10^{15} \text{ cm}^{-2}$, $V_{\text{bias}} = 200 \text{ V}$	0.1671	0.2120	0.1704	0.0961	0.0729	0.0718	0.1212
$\Phi_{eq} = 12 \times 10^{15} \text{ cm}^{-2}$, $V_{\text{bias}} = 100 \text{ V}$	0.1324	0.1159	0.0582	0.0380	0.0409	0.0322	0.0558

Table .3: CCE_{x_i} profiles of irradiated and non-irradiated diodes.

Acknowledgments

First of all, I would like to thank my supervisor, Erika Garutti, for giving me the opportunity to work in the field of silicon sensors and for supporting me throughout the journey. I thank Robert Klanner for his critical and valuable comments on my work and writings. I thank Jörn Schwandt for providing me with the simulation results and tips on practical aspects of pixel sensors.

I like to thank Daniel Pitzl and Aliakbar Ebrahimi for their introduction to test-beam measurements of silicon sensors and for providing me with the analysis codes. I thank Finn Feindt for showing me the details of his work, answering my questions with patience and proofreading my thesis. I thank Annika Vauth for reading the draft of my thesis and giving me useful comments. I thank Massimiliano Antonello for helping me with the test-beam and developing a graphic interface for the analysis code. I thank Georg Steinbrück for coordinating all the test-beam shifts.

Taking data in the lab and test-beam would not be possible without the help of our technician team, especially Peter Buhmann and Stephan Martens. I also thank our IT team, Rainer-Peter Feller and Ronald Mohrmann, for supporting us during our test-beam campaign.

I thank all my colleagues in Hamburg who have been also very good friends and made the experience enriching. Finally, I would like to thank my family for their support and patience in this journey.

Eidesstattliche Versicherung **/Declaration on Oath**

Hiermit versichere ich an Eides statt, die vorliegende Dissertationsschrift selbst verfasst und keine anderen als die angegebenen Hilfsmittel und Quellen benutzt zu haben.

Hamburg, den 19.07.2022

Unterschrift der Doktorandin / des Doktoranden